ENVIRONMENTAL EFFECTS ON CRACK HEALING AND STATIC FATIGUE BEHAVIOR OF GLASS AND POLYCRYSTALLINE CERAMICS

VOLUME I

By

Brett Allen Wilson

A DISSERTATION

Submitted to
Michigan State University
in Partial Fulfillment of the Requirements
for the Degree of

DOCTOR OF PHILOSOPHY

Department of Materials Science and Mechanics

1998

ABSTRACT

ENVIRONMENTAL EFFECTS ON CRACK HEALING AND STATIC FATIGUE BEHAVIOR OF GLASS AND POLYCRYSTALLINE CERAMICS

By

Brett Allen Wilson

An Environmental Scanning Electron Microscope (ESEM) was used for in-situ studies of static fatigue growth of Vickers indent cracks in polycrystalline alumina. Cracks advanced via static fatigue along a tortuous path with grain bridging and crack deflections on the order of a single grain diameter.

In-situ ESEM studies of healing of Vickers indent cracks in soda-lime silicate glass found healing to occur at 8 % r.h. and at 400 °C. Increased levels of initial humidity decreased the temperature at which healing initiated. The crack morphology included slow crack regression from the crack tip towards the indent impression and multiple crack pinch-off (above 550 °C). Debris in a crack hindered complete healing.

Conventional heating was used in healing of soda-lime silica glass where Vickers crack lengths were measured via optical microscopy. Microscopy showed crack tip blunting, pinch-off, and sub-surface spheroidization. The more complete healing observed for cracks aged in 45 % r.h. than in 0 % r.h. was attributed to water vapor entering the glass structure and decreasing the local glass transition temperature

and viscosity along the crack faces.

Crack healing experiments on polycrystalline alumina were performed using both conventional and microwave heating. No effect of aging environment was found for conventional healing of alumina. The relative crack healing ($[2c_{initial}-2c_{heal}]/2c_{initial}$) behavior for 49 and 98 N indent cracks was nearly identical. Crack healing was modeled by a diffusive transport model originally developed by Dutton and Stevens showing significantly lower activation energies for conventional compared to microwave heating. Microwave heating at 10 °C/minute had much greater healing than at 75 °C/minute.

DEDICATION

I would like to dedicate this Dissertation to my family (my mom and Dad, brother and sister-in-law, grandmas and grandpa, aunts and uncle). Without their love and support, I would not have had the self-confidence to try a PhD or the fortitude to survive one.

ACKNOWLEDGEMENTS

First and foremost I would like to acknowledge and thank Dr. Case for his instruction, guidance, and support throughout my time working toward a PhD. I would like to acknowledge the Michigan Research Excellence Funds for the financial support of the ESEM project and the CMSC including Dr. Drzal, Mike Rich, Steve Rozeveld, and Richard Schalek for their assistance and for the use of the ESEM and the Surface Analysis Lab. I would also like to acknowledge Dr. Clarence Suelter, Dr. Merle Heidemann, Dr. Joyce Parker and the Division of Science Education for their facilitation of my teaching growth and for awarding me a NASA Research Teaching Assistantship which partially funded my teaching work for a year and enabled my re-design of the MSM 250 Lab. I would like to thank several people for their help John Helmuth (for the composite plate), Kurt Niemeyer (for cutting tabs), Kiyong Lee (for microwaving specimens), Jong Gi Lee (for microwaving a specimen), and Ben Simkin (for running the Camscan). I would also like to acknowledge Dr. Martin Crimp for making the field emission SEM available for my use. I would like to acknowledge Pat Sneary, Ben Simkins, Mark Wilenski, and my father for useful discussions about my work. I definitely must recognize and thank Julian Ambriz, Pat Sneary, and Wendy Reffeor for their friendship, support, and help in keeping me going.

TABLE OF CONTENTS

LIST OF TABLES

LIST OF FIGURES

1. INTRODUCTION AND RESEARCH OBJECTIVES

1.1 Introduction

Ceramic materials are used in many different areas including electronics, dentistry, automotive engine components, industrial tooling, and biological prostheses. Mechanical, electrical, and magnetic properties are important for these applications. The presence of cracks in a ceramic part will change the mechanical, electrical and magnetic properties of the material.

Static fatigue (which is also termed stress rupture or environmentally-assisted slow crack growth) of ceramics and ceramic composites involves crack propagation at stresses lower than the stress required for instantaneous fracture. A ceramic material subjected to a static (constant) load thus can exhibit a decreasing mechanical strength as function of time. Strength degradation is typically linked to the stress corrosion of pre-existing flaws in the material, where stress corrosion occurs via the interaction of the ambient environment and highly strained atomic bonds at the crack tip. Water, even in concentrations of parts per million (ppm) as in the ambient environment, can lead to very significant stress corrosion and static fatigue in ceramics.

For a number of important application areas for ceramic composites, static fatigue can be an important concern. For example, ceramic engine components are stressed in high temperature environments that can include water vapor, since water is

produced during the combustion of hydrocarbon fuels.

Crack healing could be used as the last step in ceramic manufacturing to reduce or eliminate cracks in the final part. Crack healing in ceramics could also potentially be used to repair ceramic parts which had been damaged in service.

1.2 Research Objectives

The main objective of this research is to investigate the effects of time, temperature and humidity on crack healing and static fatigue crack growth behavior in ceramics.

Static fatigue crack growth was investigated in-situ using a tensile stage in the ESEM. The growth of Vickers indentation cracks over time at different levels of load and humidity was observed.

Crack healing behavior of glass was observed in-situ using a hot stage for the Environmental Scanning Electron Microscope (ESEM). Additional healing studies for glass were performed in conventional furnaces at temperatures below that for bulk viscous flow in the glass to further investigate and attempt to model the effects of time, temperature and humidity without having sample damage or bulk dimension changes which would be undesirable for industrial healing processes. Healing of polycrystalline alumina in conventional furnaces was studied at temperatures of less than 1500 °C where the specimen surfaces would not be damaged by excessive thermal etching or other bulk specimen damage or dimension changes could occur which would be undesirable for industrial healing processes. Healed polycrystalline alumina specimens where observed in a field emission scanning electron microscope to reveal the morphology changes in polycrystalline alumina during healing at

temperatures below 1500 °C. Microwave heating of polycrystalline alumina was also performed to compare crack healing behavior in conventional and microwave furnaces.

The activation energy and preexponential factor for diffusion during crack healing were re-analyzed using the original data for two investigations from the literature on crack healing in single crystal LiF ceramics. The re-calculated activation energies and preexponential factors for diffusion were compared to the originally calculated values and were used to reach different conclusions about the diffusional healing mechanism(s).

2. LITERATURE REVIEW

2.1 Static Fatigue Behavior of Ceramics

Static fatigue in ceramics refers to a time-dependent weakening of a material under constant stress due to environmentally-assisted subcritical (slow) crack growth. Static fatigue is a combination of a mechanical behavior of ceramics under tensile load and an environmental effect. The mechanical behavior of ceramics is related to the atomic bonding behavior of ceramic materials. The room temperature tensile behavior of ceramics is predominantly brittle in nature.

2.1.1 Atomic Bonding in Ceramics

Ceramics are ionically and covalently bonded inorganic materials. Examples of ceramics with ionic bonding are: NaCl (sodium chloride), MgO (magnesium oxide), LiF (lithium fluoride), SiO_2 (silica), and Al_2O_3 (alumina). Ceramic materials such as SiC (silicon carbide), Si_3N_4 (silicon nitride), BN (boron nitride), WC (tungsten carbide), and TiB_2 (titania diboride) are examples of covalently bonded ceramic materials [1-2]. Ionic and covalently bonded ceramics typically have a high bond strength, which is reflected in the high melting temperatures observed for ceramics (typically higher than 2000 °C) [3]. Close packing of the atoms in crystalline materials requires that the atoms be essentially spherical, of identical size and have

non-directional bonding between atoms [1]. Ceramic materials which are composed of two or more types of atoms often have atoms that can be very different in size and so may not be close packed even if ionically bonded. In fact, most ceramic crystal structures are very far from being close packed [2].

The open crystal structure of most ceramics coupled with the high bond strength means that very few ceramic materials have dislocation motion below 1000 to 1200 °C [2]. NaCl, LiF and MgO are examples of ceramic materials which have dislocation movement at low temperatures, however, these are not commonly used ceramic materials, at least not by themselves (MgO is commonly added to other ceramic materials such as SiO_2 and Al_2O_3). Single crystals of Al_2O_3 do not have dislocation motion until temperatures above 1260 °C [4]. Ceramic materials with covalent bonding have limited dislocation motion even at high temperatures. Ceramic glasses will not have dislocation motion either, since they are by definition non-crystalline solids.

2.1.2 Room Temperature Tensile Behavior

Since most common ceramic materials (SiC, Si_3N_4, BN, WC, Al_2O_3 and glass) do **NOT** have dislocation motion at room temperature, ceramics have **very** limited plastic deformation and fracture in a **BRITTLE** manner. The stress-strain behavior for most monolithic ceramics simply consists of elastic deformation until fracture. On an atomic level, elastic strain is actually the result of changes in interatomic spacing due to the applied stress. The elastic modulus for covalently bonded ceramics is higher than that observed in metals due to the higher strength of the covalent bonding

compared to metallic bonding. For example SiC has an elastic modulus of over 400 GPa [3], while many common steels have elastic moduli around 200 GPa [5].

The theoretical strength to break the atomic bonds during tensile loading of ceramics can be calculated using the elastic modulus, E, and is typically $\frac{E}{10}$ to $\frac{E}{5}$ [3-4]. However, the actual fracture strengths of polycrystalline ceramics are only about $\frac{E}{100}$ to $\frac{E}{1000}$[3-4]. The failure at actual applied loads well below the theoretical fracture strength is the result of the presence of pores, flaws, and cracks which cause local regions of stress concentration.

The fracture toughness, K_{Ic}, measures the material's resistance to crack growth:

$$K_{I_c} = Y \sigma \sqrt{\pi} \sqrt{c} \qquad (1)$$

where K_{Ic} is the fracture toughness (also the critical stress intensity factor), Y is a geometric factor dependent on specimen and crack geometry, σ is the stress at failure, c is the half the crack length (2c). For aluminum alloys K_{Ic} values range from 20 to 40 MPa $m^{0.5}$, while for steels, K_{Ic} values range from 60 to over 100 MPa $m^{0.5}$ [6]. The fracture toughness values for ceramics are **much** lower. For example, the fracture toughness for soda lime silicate glass ranges from 0.7 to 0.8 MPa $m^{0.5}$ [7]. Polycrystalline ceramics have fracture toughness values which are slightly higher than that for glass, but that are still much lower than that of metals. Al_2O_3 has a K_{Ic} value of 4.0 MPa $m^{0.5}$, while Si_3N_4 has about the highest fracture toughness value for non-transformation toughened ceramics with a K_{Ic} value of 5.6 MPa $m^{0.5}$ [6].

The lack of crack resistance means that very small flaws in ceramic specimens act as stress concentrators from which cracks form and subsequently grow. The flaws can be surface flaws resulting from scratches, machining or thermal shock. The flaws can also be volume flaws from pores (voids left over from sintering), or microcracks caused by thermal expansion anisotropy, thermal expansion mismatch between phases, or phase transformations. Control or elimination of flaws in ceramics during processing is the aim of research in ceramic processing, however, in practical applications it is virtually impossible. The limited ability to control the flaw size leads to a variation in the population of flaws for a given specimen.

For specimens with low crack resistance, as the applied tensile stress is increased, the cracks will continue growing until the largest crack grows to a critical length. At the critical crack length, the local stress intensity factor exceeds the fracture toughness of the material and results in fracture. The larger the size of the flaw in the ceramic specimen, the higher the stress intensity at the flaw, and consequently the lower the fracture strength of the specimen.

Due to the variation in fracture strengths in tensile loading resulting from stress concentration at flaws, along with the difficulty of preparing ceramic test specimens having normal tensile test specimen geometries, different strength testing is used for ceramics than metals and polymers. Three or four point bend testing is commonly performed on ceramics and is often referred to by ceramists as modulus of rupture (MOR) testing or bend strength testing. Since ceramics do not have plastic deformation, the stress state in bend testing is known from linear fracture mechanics analysis. The tensile forces are at a maximum on one surface, decrease to zero at the

midplane of the specimen, and reach a maximum compressive force at the other surface. Only a fraction of the specimen is under maximum tensile stress during bend testing, while in normal tensile testing the entire volume of the specimen in the reduced cross sectional area is under maximum stress. From a statistical standpoint, the chance of an unusually large flaw being under maximum stress is very small in bending and very probable in normal tensile testing. Consequently, much less scatter in fracture strength data is observed in bend testing than in tensile testing requiring fewer specimens for testing in bend testing than in tensile testing.

2.1.3 Static Fatigue Investigations

In ceramics, "fatigue" is a word that is not just used to describe the behavior of a material under varying load (as in metals). "Fatigue" is used for many different time-dependent phenomena observed in ceramics. For ceramics, the term "cyclic mechanical fatigue" is used to describe the behavior of ceramics under varying mechanical load and is the equivalent of the term "fatigue" used in metals literature. Other examples of the use of the term in ceramics include "thermal fatigue" where the strength decreases from repeated thermal shock and "static fatigue" where the phenomena of a reduction in strength and/or a growth in cracks under a constant applied load is a result of environmental effects. In static fatigue of ceramics, growth of flaws occurs at stress levels lower than required for instantaneous failure and is also referred to as subcritical crack growth [8-9]. Subcritical crack growth can continue until a critical crack length is reached and catastrophic failure ensues [8-9].

2.1.3.1 Standard Static Fatigue Testing

Testing of static fatigue subcritical crack growth in ceramics is traditionally performed by direct optical measurement of a macrocrack under constant mechanical load for double cantilever beam specimens or double-torsion specimens [9-20]. Double cantilever beam and double-torsion testing measures the crack length as a function of time under constant load. The crack length and time measurements are converted to change in crack length per unit time (da/dt or V) values while the load and the crack length measurements are converted to stress intensity (K_I) values. The data is reported as crack velocity (V) versus stress intensity (K_I) data.

The cracks in DCB specimens are macrocracks, and it is now recognized that, at least in part, the difficulty with using DCB data to predict static fatigue lifetimes is the fact that most in-service failures originate from microcracks [21]. Microcracks, include microcracks or "natural flaws" that are inherent in the material, such as microcracks that occur due to handling, processing flaws, etc. For microcracks, subcritical crack propagation behavior under constant load (static fatigue) can differ substantially from that behavior observed for macrocracks [21].

In static fatigue "lifetime" testing (where time to failure under a static load is measured), often the surfaces are abraded to approximate a "natural" flaw population, that is a flaw population that originates from handling, cutting, grinding, or the initial processing (sintering) of the ceramic specimen. However, for abraded specimens, it is impossible to obtain information on the initial flaw length and position, thus one can not determine the stress state under which the flaws begin to propagate. Furthermore, details of the crack propagation process itself are unaccessible.

2.1.3.2 Findings of Standard Static Fatigue Testing

Glass has been the focus of much of the static fatigue testing of subcritical crack growth in ceramics. Wierderhorn performed double cantilever static fatigue experiments on soda-lime-silicate glass in environments with 0.017% to 100% relative humidity and 25 °C [8]. The experiments revealed an increase in crack velocity with increasing relative humidity. The importance of water vapor on the static fatigue has been well established from many other experiments [10-12, 22]. Further studies by Wierderhorn and others have shown the existence of very slow static fatigue crack growth in vacuum (i.e. without the presence of water vapor) for soda-lime-silicate, aluminosilicate, borosilicate, and high leaded glasses [23-24]. The rate of the static fatigue slow crack growth depended strongly on the composition of the glass material tested. For example, no static fatigue slow crack growth was observed for fused silica and low-alkali borosilicate glasses tested in vacuum [23-24]. For polycrystalline ceramics, the static fatigue crack growth has been related to the amount of glassy phase located at the grain boundaries. The microstructure of the material also plays an important role in static fatigue crack growth [13, 22].

The process of static fatigue is relatively complicated, in that some researchers associate static fatigue primary with environmental attack at glassy phases between grains or at interfaces between matrix and reinforcing phases. For example, Choi and Horibe [22] relate static fatigue in alumina and silicon nitride to the glassy phase between grains of the ceramic. Choi and Horibe [22] found that silicon nitride specimens that contained an appreciable glassy phase are relatively sensitive to static fatigue, while reaction bonded silicon nitride (RBSN), which contains very little glassy

phase, is relatively insensitive to static fatigue. However, for higher temperature applications, static fatigue results from the reaction bonding process which leaves unreacted silicon in the interior of RBSN. This unreacted silicon can be converted to silica upon heating in air. The silica evolved within RBSN specimens renders RBSN useless for high temperature applications. In a study of both static and cyclic fatigue in silicon nitride, Jacobs and Chen [25] found a stress intensity-crack velocity (K-v) relation for static fatigue of silicon nitride that is similar to that observed for silicate glasses. Jacobs and Chen [25] then infer that the similarity of the static fatigue behavior for silicon nitride and silicate glasses may be due to the Y-Si-Al-O-N glass at the grain boundaries.

In both glassy silica (SiO_2) and single-crystal alumina (Al_2O_3), water and NH_3 (ammonia) chemisorb on the highly strained bonds at the crack tip [26-28]. Michalske et al. [29] give a model in which a polar molecule such as water or NH_3 undergo a "concerted reaction" with the Al-O or Si-O bonds that results in the breaking of the bond and hence the propagation of the crack. Thus static fatigue is NOT always associated with grain boundaries containing silicate glass. Single-crystal alumina certainly does not have grain boundaries and so the bonds being broken are Al-O bonds rather than Si-O bonds. Thus while silicate phases at grain boundaries may be important, such phases are apparently not required for static fatigue in ceramics.

2.2 Crack Healing in Ceramics

Crack healing has been observed in a variety of different ceramic materials including single crystals [30-32], polycrystalline ceramics [31, 33-34], inorganic glasses [35-36],

and ceramic composites [37]. Three general mechanisms have been reported for crack healing in ceramics: diffusion-driven thermal healing, adhesion from intermolecular forces, and reaction products from chemical reactions at the crack tip [33]. The environment has been found to influence crack healing in ceramics [35-36, 38-39]. In diffusion driven thermal healing, morphology changes have been treated theoretically [40-41] and observed experimentally [30-32, 34, 42-44]. Crack healing has been investigated via strength recovery testing after thermal annealing cycles [22, 31, 34, 45, 47-52]. Healing in alumina has also been investigated via Vickers indent crack length changes after thermal annealing [37].

2.2.1 Role of Environment

Crack healing studies in inorganic glasses have frequently emphasized the role of environmental humidity in the crack healing process. Holden and Frechette studied the environmental effect on thermal annealing of soda-lime-silica glass by varying the presence of humidity during different portions of the heating cycle [35]. Cracks were formed in specimens from thermal down-shock by a metal probe which gave crack depths ranging from 191 to 900 microns [35]. Five different annealing cycles were used for cracked specimens annealed to 550 °C by applying the humid environment (water vapor pressure of 30 kPa) during different portions of the heating cycle and varying the length of the hold at the annealing temperature (see Table 1 for detailed conditions) [35]. After annealing, the specimens were fractured using a ring-on-ring test and the resulting fracture surfaces were observed using differential interference contrast (see Table 1 for summary of results) [35]. Based on their results, Holden and

Table 1 Humidity conditions during five different heating cycles of Holden and Frechette [35] and resulting effects on crack closure and tested strength in soda-lime silica glass.

Heating Cycle	Humidity Applied During Cycle			Holding Time (Minutes)	Crack Closure *	Qualitative Strength **
	Heating	Hold Temperature	Cooling			
1	No	Yes	No	60	No	Very Low
2	Yes	No	No	60	Yes	Very Low
3	Yes	Yes	No	10	Yes	Low
4	Yes	Yes	No	60	Yes	Good
5	Yes	Yes	No	100	Yes	Good

* Crack closure was determined by the absence of the crack during visual examination after the heating cycle.

** The qualitative strength is a characterization of the ring-on-ring failure load for the group of samples with a particular heating cycle compared to a group of samples without thermal shock cracks.

Frechette [35] proposed an optimum healing cycle for crack healing and also a four step model for the crack healing in soda-lime silica glass [35]. The reported conditions optimum healing was: (1) presence of humidity at lower temperatures during the heating cycle, (2) presence of a residual stress before the annealing cycle, (3) the presence of humidity at the annealing temperature, (4) holding at the annealing temperature for a period much longer than that required for the relief of stresses [35]. The proposed model for crack healing in soda-lime silica glass was: (1) adsorption of water at a temperature below the glass transition temperature, (2) formation of a gel layer, (3) closure of the crack due to stress relief and (4) drying of the gel in the presence of a controlled atmosphere [35].

Using an optical microscope, Lehman, Hill, and Sigel observed crack closure of Vickers indentation cracks in heavy-metal fluoride glass [36] under different relative humidity levels at temperatures of 22, 50, and 80 °C. The crack closure rate was greater at higher levels of relative humidity, while crack closure lengths appear to reach similar values at longer times for all levels of humidity [35]. Temperature was reported by the authors as a significant factor in crack closure, however, the authors' plot of crack length as a function of temperature for different humidity levels could easily be fit by a horizontal line of zero slope (i.e. no significant crack length change with temperature) [36]. Lehman et al. found no evidence of a gel or any other reaction product which usually would be crystalline in fluoride glass and consequently readily identifiable [36].

Stravrindis and Holloway [38] investigated crack healing in glass using a double torsion loading configuration to observe crack closure and repropagation. The

closure and repropagation of cracks in soda-lime silica, borosilicate, and silica glasses was dependent on the environment [38]. For soda-lime silica specimens, the strain energy release rate for crack repropagation for a crack which was allowed to close in air, increased with room temperature aging time in air [38]. An optical reflectivity developed for the cracked specimen within a few minutes of exposure to air, but a significant increase in the energy required to repropagate the crack took hours of exposure of the crack to air [38]. Stravrindis et al. [38] state that the change in reflectivity may be due to the penetration of water to the two faces of the crack and that the initial adhesion between the faces of the closed crack may be due to the formation of a hydrogen bonded network. Stravrindis et al. [38] theorize that the subsequent increase in the energy required to repropagate the crack after a few hours of exposure of the crack to air may be due to a progressive interaction between the water layer and the SiO_2 network of the glass.

Michalske and Fuller [39] investigated crack closure and repropagation in soda-lime silica and vitreous silica glass using a double-cleavage drilled-compression fracture mechanics configuration. The energy during closing of cracks was humidity dependent at low temperatures, but was independent of glass composition which the authors state indicates that the closure may be the result of a physical process such as hydrogen bonding and not complex chemical reactions [39]. Michalske et al. [39] develop a model for the hydrogen bonding energy across the crack as a function of humidity. The model shows a drop in the closure energy at humidity levels of less than 15%. The authors [39] state that linkages of two or three water molecules between the crack faces may be possible which would mean that crack faces separated

by up to 1 nm may be adhered by hydrogen bonding.

2.2.2 Crack Morphology Changes during Thermal Healing of Cracks

Thermal-annealing induced changes in crack morphology have been treated theoretically by Nichols and Mullins [40-41]. Nichols and Mullins [40-41] showed that a semi-infinite cylindrical crack would either evolve (by diffusive transport) into a string of small spherical pores (ovulation) or into a large sphere (spheroidization).

Experimental observations of crack morphology changes [30-32, 34, 42-44] are consistent with Nichols and Mullins' theoretical observations [40-41]. For example, Yen and Coble [32] thermally annealed internal cracks in single crystal sapphire in air at temperatures ranging from 1650 to 1810 °C and found that the original continuous internal cracks broke up into channels of tubular voids which subsequently evolved into rows of spherical pores. Wang and Harmer [30] used an in-situ optical microscope to observe healing of internal cracks in single crystal LiF during isothermal annealing in the temperature range of 620 °C to 820 °C and found that annealing occurred in three stages: pinching off of plane cracks into cylindrical pores, ovulation of cylindrical pores, and shrinkage of isolated pores [30]. Gupta investigated healing in MgO [34], sapphire [31], and alumina [31]. Specimens, which had cracks formed from thermal down-shocking, were thermally annealed at temperatures in the 1400 °C to 1700 °C range, fractured in four point bend, and observed in an SEM [31, 34]. Gupta observed that the cracks at grain boundaries pinched-off (for MgO and alumina), that the cracks evolved into cylindrical voids which became rows of spherical pores, and that with further annealing the spherical

pores underwent continuous shrinkage [31, 34].

Hrma, Han, and Cooper [42] investigated indentation crack healing in soda-lime silica glass at 600, 650, and 675 °C using transmission optical microscopy and multiple beam interference microscopy on cooled samples. Hrma et al. [42] found a process of crack healing characterized by several stages with distinct morphological changes. In the first stage of healing, two different phenomena were reported: 1a) relaxation of the residual stress created during indentation occurred, 1b) subsurface crack outlines (which were barely detectable before annealing) became visible after a short time of heat treatment (e.g. less than 45 minutes at 600 °C) as a result of blunting of the crack tips via capillarity driven viscous flow of the glass [42]. In the second stage of healing, the indent cracks receded with a inward motion of the crack boundaries and radial cracks broke up via pinch off into oval cavities [42]. Grooving of the crack edges at the crack surface and shrinking of the subsurface cracks into cylinders and oval cavities characterized the third stage of healing [42]. The last healing stage consisted of spheroidization of the remaining subsurface cracks and gradual smoothing of the surface in the region of the indent impression [42].

Cassidy and Gjostein investigated the capillarity-induced smoothing of soda-lime-silica glass surfaces after heating in air to 640-670 °C [43]. The decay in the amplitude of periodic surface perturbations was measured with an interference microscope for specimens cooled to room temperature after being held for 30 to 120 minutes at a set healing temperature [43]. The smoothing process was dominated by viscous flow (from the convex surface to the concave surface) [43]. Kishi et al. [44] investigated the surface flattening in soda-lime silica glass in dry nitrogen at 610-670

°C and found that viscous flow dominated the smoothing process. The surface viscosity was higher than the bulk viscosity of the glass [44]. Kishi et al. [44] noted that residual water in glass will reduce the viscosity and so heating at temperatures above 600 °C may deplete the surface of water and result in an increased surface viscosity [44].

2.2.3 Crack Healing Investigations Via Strength Recovery Testing

Crack healing has been investigated via strength recovery testing after thermal annealing cycles [22, 31, 34, 45-52]. Lange and Gupta [45] investigated the flexural strength recovery of thermally shocked ZnO specimens after thermal heating to the sintering temperature (1100 °C) for 10, 20, and 35 hours. No explicit mention of the environment in which the specimens were heated is made by the authors other than a comment that the specimens were heated in a closed ZnO boat [45]. The four-point bend strength of the thermally shocked specimens before healing was 40% of the strength of the original, as-machined strength. The healed specimen strength increased from about 70% of the as-machined strength for 10 minutes of healing at 1100 °C to nearly 100% of the as-machined strength for the specimens heated for 35 hours at 1100 °C [45]. The grain size in the ZnO specimens also increased with increasing time at 1100 °C [45].

Lange and Radford [46] investigated the flexural strength recovery of thermally shocked Al_2O_3 specimens after thermal heating in air to the 1700 °C for 1, 7, 25, and 50 hours. The thermally shocked specimens had 36% of the strength of as-machined specimens. The strength of the specimens increased for the 1 and 7 hour specimens to

76 and 86% of the as-machined strength, respectively. The specimens heated for 25 and 50 hours had a steadily decreasing strength of 80 and 78% of the as-machined strength, respectively, which was attributed to grain growth in the specimen [46].

Gupta investigated the bend strength recovery in thermally shocked polycrystalline MgO specimens after heating in air to 1400, 1500, 1600, and 1650 °C for 1 to 10 hours [34]. The four-point bend strength of the thermally shocked specimens was about 30% of the as-machined strength. The amount of recovered strength increased with increasing temperature from a maximum of about 45% of the as-machined strength at 1400 °C to about 90% of the as-machined strength at 1600 °C [34]. The amount of strength recovered also increased dramatically with time for temperatures above 1400 °C, for example, at 1600 °C the strength increased from about 60 to 90 % of the as-machined strength for 1 minute of healing compared to 2 minutes of healing [34]. The grain size in the MgO specimens also increased with increasing time and temperature [34].

Gupta also investigated the strength recovery in thermally shocked polycrystalline Al_2O_3 specimens after heating in vacuum to temperatures 1400, 1500, 1600, and 1700 °C for up to 110 minutes [31]. The temperatures tested were below the sintering temperature so that grain growth was avoided [31]. The amount of strength recovery increased both as a function of time and temperature for temperatures below 1700 °C [31]. The four-point bend strength of the thermally shocked specimens was about 30% of the as-machined strength. The strength after 10 minutes of healing increased from about 35 to 80 % of the as-machined strength for healing at 1400 and 1700 °C, respectively. The strength for healing at 1600 °C

increased from about 60 to 85 % of the as-machined strength for 10 and 90 minutes, respectively. At 1700 °C, there was an un-explained decrease in strength (of less than 10% of the as-machined strength) as the time at 1700 °C increased to 110 minutes. Cracks formed along the grain boundaries after thermal shock [31]. Healing occurred via the gradual disappearance of the void space between neighboring grains [31]. Grain boundary diffusion was thought by Gupta to aid the healing process since the healing and strength recovery was more rapid for the polycrystalline alumina than for similar testing of sapphire (single crystal alumina) [31].

Roberts and Wrona [47] investigated the bend strength recovery in thermally shocked polycrystalline UO_2 specimens after heating in a static helium environment to 1600, 1800, and 2000 °C for 1 to 10 hours [34]. The four-point bend strength of the thermally shocked specimens was about 20% of the as-machined strength. Full strength recovery occurred after heating for approximately 3 hours at 2000 °C and approximately 11 hours at 1800 °C [34]. The strength after 4 and 32 hours of healing at 1600 °C was about 50 and 70 % of the as-machined strength, respectively. The cracks healed initially via crack pinch-off into a line of pores of irregular cylindrical or spherical shape [34]. Healing continued via shrinkage of the pores into nearly spherical shaped pores which remained as grain-boundary porosity [34]. A model by Nichols and Mullins for the shape change of pores during sintering [41]

$$-\frac{\partial C}{\partial t} = \left(A \exp(-Q/RT)\right) C^2 = k C^2 \qquad (2)$$

was used by Roberts and Wrona [47] to help model the change in strength from

$$\left(\frac{\sigma_t}{\sigma_f}\right)^2 = \left(\frac{\sigma_s}{\sigma_f}\right)^2 + \frac{k' t}{\sigma_f^2} \qquad (3)$$

healing where C is the pore diameter, t is the time at temperature, T is the temperature, A is a pre-exponential constant, Q is the activation energy for healing, R is the gas constant, k is a constant containing the activation energy in an Arrhenius relationship, σ_s is the as-shocked strength, σ_f is the uncracked fracture strength, σ_t is the strength after healing for a time, t, and k′ is a constant that can be related to temperature with an Arrhenius relationship. Roberts and Wrona [47] found an activation energy for healing of 230 kJ/mole, while reporting that for UO_2 the activation energy for volume diffusion is about 419 kJ/mole and for grain boundary diffusion in sintering it is about 314 kJ/mole. The authors conclude that the healing is probably dominated by grain boundary diffusion [47].

Bandyopadhyay and Roberts [48] investigated the bend strength recovery in thermally shocked polycrystalline UO_2 specimens after heating in a static helium environment to temperatures of 1290 to 1740 °C for 1 hour and to 1400 °C for times up to 8 hours [49]. Healing, in the form of strength recovery, occurred in two stages [48]. The first stage of healing was characterized by crack pinch-off and some sintering of the crack-like pores [48]. The second stage of healing was controlled by continued sintering of crack-like pores by a diffusional process [48].

Bandyopadhyay and Kennedy [49] investigated the bend strength recovery in thermally shocked polycrystalline UO_2 specimens after heating in a static helium environment to temperatures ranging from 1450 to 1920 °C for 1 to 48 hours [49].

The healing behavior of specimens with different levels of thermal shock was studied [49]. The four-point bend strength of specimens thermally shocked at 130 to 700 °C decreased from about 35 to 19 % of the as-machined strength, respectively. As the thermal shock quench increased from 120 to 700 °C, the number crack density per cm increased from 1 to more than 20 and the maximum crack width increased from about 4 to 12 μm [49]. The authors state that an empirical relationship between crack density and maximum crack width could be determined so that either parameter could be used to further study healing at different levels of thermal shock [49]. An exponential relationship was found between the time required for complete healing and the crack density [49]. The activation energy for healing was 410 kJ/mole using the following equation

$$t_c = m\,T \exp\left(\frac{Q}{RT}\right) \tag{4}$$

where t_c is the time required for complete healing, m is a temperature independent constant, T is the healing temperature, Q is the activation energy for healing, and R is the gas constant [49]. Volume diffusion was reported as the process for the healing of the thermal shock cracks in UO_2 since the activation energy for healing calculated using Equation 4 (410 kJ/mole) was near the reported activation energy for volume diffusion of 419 kJ/mole [49].

Tomozawa, Hirao and Bean [50] investigated the bend strength increase in soda-lime silica glass after annealing. Cylindrical specimens with a Vickers indent were thermal shocked to cause the indent crack to extend beyond the range expected for the residual stress created during indentation [50]. The thermal shocked specimens

were annealed at 510 °C for one hour and furnace cooled before four-point bend testing at liquid nitrogen temperatures [50]. The strength of the annealed specimens increased by 20 to 30% without a decrease in the crack length during annealing [50]. The increase in strength was attributed to blunting of the crack tip during the thermal annealing [50].

Hirao and Tomozawa [51] further investigated the bend strength increase after annealing in Vickers indented cylindrical specimens of soda-lime silica glass. The specimens were annealed in air and in vacuum at both 510 °C and 570 °C for one hour [51]. The specimens annealed in vacuum had a strength increase of about 16 and 26 MPa for 20 minutes of healing at 510 and 570 °C, respectively, without a decrease in the crack lengths [51]. The specimens annealed in air had a strength increase of about 28 and 38 MPa for 20 minutes of healing at 510 and 570 °C, respectively, without a decrease in the crack lengths [51]. The strength increased faster with respect to time and reached a higher strength value for the specimens annealed at 570 °C compared to the specimens annealed at 510 °C [51]. Residual stress was eliminated during the annealing process in both environments according to measurements via a polarmicroscope [51]. Crack tip blunting is mentioned as the cause of the strength increase in the glass after reference to the Inglis equation for stress concentration

$$\sigma_f = \frac{1}{2}\sigma_{th}\left[\frac{\rho}{C}\right]^{\frac{1}{2}} \qquad (5)$$

where σ_f is the fracture strength, σ_{th} is the theoretical strength of the material, ρ is the crack tip radius, and C is the crack length. The authors comment that slow crack

growth effects of the environment would result in a decrease in strength and not an increase in strength, that the measured crack length did not change, and consequently conclude that the only mechanism for a fracture strength increase after annealing would be an increase in the crack tip radius (i.e. crack tip blunting).

Hirao et al. [51] also investigated the surface flattening of soda-lime silica glass after annealing in vacuum and environments with water vapor present using similar techniques originally used by Kishi et al. [44]. Viscous flow was the dominant mechanism for the smoothing process in vacuum and in the presence of water vapor. The surface viscosity was lower for specimens annealed in the presence of water vapor than for specimens annealed in vacuum [51]. The increased viscous flow for specimens annealed in the presence of water was used as an explanation for the increased strength recovery for specimens annealed in air compared to specimens annealed in vacuum [51].

Choi and Tikare investigated the crack healing of an alumina with a residual glassy phase (Coors ADS96R with 4% silicates added as sintering aids) using four-point bend testing of specimens with Vickers indents and single-edge-precrack-beam testing [22]. Specimens with 49 N Vickers indent cracks were annealed for 30 minutes in air at temperatures ranging from 25 to 1400 °C and in argon gas at 1200 °C [22]. Annealed and as-indented specimens were tested in four-point bend at room temperature [22]. As-indented bend strength was about 215 MPa [22]. Specimens annealed at 800 °C had bend strengths of about 256 MPa, while specimens annealed at 1200 °C and higher had strengths equal to the as-machined strength of about 375 MPa and had the indent impression essentially disappear completely from optical

microscopy examination [22]. The crack healing was reported to occur from a material transport mechanism within the specimen [22]. The specimens annealed at 1200 °C in argon exhibited similar strength increases to specimen annealed in air at 1200 °C [22].

Healing of large macrocracks in single-edge-precrack-beam specimens was also investigated by Choi and Tikare [22] using SEM observation of fracture surfaces of as-precracked specimens and healed precracked specimens [22]. The as-precracked specimens predominantly fractured intergranularly with straight cleavage planes and some crack branching along other cleavage planes and sharp grain edges [22]. The healed precracked specimens had rounded crack edges and glassy striations on the cleavage planes [22]. Healed specimens exhibited degraded fatigue resistance in slow crack growth testing via dynamic fatigue experiments with a decrease in the fatigue susceptibility parameter, N, from 107 for the as-indented specimens to 68 for the specimens healed for 30 minutes at 1200 °C [22]. The authors suggest that since the healed specimens have degraded fatigue resistance and since glass has poor fatigue (N values of 20 to 40), then the crack healing mechanism was viscous flow of the glassy grain boundary driven by capillary forces [22].

2.2.4 Crack Healing Investigations of Vickers Indent Cracks Lengths

Thompson, Chan, Harmer, and Cook investigated the Vickers indent crack lengths during healing of Al_2O_3 and Al_2O_3-SiC nanocomposite [37]. The specimens were viewed un-coated in an SEM at a 3.1 KeV accelerating voltage after being indented and after annealing for 2 hours in argon at 1300 °C [37]. The specimen aging time

between indenting and thermal annealing was not explicitly stated [37]. The crack path for a 10 N indent in a composite specimen was predominantly transgranular while in a monolithic alumina specimen the crack path was predominantly intergranular [37]. In the annealed composite, the crack opening displacement decreased such that the faces of the crack came into contact. A "surface trace" along the original crack plane was observed on SEM micrographs which the authors state indicates that the fracture surface did not bond completely [37]. In the annealed composite, the last 2-3 microns of the crack at the original crack tip disappeared and was termed by the authors as the only true healing of the crack [37]. The authors conclude that the healing mechanism must have been adhesion of the crack faces rather than a diffusive transport healing of the crack since the crack morphology did not change via pinch-off into isolated pores or continuous reduction of the spheroidized pores [37].

In the annealed monolithic Al_2O_3, crack healing (in the form of a decrease in the crack length) did not occur, instead, crack length and the crack opening displacement increased [37]. The crack grew as a result of a more rapid decay of the microstructural toughening than the residual stress field driving force [37]. (The microstructural toughening was attributed to frictional traction between adjacent gains and the decay during annealing was the result of the reduction in the thermal expansion mismatch with increasing temperature [37].) The authors explain that the extended cracks failed to heal (once the residual stress was relieved) because: 1) the tortuous fracture path may have made it difficult for the crack faces to match and come together and 2) the frictional tractions may not have disappeared upon annealing and may inhibit asperities from sliding past each other thus preventing crack closure

[37].

2.3 Capabilities of an Environmental Scanning Electron Microscope

Conventional scanning electron microscopes (SEM) use electrons to form an image of a specimen's surface. The Everhart-Thornley detector collects secondary electrons (SE) and back scattered electrons (BSE) generated from interactions between the incident electrons and the surface [53]. The specimen chamber in an SEM must remain under vacuum for an image to be formed by using the Everhart-Thornley detector [53].

An environmental scanning electron microscope (ESEM) also uses electrons to form an image of a specimen's surface. However, the ESEM uses a gaseous detection device (GDD) to collect SE and BSE electrons and thus the sample chamber in an ESEM can have a gaseous environment [54]. The ESEM has a number of pressure levels along the path of the electron beam. The differing pressure levels are separated by pressure limiting apertures (PLA) which allow the electron gun to be under high vacuum while the specimen chamber can be pressurized up to 25 Torr [54]. The GDD operates with a positive bias of a few hundred volts. A SE emitted from the sample surface is accelerated toward the detector. Along the way, the emitted SE collides with a gas molecule which ejects an electron from the gas molecule. This process is repeated and results in an avalanche process [54] which amplifies the SE signal. The process of electron ejection from a gas molecule creates positive gas ions which help neutralize the buildup of a negative charge on the sample surface and allows the use of nonconducting samples without a conductive coating [53]. Danilatos has shown no

loss of resolution using the GDD detector in a gaseous environment compared to using an Everhart-Thornley detector at high vacuum [54].

The unique capabilities of the ESEM allow in-situ study of the crack healing and static fatigue crack growth of ceramics. The ability to have pressures up to 25 Torr in the specimen chamber allow the ceramic specimens to be in a humid environment, at least initially. (As the temperature increases the relative humidity drops rapidly, such that at temperatures above 100 °C, the relative humidity at pressures below 10 Torr becomes negligibly small [54]). Also, the ESEM can examine ceramic specimens without the conductive coating required for a conventional SEM. The absence of the surface coating allows the surface of the specimen to be exposed to the environment in the ESEM chamber and make static fatigue testing possible in the ESEM.

2.4 Focus of the Current Investigation

In the literature, no static fatigue studies reported observations of static fatigue crack growth in-situ. The present investigation will develop a technique to study crack growth in ceramics in the presence of water vapor in-situ using an Environmental Scanning Electron Microscope (ESEM). Tensile specimens of a soda-lime silica and a polycrystalline alumina will be tested in-situ using this technique. The effect of the level of relative humidity and the magnitude of the applied stress on the static fatigue crack growth in polycrystalline alumina will be investigated. The study will also focus on in-situ observation of the crack path in polycrystalline alumina to determine if the static fatigue crack growth is intergranular or intragranular and if grain bridging

occurs.

In the literature, only a single in-situ crack healing study of crack healing in ceramics has been reported [30] and no in-situ healing studies of glass specimens or polycrystalline specimens have been reported in the literature. The present investigation will study crack healing in soda-lime silica glass in-situ using an Environmental Scanning Electron Microscope (ESEM). The crack morphology changes during healing for temperatures up to 600 °C will be studied in the soda-lime silica glass.

Limited crack healing studies in soda-lime silica glass below 600 °C have been performed [35-36, 50-51]. At temperatures of 600 °C and above, bulk viscous flow occurs in soda-lime silica glass and can result in bulk dimensional changes or sample damage which would be undesirable for an industrial healing process. Of the studies of healing in soda-lime silica at temperatures below 600 °C, some have observed crack length reductions upon annealing [35-36], while others have observed no change in crack length after annealing [50-51]. The present investigation observes the crack healing behavior of soda-lime silica glass at temperatures below 600 °C both in-situ in an ESEM and with optical microscopy before and after thermal annealing in a conventional furnace. The effect of time and temperature on the length of Vickers indent cracks in soda-lime silica glass will be studied.

Investigations into the effect of humidity on healing in glass have been in the form of studies of crack closure at temperatures below 100 °C [36, 38-39] or of studies of high temperature healing using an induced humidity at high temperatures [35, 50]. Investigations of the effect of the **initial** humidity (before heating) on the

crack healing behavior of glass at temperatures below 600 °C would be useful in determining the potential usefulness of the process for industrial repair of glass parts damaged in service. Crack length changes during thermal annealing of soda-lime silica specimens initially held at different levels of humidity are observed in this study using both in-situ ESEM measurements and with optical microscopy measurements before and after thermal annealing in a conventional furnace. The in-situ study will investigate the effect of initial humidity on the temperature at which crack healing begins and on crack healing behavior for an isothermal hold. The current investigation also studied the effect of an initial 24 hour aging cycle with relative humidities of 0, 45, and 100 % on the crack healing behavior of soda-lime silica glass after annealing in a conventional furnace.

While some crack healing studies of Al_2O_3 have used inert atmospheres during annealing [31, 37] and other studies have used air as the atmosphere during annealing [22, 46], no study has specifically investigated the effect of humidity on the crack healing behavior of Al_2O_3. Crack healing in Al_2O_3 has been predominantly studied via strength testing [21, 31, 46] where crack healing effects inferred from changes in strength can be confused by strength changes due to increases in grain size by diffusion at the annealing temperatures [46], and crack tip blunting [50-51] during heating. This study investigates crack length changes in polycrystalline Al_2O_3 during thermal annealing in a conventional furnace for specimens initially held for a 24 hour aging cycle with relative humidities of 0, 45, and 100 %. The study will also investigate the healing behavior of two different polycrystalline Al_2O_3 materials, a microwave sintered alumina made at Michigan State University, and a commercially

available alumina made by Coors. The effect of indent crack size on the healing behavior of Al_2O_3 will also be investigated.

Heating in microwave furnaces has been found to increase sintering of alumina and silicon nitride, increase oxygen diffusion in single crystal alumina, and increase grain growth in alumina compared to heating to similar temperatures in conventional furnaces. No studies in the literature have considered the healing behavior of ceramics annealed in a microwave furnace. The present study includes investigating crack length changes as a function of microwave and conventional heating. The effect on the crack length behavior of a slow and fast ramp rate during microwave annealing will also be investigated.

Few studies in the literature have attempted to determine the activation energies for diffusion during the healing process [30, 47, 55]. A model by Stevens and Dutton [56] for high temperature static fatigue crack growth via diffusion will be used in the current study to determine diffusive activation energies for the healing process in polycrystalline Al_2O_3 from microwave and conventional annealing. A re-analysis of work by Raj et al. [55] and Wang et al. [30] using the model by Stevens and Dutton [56] will also be performed in the current work.

3. EXPERIMENTAL PROCEDURE

3.1 Materials

Static fatigue and crack healing experiments on soda-lime silica glass and alumina were performed. Commercially available glass slides were used to make soda-lime silica specimens because of the ease of availability, low cost, and dimensional uniformity. Commercially available electronic substrates made of alumina were used to make alumina specimens because of their availability and dimensional uniformity. Microwave sintered alumina disks manufactured at Michigan State University were also used to make alumina specimens due to their availability and low cost.

3.11 Soda-Lime Silica Glass

The soda-lime silica glass material used in this study was in the form of glass slides (Plain End Micro Slides, VWR Scientific, Media, Pennsylvania). The glass slides were received precleaned and fully annealed. The as-received dimensions of the glass sides were 76.2 mm X 25.4 mm X 1.1 mm (3.0 in X 1.0 in X 0.045 in). The manufacturer reported composition was 72 wt.% SiO_2, 14.3 wt.% Na_2O, 6.3 wt.% CaO, 4.1 wt.% MgO, 1.1 wt.% Al_2O_3, and 1.2 wt.% K_2O, with less than 1 wt.% of other materials. The manufacturer reported that the density was 2.4024 g/cm^3. The manufacturer reported softening point, annealing point, and strain point were 724, 545,

and 511 °C, respectively. The annealing temperature of the glass was previously experimentally determined to be around 580 °C [57]. Viscous flow was reported to occur in the glass slides at temperatures above 600 °C [57].

3.12 Coors Alumina

Specimens (here-after referred to as Coors Alumina) were made from commercially available alumina (Coors Ceramics, ADS-995 Alumina Substrate). The manufacturer reported that the material is 99.5% pure alumina. The alumina was manufactured using a tape casting process and was received in 114.3 mm X 114.3 mm X 1.0 mm (4.5 in X 4.5 in X 0.04 in) billets. The manufacturer reported that the mean grain size of the alumina was less than 2.5 microns (using an intercept method) and that the density was 3.88 g/cm^3 (using ASTM specification C373).

3.1.2 Microwave Sintered Alumina

The material referred to here-after as Microwave Sintered Alumina was made at Michigan State University [58]. The specimens were made using Sumitomo AKP-50 powder which is 99.9% pure alumina. The AKP-50 powder and no other powders (i.e. no sintering aids or other additions) was uniaxially dry pressed into disks 15.0 mm (0.6 inch) in diameter and 1.0 mm (0.04 inch) thick. The microwave sintering was done using a 2.45 GHz single-mode microwave cavity (Wavemat CMPR250 Microwave), equipped with an automated sliding short and launch probe positions controls [59, 60].

3.2 Basic Sample Preparation

Sample preparation for material characterization, static fatigue testing, and crack healing testing required use of many of the same basic techniques of cutting, polishing, and indenting.

3.2.1 Sample Cutting

Samples were cut into the desired dimensions for static fatigue and crack healing testing using either a low speed diamond saw or a high speed diamond saw.

3.2.1.1 Low Speed Diamond Saw

Preparing samples for static fatigue or crack healing using the low speed diamond saw required actual cutting with the low speed saw as well as cleaning after cutting and grinding to remove chips made during cutting.

3.2.1.1.1 Cutting

Low speed cutting was performed using a commercial low speed diamond saw (Buehler Isomet Low Speed Saw) with commercially available diamond wafering blades (Norton 101.6 mm (4 in.) diameter and 0.3 mm (0.012 in.) thick Diamond Wheel) and cutting oil (Leco VC-50 Cutting Oil). The saw had a stationary rotating blade with a movable arm which held the sample above the saw (Figure 1). Specimens were cut to the desired length by adjusting the micrometer connected to the saw arm. In the schematic shown in Figure 1, the micrometer moved the cutting arm and sample into and out of the plane of the paper.

Weights were placed on the arm to help increase cutting speed (Figure 1). However, there was a limit to the weight that could be added since too much weight on the arm would result in a sizable chip at the edge of the sample before the cut was complete. The most effective weights found for cutting were 35 g (1.2 oz) washers. The smaller weight of each individual washer resulted in the ability to get the optimum combination of high cutting rate and small chip size. The washers were added or removed during testing when the cutting rate slowed or as the saw cut neared completion, to reduce the weight and consequently reduce the chip size.

3.2.1.1.2 Cleaning and Grinding

After cutting on the low speed saw and removing the specimens from the cutting oil reservoir, the samples were cleaned to remove the cutting oil. The samples were first soaked in water with powdered glassware soap added (Alconox Powder Detergent). The samples were removed, rinsed with tap water, wiped by hand with more powdered glassware soap, rinsed again with tap water, and placed on laboratory paper towels (Forthoward Envision Singlefold Towels) to dry.

To remove the chips made during cutting, the edges of the specimens were ground using SiC grinding paper (Mager Scientific C Weight Waterproof Paper). The areas with larger chips were ground first with a 240 grit paper. All specimen edges were ground to a 400 grit finish with 400 grit paper. The specimens were then rinsed with tap water, washed by hand with powdered glassware soap, rinsed with tap water, rinsed with deionized (D.I.) water, and placed on laboratory paper towels.

To remove grinding debris from the samples, the samples were ultrasonicated.

A 150 ml beaker of D.I. Water was placed in an ultrasonic cleaner (Buehler Ultrasonic Cleaner) which was half filled with D.I. water. The samples were placed in the beaker with tweezers and left in the ultrasonic bath for 15 minutes. The samples were removed with tweezers from the beaker with the ultrasonic cleaner still on. The samples were rinsed with D.I. water and then placed on laboratory paper towels to dry. From this point on samples were always handled with tweezers to prevent contamination of the samples with finger grease.

3.2.1.2 High Speed Diamond Saw

High speed cutting was done on a commercial computer controlled machine (K.O. Lee Slicer/Dicer) with a 1.4 mm (0.055 in.) thick diamond wheel (Norton Diamond Wheel with a 177.8 mm (7.0 in.) diameter and a inner opening of 31.8 mm (1.25 in). Cutting fluid (5% concentration of Mobil Oil's Mobilnet S-122 in tap water) cooled the saw blade and rinsed away cutting debris. To prevent bacteria from becoming airborne during cutting an anti-bacterial agent ("00" wafers by Malacron) was added to the cutting fluid.

The high speed saw had a cutting table which moved back and forth in the x-direction at a set rate of speed (usually set at 6.3) (Figure 2). The blade itself moved in both the y- and z-directions (Figure 2). The blade was computer controlled to move down in the z-direction in programmed increments to make a cut in the sample. Once a cut of programmed depth was completed via computer control, the blade moved in the negative z-direction and then in the y-direction a programmed distance to the location of the next cut.

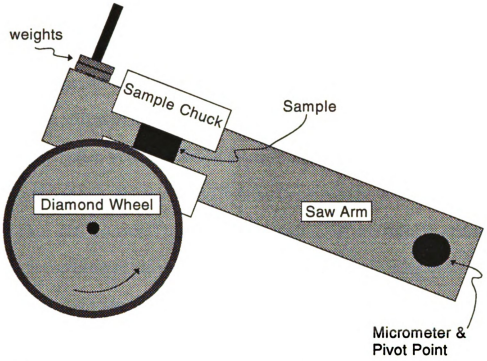

Figure 1 Schematic of low speed cutting saw showing the cutting arm, the diamond wheel and the specimen location.

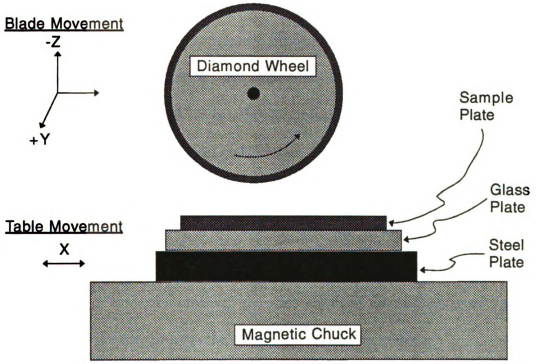

Figure 2 Schematic of the high speed cutting saw showing the specimen plate, glass and steel mounting plates, and the magnetic chuck.

3.2.1.2.1 Mounting a Sample on the High Speed Saw

The sample was mounted on the table of the high speed saw via a magnetic chuck (Walker Ceramax Permanent Magnetic Chuck, Figure 2). Non-metallic materials, like ceramics, were affixed to a magnetic steel plate (Figure 2) and then to the plate with the specimen in place were mounted on the saw. The steel plate was 127 mm X 127 mm X 9.5 mm (5.0 in. X 5.0 in. X 0.375 in.). To prevent the saw from cutting into the steel plate and "gumming" up the diamond blade, a 6.4 mm (0.25 in.) thick glass plate was placed between the sample to be cut and the steel plate (Figure 2). Several different glass plates were used. Each glass plate was cut with a hand held glass cutter to approximate dimensions of 108 mm X 108 mm X 6.4 mm (4.25 in. X 4.25 in. X 0.25 in.).

Thermoset (Buehler Thermoplastic Cement) was used to affix the glass plate to the steel plate as well as to bond the cutting sample to top of the glass plate. The steel plate was first placed on a hot plate (Cole Parmer Model 4658 Stirrer/Hot Plate). The hot plate was turned on and the temperature was set to 6 ⅔ on the hot plate's scale, which goes from 0 to 10. When the steel plate was hot enough to melt the thermoset, the entire top of the steel plate was covered with thermoset. After a few minutes had passed so that the thermoset had spread out as evenly as possible, the glass plate was placed on top of the steel plate. The glass plate was moved in small circles on the steel plate until almost all of the air bubbles between the two plates were removed. At least two corners of the glass plate and the steel plate were lined up so as to make it easier to align the sample on the saw for cutting.

To mount the sample on the glass plate, the glass plate was covered with

thermoset in an area slightly larger than the area of the specimen to be cut. Once the thermoset spread out evenly on the glass surface, the sample was placed on the glass plate and moved in small circles in order to remove the air bubbles. The sample was then lined up with the edges of the glass and steel plates to aid in alignment of the sample before cutting. The hot plate was then turned off and unplugged. Care was taken to make sure that during cooling the samples did not move relative to one another.

The specimen was typically allowed to cool for 24 hours, then was mounted on the saw. The lever on the front, right side of the magnetic chuck activated the magnet. When the sample was loaded into the saw, the lever was rotated 180° clock-wise so that the lever rested in the far right position. The sample was placed on the top surface of the magnetic chuck and aligned with the back, left corner of the chuck. The magnetic chuck was then activated by rotating the lever 180° counter-clock-wise so that the lever rested in the far left position.

3.2.1.2.2 Locating the sample in the cutting saw's y-z space

Before cutting, the computer, which controlled the cutting process, had to be oriented with respect to the sample top surface (z-direction) and sample back edge (y-direction) (Figure 2). Errors in locating the sample in the cutting saw's y-z space resulted in saw cuts in the wrong places or in the saw cutting through the sample, glass plate, and steel plate in a fraction of a second. Thus, sample location errors may cause a great deal of damage to the sample, the saw blade, the cutting saw itself, and/or the saw operator.

The top surface of the sample was the first to be defined. The "Jog" mode of the cutting saw computer was entered. The left handwheel controlled the mechanical movement of the saw in the z-direction. Each division on the handwheels corresponds to a 0.0025 mm (0.0001 in.) in travel of the saw blade. The saw was lowered using the z-direction handwheel until the blade was within about 1 mm (0.04 in.) above the surface of the material to be cut. A small ~6 cm^2 (~1 in^2) piece of notebook paper was placed between the saw blade and the sample surface. The paper was used as a 0.05 mm (0.002 in.) spacer between the saw blade and the sample. The "Move Dog" button on the computer key pad was depressed and held to move the saw table back and forth in the x-direction. The handwheel was used to lower the saw blade while the piece of paper was kept between the sample and the saw blade. The lowering of the saw blade via the handwheel was continued until the piece of paper would catch between the saw blade and sample and cause the saw blade to rotate. The z-direction height on the handwheel was noted. The z-height was increased and the saw was moved across the sample in the y-direction and the process was repeated to find the highest point on the sample. Many other different y-direction locations were used across the entire sample so that the maximum z-height for the entire sample surface could be determined.

Once the maximum z-sample-height was determined, the saw then was moved in the y-direction so that the saw was not above the sample. The handwheel was used to lower the saw to the maximum specimen z-height. In the "Jog Z-Direction" mode screen the saw was jogged down 0.05 mm (0.002 in.) which was the assumed thickness of the paper. Finally, the computer read out for the z-height was zeroed in

the "Jog Z-Direction" mode screen.

The y-distance for the back edge of the sample was found in a similar manner using a small piece of notebook paper between the saw blade and the back edge of the sample, the y-direction handwheel, and the "Jog Y-Direction" mode screen. When the minimum y-distance for the back edge was found, the z-height was increased using the "Jog Z-Direction" mode screen. In the "Jog Y-Direction" mode screen the saw was jogged forward 0.05 mm (0.002 in.) (the assumed thickness of the paper) and then jogged forward to the location of the first saw cut. The computer read out for the y-height was zeroed in the "Jog Y-Direction" mode screen. Finally, the z-height was increased to a reading of -25.400 mm (-1.0000 in.) using the "Jog Z-Direction" mode screen and the z-direction read out was re-zeroed.

3.2.1.2.3 Setting the saw table's x-limits

The mechanical movement of the table back and forth in the x-direction was controlled by two Dog Stops which indicate the end of travel to the left and right. The end of movement to the left or to the right was signalled to the computer via a magnetic sensor and two Sensor Stops.

The Dog Stops had to be adjusted depending on the location of the specimen on the chuck and on the width of the specimen in the x-direction. Each Stop Dog was adjusted by loosening a lock nut, sliding the Stop Dog on the rail to a new location, and re-tightening the lock nut. The location of the left and right stop dogs were adjusted so that the saw cut all the way across the specimen in the x-direction and would move passed the specimen approximately an extra 6.4 mm (0.25 in.).

The Sensor Stops were also adjusted by loosening a lock nut, sliding the Sensor Stop on the rail to a new location, and re-tightening the lock nut. The Sensor Stops were adjusted so that they would just trip the magnetic sensor as the table started to change directions. The magnetic sensor had a small red light which would be lit when the sensor was tripped by one of the two Sensor Stops.

3.2.1.2.4 Setting the computer to control cutting

The computer for the high speed saw operated in the English system of units. Computer controlled cutting of specimens was performed using the "Slot Cut" mode of the computer. Table 2 is an example of the program data entered in order to cut a single 114.3 mm X 114.3 mm X 1.0 mm (4.5 in. X 4.5 in. X 0.04 in.) Coors alumina plate into 1 cm^2 (0.16 in^2) samples. Figure 3 is a schematic showing slot cutting process for the first two cuts of a sample cut using the data values shown in Table 2. The program data in Table 2 were set up to make nine initial cuts which made ten 10 mm X 114.3 mm X 1.0 mm (0.4 in. X 4.5 in. X 0.04 in.) strips. The sample plate mounted on the saw was then rotated 90° and remounted, and the computer controlled cutting was then resumed to make the 9 additional cuts necessary to make 10 mm X 10 mm X 1.0 mm (0.4 in. X 0.4 in. X 0.04 in.) square samples.

During computer control cutting, the sample was cyclically moved back and forth to the left and right (Figure 3). When the sample was changing directions, the saw blade was moved down toward the sample in incremental steps (Figure 3). Initially, the saw blade was moved down a larger distance referred to as a rough

Table 2 Example of the program data entered in order to cut a single 114.3 X 114.3 X 1.0 mm (4.5 X 4.5 X 0.04 inch) Coors alumina plate into 1 cm^2 (0.16 in^2) samples using the computer control of the high speed cutting saw. (Note that <> indicates keyboard keys that were hit or data that was entered).

Main Menu
<F2> Program Selection
<F2> Slot Grind
<Page>
<F1> Routines <01>
<F2> Cycles <0>
<F3> R-Rghinc <00.2>
<F4> L-Rghinc <00.2>
<F5> R-Fininc <00.00005>
<F6> L-Fininc <00.00005>
<F7> Dwell <0.5>
<F8> x-alt-y <Yes>
<Page>
<F1> Spindle <Yes>
<F2> Coolant <Yes>
<F3> Wrkhead <No>
<F4> Aux <No>
<F5> Sprkout <00>
<F6> Z-Ref <0.5>
<F7> Dress <No>
<Page>
<F1> Z1 Total <01.0450>
<F2> Rapid <0.0>
<F3> RH Dis <00.9999>
<F4> Y1 Index <00.45>
<F5> Repeats <008>
<F6> Y2 Start <0.0>
<Page>

increment. After moving in rough increments for a preset distance, RH Dis (Table 3), the sample was moved a smaller distance referred to as a fine increment (Figure 3). The saw continued to increment down in the z-direction and cutting through the sample in fine increments until a preset distance of travel was reached which was referred to as Z1 Total (Table 3 and Figure 3). When the cut was completed, the saw blade raised above the sample and moved in the y-direction to the location of the next cut (Figure 3) where the process was repeated.

3.3.2 Polishing

Polishing of the ceramic materials was performed on an automatic polisher (Leco VP-50 12" Wheel Polisher with AP-50 Auto Polishing Attachment). To automatically polish samples, the samples had to be mounted on a special polishing plate (Figure 4). The samples were mounted using thermoset in a similar manner to that described in Section 3.3.1.2.1. The polishing plate was heated on the hot plate and thermoset was melted on the surface in locations where samples were to be placed. From four to twenty one specimens were placed in a circular pattern and about 32 mm (1.25 in.) from the edge of the polishing plate (Figure 4). The samples were also placed such that they were evenly spaced with respect to distance between each sample.

3.3.2.1 Polishing Compound

Diamond polishing compound (Warren Diamond Synthetic Diamond Paste - Medium Concentration) was used to polish the specimens with the usual sequence of polishing compounds being 20, 17, 15, 10, 6, and 1 micron. The time at each grit size varied,

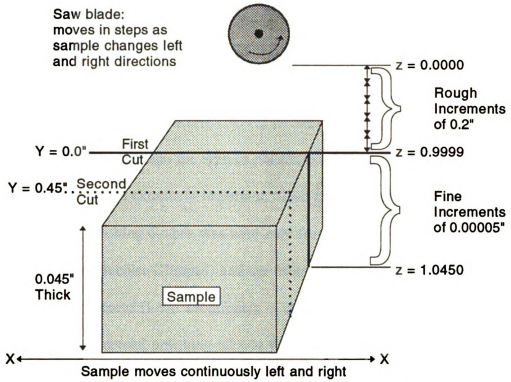

Figure 3 Schematic of computer controlled cutting on the high speed saw showing rough and fine incremental movements of the saw blade, continuous movements of the sample, and locations of the first two cuts, for a sample cut using the data values shown in Table 2.

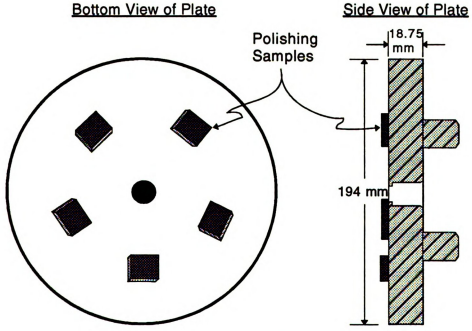

Figure 4 Schematic of samples mounted on polishing plate for automatic polishing. (From four to twenty one specimens were polished at one time).

but the normal polishing times were 15, 45, 30, 30, 30, and 30 minutes, respectively, for the normal sequence of polishing compounds.

3.2.2.2 Polishing Cloth and Oil

The type of polishing cloth and the type of polishing oil used with the diamond polishing compound was extremely important. Two types of polishing cloths were used. One of the polishing clothes was used only for the diamond paste sizes of 20 microns and larger (Buehler Ultrapad) and the other was used for all diamond paste sizes less than 20 microns (Leco Techtronic). Originally silicon oil was used during polishing, but a commercial polishing oil was found to be more effective (Leco Microid Diamond Compound Extender). While the silicon oil could be handled without worry of skin contact, the commercial polishing oil which contained ethylene glycol was an **EXTREME** skin irritant. Whenever polishing was performed with the commercial polishing oil, contact with the oil was avoided and protective gloves were worn.

The polishing cloths had adhesive backing and were mounted directly onto the polishing platen (Leco 12" Aluminum or Leco 12" Brass Platen). The polishing cloths were expensive and the adhesive backing was extremely sticky, so care had to be taken when mounting the polishing cloths. To mount the cloths, a ring cover was made from the protective circular cover which was placed over the adhesive of a polishing a polishing cloth by the manufacturer. The circular cover was removed from the back of a polishing cloth and had the center cut out so that a ring of only the outside 75 mm (3 in.) remained. The ring cover also had a single cut across it so that

it was no longer continuous. The ring cover was placed on the adhesive back of the new polishing cloth. The polishing cloth was then aligned on the polishing platen. The center of the polishing cloth was depressed so that the adhesive stuck and the ring cover was removed from the adhesive back. The rest of the adhesive back was depressed starting at the center and working outward so as to try to prevent any air bubbles to be trapped. Air bubbles in the cloth can result in the tearing of the cloth during polishing and possible damage to the samples and/or the polisher.

3.2.2.3 Charging the Polishing Cloth

Once a polishing cloth was placed on a platen, the platen was placed on the polisher and the polishing cloth was charged with diamond paste. About 1-2 ml of polishing oil was placed on the polishing cloth. The polishing wheel was then started and the polishing oil was spread evenly across the surface of the polishing cloth. The polishing wheel was subsequently shut off and diamond paste was placed in several spots on the polishing cloth and spread evenly across the cloth surface.

3.2.2.4 Polishing Samples

Polishing consisted of a general polishing procedure that could be used for polishing any ceramic materials and a specific polishing procedure used for polishing the alumina.

3.2.2.4.1 Polishing of Ceramic Materials

To start polishing, the appropriate platen with a polishing cloth for whichever micron diamond paste was to be used was placed on the polisher and charged as described in section 3.2.2.3. The sample plate was placed on the polishing wheel and the automatic polishing unit was moved over onto the sample plate. The polisher was started at a speed of 125 RPM and the automatic polishing unit was started to move the sample plate. The polishing was continued for the appropriate amount of time. The polisher was then turned off and the sample plate was removed. The samples were washed with a big brush (6 in. long and 3 in. diameter beaker brush) along with soap (Alconox Detergent) and water to remove the polishing compound and oil. The samples were not ultrasonically cleaned since an ultrasonic cleaner large enough to hold the polishing plate was not available. The polishing plate and samples were dried with paper towels. The process was then repeated for a different size polishing compound.

3.2.2.4.2 Polishing of Alumina Specimens

The first diamond size used in polishing samples was 20 micron diamond paste. The purpose of this step was to grind flat and polish each of the mounted samples. For most samples, 15 minutes of polishing at 20 micron grit size was sufficient to grind each of the mounted samples so that they were flat and all of their surface area was ground. Some samples having irregular height or other problems were not ground flat having portions which were not being polished after 30 minutes of polishing at 20 microns. For these samples longer times at 20 microns were necessary or larger sized

diamond paste was used (e.g. 25 or 35 microns).

After each of the mounted samples was ground flat, the samples were polished for 45 minutes with the 17 micron diamond paste. The criteria for a sufficient polish with the 17 micron diamond paste was that all of the specimens have a slightly shiny surface. It was very important that all of the samples were slightly shiny before moving on to the next diamond compound or **very** long times at the next size diamond compound was necessary. Once the samples were sufficiently polished at 17 microns, the samples were polished for 30 minutes with the 15 micron diamond paste. The criteria for a sufficient polish with the 15 micron diamond paste was that all of the specimens have a mirror-like surface. Samples that did not have a mirror surface after the 15 micron stage never had a polished finish. Samples with a mirror finish were then polished for 30 minutes at each of the remaining polishing steps (10, 6, and 1 micron diamond paste).

3.2.3 Indentation

Indentation was done using a commercial hardness tester (Buehler Semimacro Hardness Tester). The loads available with the hardness tester used were 0.98, 4.9, 9.8, 49, 98, 196 N. Along with indentation load, the loading rate could be set with a dial in the range of 40 to 300 microns/second and the loading time could be set with a dial in a range of 5 to 35 seconds. A Vickers indentor tip (Osaka Diamond Vickers Indentor) was used for all indentations. The sample stage could be moved in the x- and y-directions using two separate micrometers. The micrometers were delineated in the SI units of millimeters and had a range of 0 to 25 mm (0 to 0.984 in.).

The hardness tester had an optical microscope attached which had a magnifying factor of 200x. The optical microscope allowed for the measurement of width of the indent impressions and length of the cracks on specimens. In the optical display there were two lines that could be moved within the display. The distance between the lines could be adjusted using a digital micrometer. The digital display of the micrometer was zeroed by depressing the zeroing button, once the two lines were moved together until they were just barely touching using the micrometer movement controls. After being properly zeroed, the digital micrometer display gave the distance between the lines as displayed on the specimen surface in tenths of micrometers.

3.3 Materials Characterization

The soda-lime silica glass, Coors alumina and microwaved alumina material used for experimental studies of static fatigue and crack healing were characterized before testing. The density of the glass and alumina was measured. The grain size of Coors alumina and microwave alumina was measured from micrographs.

3.3.1 Density Determination

An Archimedes' method was used to determine the density of soda-lime silica glass, Coors alumina and microwave sintered alumina. The testing used ASTM specification C378 as a guideline.

3.3.1.1 Materials Preparation for Density Measurements

Specimens of glass and Coors alumina were first cut to a smaller size from the as received material while the microwave sintered alumina disks were used as-received for density measurement testing. Glass specimens were cut using a low speed saw to nominal dimensions of 76 mm X 10 mm X 1.1 mm (3.0 in X 0.4 in X 0.045 in) and Coors alumina specimens were cut with the high speed saw to nominal dimensions of 55 mm X 10 mm X 1 mm (2.2 in X 0.4 in X 0.04 in). The glass and Coors alumina samples were cleaned after cutting using acetone to remove the thermoset and the cutting oil. To remove any residual oil or other possible contamination, all samples were cleaned with soap and water (Alconox Powder Detergent), rinsed with deionized (D.I.) water, and allowed to dry at room temperature for at least 24 hours.

3.3.1.2 Density Measurements

Weighing was performed using a balance with a display to 0.0001 g (Sartarous Model A210P). The dry weight (W_{dry}) of the samples was measured initially. Samples were then placed in a beaker of D.I. water. To completely wet the samples, the beaker and samples were placed in a vacuum chamber and the vacuum chamber was evacuated with a rotary vacuum pump for at least 5 minutes. The suspended weight (W_{susp}) of the samples was measured using the balance with a hook holding the sample in D.I. water. Before the sample suspended weights were taken, the balance was tared with the hook suspended in the D.I. water without a sample. After each specimen's suspended weight was measured, the sample was again placed in D.I. water. The wet weight (W_{wet}) of each sample was measured by removing the sample from the D.I.

water, dabbing it with a KimWipe to remove excess water, and placing the sample on the balance pan.

The measured density (ρ_{meas}), was calculated using

$$\rho_{meas} = \frac{W_{dry}}{W_{wet} - W_{susp}} \quad . \tag{6}$$

For a sintered polycrystalline sample, the maximum, theoretical, sample density is the atomic density of a single crystal of the compound. For Al_2O_3, the theoretical density (ρ_{theo}) is 3.965 g/cm^3 [61]. Samples with a measured density less than the theoretical density did not completely densify during sintering. The difference between the measured density and the theoretical density of a sample indicates the degree of sintering. The percentage of theoretical density was found using

$$\%\ theoretical\ density = \frac{\rho_{meas}}{\rho_{theo}} * 100\% \quad . \tag{7}$$

3.3.2 Microstructure

Micrographs of thermally etched surfaces of Coors alumina and microwave alumina were taken using the ESEM. The surfaces of the two types of alumina were thermally etched during microwave heating to temperatures above 1500 °C. The grain size for the polycrystalline alumina samples was calculated from the micrographs using a line intercept method with a stereographic correction of 1.5. For each alumina material, a minimum of 37 lines from three separate micrographs was used for the grain size

calculation.

3.4 Indentation Measurement Testing

The crack system used to study both crack healing and static fatigue in the current investigation was the Vickers indent crack system. For a Vickers indent, the surface lengths of the radial cracks in the x- and y-direction were measured and recorded as $2c_1$ and $2c_2$, respectively. The crack lengths and especially the change in crack lengths were used to indicate changes in crack healing or static fatigue phenomena with changes in different variables such as time, humidity, temperature, and stress level. Due to the importance of indentation measurements to the crack healing and static fatigue investigations, experiments were performed to compare optical measurements between different researchers and to compare optical and ESEM measurements, as described below.

3.4.1 Multiple Experimenter Measurements

Samples of borosilicate glass, Coors Alumina, Microwave Alumina and Silicon Nitride were used. The samples were cut with a low speed diamond saw (Section 3.2.1.1) and the polycrystalline samples were polished to a 1 micron finish (Section 3.2.2). Each sample had a Vickers indent placed on the polished surface (Section 3.2.3) by a single experimenter. The x- and y-direction crack lengths ($2c_1$ and $2c_2$) of the indents were measured five different times by each of six different experimenters using the optical microscope attached to the indentor (Section 3.2.3). The mean and standard deviation was determined for each experimenter's five measurements of a given crack length. A

group average for a given crack was determined from the mean crack lengths recorded for each of the six experimenters.

3.4.2 Optical and Environmental Scanning Electron Microscope Measurements

The x- and y-direction crack lengths ($2c_1$ and $2c_2$) of the indents for the glass, Coors Alumina and Microwave Alumina were measured using the Environmental Scanning Electron Microscope (ESEM). The indent lengths were measured: (1) on the ESEM screen using the ESEM computer and (2) manually from the micrographs taken on the ESEM. The crack lengths measured on the ESEM screen used the ESEM computer measurement tool which entailed clicking the computer mouse at both ends of the crack being measured and recording the computer determined length. The cracks were measured from 200 X 200 mm (8 X 8 inch) micrographs by measuring the length of the crack with a ruler, measuring the micron bar length with a ruler, and calculating the crack length.

3.5 Static Fatigue: ESEM Crack Growth Investigations

In-situ observation of crack growth in ceramics under constant applied load was performed using the Environmental Scanning Electron Microscope. Tensile specimens of glass and Coors alumina were prepared for the study. A Vickers indent was placed on the center of one of the tensile specimen faces, was located, and observed in the ESEM. The effects of constant applied load, humidity, and time upon crack growth were investigated

3.5.1 Ceramic Tensile Specimen Preparation

Tensile specimens for static fatigue testing of soda-lime silica glass and Coors alumina were made by using a tabbing technique normally used in the tensile testing of composite materials (ASTM D3039). The tabs were made from either a glass-epoxy composite or stainless steel. The tabs were mounted onto the specimens using an epoxy adhesive or a high temperature cement (Figure 5).

3.5.1.1 Preparation of Rectangular Specimens of Glass and Coors Alumina

Rectangular specimens of soda-lime silicate glass were cut using the low speed diamond saw (Section 3.2.1.1) to dimensions of 10 mm X 50 mm X 1.1 mm (0.4 in. X 2.0 in. X 0.04 in.). After cutting, the lengthwise edges of the rectangular specimens were beveled with 240, 320, 400 and 600 grit SiC fixed-abrasive paper. The samples were ultrasonically cleaned in D.I. water to remove grinding debris.

Coors alumina specimens were cut using the high speed diamond saw (Section 3.2.1.2) to dimensions of 10 mm X 55 mm X 1 mm (0.4 in. X 2.17 in. X 0.04 in.). After cutting, the specimens were polished to a 1 micron finish using an automatic polisher, as described in Section 3.2.2. Four or five specimens were mounted at a time for polishing. Once the specimens were removed from the polishing plate, the edges of static fatigue specimens were beveled with 240, 320, 400 and 600 grit SiC fixed-abrasive paper. After edge beveling the samples were ultrasonically cleaned in D.I. water to remove debris from polishing or grinding.

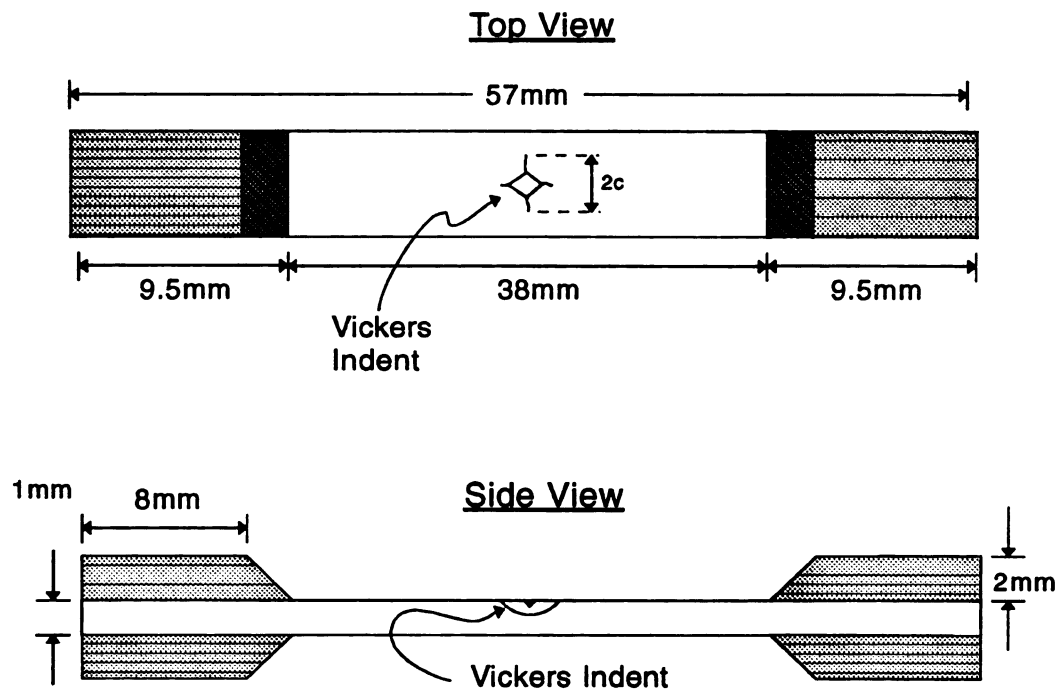

Figure 5 Schematic of tabbed tensile specimens used in static fatigue testing (note indent size is exaggerated).

3.5.1.2 Preparation of Specimen Tabs

Tabs for making tensile specimens were fabricated from either a glass-epoxy composite or stainless steel. The composite tabs were made from a 1.9 mm (0.075 in.) thick composite plate composed of alternating 0°/90° layers of E293 epoxy reinforced with 7781 glass fibers. The stainless steel tabs were made from a 3.175 mm (0.125 in.) thick, 304 stainless steel strip.

The composite material and stainless steel strips were cut into 10 mm X 10 mm (0.394 in. X 0.394 in.) squares. In some cases, the stainless steel squares were then cold rolled to a thickness of 2.1 mm (0.09 in.). All composite and cold rolled stainless steel squares were ground on a 120 grit belt grinder to smooth rough sides and to place an angle of approximately 45° on one of the sides.

3.5.1.3 Tab Attachment onto Rectangular Ceramic Specimens

The tabs were mounted on rectangular specimens (Figure 5) of soda-lime silicate glass and polished Coors alumina using either epoxy (Omega, Omegabond 200) or high temperature cement (Omega cc High Temperature Cement). The epoxy adhesive was purchased in packages which had premeasured quantities of resin and catalyst. The epoxy was mixed in the package before mounting the tabs. The high temperature cement was mixed using approximately 3 parts powder to 1 part of the liquid. The liquid was added to the cement mixture until the cement paste reduced in viscosity to the point that the cement could be spread evenly.

To keep the adhesive from getting on the glass and Coors alumina specimen surfaces, and to help keep the desired gage length, the rectangular specimens were

wrapped in paper cut to a width of 27 mm (1.063 in.) or 35 mm (1.378 in.) for glass and Coors alumina, respectively. After the specimens were wrapped, the epoxy or cement adhesive was placed on the ends of the specimens using 2.1 mm (0.083 in.) diameter wooden applicators and 4 tabs were placed on the top and bottom of each specimen's ends (Figure 5). The tabs were moved in a small circular motion to aid in getting complete wetting of the adhesive to the tab and the specimen. The tabs were re-aligned by hand once the specimen was set down.

The adhesives used had to cure before the specimens were ready for testing. The tensile specimens prepared using the epoxy adhesive were cured at 220 °C for 3.5 hours in a furnace (Lindburg 1200 °C Box Muffle Furnace). Tensile specimens prepared using the high temperature cement were cured for 24 hours at room temperature. For some of the stainless steel tabbed specimens, after the tabs were cured, each side of the specimen was ground on 240 grit SiC paper to help reduce non-parallelness between the tabs at either end of the specimen and thus reduce torsional forces upon loading.

3.5.2 Vickers Indentation Cracks on Tensile Specimens

A single Vickers indent was placed in the center of the face of the glass and Coors alumina tensile specimens. For the glass specimens, the Vickers indent was made using a 9.8 N load, a loading rate of 70 μm/sec, and a load time of 15 seconds. For the Coors alumina specimens, the Vickers indent was made using a 49 or 98 N load, a loading rate of 70 μm/sec, and a load time of 15 seconds. The location of the indent was marked with a black marker (Sanford Sharpie Permanent Marker). The location

was indicated by two lines starting next to the indent, with one line going at a +45° angle and the other going at a -45° angle to the edge of the specimen.

As a Vickers indentor tip is unloaded from the surface of a ceramic, a residual tensile field is developed from the indentation impression that was formed. The residual stress provides a driving force for the growth of radial cracks [62]. The growth of the radial cracks is balance by the fracture toughness of the material [62]. After an indentor is removed from a ceramic surface, the radial cracks may continue to grow due to environmental subcritical crack growth [63]. The slow crack growth of the radial cracks will decrease as the crack length increases [63] and will saturate in time. Consequently, all specimens indented in this work were aged for 24 hours before testing to allow for the slow crack growth to saturate. For the static fatigue testing, indented tensile specimens were aged for 24 hours in air so that the crack length changes measured during testing would be the result of static fatigue crack growth from the externally applied stress and not the result of slow crack growth from the residual stress field of the indent impression.

3.5.3 ESEM Testing

All Environmental Scanning Electron Microscopy testing in the current study was performed using a Philips Electroscan Model 2020 ESEM with water vapor as the fill gas. All specimens tested in the current study were observed in the ESEM **without** a conductive coating. A LaB_6 filament with a 20 KeV accelerating voltage was used along with the second largest objective aperture to image the ceramic specimens. When micrographs were taken, the ESEM chamber pressure was maintained in the

range of 1.7 to 2.5 Torr to provide the optimum balance between a pressure large enough to reduce charging and provide a strong signal for increased resolution and a pressure low enough to not cause a reduction in the signal from interference from the increased number of gas molecules between the sample and the electron detector.

For static fatigue testing a tensile stage (No. 18211 Tensile Substage, Ernest F. Fullam Inc., Latham, NY) was used along with the bullet gaseous electron detector. The tensile stage had a self tightening grip design with load applied by a screw driven mechanism. The load measured by the tensile stage load cell was displayed on an external display in units of pounds. The load was controlled manually through the ESEM's Rotation stage control.

3.5.3.1 Control of Relative Humidity in the ESEM

The relative humidity was controlled in the ESEM sample chamber using H_2O as the fill gas. Danilatos [54] details the functional dependance of relative humidity on temperature and pressure and the control of relative humidity in an ESEM (Figure 6).

The relative humidity in the ESEM specimen chamber was regulated by the ESEM chamber pressure and the sample temperature. The chamber pressure was computer controlled to levels set by the operator. The chamber pressure could be varied between 0 and 10 Torr. For optimum resolution for the ceramic specimens tested, the ideal chamber pressure was in the range of 1.7 to 2.5 Torr. At lower (less than about 1.5 Torr) and higher (greater then about 3.0 Torr) pressure the resolution of the ESEM decreased.

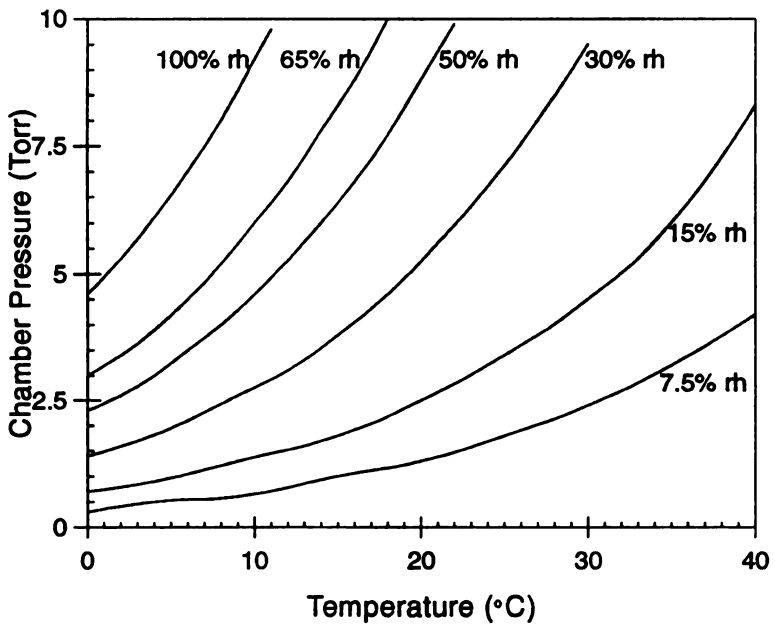

Figure 6 Plot of ESEM chamber pressure versus temperature showing curves of constant relative humidity [after 53].

3.5.3.2 Placement of Specimens in the Tensile Stage

During standard operating procedures for ESEM operation, the stage controls went through an automatic calibration sequence. The tensile stage had to be disconnected and removed from the ESEM before this calibration sequence or the large tensile stage would damage the ESEM. In order to mount the specimen for testing, the rotation control switch was used to increase or decrease the tensile stage's gage length. Once the proper gage length was reached, the specimen could be mounted in the tensile stage by tightening the two bolts on each of the two top grip plates. Due to the self-tightening design of the grips, a small tensile load was applied as the bolts on the grip plates were tightened.

After the specimen was mounted in the tensile stage, the tensile stage needed to be removed from the ESEM and the ESEM stage controls needed to be calibrated again. The re-calibration of the stage controls was performed in order to zero the rotation stage control. The ESEM automatically zeros the rotation when the ESEM chamber door is closed. If the rotation was not already at zero, then specimen fracture occurred as the ESEM returned the rotation to zero which resulted in a large tensile or compressive load applied to the sample. After re-calibration, the tensile stage was attached to the ESEM, the ESEM chamber door was closed, and the specimen chamber was evacuated down to the single digit Torr range.

3.5.3.3 Static Fatigue Testing

Normal ESEM operating procedures were followed with a sample chamber pressure of about 2.4 Torr, which resulted in a humidity level of about 10%. After the electron

beam was aligned and the indent was located, micrographs of the indentation cracks were taken to determine the initial specimen's crack lengths. The load applied to the sample was increased to the level at which static fatigue testing was to occur. Micrographs of the indentation cracks were taken at this point to determine whether or not crack growth had occurred due to the increase in load.

When the desired load for static fatigue testing was reached, the relative humidity was increased to 21, 32, or 42 % by increasing the water vapor pressure to 5.0, 7.5, or 10.0 Torr in the ESEM sample chamber. The increased humidity level was held for time intervals of usually 25 minutes or more. After the desired time interval at the raised humidity level, the ESEM sample chamber pressure was reduced to 2.5 Torr so that micrographs were taken at maximum resolution. After the micrographs were taken, the humidity and applied load were adjusted to desired levels for another static fatigue time interval and the process was repeated.

3.6 Crack Healing

Crack healing investigations were performed with: 1) in-situ heating and in-situ observation using an Environmental Scanning Electron Microscope (ESEM), 2) conventional heating and observation using optical microscopy before and after thermal annealing, and 3) microwave heating and observation using optical microscopy before and after thermal annealing.

3.6.1 In-Situ Healing Investigations using an ESEM

In-situ observation of the healing of Vickers indents in soda-lime-silicate glass was performed using an Environmental Scanning Electron Microscope. The change in crack length and crack morphology as a function of time and temperature was studied. The effect of the initial humidity level on the crack healing behavior was also investigated in-situ by varying the initial temperature of the sample and ESEM sample chamber pressure to change the initial humidity conditions of the sample.

3.6.1.1 Soda-Lime Silica Glass Specimens

The glass specimens used for the in-situ ESEM crack healing study were cut using a low speed diamond saw (described in Section 3.2.1.1). The corners of the cut 4 mm X 4 mm X 1.1 mm (0.158 in. X 0.158 in. X 0.045 in.) specimens were slightly rounded by sequentially using 240 and 400 grit SiC fixed-abrasive paper. A Vickers indent was placed in the center of a 4 mm X 4 mm (0.158 in. X 0158 in.) specimen face with a 9.8 N load applied using a loading speed of 15 μm/sec and load time of 70 seconds. The location of the indent was marked with a black marker (Sanford Sharpie Permanent Marker) to aid in locating the indent on the sample surface in the ESEM (Figure 7). The indented specimens were aged for at least 24 hours before testing.

3.6.1.2 Setting Relative Humidity before Crack Healing Testing

As described in Section 3.5.3.1, the level of relative humidity can be set in an ESEM by controlling the ESEM sample chamber pressure and the temperature. For optimum resolution for the glass specimens tested, the chamber pressure used was in the range

of 1.7 to 2.5 Torr. The initial temperature of the specimen was regulated by the circulating water system for the hot stage in order to set the relative humidity of the sample chamber using pressures in the range of 1.7 to 2.5 Torr. The water temperature was controlled by a chiller (Endocal RTE-100, NESLAB Instruments, Inc., Newington, NH) which was capable of both heating and cooling the water. The water chiller temperature was adjusted by the temperature dial on the chiller and measured by a mercury in glass thermometer submerged in the cooling water reservoir.

3.6.1.3 In-situ ESEM Testing

The glass specimens were tested in an ESEM (Philips-Electroscan Model 2020 ESEM) using a special high temperature gaseous electron detector and a hot stage (Philips-Electroscan ESEM Hot Stage) capable of temperatures up to 1000 °C. A small ceramic crucible with an inner diameter of 5.7 mm (0.224 in.) and an inner depth of 1.15 mm (0.045 in.) held the sample in the hot stage. The sample was fixed to the crucible using silver paint. The crucible was placed on top of a small silicon carbide disk (approximately 0.75 mm (0.03 in.) thick) which rested on the top of the small heating elements of the hot stage (Figure 8).

Once the specimen was placed in the ESEM hot stage, the chamber was evacuated and the ESEM electron beam was aligned. The initial relative humidity was set by the temperature of the sample (which could be reduced from room temperature via the cooling water) and by the pressure in the ESEM sample chamber (Section 3.6.1.2). Micrographs of the initial indent cracks were taken before the specimen was heated.

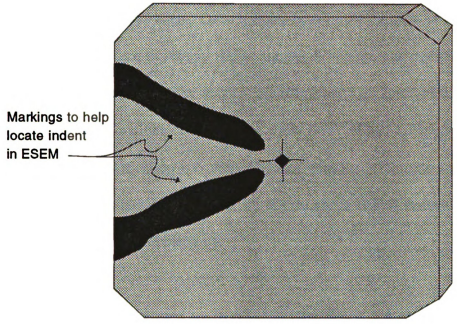

Figure 7 Schematic of soda-lime silica glass specimens used in ESEM investigations of crack healing.

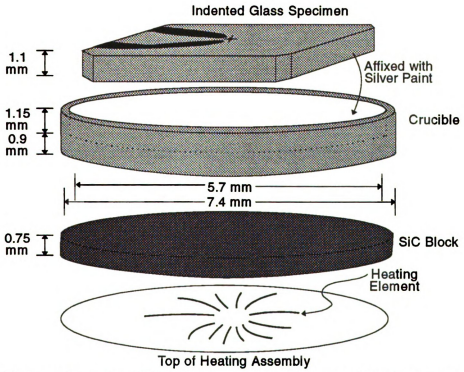

Figure 8 Schematic of the ESEM hot stage showing the top of the heater assembly, the silicon carbide spacer, the crucible and the indented glass specimen.

The heating schedule was selected by specifying a list of data for temperature set point, ramp rate, and dwell time. Once heating began, micrographs of the indent cracks were taken at selected times and temperatures. When the micrographs were taken, the water flow from the chiller was temporarily turned off in order to increase resolution by reducing vibrations caused by the water flow. When micrographs were not being taken, the magnification was reduced along with the brightness and contrast. A complete experiment typically took from 3.5 to 6 hours of ESEM beam time along with about 2 hours of setup and clean up.

3.6.1.3.1 Healing at Temperatures up to 600 °C (Experiments A and B)

The reduction in crack length and the changes in crack shape for glass specimens were investigated for healing temperatures up to 600 °C or higher. The heating rates and dwell times for the two samples heated to temperatures of 600 °C and higher are shown in Tables 3 and 4.

3.6.1.3.2 Healing as a Function of Temperature (Experiment C)

The healing behavior of the indent crack in glass was investigated as a function of temperature from room temperature to 490 °C. The heating rates and dwell times for this experiment are shown in Table 5.

3.6.1.3.3 Healing as a function of Time at 430 °C (Experiment D)

Healing was investigated as a function of time with temperature fixed at 430 °C. The heating rates and dwell times for Experiment D are shown in Table 6.

Table 3 ESEM hot stage heating schedule for the experiment investigating healing up to 600 °C (Experiment A).

Ramp Cycle	Set Point (°C)	Ramp Rate (°C/minute)	Dwell Time (min.)
1	300	20	5
2	400	20	10
3	500	10	20
4	550	5	30
5	600	2	135

Table 4 ESEM hot stage heating schedule for the experiment investigating healing up to 610 °C (Experiment B).

Ramp Cycle	Set Point (°C)	Ramp Rate (°C/minute)	Dwell Time (min.)
1	400	20	1
2	500	10	30
3	550	5	110
4	560	1	15
5	575	1	35
6	600	1	30
7	610	1	10

Table 5 ESEM hot stage heating schedule for experiment investigating healing as a function of temperature (Experiment C).

Ramp Cycle	Set Point (°C)	Ramp Rate (°C/minute)	Dwell Time (min.)
1	400	20	10
2	430	5	35
3	450	1	10
4	470	1	10
5	490	1	40

Table 6 ESEM hot stage heating schedule for initial experiment investigating healing as a function of time at a fixed temperature of 430 °C (Experiment D).

Ramp Cycle	Set Point (°C)	Ramp Rate (°C/minute)	Dwell Time (min.)
1	370	20	15
2	400	5	15
3	430	2	30
4	*25*	*20*	***
5	370	20	15
6	430	10	175

* ESEM shut down, so specimen was cooled to room temperature and the ESEM was re-booted.

3.6.1.3.4 Healing as a function of Relative Humidity (Experiments E-H)

Healing was investigated as a function of initial relative humidity levels for isothermal holds at 430 °C. For Experiments E-H, the initial relative humidity levels were set at 8, 16, 32, or 64%, respectively. The heating rates and dwell times used for Experiments E-H were identical and are shown in Table 7.

3.6.1.3.5 Healing with New Hot Stage Heater (Experiments I-M)

After another operator had damaged the hot stage and a new heater was installed on the hot stage, healing was investigated as a function of initial relative humidity levels for isothermal holds at 430 °C. For Experiments I-M, the initial relative humidity level was set at 48%. The heating rates and dwell times used for Experiments I-M were the same as Experiments E-H and are shown in Table 7.

In Experiment M, a K-type thermocouple (Omega 0.005 inch diameter K-Type Wire) was mounted to a glass specimen using high temperature cement (Omega cc High Temperature Cement) and the specimen was mounted to the crucible with high temperature cement (Figure 9). The K-type thermocouple was connected to the extra thermocouple connection in the door of the ESEM. The connection on the outside of the ESEM door was connected to a K-type Ice Point (Omega K-type Ice Point) which was connected to a digital voltmeter. The temperature was found using the voltage reading and standard thermocouple tables.

Table 7 ESEM hot stage heating schedule for experiments investigating healing as a function of time at a fixed temperature of 430 °C (Experiments E-H).

Ramp Cycle	Set Point (°C)	Ramp Rate (°C/minute)	Dwell Time (min.)
1	370	20	15
2	400	10	15
3	430	5	90

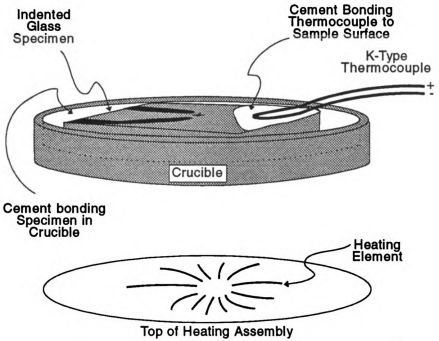

Figure 9 Schematic of the second ESEM hot stage showing the top of the heater assembly, the crucible and the glass specimen with a K-Type thermocouple attached.

3.6.1.4 Temperature Measurement of New Hot Stage Heater

The temperature at the sample surface was compared to the ESEM controller temperature reading for three sets of conditions. The first and second investigations used a sample cemented in a crucible with a thermocouple bonded to the sample surface (Figure 9). For the third investigation a thermocouple was bonded directly to the crucible with silver paint. In the first investigation, the crucible was set on top of the heater assembly, while in the second and third investigations the crucible was bonded to the heater assembly with silver paint. In all three investigations the thermocouple was connected to the extra thermocouple connection in the door of the sample chamber. The sample temperature was measured using an ice point, digital voltmeter, and thermocouple tables. The ESEM controller temperature was read directly from the hot stage controller digital display.

Also studied during the first investigation was the precision of the thermocouple reading using the ESEM chamber door pass-through port. The precision of the thermocouple reading using the pass-through port was determined during an isothermal hold at 430 °C by comparing the temperature reading using the pass-through to a direct thermocouple reading inside the ESEM chamber. The temperature inside the sample chamber was determined by connecting the thermocouple to an ice point and voltmeter inside the sample chamber and reading the voltmeter through a sample chamber view port. The temperature using the pass-through was determined by connecting the thermocouple to the pass-through port inside the ESEM chamber, connecting an ice point and voltmeter to the pass-through port outside the ESEM, and reading the voltmeter.

3.6.2 Conventional Experiments

Conventional crack healing experiments were performed on soda-lime silica glass, Coors alumina and microwave sintered alumina specimens. In conventional crack healing experiments, cracks were made in a specimen, aged, characterized, heated in a furnace, and then re-characterized to note changes in the cracks brought on by the healing cycle.

3.6.2.1 Conventional Healing Procedure

Specimens of a specific geometry and size were prepared. Selected glass samples then underwent a heating cycle to remove the residual stresses created by sample preparation. Vickers indent cracks were made in the sample with a set load, loading rate, and load time. The specimens with the indent cracks were aged for 24 or 48 hours in laboratory air (about 45 %r.h.), a desiccator (about 0 %r.h.), or a wet chamber (about 100 %r.h.) before characterization and healing. Characterization was performed using the optical microscope part of the indentor to measure the crack lengths ($2c_1$ and $2c_2$) and to sketch the crack shapes. Thermal annealing via conventional furnace heating consisted of placing the sample in a furnace boat, placing the boat in a tube furnace, ramping to a predetermined temperature, holding for a predetermined amount of time, and cooling to room temperature. After the thermal annealing cycle, the crack lengths ($2c_1$ and $2c_2$) were measured and the crack shapes were sketched using the optical microscope part of the indentor.

3.6.2.1.1 Temperature Measurement during Conventional Healing

The temperature was measured during conventional healing using either a J-Type thermocouple or an R-Type thermocouple. The J-Type thermocouple wire (Omega 0.010 inch Iron-Constantan Thermocouple wire) was used for temperature measurements of less than 700 °C. The R-Type thermocouple wire (Omega 0.015 inch Platinum-Platinum/13%Rhodium Thermocouple wire) was used for temperature measurements above 700 °C.

The thermocouples were attached to an Ice-Point of the same type as the thermocouple wire (Omega J-Type or R-Type Ice Point). The J-Type thermocouple voltage was read with a digital voltmeter (Fluke Model 77 Multimeter) attached to the output of the Ice-Point using the 300 mV scale. The R-type thermocouple voltage was recorded on a chart recorder (Cole Parmer 2 Channel 200 mm Flatbed Chart Recorder) with 20 mV full scale and a chart speed of 10 cm per hour. The voltage (read from the digital voltmeter or the chart recording) was converted to temperature using Thermocouple Reference Tables (Omega Thermocouple Reference Tables).

3.6.2.1.2 Conventional Furnaces Used for Healing

Two furnaces were used for conventional healing: 1) a large tube furnace capable of temperatures up to 1500 °C and 2) a small tube furnace capable of temperatures up to 1000 °C. The large tube furnace (MRL Thermtec Horizontal 30" Hot Zone Tube Furnace) had a controller (Omega 812 Four Segment Programmable Controller) which allowed ramp rate, hold temperature and hold time to be set. The furnace cooled at the rate set on the controller until the temperature decreased to approximately 450 °C,

after which the furnace "free" cooled to room temperature due to the large thermal mass of the furnace.

The small tube furnace was made at MSU. The tube furnace had a 76 mm (3 inch) inner diameter and 305 mm (12 inch) long heating element (NR3-4 Insulated Nicrome Wire Electric Heating Element by CM, Inc., Bloomfield, N.J.) which was surrounded by insulation and encased in a 305 mm (12 inch) diameter by 380 mm (15 inch) long stainless steel cover. Inserted inside the cylindrical heating element was a 25 mm (1 inch) diameter, 1.5 mm (0.6 inch) thick and 405 mm (16 inch) long, open ended, glass tube. On the top, outer surface of the glass tube was a K-Type thermocouple (Omega 0.0005 inch thick "cement on" foil thermocouple) which was mounted with thermocouple cement (Omega cc high temperature cement). The thermocouple was connected to a controller (Omega CN5001K2). The controller only allowed a single temperature to be set and did not allow other parameters such as heating rate or hold time to be set. Since the hold time was not automatically controlled, when the sample temperature reached the desired temperature the time was noted and after the desired amount of time had passed the furnace was unplugged and allowed to cool to room temperature. The furnace ramp rate was approximately 7 °C/minute.

3.6.2.1.3 Specimen Placement into the Tube Furnaces

The indented and aged specimens were placed in a boat with a 1-2 mm (0.04-0.08 in.) thick layer of alumina powder (Buehler Micropolish A) in the bottom (to prevent the sample sticking to the boat). For the small tube furnace, the boat (Coors CB 10

65564) was inserted into the furnace tube a distance of 229 mm (9 in.). For the large tube furnace, a rectangular boat (Coors 03526) with dimensions of 100 mm X 45 mm X 19 mm (3.94 in. X 1.77 in. X 0.75 in.) or a tube dee with dimensions of 254 mm X 38.1 mm (10 in. X 1.5 in.) was inserted into the furnace tube a distance of 765 mm (30.13 in.). The thermocouple used for temperature measurement was inserted with the boat such that the thermocouple was at the same position in the furnace tube as the specimens. Once the sample and thermocouple were in place, a piece of fibrous insulation (AP Green Inswool HTZ) was used to fill and insulate the opening of the furnace tube.

3.6.2.2 Healing in Soda-Lime Silica Glass

Seven different experiments with a total of 113 specimens and 654 cracks were used to investigate healing in soda-lime silica glass (Table 8). The specimens were prepared (Table 9), heated to remove residual stress (Table 9), indented (Table 9 and 10), aged for 24 hours (Table 9), and annealed (Table 8 and 9). Some specimens underwent a heating cycle after preparation to relieve the specimen residual stress (Table 9 and 11).

3.6.2.2.1 Soda-Lime Silica Healing Specimen Preparation

For crack healing in soda-lime silica glass, long rectangular specimens and small square specimens were used (Table 9). The long rectangular specimens were cut with the high speed saw (Section 3.2.1.2) to nominal dimensions of 76 mm X 11.4 mm X 1.1 mm (3.0 in. X 0.45 in. X 0.045 in.). The small square specimens were cut with

Table 8 Thermal annealing temperature and times for conventional healing in soda-lime silica glass (Experiments 1 to 7). Specimen, indent, aging and annealing condition are detailed in Table 9.

Experiment	Temperature (°C)	Time (Minutes)	Total Number of Specimens	Total Number of Cracks
1	600	30	10	60
2	550	30	6	12
3	350, 375, 400, 425, 450, 475, 500, 525, 550, 575	15	14	84
	525, 550, 575	30	9	54
	525, 550, 575	45	9	54
	525, 575	120	5	30
4	525, 538, 550, 563, 575	60	15	90
5	525	60, 90, 120, 150, 180	15	90
6	575	60, 90, 120, 150	12	72
7	550	60, 90, 120, 240, 480	18	108

Table 9 Details of specimen, indent, aging, and annealing conditions for conventional healing in soda-lime silica glass (Experiments 1-7).

Experiment	Specimen Geometry	Stress Relief Cycle	Indents per Specimen	Indent Geometry	Indenting Condition	Aging Time (Days)	Aging Humidity (~%r.h.)	Tube Furnace	Furnace Boat	Thermo-couple
1	Rectangle	None	3	Figure 10	α	24	45	Large	Figure 12	None
2	Rectangle	None	1	Indent B Figure 10	α	24	45	Large	Figure 12	None
3	Square	None A B	3	Figure 11	β	24	45	Small	Figure 13	J-Type
4	Square	C	3	Figure 11	β	24	45 0 100	Small	Figure 13	J-Type
5	Square	D	3	Figure 11	β	24	45 0 100	Small	Figure 13	J-Type
6	Square	D	3	Figure 11	β	24	45 0 100	Small	Figure 13	J-Type
7	Square	E	3	Figure 11	β	24	45 0 100	Large	Figure 14	J-Type

Table 10 Indentation conditions referred to in Table 9 for soda-lime silica specimens used in conventional healing (Experiments 1-7).

Indenting Condition	Load (N)	Loading Rate (μm/s)	Loading Time (s)
α	9.8	50	10
β	9.8	70	15

Table 11 Stress relief cycles referred to in Table 9 for soda-lime silica specimens used in conventional healing (Experiments 1-7).

Stress Relief Cycle	Prior Stress Relief Cycle	Furnace	Hold Temperature (°C)	Hold Time (Minutes)	Ramp Rate (°C/Minute)
A	None	Box Muffle	550	30	Unknown
B	None	Box Muffle	600	60	Unknown
C	None	Rapid Temp	587	180	~ 8
D	C	Large Tube	587	180	10
E	D	Large Tube	587	180	5

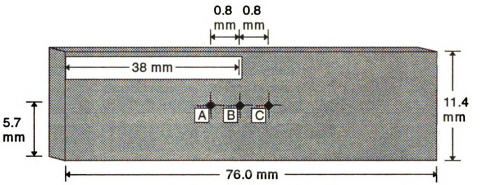

Figure 10 Schematic of indent placement in the rectangular glass specimens used in conventional healing Experiments 1 and 2 (note that the while the indent locations are to scale the indent sizes are exaggerated).

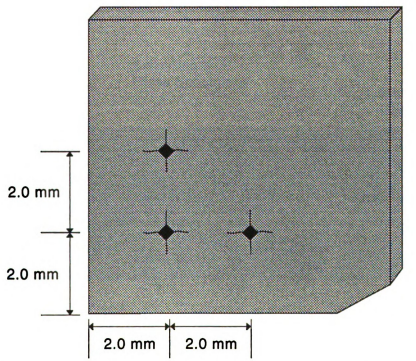

Figure 11 Schematic of indent placement in the square glass specimens used in conventional healing Experiments 3 - 7 (note that the while the indent locations are to scale the indent sizes are exaggerated).

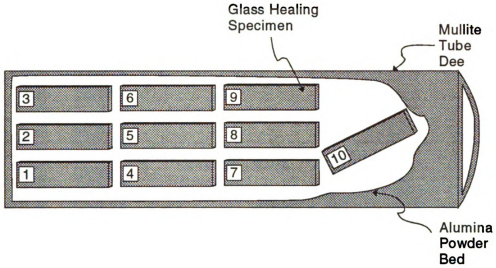

Figure 12 Schematic of specimen location on the tube dee for conventional healing in glass Experiments 1 and 2.

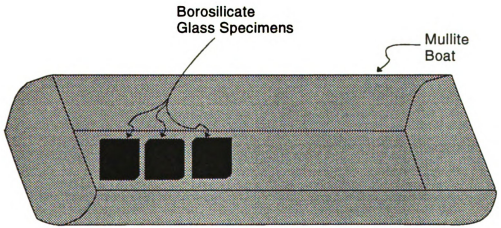

Figure 13 Schematic of specimen location on the boat for conventional healing in glass Experiments 3 - 7.

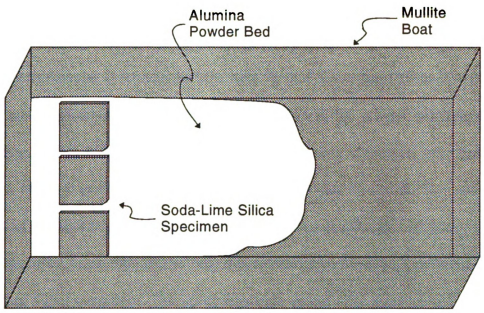

Figure 14 Schematic of specimen location in the boat for conventional healing in glass Experiment 7 and conventional healing in alumina Experiment 2.

the low speed saw (Section 3.2.1.1) to nominal dimensions of 7.5 mm X 7.5 mm X 1.1 mm (0.3 in. X 0.3 in. X 0.045 in.).

The rectangular specimens had the long 76 mm X 1.1 mm (3.0 in. X 0.045 in.) edges of the specimens beveled using 240, 320, 400, and 600 grit SiC grinding paper (Mager Scientific C Weight Waterproof Paper). The square specimens were ground using 240, and 400 grit SiC grinding paper to remove chips formed during cutting. For some of the square samples, one, two, or three corners were ground flat to help indicate specimen orientation and to help differentiate specimens with different annealing or aging conditions. All specimens were rinsed after grinding or beveling with tap water and placed on laboratory paper towels.

3.6.2.2.2 Relief of Specimen Residual Stress

Before indentation, some soda-lime silica healing specimens underwent a heating cycle to relieve the residual stress created during sample preparation (Tables 9 and 11). Heating was performed in one of three different furnaces: 1) a box muffle furnace (Lindburg 1200 °C Box Muffle Furnace: 7.5 in. X 5.25 in. X 14 in.) without an independent means of sample temperature measurement, 2) a rapid temp furnace (C*M Rapid Temp Furnace) with a J-Type thermocouple used for sample temperature measurement, 3) the large tube furnace (Section 3.6.2.1.2) with an R-Type thermocouple used for sample temperature measurement.

3.6.2.2.3 Strength Testing and Sub-Surface Healing (Experiments 1 and 2)

In addition to the 10 healing samples prepared for Experiment 1 (Table 7 and 8), two additional samples were prepared and were left to continue to age in air without thermal annealing. After the annealed samples had cooled and all the crack lengths were measured, all 12 specimens were tested in three-point bend using a displacement controlled mechanical testing machine (Instron model 4206 Automated Testing System, Canton, MA). The samples were tested in laboratory air with a crosshead speed of 0.50 mm/minute (0.02 inch/minute) and an outer span distance of 60 mm (2.4 inch). The initial dimensions of width and thickness, the fracture load and displacement, and the location of the fracture were recorded for each sample. From the initial sample dimensions and the fracture load, the fracture stress (Modulus of Rupture) was calculated.

To investigate the sub-surface crack healing for each of the 6 specimens healed in Experiment 2 (Table 7 and 8), a method originally developed by Kirchner [64] was used in an attempt to fracture through the partially healed indents. Kirchner's [64] technique was used to avoid subcritical crack extension of the partially healed indentation crack by avoiding direct loading on the partially healed crack. By focusing through the transparent glass specimen, a series of four to six 9.8 N indents was placed on the specimen face opposite the partially healed indentation crack, aligned with the partially healed indent crack. From four to eight, 49 N indents (collinear with the 9.8 N indents) led to crack coalescence and catastrophic failure of the partially healed specimen being indented.

Specimens which were fractured through the partially healed indent using

Kirchner's method (Experiment 1) or three-point bend testing (Experiment 1) were analyzed in an SEM (JEOL JSM-6400V). The SEM was operated with a LaB_6 filament having a 20 KeV accelerating voltage. The second largest aperture was used to help increase the resolution. The fractured samples needed to be less than 2 or 3 mm (0.8 or 0.12 inch) in height in order to further increase resolution by having the smallest working distance possible and to allow the samples to be inserted in the small sample exchange of the SEM. Since the fractured specimen halves were 38 mm (1.5 inch) long, the fracture specimens were cut 2 or 3 mm (0.8 or 0.12 inch) from the fractured ends with the low speed diamond saw (Section 3.2.1.1). After cutting, the samples were washed with powdered glassware soap (Alconox Powder Detergent), rinsed with tap water, and dried. To ensure removal of the cutting oil from the samples before placing in the SEM vacuum environment, the samples were also soaked for 30 minutes in acetone, and dried again.

Both halves of the fractured specimens were placed next to each other on an SEM stub with one of the two halves rotated 180° such that the fractured ends were together when mounted and the top surfaces were parallel. The samples were mounted on the SEM stub using five minute epoxy (Five Minute Epoxy Gel, Devcon Corporation, Davers, MA). After the epoxy had dried, conductive carbon paint (SPI Supplies, West Chester, PA) was applied to the top corners of the samples to the base of the SEM stub to help in charge removal during SEM analysis of the non-conducting samples. The carbon paint was allowed to dry for a minimum of 30 minutes. After the sample the carbon paint was dry, the samples were gold coated to eliminate charging during SEM analysis.

3.6.2.2.4 Effects of Stress Relief Cycle (Experiment 3)

An initial survey of the healing behavior of the soda-lime silica glass was done for a range of temperatures and times for square specimens (Tables 8 and 9). As a part of this study the effects of the stress relief cycle (Table 9 and 11) on crack healing was investigated using samples that had undergone two different stress relief cycles (A and B from Table 11) and samples that had not ben annealed.

3.6.2.2.5 Effect of Aging Environment, Time and Temperature (Experiments 4-7)

The effects of aging environment, annealing temperature, and annealing time on crack healing was investigated using samples that had undergone aging in three different environments (Table 9) and thermally annealing them for different times at different temperatures (Table 8).

3.6.2.2.6 Residual Stress Relief Testing

Machining such as cutting and grinding can lead to development of residual stresses on the surfaces of the machined samples. Residual surface stresses created during machining change the driving force for radial indent crack growth discussed in Section 3.5.2 and result in an increase or decrease in the indent crack length. The driving forces for the healing process could also be affected by the residual surface stresses created during specimen preparation and result in a change in observed crack healing. Radial crack lengths of indents made before and after different heating cycles in machined soda-lime silica specimens were used to calculate the residual stress relieved during the thermal cycle and to determine the optimum stress relied heating cycle

conditions for the glass specimens.

Rectangular residual stress specimens were cut using the low speed diamond saw (Section 3.2.1.1) to nominal dimensions of 25.4 X 7.5 X 1.1 mm (1.0 X 0.3 X 0.045 inch, Figure 15) and square specimens were prepared as described in Section 3.6.2.2.1. Testing began by indenting (with conditions α from Table 10) at the numbered indent locations (Figure 15). After 24 hours, the cracks for each of the numbered indents was measured and sketched. The samples subsequently underwent a heating cycle to relieve residual stress created during machining. Testing continued by indenting in the capitol lettered indent locations (Figure 15). After 24 hours, the cracks for each of the lettered indents was measured and sketched.

At higher temperatures, there was concern that the glass would begin to flow viscoelastically. To protect the mullite boat from possible molten glass, a 2 to 3 mm (0.08 to 0.13 inch) bed of alumina powder (Buehler Micropolish A) was placed in the bottom of a 87.4 X 17.5 mm (3.44 X 0.69 inch) mullite boat (Coors CB 10 65564) and an ~50 X ~10 X 1.0 mm (~2.0 X ~0.4 X 0.04 inch) Coors alumina sample was placed on top of the powder bed as a setter. The residual stress specimen was placed on top of the alumina setter as shown in Figure 16. In addition to the 25.4 X 7.5 X 1.1 mm (1.0 X 0.3 X 0.045 inch) rectangular residual stress specimen, two 7.5 X 7.5 X 1.1 mm (0.3 X 0.3 X 0.045 inch) square specimens were stacked on top of each other and placed on the alumina setter as shown in Figure 16. The boat was placed in the small tube furnace (Section 3.6.2.1.2) and heated with the sample temperature measured using a J-Type thermocouple (Section 3.6.2.1.1).

3.6.2.3 Healing in Alumina

Two different experiments with a total of 72 specimens and 540 cracks were used to investigate healing in two different kinds of alumina (Table 12). Specimens were prepared (Table 13), indented (Table 13 and 14), aged (Table 13), and thermally annealed (Table 15).

3.6.2.3.1 Alumina Specimen Preparation

The Coors alumina samples were cut to nominal dimensions of 10 mm X 10 mm X 1 mm (0.4 in. X 0.4 in. X 0.04 in.) using the high speed cutting saw (Section 3.2.1.2). The cut Coors alumina squares and the as-received microwave alumina disks were polished using the automatic polisher (Section 3.2.2). To identify the orientation of the square Coors alumina samples in Experiment 1 the bottom right corner was ground flat using 240 grit SiC grinding paper. To identify the orientation of square Coors alumina samples and distinguish between the three samples aged under different conditions in Experiment 2, the bottom right corner of the specimens either had one, two or three 1.5 mm (0.06 inch) round holes sonic milled to a depth of about 0.4 mm (0.016 inch). The polished microwave sintered alumina disks were cut into quarters using the low speed diamond saw (Section 3.2.1.1). The quartered microwave sintered alumina specimens were ground to remove chips formed during cutting with the low speed saw. The Coors alumina squares and the microwave alumina quarters were washed with powdered glassware soap (Alconox Powder Detergent), rinsed with tap water, and placed in an ultrasonic bath of De-Ionized (D.I.) water for 10 to 15 minutes to remove any debris from polishing or from grinding.

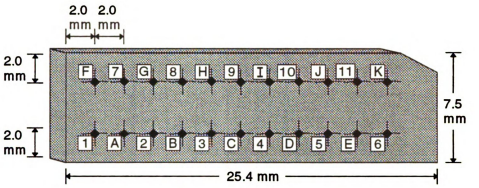

Figure 15 Schematic of the rectangular glass specimens used for the residual stress measurement experiments showing the ground upper right hand corner (note that while the indent locations are to scale the indent sizes are exaggerated).

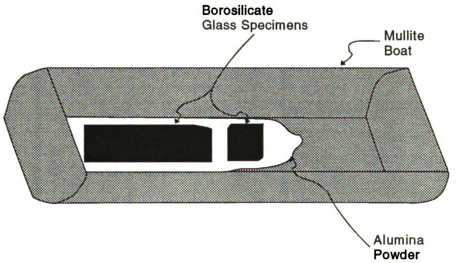

Figure 16 Schematic of rectangular glass specimen location in boat for residual stress measurement experiments.

Table 12 Thermal annealing temperature and times for conventional healing in alumina (Experiments 1 and 2). Specimen, indent, aging and annealing condition are detailed in Table 13.

Experiment	Temperature (°C)	Time (Minutes)	Types of Alumina Tested	Total Number of Specimens	Total Number of Cracks
1	1005	60	Coors and Microwave	6	216
	1237			6	
	1469			6	
2	1005	60, 90, 120, 1410	Coors	12	72
	1121	60, 90, 120	Coors	9	54
	1237	60, 90, 120, 180	Coors	15	90
	1353	60, 90, 120	Coors	9	54
	1469	60, 90, 120	Coors	9	54

Table 13 Details of specimen, indent, aging, and annealing conditions for conventional healing in alumina (Experiments 1-2).

Experiment	Type of Alumina	Specimen Geometry	Indents per Specimen	Indent Geometry	Indenting Condition	First Aging Time (Days)	First Aging Humidity (~%r.h.)	Second Aging Time (Days)	Second Aging Humidity (~%r.h.)
1	Coors	Figure 16	6	Figure 16	α	24	45	24	45 0 100
1	Microwave	Figure 17	6	Figure 17	β	24	45	24	45 0 100
2	Coors	Figure 19	6	Figure 19	α	24	45 0 100	None.	None.

Table 14 Indentation conditions referred to in Table 13 for alumina specimens used in conventional healing (Experiments 1-2).

Indenting Condition	Load (N)	Loading Rate (μm/s)	Loading Time (s)
α	49	50	10
β	98	65	5

Table 15 Thermal annealing cycle for alumina specimens used in conventional healing (Experiments 1-2).

Experiment	Initial Ramp Rate (°C/Minute)	Temperature of Ramp Rate Change (% of the Set Temperature in K)	Final Ramp Rate (°C/Minute)	Cooling Rate (°C/Minute)
1	10	84	2.5	10
2	10	80	2.5	10

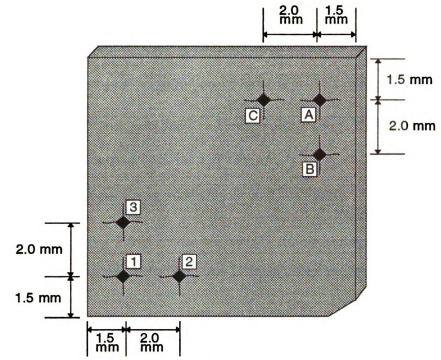

Figure 17 Schematic of Coors alumina specimens used in conventional healing Experiment 1 (note that the while the indent locations are to scale the indent sizes are exaggerated).

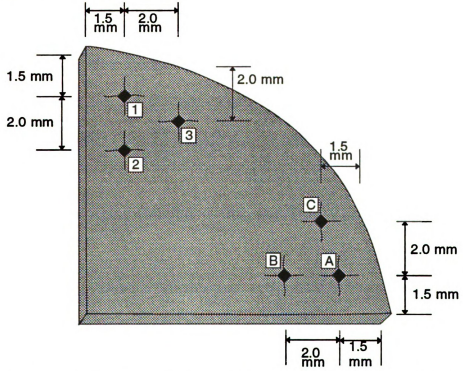

Figure 18 Schematic of Coors alumina specimens used in conventional healing Experiment 1 (note that the while the indent locations are to scale the indent sizes are exaggerated).

Indents were made in the Coors alumina and Microwave sintered alumina [65] (Tables 13 and 14). Crack healing cycles were performed in the large tube furnace with the samples placed in a ceramic boat (Figure 20). The cooling rate and the initial heating rate were set to 10 °C/minute. To reduce the furnace temperature overshoot, for some samples the heating rate was reduced to 2.5 °C when the furnace reached 80 or 84% of the final temperature (calculated in Kelvin) (Table 15).

3.6.2.3.2 Effects of Aging Humidity and Temperature in Two Aluminas (Experiment 1)

Initially, indents 1 - 3 were made (Figure 17 and 18), measured after about 30 minutes, and then were aged in laboratory air (Table 13). After 24 hours a second set of indents (A - C in Figures 17 and 18) was made for each sample. The crack lengths were measured about 30 minutes after indentation. Both specimens then were aged another 24 hours in either laboratory air, a desiccator, or a wet chamber (Table 13). After the second 24 hour age the indent crack lengths were again measured. Samples were thermal annealed (Table 12 and 15) and the indent crack lengths were measured.

3.6.2.3.3 Effects of Aging Humidity, Time, and Temperature in Coors Alumina (Experiment 2)

Three indented Coors alumina samples were aged under different humid environments for 24 hours (Table 13). The aged samples were thermally annealed together (Table 12 and 13) in a furnace boat (Figure 13) in the large tube furnace (Section 3.6.2.1.2).

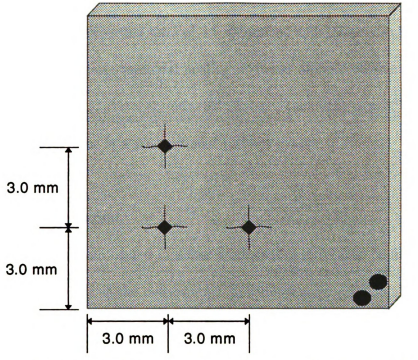

Figure 19 Schematic of Coors alumina specimens used in conventional healing Experiment 2 (note that the while the indent locations are to scale the indent sizes are exaggerated).

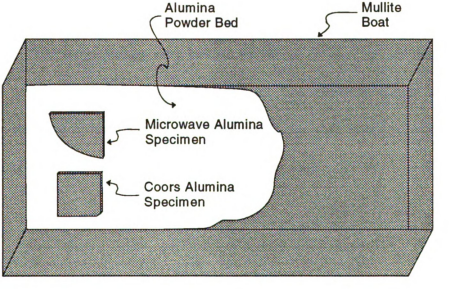

Figure 20 Schematic of Coors alumina and microwave sintered alumina specimen location in ceramic boat for conventional healing Experiment 1.

3.6.3 Microwave Healing

Three different experiments with a total of 15 specimens and 180 cracks were used to investigate microwave and conventional healing in Coors alumina (Table 16). Specimens were prepared (Table 17), indented (Table 17 and 18), aged (Table 17), and annealed in a microwave or in a conventional furnace (Table 16).

3.6.3.1 Specimen Preparation

Coors alumina samples were heated in either a conventional furnace or in a microwave furnace. Specimens heated in the conventional and microwave furnace were prepared in the same manner. The Coors alumina specimens were prepared in the same manner as the samples for conventional crack healing in alumina Experiment 2 (Section 3.6.2.3.3).

3.6.3.2 Microwave and Conventional Heating

Microwave heating was performed in the same microwave apparatus described in Section 3.1.2.. The temperatures were held to within +/- 2 °C of the set temperature for one hour without an overshoot greater than 2 °C. Conventional heating was performed in the tube furnace described in Section 3.6.2.1 with samples placed in a ceramic boat (Figure 22).

Table 16 Thermal annealing temperature and times for microwave and conventional healing in alumina (Experiments 1-3). Specimen, indent, aging and annealing condition are detailed in Table 17.

Experiment	Temperature (°C)	Time (Minutes)	Heating Mode	Heating Rate (°C/Minute)	Total Number of Cracks
1	1237	60	Microwave	10	12
	1295				12
	1353				12
	1411				12
	1469				12
2	1237	60	Microwave	30	12
	1295				12
	1353				12
	1411				12
	1469				12
3	1237	60	Conventional	10	12
	1295				12
	1353				12
	1411				12
	1469				12

Table 17 Details of specimen, indent, aging, and annealing conditions for microwave and conventional healing in alumina (Experiments 1-3).

Experiment	Type of Al_2O_3	Indent Geometry	Indenting Condition for Indents 1, 2, 3	Indenting Condition for Indents A, B, C	Aging Time (Days)	Aging Humidity (~%r.h.)
1	Coors	Figure 30	α	β	24	45
2	Coors	Figure 30	α	β	24	45
3	Coors	Figure 30	α	β	24	45

Table 18 Indentation conditions referred to in Table 16 for alumina specimens used in conventional healing (Experiments 1-2).

Indenting Condition	Load (N)	Loading Rate (μm/s)	Loading Time (s)
α	49	70	15
β	98	70	15

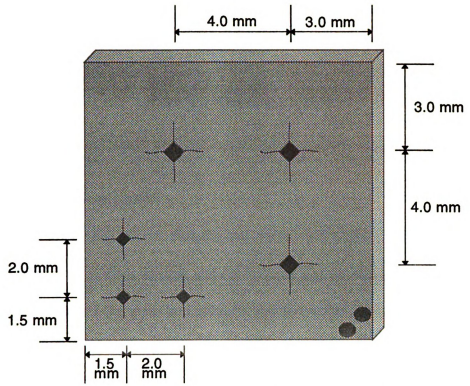

Figure 21 Schematic of Coors alumina specimens used in microwave and conventional healing experiments (note that the while the indent locations are to scale the indent sizes are exaggerated).

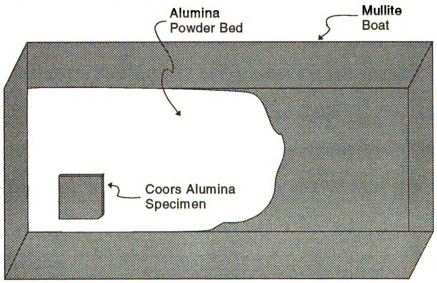

Figure 22 Schematic of Coors alumina specimen location in ceramic boat for microwave healing experiments.

4. RESULTS AND DISCUSSION

4.1 Materials Characterization

The soda-lime silica glass, Coors alumina and microwave alumina material used for experimental studies of static fatigue and crack healing were characterized before testing. The density of the glass and alumina was measured. The grain size of Coors alumina and microwave sintered alumina was measured from micrographs.

4.1.1 Density Measurements

Specimens of soda-lime silica glass, Coors alumina and microwave sintered alumina were prepared as described in Section 3.3.1.1. The density was determined using an Archimedes' described in Section 3.3.1.2 on four samples of each material. The average density and standard deviation were determined (Table 19). The percent theoretical density for the Coors alumina and microwave alumina were 97.3±0.3 and 98.1±0.2%, respectively, based on a theoretical density of 3.965 g/cm^3 [61].

4.1.2 Microstructure

Micrographs of thermally etched surfaces of Coors alumina and microwave alumina were taken using the ESEM to determine the grain size using a line intercept method. An example of the thermally etched surface of the Coors alumina and microwave

Table 19 Density measurements for soda-lime silica, Coors alumina, and microwave alumina specimens using an Archimedes' method.

Specimen	Soda-Lime Silica Glass				Coors Alumina				Microwave Sintered Alumina			
	W_{dry} (g)	W_{susp} (g)	W_{wet} (g)	ρ (g/cc)	W_{dry} (g)	W_{susp} (g)	W_{wet} (g)	ρ (g/cc)	W_{dry} (g)	W_{susp} (g)	W_{wet} (g)	ρ (g/cc)
1	1.447	0.858	1.446	2.461	2.174	1.610	2.173	3.861	1.812	1.345	1.812	3.880
2	1.455	0.865	1.454	1.470	2.119	1.568	2.115	3.874	1.815	1.346	1.813	3.887
3	1.422	0.841	1.421	1.452	2.195	1.623	2.194	3.844	1.807	1.641	1.805	3.894
4	1.421	0.839	1.420	1.446	2.137	1.582	2.136	3.857	1.826	1.357	1.826	3.893
Average				2.457				3.859				3.889
Standard Deviation				0.011				0.012				0.006

alumina can be seen in Figures 23 and 24, respectively. The Coors alumina grain size was 2.1±0.2 microns and the microwave sintered alumina grain size was 20.6±3.6 microns.

4.2 Indentation Measurement Testing

Indentation measurements experiments were performed to compare optical measurements between different researchers. Additional indentation measurement experiments were performed to compare optical and ESEM measurements.

4.2.1 Multiple Experimenter Measurements

Measurements of crack lengths in soda-lime-silicate glass, Coors alumina, microwave alumina, and silicon nitride were made by multiple experimenters as outlined in Section 3.4.1. The average and standard deviation of five different measurements were reported by each of six different researchers for each material (Table 20-23). From the data reported by the six researchers the average for the group was calculated (Table 20-23).

4.2.1.1 Crack Length Measurement Variation with Experimenter

The standard deviations for indent crack length measurements by each researcher for glass, Coors alumina, microwave alumina, and silicon nitride were less than 3, 5, 6, and 9 microns, respectively (Tables 20 - 23). The indent crack length measurement standard deviations by each researcher were less than 1.5%, 2.5%, 2%, and 3% of the group average crack length measurement for glass, Coors alumina, microwave

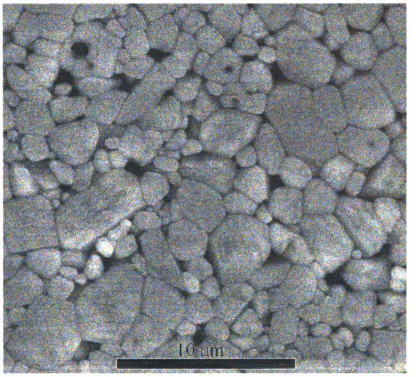

Figure 23 ESEM micrograph of thermally etched Coors alumina used in grain size determination showing a small grain size of 2.1 ± 0.2 µm.

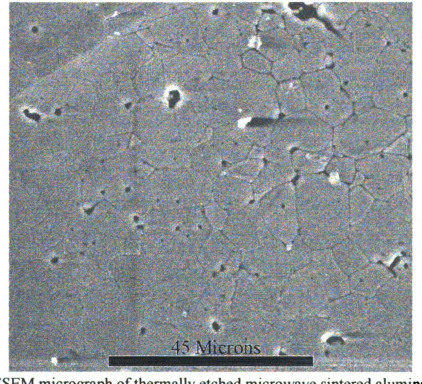

Figure 24 ESEM micrograph of thermally etched microwave sintered alumina used in grain size determination showing a grain size of 20.6 ± 3.6 µm.

Table 20 Average and standard deviation of indent crack lengths in soda-lime silica glass measured by six different researchers using an optical microscope to determine the level of operator error typically present in Vickers indentation measurements.

Researcher	$2c_1$ (microns) Mean and Standard Deviation	$2c_2$ (microns) Mean and Standard Deviation
1	225.3 ± 2.0	221.8 ± 2.7
2	215.8 ± 1.4	215.3 ± 1.4
3	210.6 ± 2.3	214.9 ± 1.2
4	209.2 ± 0.6	210.9 ± 0.6
5	214.4 ± 0.5	214.8 ± 0.8
6	210.8 ± 0.3	221.3 ± 0.3
Group Average	214.4	216.5
ESEM Micrograph	215.0 ± 2.3	216.3 ± 1.2
ESEM Computer Screen	210.0 ± 1.2	212.0 ± 0.0

Table 21 Average and standard deviation of indent crack lengths in Coors alumina measured by six different researchers using an optical microscope to determine the level of operator error typically present in Vickers indentation measurements.

Researcher	$2c_1$ (microns) Mean and Standard Deviation	$2c_2$ (microns) Mean and Standard Deviation
1	272.9 ± 4.8	253.2 ± 1.0
2	262.2 ± 4.8	240.0 ± 0.8
3	267.5 ± 1.2	243.1 ± 2.5
4	267.1 ± 1.4	242.6 ± 3.4
5	248.8 ± 2.4	229.3 ± 4.5
6	239.4 ± 3.3	216.7 ± 0.5
Group Average	259.7	237.5
ESEM Micrograph	264.1 ± 2.2	261.2 ± 1.4
ESEM Computer Screen	266.0 ± 0.5	264.0 ± 2.0

Table 22 Average and standard deviation of indent crack lengths in microwave sintered alumina measured by six different researchers using an optical microscope to determine the level of operator error typically present in Vickers measurements.

Researcher	$2c_1$ (microns) Mean and Standard Deviation	$2c_2$ (microns) Mean and Standard Deviation
1	353.6 ± 1.9	355.3 ± 1.5
2	388.8 ± 3.4	368.7 ± 7.7
3	432.3 ± 2.5	393.7 ± 2.8
4	385.4 ± 2.8	359.3 ± 1.4
5	389.4 ± 1.7	382.8 ± 2.7
6	324.7 ± 5.3	331.4 ± 0.5
Group Average	379.0	365.1
ESEM Micrograph	376.7 ± 1.8	356.3 ± 1.1
ESEM Computer Screen	377.0 ± 1.0	353.8 ± 0.8

Table 23 Average and standard deviation of indent crack lengths in silicon nitride measured by six different researchers using an optical microscope to determine the level of operator error typically present in Vickers indentation measurements.

Researcher	$2c_1$ (microns) Mean and Standard Deviation	$2c_2$ (microns) Mean and Standard Deviation
1	351.5 ± 1.3	376.3 ± 1.8
2	345.6 ± 3.5	365.7 ± 8.8
3	350.6 ± 1.3	373.0 ± 1.5
4	344.2 ± 3.0	368.5 ± 2.7
5	355.0 ± 2.9	370.3 ± 5.1
6	334.8 ± 5.4	349.0 ± 3.5
Group Average	346.0 ± 7.2	367.1 ± 9.6

alumina, and silicon nitride, respectively (Tables 20 - 23, Figure 25).

For glass, Coors alumina, microwave alumina, and silicon nitride, each researcher's mean measured indent crack length, $2c_1$, is shown in Figure 25 as a data point. The average of all the researcher's measured means is shown in Figure 25 as a horizontal line. The data points for glass, Coors alumina, and silicon nitride are scattered near to the line representing the group average, however, the data points for microwave alumina show a higher degree of scattering about the average (Figure 25). The coefficient of variation, CV, is a measure of the relative variability in a data set and is given by

$$CV = \frac{s}{\bar{X}} * 100\% \qquad (8)$$

where s is the standard deviation and $\bar{X}$ is the mean for the data set. The low coefficient of variation for each researcher of less than 2.0% for the glass and Coors alumina materials, together with the small scatter of the individual researcher's measurements around the average measurement for all researchers (Figure 25) showed that the glass and Coors alumina would make good materials for further crack length investigations.

4.2.2 Optical and ESEM Measurements

The Vickers indented soda-lime-silicate glass, Coors alumina, and microwave alumina specimens (Section 4.2.1) were also analyzed via an Environmental Scanning Electron Microscope (ESEM) by the first researcher (Section 3.4.1). The crack lengths were

measured from micrographs of the indent cracks at a magnification of 325x (Figures 26 - 28 and Tables 20 - 23). Indent crack length measurements were also made "on screen" by the first researcher using the ESEM computer measurement tool (Tables 20 - 23). The ESEM indent crack length measurement differed from the optical microscope measured group average by 1% to 6.5% for glass and 2% to 9% for Coors alumina. The difference in optical and ESEM measurements for glass and Coors alumina was a result of the higher resolution of the electron microscope compared to the optical microscope as well as the higher magnification used for the ESEM measurements.

4.3 Static Fatigue: ESEM Crack Growth Investigations

In-situ observation of crack growth in ceramics under constant applied load was performed using the Environmental Scanning Electron Microscope (ESEM). Tensile specimens of glass and Coors alumina were prepared for the study. A Vickers indent was placed on the center of one of the tensile specimen faces and was observed in the ESEM. The effects of constant applied load, humidity, and time upon crack growth were investigated

4.3.1 Soda-Lime Silica Glass

Soda-lime silica glass tensile specimens were prepared as described in Section 3.5.1. Thirteen glass tensile specimens were prepared using composite tabs affixed with epoxy. One specimen was prepared with composite tabs affixed with high temperature cement. A 9.8 N Vickers indent was placed in the face of each of the tensile

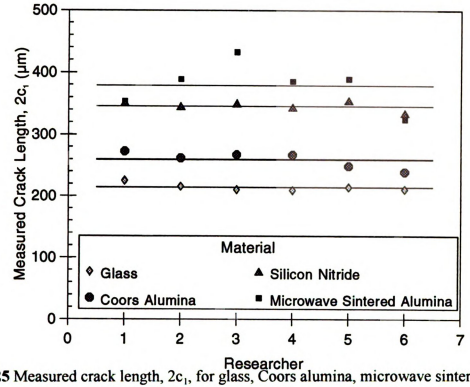

Figure 25 Measured crack length, $2c_i$, for glass, Coors alumina, microwave sintered alumina, and silicon nitride. Each data point was an average of five measurements by an individual researcher and horizontal lines were group averages of six researchers.

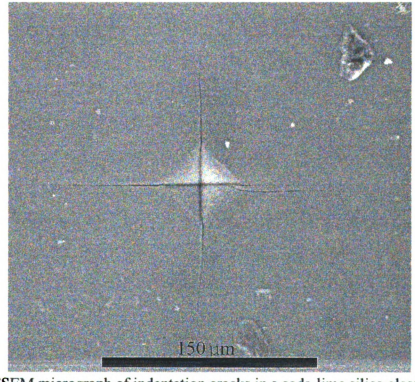

Figure 26 ESEM micrograph of indentation cracks in a soda-lime silica glass specimen used in multiple researcher measurement experiments.

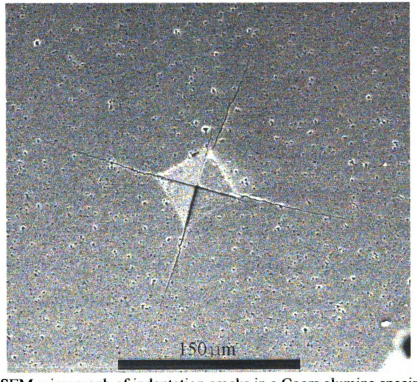

Figure 27 ESEM micrograph of indentation cracks in a Coors alumina specimen used in multiple researcher measurement experiments.

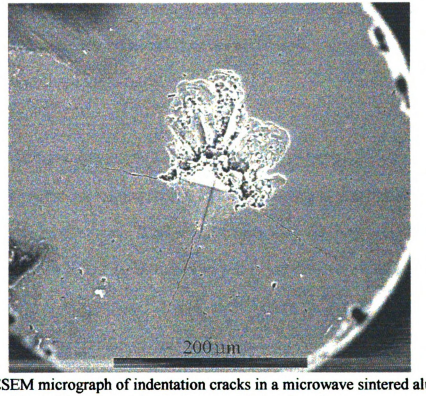

Figure 28 ESEM micrograph of indentation cracks in a microwave sintered alumina specimen used in multiple researcher measurement experiments.

specimens and allowed to age for 24 hours as described in Section 3.2.3.

4.3.1.1 Failures from Mounting Specimens in the Tensile Stage

The indented tensile specimens were placed in the tensile stage of the ESEM as described in Section 3.5.3.2. Eleven of the thirteen composite tab/epoxy adhesive tensile specimens fractured during mounting into the tensile stage. Of the eleven specimen failures during mounting, 5 failures occurred at a tab, 5 failures occurred between the indent and a tab, and one of the failures occurred at the indent.

With the edges beveled to reduce the stress concentration, the indent crack of about 200 microns in length should be the largest flaw in the specimens. Failure at locations other than through the indent, indicated that other flaws, perhaps loaded by non-tensile stresses, developed in the specimens. The most likely type of non-tensile stress would be torsional stress from tabs which were not perfectly parallel. Since five specimens failed at the tab, torsional stress from tabs which were not perfectly parallel seemed to be the major problem.

4.3.1.2 Failures from Automatic ESEM Stage Control Procedures

Two of the thirteen composite tab/epoxy adhesive tensile specimens were successfully mounted into the tensile stage. When the specimen chamber door was closed, the ESEM automatically zeroed the Rotation stage control, which regulates the tensile stage displacement. Consequently, large compressive or tensile stresses fractured the glass samples. To prevent the fracture of specimens by the automatic stage control procedure of the ESEM, additional steps of removing the tensile stage after specimen

mounting and then re-calibrating the stage controls were added to the experimental design (Section 3.5.3.2).

4.3.1.3 Testing of a Mounted Sample

High temperature cement adhesive was used in lieu of epoxy to bond tabs to a specimen (Section 3.5.1.3). The specimen with composite tabs affixed with cement was successfully mounted into the tensile stage. The self tightening grips applied a tensile load of about 3 to 4 MPa after mounting. The chamber door was successfully closed without fracture of the specimen using the additional procedural steps of removing the tensile stage, re-calibrating the stage controls, and replacing the tensile stage before closing the door. Static fatigue testing was started as described in Section 3.5.3.3. Micrographs of the initial indent crack length were taken and then the load was increased.

The specimen with cement bonded composite tabs fractured during the increase of load at about 17 MPa at the tab. The fracture of the tabs at 17 MPa indicated that even though there was an improvement in getting parallel faces for the tabs using the high temperature cement, there was still too much torsional stress developing in the tabs. The static fatigue testing of glass was suspended at this point and testing of Coors alumina was undertaken. The alumina, a polycrystalline material, was expected to be more resistant to small torsional forces caused by specimen preparation problems. It was hoped that improvements in the specimen preparation procedures could be found with the alumina and later be applied to the testing glass.

4.3.2 Coors Alumina

Coors alumina tensile specimens were prepared as described in Section 3.5.1. Alumina tensile specimens were prepared using composite and stainless steel tabs affixed with epoxy or high temperature cement. A 49 or 98 N Vickers indent was placed in the face of each of the tensile specimens and allowed to age for 24 hours as described in Section 3.2.3. The indented tensile specimens were placed in the tensile stage of the ESEM as described in Section 3.5.3.2.

A summary of the ESEM static fatigue testing of the Coors alumina specimens is shown in Table 24. Indent cracks which opened or grew during testing were perpendicular to the direction of the applied stress. References to the left or right half cracks were with respect to the orientation of the crack in the ESEM micrograph. Before static fatigue testing began, failure occurred at the tabs for specimens B, D, E, G, and I. Whether the tabs for the specimens were made from the glass fiber/ epoxy matrix composite or from stainless steel did not appear to make a difference with respect to failure at the tabs.

4.3.2.1 Stainless Steel Tabs

The stainless steel tabs and the cement adhesive are capable of operating at temperatures approaching 1000 °C. The use of stainless steel tabs and cement adhesive in the static fatigue testing procedure developed in the current investigation, will allow the testing procedure to be used by other investigators for high temperature testing of ceramic specimens.

The lower viscosity of the cement compared to the epoxy yielded an adhesive

Table 24 Summary of ESEM static fatigue testing of Coors alumina tensile specimens. (S.S. indicates stainless steel and C.R.S.S. indicates cold rolled stainless steel).

Test	Indent Size (N)	Tab Material	Tab Adhesive	Grip Load (MPa)	Test Details Failure Details
A	49	Composite	Cement	10	Failure before testing Indent failure at ~99 MPa
B	49	Composite	Epoxy	10	Testing detailed in Table 25 Tab failure at 99 MPa
C	49	Composite	Epoxy	10	Testing detailed in Table 26 Indent failure at 132 MPa
D	49	Composite	Epoxy	11	Failure before testing Tab failure at ~43 MPa
E	49	Composite	Cement	11	Failure before testing Tab failure at 11 MPa
F	98	S.S.	Cement	15	Testing detailed in Table 27 No failure at end of testing
G	98	C.R.S.S.	Cement	~10	Failure before testing Tab failure at 10 MPa
H	98	C.R.S.S.	Cement	13 16	Grips slipping initially Grips tightened Testing detailed in Table 28 Indent failure at 70 MPa
I	98	C.R.S.S.	Cement	31	Failure before testing Tab failure at ~60 MPa
J	98	Composite	Cement	17	Testing detailed in Table 29 Indent failure at 100 MPa

layer of uniform thickness easier than the epoxy adhesive. The more uniform adhesive layer thickness and the possibility of future high temperature testing, led to using cement predominantly in later testing. Stainless steel tabs made high temperature testing possible.

The stainless steel material was received in 3.175 mm (0.125 inch) thick strips. The stainless steel thickness was too large to mount in the small tensile stage of the ESEM. A reduction in thickness of the stainless steel tabs was necessary. First, the tensile specimens were prepared with the as-received stainless steel thickness and then the affixed tabs were ground. Unfortunately, specimens were easily fractured during grinding. Cold rolling the stainless steel (described in Section 3.5.1.2) led to problems with the slipping of specimens in the tensile grips due to the increased hardness that resulted from cold rolling.

Specimen H was made with cold rolled stainless steel tabs and was loaded in the self tightening tensile grips in a similar manner as other specimens with 13 MPa of tensile force applied. When the displacement in the tensile fixture was increased to increase the load of the specimen, the grips slipped over the hardened, cold rolled stainless steel tabs. Consequently, to increase the load on the sample, the tensile stage had to be removed from the ESEM, the grips had to tightened, and the tensile stage had to be remounted in the ESEM. On sample I, the grips were initially tightened to give an tensile load of 31 MPa to prevent slippage which would necessitate tensile stage removal and grip tightening. Upon increasing the load in Specimen I, the sample failed at about 60 MPa. The failure was most likely caused by torsional stress as a result of uneven tightening of the grip bolts while increasing the load applied by

the self tightening grip to 31 MPa.

Future specimen preparation for testing after the present investigation would use cold rolled stainless steel and high temperature cement for tabbing. The cold rolled stainless steel would be annealed before mounting to reduce the hardness which caused problems with the grips slipping. Future specimen preparation for testing after the present investigation would also be aided with the design of a fixture which could aid in alignment of the tabs during the curing of the adhesive to give parallel tab faces thus reducing problems with torsional stress and failure at the tabs.

4.3.2.2 Specimen B

Tests performed on Specimens B, C, F, H, and J (which did not fail at the tabs before testing began) are detailed in Tables 25 through 29. The first test was performed on Specimen B (Table 25) which was made with composite tabs affixed with epoxy. The 49 N indent of Specimen B had no crack growth at 21% r.h. (relative humidity) for loads of 77, 89, and 94 MPa and time intervals ranging from 5 to 30 minutes (Table 25). Due to the nature of fracture in brittle materials such as alumina, it is difficult to make assertions from small sample populations, however, the lack of crack growth for Specimen B at 21% r.h. and loads up to 94 MPa, seems to indicate that static fatigue crack growth did not occur in the Coors alumina at 21% r.h. for the loads and times investigated. The lack of crack growth for Specimen B at 21% r.h. also indicates that the experimental procedure step (Section 3.5.3) of dropping the humidity to 10% to take micrographs (in order to increase the resolution of the ESEM) should not have resulted in crack growth while micrographs were taken at the lower humidity.

Table 25 ESEM static fatigue testing of the 49 N Vickers indent in Coors alumina tensile Specimen B (Table 24) which was made with composite tabs affixed with epoxy.

Load (MPa)	Humidity (%)	Time Interval (min)	Comments
77	21	5	No Crack Growth
89	21	30	No Crack Growth
94	21	15	No Crack Growth
99	21	3	Failure at tab

Table 26 ESEM static fatigue testing of the 49 N Vickers indent in Coors alumina tensile Specimen C (Table 24) which was made with composite tabs affixed with epoxy. (References to the left or right half cracks were with respect to the orientation of the crack in the ESEM micrograph).

Load (MPa)	Humidity (%)	Time Interval (min)	Comments
92	10	-	No Crack Growth from load increase
	32	25	26 micron growth of left crack
	32	25	8 micron growth of left crack
	32	35	No growth of left crack
	42	25	No growth of left crack
100	10	-	No Crack Growth from load increase
	32	25	7 micron growth of left crack
	32	25	No growth of left crack
	32	25	No growth of left crack
105	10	-	No Crack Growth from load increase
	32	25	6 micron growth of left crack
111	10	-	No Crack Growth from load increase
	32	25	10 micron growth of left crack
116	10	-	No Crack Growth from load increase
	32	25	1 micron growth of left crack
132	10	2	Failure through indent

Table 27 ESEM static fatigue testing of the 98 N Vickers indent in Coors alumina tensile Specimen F (Table 24) which was made with non-cold rolled stainless steel tabs affixed with high temperature cement. (References to the left or right half cracks were with respect to the orientation of the crack in the ESEM micrograph).

Load (MPa)	Humidity (%)	Time Interval (min)	Comments
50	10	-	No Crack Growth from load increase
	32	25	growth of 9 μm for left and 8 μm for right crack
	32	25	no growth for left and 1 μm growth for right crack
60	10	-	No Crack Growth from load increase
	32	25	no growth for left or right crack
70	10	-	No Crack Growth from load increase
	32	25	6 μm growth for left and no growth for right crack
80	10	-	No Crack Growth from load increase
	32	25	10 μm growth for left and no growth for right
85	10	-	No Crack Growth from load increase
	32	25	no growth for left or right crack
90	10	-	No Crack Growth from load increase
	32	25	growth of 3 μm for left and 15 μm for right crack
	32	25	no growth for left and 1 μm growth for right crack
18	10	2	Reduced load to remove specimen - no failure

Table 28 ESEM static fatigue testing of the 98 N Vickers indent in Coors alumina tensile Specimen H (Table 24) which was made with cold rolled stainless steel tabs affixed with high temperature cement. (References to the left or right half cracks were with respect to the orientation of the crack in the ESEM micrograph).

Load (MPa)	Humidity (%)	Time Interval (min)	Comments
13	10	-	Load could not be increased - grips were slipping
16	10	-	Self-tightened grips tightened slipping eliminated growth of 33 μm for left and 35 μm for right
40	10	-	No crack growth from load increase
	32	25	growth of 28 μm for left and 28 μm for right
	32	25	growth of 12 μm for left and 13 μm for right
	32	25	no growth for left and 2 μm growth for right crack
	32	25	no growth for left and 6 μm growth for right crack
	32	25	no growth for left and 8 μm growth for right crack
	32	25	6 μm growth for left and no growth for right crack
50	10	-	No Crack Growth from load increase
	32	25	growth of 12 μm for left and 6 μm for right
	32	25	no growth for left and 2 μm growth for right crack
	32	25	8 μm growth for left and no growth for right crack
70	10	7	Continuous indent crack growth until failure

Table 29 ESEM static fatigue testing of the 98 N Vickers indent in Coors alumina tensile Specimen J (Table 24) which was made with composite tabs affixed with high temperature cement. (References to the left or right half cracks were with respect to the orientation of the crack in the ESEM micrograph).

Load (MPa)	Humidity (%)	Time Interval (min)	Comments
40	32	25	no growth for left or right crack
	32	25	no growth for left or right crack
	32	25	no growth for left or right crack
	32	75	no growth for left or right crack
17	10	-	ESEM computer crashed - load decreased
17	45	?	Tensile stage with sample removed - ESEM re-booted
	10	-	No crack growth with sample put back in ESEM
50	10	-	No Crack Growth from load increase
	32	25	no growth for left or right crack
60	10	-	No Crack Growth from load increase
	32	25	no growth for left and 4 μm growth for right crack
70	10	-	No Crack Growth from load increase
	32	25	growth of 8 μm for left and 9 μm for right
80	10	-	growth of 6 μm for left and 6 μm for right
	32	25	growth of 5 μm for left and 7 μm for right
	32	25	11 μm growth for left and no growth for right
90	10	-	growth of 4 μm for left and 15 μm for right
	25	25	growth of 33 μm for left and 16 μm for right
100	10	?	Continuous indent crack growth until failure

4.3.2.3 Specimen C

The second successful experiment was performed on Specimen C which was made with composite tabs affixed with epoxy (Table 26). The 49 N indent of Specimen C had the applied load increased to 92 MPa. Micrographs of the left indent crack were taken at the initial load of 10 MPa and when the load was increased to 92 MPa. No crack growth was observed from the micrographs as a result of the load increase from 10 to 92 MPa. The lack of crack growth during the load increase from 10 to 92 MPa appears to show that non-static fatigue crack growth did not occur in the Coors alumina specimens at the load levels used in the study.

After the first 25-minute cycle at 32% r.h. and 92 MPa, the left indent crack of Specimen C increased 26 microns in length and after a second 25-minute cycle at 32% r.h. and 92 MPa the crack increased 8 microns in length (Table 26). Indent crack growth at 32% r.h. indicates that static fatigue crack growth occurred in the Coors alumina under the conditions tested. The crack did not increase in length during the subsequent cycles at 92 MPa even for the cycle for which the humidity was increased to 42%r.h. (Table 26). Crack arrest after the second static fatigue cycle indicates that the static fatigue crack growth saturates or dramatically slows after a certain time under a constant applied stress even with an increase in the humidity level.

Specimen C failed after 2 minutes at 132 MPa and 10% r.h.. The crack length constantly increased during the two minutes before rapid crack propagation and failure. The stress intensity factor, K_I, for Specimen C at an applied stress, σ, of 132 MPa and with a half crack length, c, of 203 microns was 2.38 MPa$\sqrt{m}$ from

$$K_I = Y\sigma\sqrt{\pi}\sqrt{c} \quad (9)$$

where the geometric factor, Y, was taken as $2.24/\pi$ for a semi-circular surface crack in a bar under tensile stress [7]. The stress intensity from the applied tensile load at the crack tip was about 64% of the reported fracture toughness, K_{Ic}, for Coors alumina of 3.70 MPa$\sqrt{m}$ [66]. The stress intensity at the crack tip was most likely increased slightly from bending and/or torsional forces caused by mis-alignment of the specimen tabs. However, assuming only a tensile load on the crack tip, the calculated stress intensity at the crack tip would exceed the fracture toughness of the Coors alumina at the applied constant load of 132 MPa when the half crack length increased to 492 microns. Continuous crack growth and ultimate failure of Specimen C at 132 MPa indicates that there is a maximum in constant applied stress or crack length (since both will increase the stress intensity factor at the crack tip) above which static fatigue crack growth does not saturate, resulting in catastrophic failure even at the reduced humidity level of 10%.

After 25 minutes at 32% r.h. and 92 MPa, one of the two indent half cracks perpendicular to the direction of the applied stress for Specimen C grew 26 microns from its original length at 10% and 92 MPa (Table 26 and Figure 29). The same indent crack continued to grow an additional 8 microns in length after an additional 25-minute static fatigue cycle at 32% r.h. and 92 MPa (Table 26 and Figure 29). The crack path followed during the static fatigue cycles at 32% r.h. and 92 MPa was semi-tortuous with grains that bridge the crack behind the crack tip (Figure 29) and crack deflections (Figure 29) similar in size to those reported for Coors alumina (Section

4.1.2). The indent crack also grew during static fatigue cycling at 100, 105, 111, and 116 MPa and 32% r.h. and also followed a tortuous path with crack deflections on the order of the grain size of the material (Table 26, Figure 30 and 31).

4.3.2.4 Specimen F

A 98 N indent crack on Specimen F was tested at 32% r.h. for loads ranging from 50 to 90 MPa (Table 27). For Specimen F, the crack length increased from 417 microns to 470 microns after the second static fatigue cycle at 90 MPa. Specimen F did not fail during testing. After the second cycle at 90 MPa, the applied load was decreased to 18 MPa and Specimen F was removed intact from the tensile stage fixture. Two 25-minute static fatigue cycles were performed on Specimen F at 50 and 90 MPa. The second cycles at these constant applied load levels had either no crack growth or a crack growth of only 1 micron (Table 27). The low crack growth rate for the second cycles again indicates the static fatigue crack growth saturates at a constant applied load (at least below some critical level of constant applied load). For an applied load of 90 MPa and a crack length of 470 microns the stress intensity factor was 2.47 MPa$\sqrt{m}$ (67% of K_{Ic}).

4.3.2.5 Specimen H

Specimen H was prepared with cold rolled stainless steel tabs affixed with high temperature cement (Table 28). The load from the self tightening grips was initially 13 MPa. When the displacement on the tensile stage was increased to increase the load, the grips slipped across the cold rolled stainless steel tabs of Specimen H. The

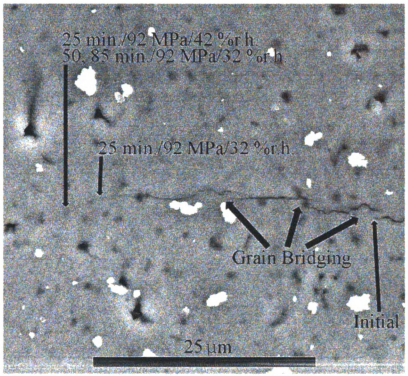

Figure 30 ESEM micrograph of the left indent crack of Coors alumina Specimen C (Tables 24 and 26) showing the growth after 25, 50 and 85 minutes at 92 MPa and 32% r.h. and 25 minutes at 92 MPa and 42% r.h..

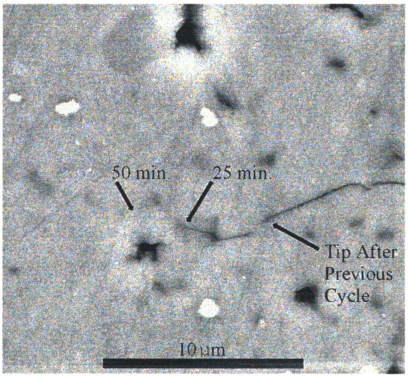

Figure 29 ESEM micrograph of the left indent crack of Coors alumina Specimen C (Tables 24 and 26) showing the growth after 25 and 50 minutes at 100 MPa and 32% r.h..

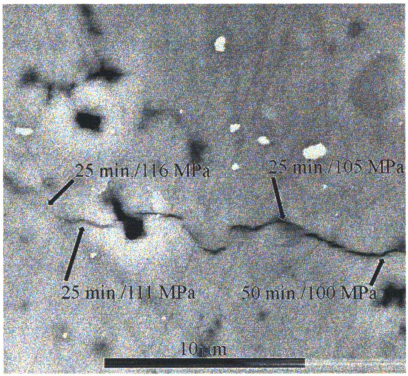

Figure 31 ESEM micrograph of the left indent crack of Coors alumina Specimen C (Tables 24 and 26) showing the growth after 25 minutes at 32% r.h. and 105, 111, and 116 MPa.

slippage indicated that the increased hardness of the cold rolled stainless steel tabs necessitated a larger initial grip load. The tensile stage and sample were removed from the ESEM sample chamber and the self-tightening grips were tightened increasing the load applied to the sample to 16 MPa. After the tensile stage and sample were returned to the ESEM sample chamber, micrographs of the indent cracks were taken. The crack lengths increased by 33 and 35 microns for the left and right indent cracks, respectively (Table 28). The crack length increase resulted from torsional load applied as the 4 grip plate bolts were tightened un-evenly. The load on the sample was increased to 40 MPa (at 10% r.h.) and no further crack growth occurred.

Specimen H was tested at 32% r.h. for six 25-minute cycles at 40 MPa and three 25-minute cycles at 50 MPa (Table 28). The crack length increased from an initial length of 399 microns to 530 microns after the third static fatigue cycle at 50 MPa. Specimen H failed during testing after 7 minutes of continuous crack growth at 70 MPa constant applied load and 10%r.h. (Table 28).

After the first 25-minute cycle at 40 MPa and 32% r.h., the left and right indent cracks each lengthened by 28 microns (Table 28). During the second 25-minute cycle at 40 MPa and 32% r.h., the left and right indent cracks lengthened by less than half the amount of the first 25-minute cycle (Table 28). The third 25-minute cycle gave crack length increases of 2 microns or less (Table 28). After each of the next three cycles only one of the two cracks grew (by 8 microns or less) (Table 28). The decrease in the static fatigue crack growth on the second cycle and the limited static fatigue crack growth of the third cycle was similar to the static fatigue crack

growth of Specimens C and F (Tables 26 and 27). The static fatigue crack growth for the fourth, fifth and sixth static fatigue cycles at 32% r.h. and 40 MPa did not saturate after holding at the same level of applied stress, but merely slowed (Table 28).

The first 25-minute cycle of static fatigue Specimen H at 32% r.h. and a fixed 50 MPa applied load resulted in a 12 and 6 micron growth for the left and right indent half cracks, respectively (Table 28). The second cycle resulted in very small crack growth, while the third cycle resulted in only one of the two cracks growing by 8 microns or less (Table 28). Thus for static fatigue of Coors alumina at both 40 MPa and 50 MPa constant applied load, both cracks grew significantly upon the first static fatigue cycle, both cracks had limited growth for subsequent static fatigue cycle, and only one of the two cracks grew by 8 microns or less during further static fatigue cycling.

The indent crack tip of Specimen H did not advance after the load was increased from 16 MPa to 40 MPa (Figures 32 and 33). After the first 25-minute static fatigue cycle at 32% r.h. and 40 MPa, the left crack advanced along a tortuous path with crack deflections on the order of the diameter of a single Coors alumina grain (Figure 34). For the second static fatigue cycle at 40 MPa and 32% r.h., an alumina grain bridged the crack from the end of the first cycle and the start of the second (Figure 35).

4.3.2.6 Specimen J

A 98 N indent crack on Specimen J was tested under humidity conditions of 32% r.h. for loads ranging from 40 to 90 MPa (Table 29). For Specimen J, the crack length

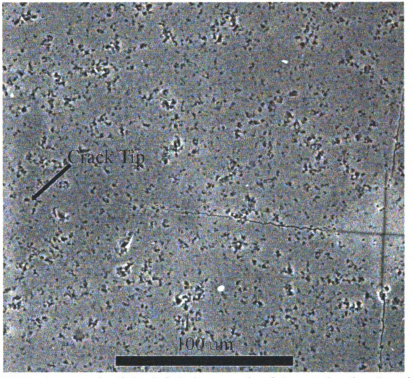

Figure 32 ESEM micrograph of the left indent crack of Coors alumina Specimen H (Tables 24 and 28) showing the initial left indent crack with an applied stress of 16 MPa from the self tightening grips.

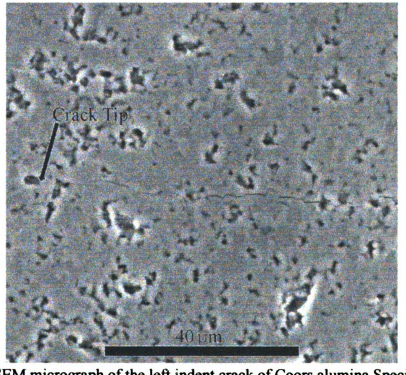

Figure 33 ESEM micrograph of the left indent crack of Coors alumina Specimen H (Tables 24 and 28) showing the initial left indent crack after increasing the applied stress to 40 MPa.

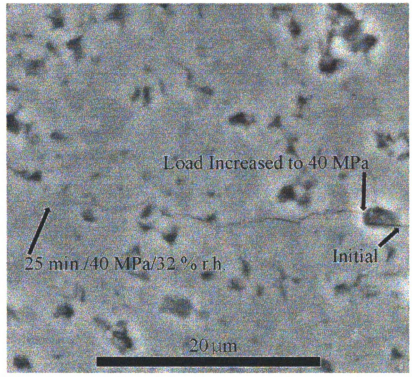

Figure 34 ESEM micrograph of the left indent crack of Coors alumina Specimen H (Tables 24 and 28) showing the growth after 25 minutes at 40 MPa and 32% r.h..

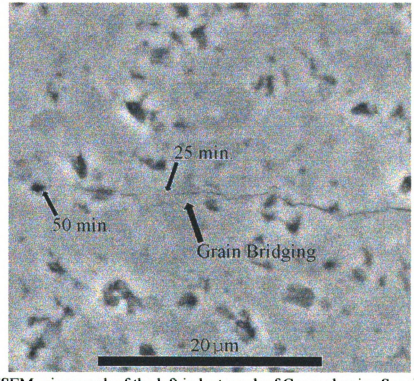

Figure 35 ESEM micrograph of the left indent crack of Coors alumina Specimen H (Tables 24 and 28) showing the growth after 50 minutes at 40 MPa and 32% r.h. along with the bridged grain which is located at the end of the 25 minute crack tip.

increased from 360 microns to 484 microns after the static fatigue cycle at 90 MPa. Specimen J failed via continuous crack growth at 100 MPa and 10% r.h.. No crack growth occurred after three 25-minute and one 75-minute cycle at 40 MPa and 32% r.h.. No crack growth occurred after a 25-minute cycle at 50 MPa and 32% r.h.. The right indent crack increased 4 microns while the left crack did not increase after 25 minutes at 60 MPa and 32% r.h.. The small crack growth after the first cycle at a fixed constant applied load was contrary to the behavior of Specimens C, F, and H.

The crack path followed during the 32% r.h. static fatigue cycles at 60, 70, 80, and 90 MPa were semi-tortuous with grains that bridge the crack behind the crack tip (Figure 36) and crack deflections (Figure 36) similar in size to those reported for Coors alumina (Section 4.1.2). The indent crack grew after the load was increased to 80 and 90 MPa and while the humidity was at 10 % r.h. (Table 29 and Figure 36) which was not a behavior observed in other specimens (Tables 26 - 28). Two grains bridged the crack formed during the second 25 minute cycle at 80 MPa and during the first cycle at 90 MPa (Figures 37 and 38).

4.3.2.7 Relative Crack Length and Applied Tensile Load

Four ESEM static fatigue crack growth experiments were performed under constant load and increased humidity conditions using tabbed tensile specimens (Specimens C, F, H, and J). The relative half crack length (C_t / C_o) increased with applied tensile stress for the composite tab Specimen C (Figure 39). Similarly, the relative indent crack length ($2C_t$ / $2C_o$) increased with the applied tensile stress for Specimens F, H, and J (Figures 40 - 42). The relative indent crack length ($2C_t$ / $2C_o$) also increased

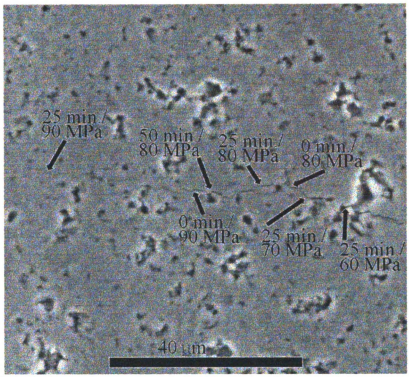

Figure 36 ESEM micrograph of the left indent crack of Coors alumina Specimen J (Tables 24 and 29) showing the growth after time at 32% r.h. and 60 to 90 MPa along with the growth which occurred as the load was increased to 80 and 90 MPa.

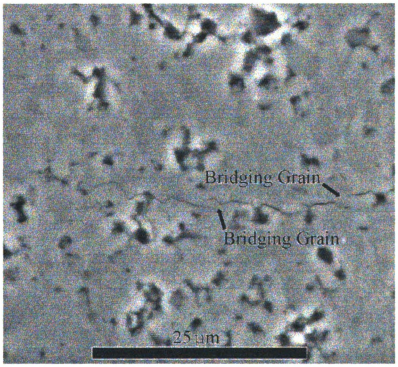

Figure 37 ESEM micrograph of the left indent crack of Coors alumina Specimen J (Tables 24 and 29) revealing two instances of grain bridging from the 80 and 90 MPa static fatigue cycles.

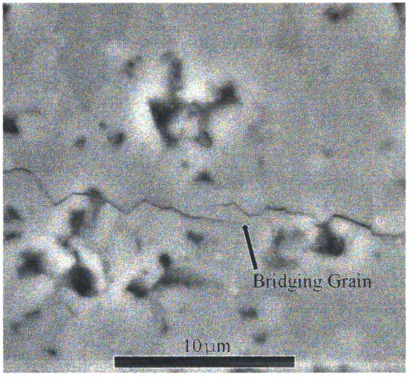

Figure 38 A higher magnification ESEM micrograph of Figure 37 revealing the instances of grain bridging from the 90 MPa static fatigue cycle of the left indent crack of Coors alumina Specimen J (Tables 24 and 29).

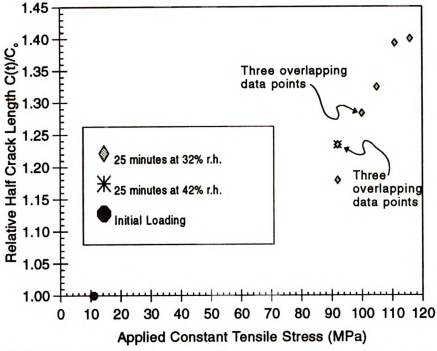

Figure 39 Plot of static fatigue crack growth for the left indent crack as a function of constant applied load for Coors alumina Specimen C (Tables 24 and 26) with a 49 N indent and composite tabs.

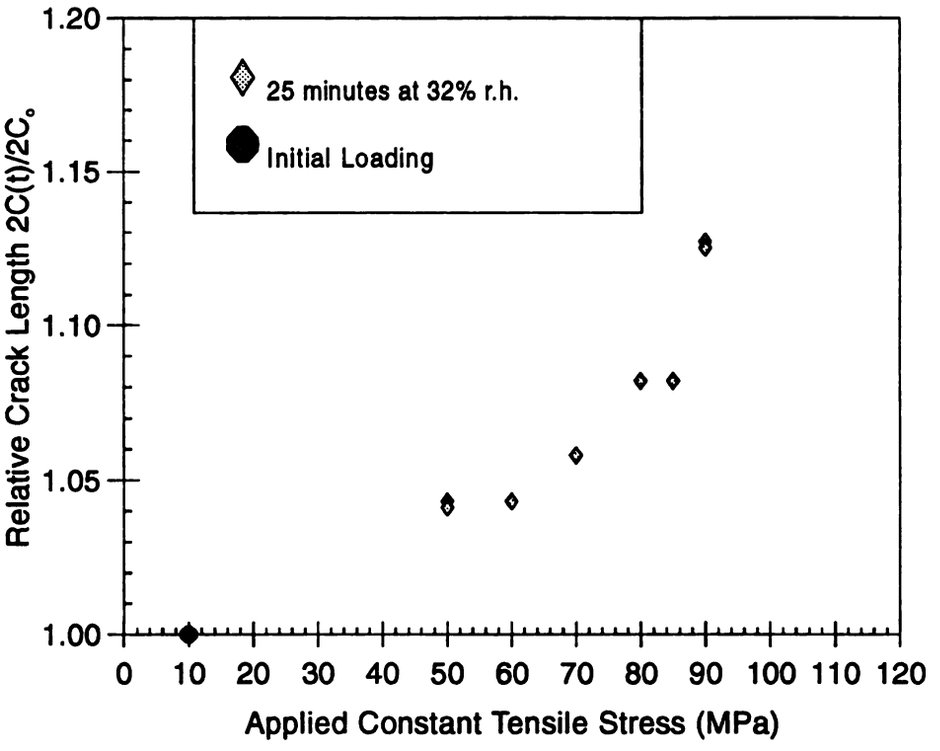

Figure 40 Plot of static fatigue crack growth as a function of constant applied load for Coors alumina Specimen F (Tables 24 and 27) with a 98 N indent and stainless steel tabs.

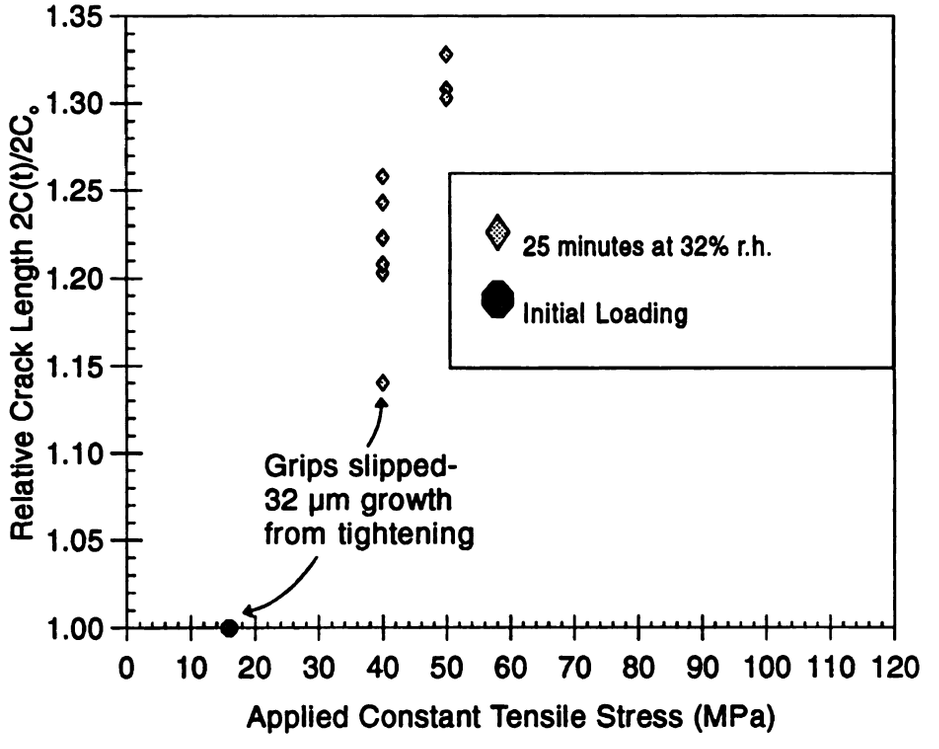

Figure 41 Plot of static fatigue crack growth as a function of constant applied load for Coors alumina Specimen H (Tables 24 and 28) with a 98 N indent and cold rolled stainless steel tabs.

with increasing time at a constant applied tensile stress (Figures 40 - 42). Specimens C, F, and J show very similar static fatigue behavior (Figure 43) while Specimen H appears to be offset from the other specimens (Figure 43). The offset of Specimen H may result from torsional stress which could have developed when the tensile grip was tightened to stop the grip from slipping. Torsional stress would increase the load on the crack shifting the specimen data to the right by the amount of the torsional stress (Figure 43).

4.4 Crack Healing

Crack healing investigations were performed with: 1) in-situ heating and in-situ observation using an Environmental Scanning Electron Microscope (ESEM), 2) conventional heating and observation using optical microscopy before and after thermal annealing, and 3) microwave heating and observation using optical microscopy before and after thermal annealing.

4.4.1 In-Situ ESEM Investigations of Healing in Soda-Lime Silica Glass

In-situ observation of the healing of Vickers indents in soda-lime-silicate glass was performed using an Environmental Scanning Electron Microscope. The change in crack length and crack morphology as a function of time and temperature was studied. The effect of the initial humidity level on the crack healing behavior was also investigated.

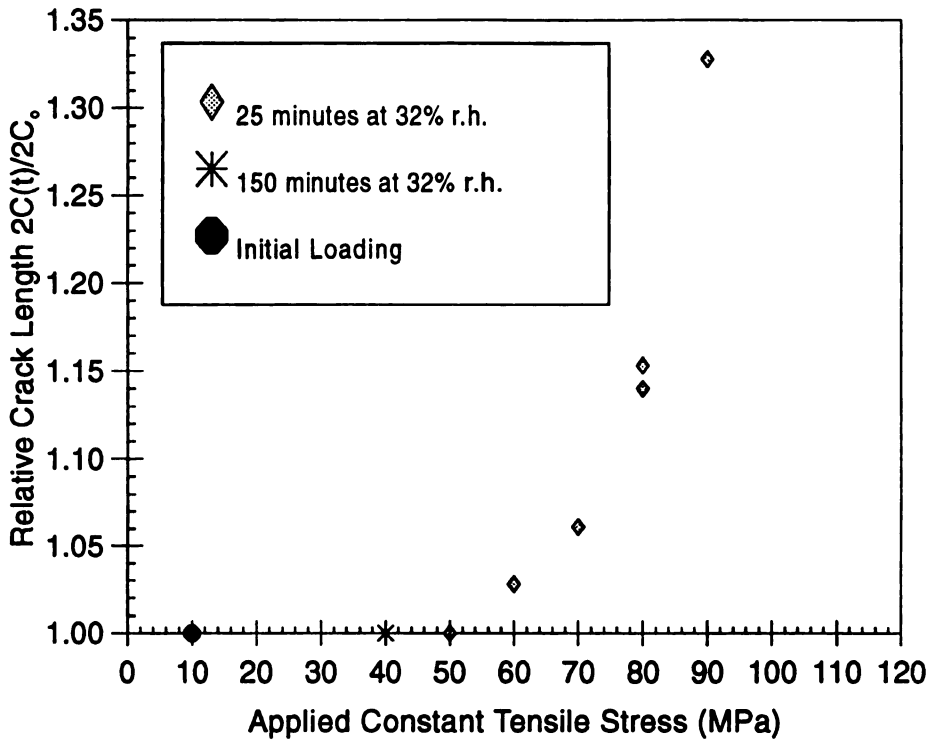

Figure 42 Plot of static fatigue crack growth as a function of constant applied load for Coors alumina Specimen J (Tables 24 and 29) with a 98 N indent and composite tabs.

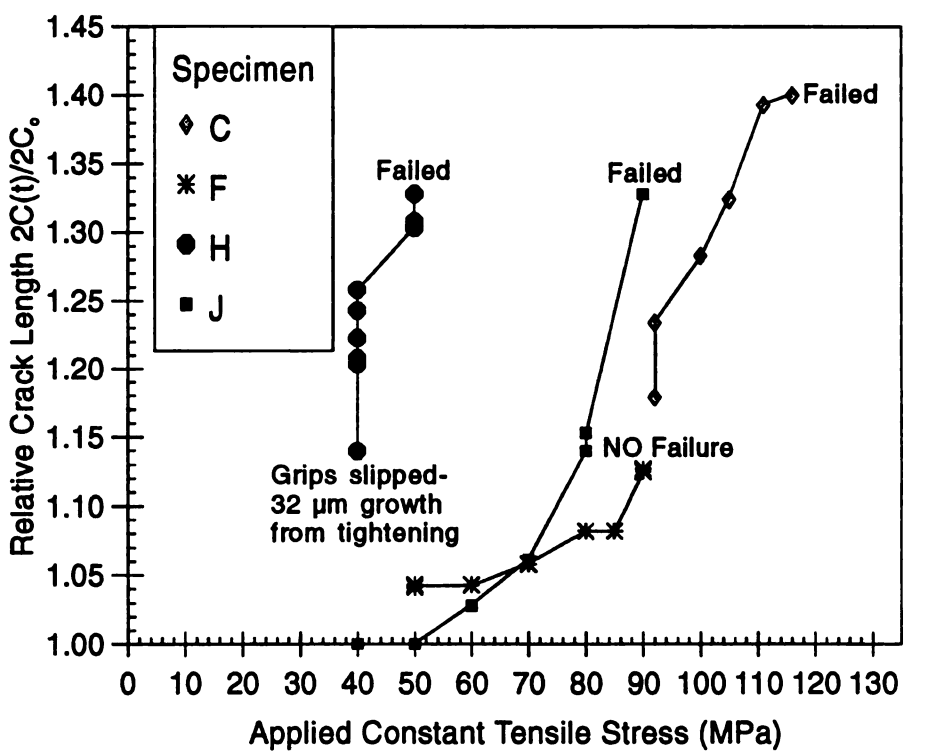

Figure 43 Plot of crack growth for static fatigue cycles at constant applied load and relative humidity for Coors alumina Specimens C, F, H, J (Tables 24 to 29).

4.4.1.1 In-Situ ESEM Testing

Specimens of soda-lime silica glass were prepared for in-situ ESEM crack healing testing as described in Section 3.6.1.1. The initial relative humidity conditions were set in the ESEM by adjusting the initial sample chamber pressure and the initial sample temperature via the cooling water temperature as described in Section 3.6.1.2. The micrographs of the initial crack lengths were taken before the specimens were heated. The heating schedules used are described in detail in the subsequent subsections (Sections 4.4.1.1.1 to 4.4.1.1.5).

4.4.1.1.1 Healing at Temperatures up to 600 °C (Experiments A and B)

The reduction in crack length and the changes in crack shape for soda-lime silica glass specimens were investigated for healing temperatures of 600 °C or higher. The heating rates and dwell times for the two samples heated at 600 °C and higher are described in Section 3.6.1.3.1.

In Experiment A, the specimen was initially held in the ESEM chamber at 25 °C and a water vapor pressure of 2.5 Torr, which corresponds to 10% relative humidity. The initial indentation crack lengths in the specimen were approximately 190 μm. The crack length at 300 °C was identical to the initial crack length (Figure 44). As the crack was heated from 300 °C to 600 °C, the crack length continually regressed from the tip toward the indent impression and the crack opening displacement appeared to reduce as well. At temperatures above 500 °C, crack pinch off also occurred along the length of the radial indent cracks as the crack tip regressed toward the indent impression. When the specimen reached 600 °C, the average

indentation crack length had decreased to 96 μm, a decrease of 50 percent from the initial crack length (Figure 45). Faint outlines along the healed portions of the crack made the crack length hard to measure since it was difficult to define the end of the crack (Figure 46). The faint outline along the healed portion of the crack in Figure 46 (at increased magnification in Figure 47) corresponds to closed portions of the crack which have a small depression at the surface along the trace where the original crack was located. After longer times at 600 °C the faint portions of the cracks disappear as the small depressions along the surface trace heal completely (Figure 48).

While the specimen in Experiment A was held at 600 °C, multiple areas of crack pinch-off were evident along the length of the crack (Figure 49). The pinch-off exhibited during healing at 600 °C in the soda-lime silica glass was the result of a change in crack morphology rather than a simple closing of the crack (Figure 49), which demonstrates that the healing mechanism was not adhesion due to intermolecular forces [33, 35].

Crack pinch-off behavior observed in the glass during Experiment A (Figure 49) was similar to that seen in other ceramic materials by other investigators [30-31, 34]. The pinched-off portions of the cracks appear to take on semi-elliptical shape with the ends of each pinched-off segment being quasi-circular (Figure 50). However, the indent crack pinch-off (Figure 49) does not show the evenly spaced pinch-off proposed by Nichols and Mullins [40-41] and observed by other investigators [30-31, 34]. The uneven spacing between crack pinch-off locations may be related to the increase in crack opening displacement along the length of the crack as one proceeds from the crack tip to the indent impression. As the crack opening displacement along

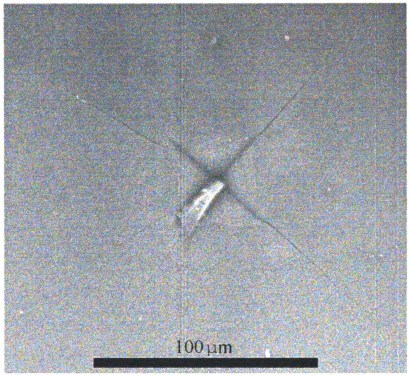

Figure 44 ESEM micrograph of indent cracks of the soda-lime silica glass specimen at 300 °C with an initial relative humidity of 10% (Experiment A).

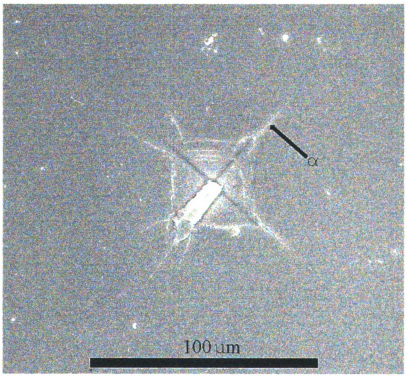

Figure 45 ESEM micrograph of the soda-lime silica glass specimen upon reaching 600 °C exhibiting crack healing. The same indentation crack system prior to healing, is shown in Figure 44 (Experiment A).

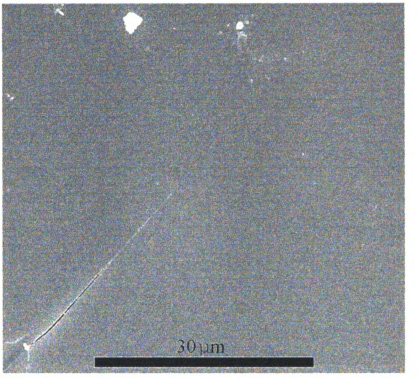

Figure 46 ESEM micrograph of the indent crack (labeled in Figure 45) five minutes after reaching 600 °C exhibiting a faint outline along the healed portion of the crack (Experiment A).

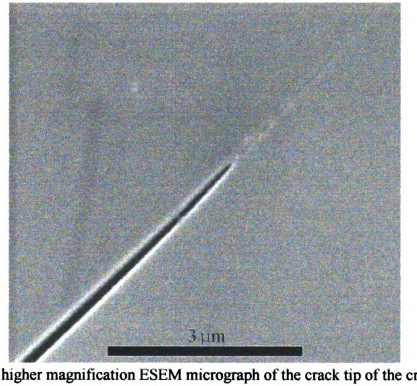

Figure 47 A higher magnification ESEM micrograph of the crack tip of the crack shown in Figure 46 demonstrating that the faint outline was a closed portion of the crack with a small depression at the specimen surface (Experiment A).

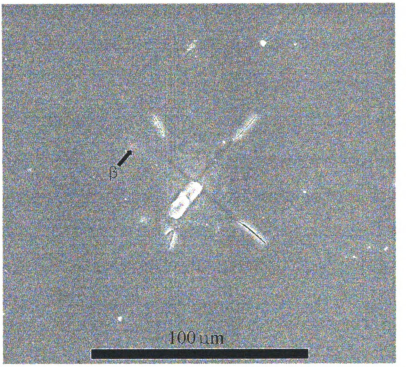

Figure 48 ESEM micrograph of indent cracks of the soda-lime silica glass specimen after 2 hours and 20 minutes at 600 °C illustrating the disappearance of the faint portion of the crack depicted in Figures 46 and 47 (Experiment A).

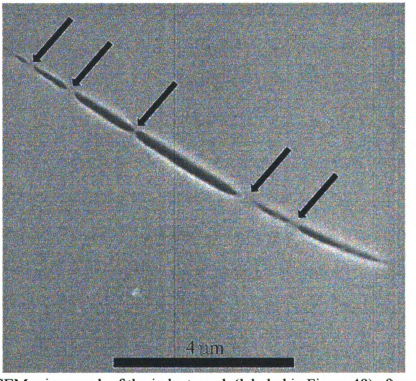

Figure 49 ESEM micrograph of the indent crack (labeled in Figure 48) after an hour and 22 minutes at 600 °C showing multiple areas of crack pinch-off (arrows) (Experiment A).

the crack increases (from upper left to lower right hand portion of Figure 49), the distance between crack pinch-off locations also increases (Figure 49). After a total of 123 minutes at 600 °C (Figure 50), the crack opening displacement decreased. For example, the crack opening displacements after 82 minutes at 600 °C in the pinch off regions A, B, and C were 0.12, 0.18, and 0.21 μm, respectively (Figure 49), and after a total of 123 minutes at 600 °C the crack opening displacements in the pinch off regions A, B, and C decreased to 0.09, 0.12, and 0.18 μm, respectively (Figure 50). The quasi-circular ends of the pinched-off regions of the crack, after 82 minutes at 600 °C (Figure 49) became much less rounded after the additional 41 minutes at 600 °C (Figure 50).

In Experiment B, the glass specimen was initially held in the ESEM chamber at 25 °C and a water vapor pressure of 2.5 Torr (10% relative humidity). Problems with the hard drive of the storage computer networked to the ESEM resulted in the loss of all of the micrographs from the initial indent crack, including the micrographs of the indent crack after 25 minutes of heating at 550 °C. Crack pinch-off occurred in soda-lime silica glass at healing temperatures of 550 °C (Figure 51). The pinched-off portions of the crack had a semi-elliptical shape (Figure 52) and the ends of the pinched-off portions were quasi-circular in shape (Figure 52).

For one of the cracks in Experiment B, a piece of debris was observed in one of the cracks (Figure 53), in the pinched-off portion of the crack closest to the indent impression (Figure 54). Figures 55 to 57 depict, respectively, a close up of the region of the crack with the debris after 30 minutes at 575 °C, the same region after 5 minutes at 600 °C, and the crack morphology immediately after reaching 610 °C for a

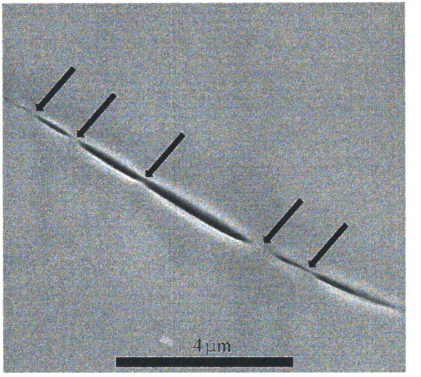

Figure 50 ESEM micrograph of the indent crack (labeled in Figure 48 and shown in Figure 49) after two hours and 3 minutes at 600 °C demonstrating further morphology changes of the pinched-off regions of the crack (Experiment A).

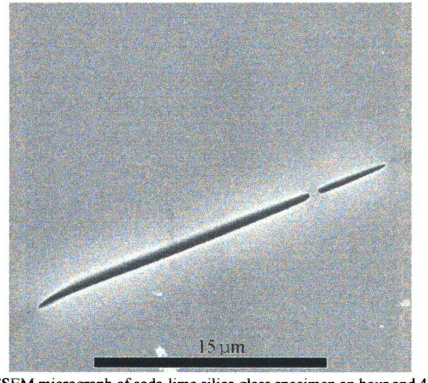

Figure 51 ESEM micrograph of soda-lime silica glass specimen an hour and 42 minutes after reaching 550 °C exhibiting crack pinch-off (Experiment B).

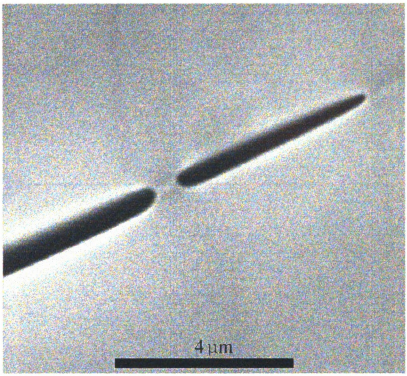

Figure 52 A higher magnification ESEM micrograph of the same crack shown in Figure 51 revealing the crack and crack tip shape in the pinched off regions (Experiment B).

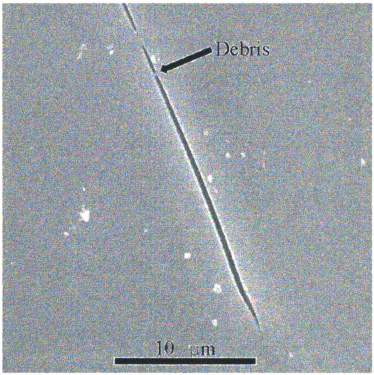

Figure 53 ESEM micrograph of glass specimen after 28 minutes at 550 ℃ displaying pinch-off and showing the location of the debris with an arrow (Experiment B).

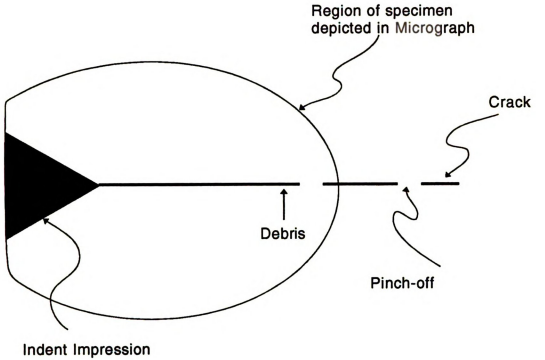

Figure 54 Schematic of the half indent crack (Figure 53) depicting the multiple crack pinch-off, and the location of the debris (Experiment B).

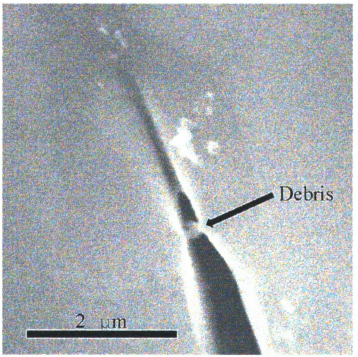

Figure 55 ESEM micrograph of the indent crack (Figure 53) at 575 °C showing a close up of area near the debris (arrow) and crack healing approaching the debris (Experiment B).

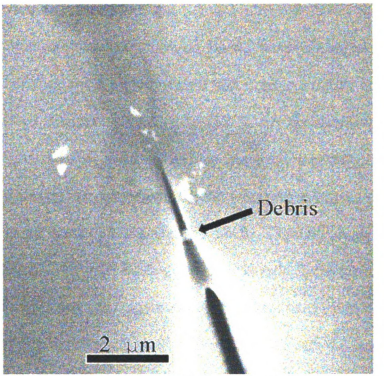

Figure 56 ESEM micrograph of the indent (Figure 53) at 600 ºC showing a close up of area near debris (arrow) and crack healing passing the debris without complete healing (Experiment B).

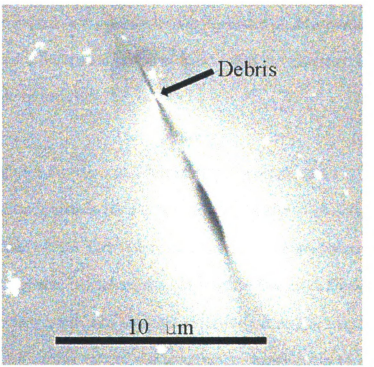

Figure 57 ESEM micrograph of the indent (Figure 53) at 610 ºC showing healing from the bottom part of the crack approaching the debris (arrow) without complete healing in the area of the debris (Experiment B).

similar field of view as Figure 53.

Healing progressed from the crack tip toward the indent impression (Figure 58) for each of the radial cracks in Experiments A and B, except for the one radial crack containing the debris (Experiment B, Figures 53-57). For the radial crack that contained the debris, crack tip pinch-off and crack regression initially occurred from the crack tip (Figure 55), as was the case for the other cracks without debris (Figure 58). However, as the crack tip regression and pinch-off healing progressed to the debris site (Figure 56), the crack healing process changed. In the vicinity of the debris, the crack is wedged open, apparently without healing (Figure 56). The crack then regressed toward the debris from the end of the crack near the indent impression (Figure 57). Also, the crack pinched-off between the debris and the nascent crack tip (Figure 57 and Figure 58). Near the debris, complete healing still had not occurred (Figure 57). The impediment of crack healing by debris could adversely affect the healing of mechanically fatigued ceramics, since debris are generated during the mechanical fatigue of ceramics [67].

4.4.1.1.2 Healing as a Function of Temperature (Experiment C)

In Experiment C, the specimen initially was held in the ESEM chamber at 27 °C and a water vapor pressure of 2.1 Torr (8% relative humidity). Subsequently, the specimen was thermally annealed at temperatures up to 490 °C. The crack healing behavior of one of the four indent cracks was observed exclusively during heating so that the healing behavior for smaller intervals of temperature change could be examined (than if time was divided between observing four cracks). The initial length of the half

indent crack studied in Experiment C was 105 μm (Figure 59).

Experiment C exhibited crack healing at lower initial relative humidities and lower temperatures than in the Experiment A. The half crack length at 400 °C had decreased by only 4 μm from the original crack length (Figure 60) and after 10 minutes at 430 °C the half crack length was reduced by 30% (Figure 60). Approximately 8 minutes after the specimen reached 490 °C (Figure 61), the crack length decreased to 46 μm (a 55% reduction in crack length compared to the initial crack length). Thus, significant crack healing can occur in soda-lime silica glass at 490 °C and some significant healing occurs at temperatures as low as 430 °C.

4.4.1.1.3 Healing as a function of Time at 430 °C (Experiment D)

In Experiment D (an isothermal hold at 430 °C), the specimen initially was held in the ESEM chamber at 21 °C and a water vapor pressure of 2.4 Torr (14% relative humidity). Before the sample was heated, the crack (with half cracks labeled α and β in Figure 62) had a length, $2C_{\alpha\beta}$, of 182 μm at room temperature. After heating to 400 °C, the crack length ($2C_{\alpha\beta}$) remained unchanged. Once the specimen temperature reached 430 °C, the ESEM computer crashed. The sample was cooled at 20 °C per minute to room temperature and the ESEM computer was re-booted. The ESEM electron beam was re-aligned, micrographs of the indent cracks were taken. Comparison of the micrographs taken before and after the ESEM was re-started, revealed that the crack length, $2C_{\alpha\beta}$, had decreased in length to 170 microns as a result of the heating from 400 to 430 °C before the computer crash. The crack length $2C_{\alpha\beta}$ remained unchanged after re-heating from room temperature to 370 °C. The change in

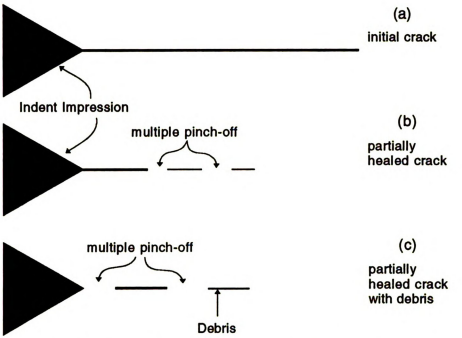

Figure 58 Schematic of half of a Vickers indentation crack (a) before heat-treatment, (b) after partial healing showing the typical regression of the crack from the tip toward the indent impression together with multiple pinch-off, and (c) containing debris (Experiment B) after partially healing that includes crack regression toward the debris from the end of the crack near the indent impression.

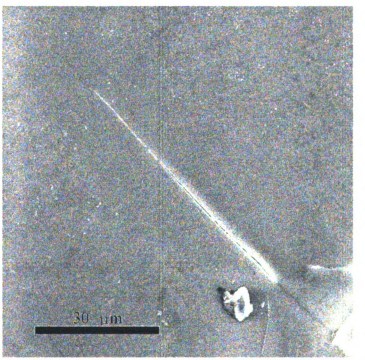

Figure 59 ESEM micrograph of a 105 µm long indention crack in a soda-lime silica glass specimen at 27 °C and 8% initial relative humidity (Experiment C).

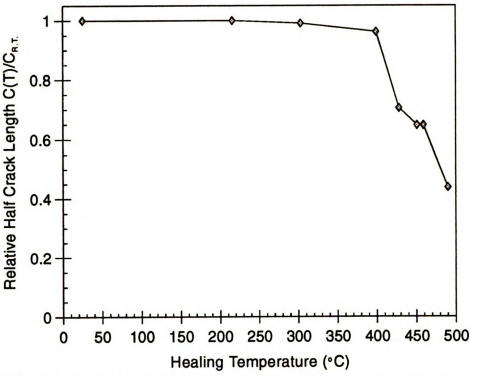

Figure 60 Relative change in crack length (C(T)/C(R.T.)) as a function of temperature for a soda-lime silica glass specimen observed in-situ in an ESEM (Experiment C).

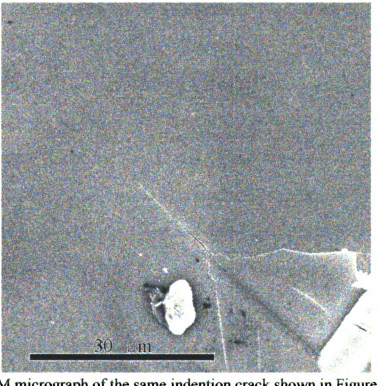

Figure 61 ESEM micrograph of the same indention crack shown in Figure 59 after 8 minutes at 430 °C displaying a decrease in the crack length to 46 μm (Experiment C).

length of crack β was measured as a function of time at 430 °C. During thermal annealing at 430 °C, the crack length initially decreased rapidly but the rate of change of crack length decreased in time (Figures 63-64).

4.4.1.1.4 Healing as a function of Relative Humidity (Experiments E-H)

For an isothermal hold at 430 °C, the effect of relative humidity on the temperature at which healing begins was investigated in Experiments E-H. The effect of the initial relative humidity on the rate of healing and on the total amount of healing also was investigated in Experiments E-H. Samples in Experiments E, F, G, and H were held at initial relative humidities of 8, 16, 32, and 64 %, respectively, before heating as described in Section 3.6.1.3.4.

4.4.1.1.4.1 Effect of Humidity on the Temperature where Healing Initiates

For the healing specimen initially held at 8% relative humidity (Experiment E), the relative crack length did not change at 370 and 400 °C, but had a significant 28.5% drop by 430 °C (Table 30, Figure 65). For the 16% relative humidity sample (Experiment F), the relative crack length was not changed at 370 °C, but changed by 6.5% at 400 °C. The 32% r.h. sample (Experiment G) changed 0.6% by 370 °C, while the 64% r.h. sample (Experiment H) exhibited 25% healing by 370 °C (Table 30, Figure 65). For Experiments E-H, as the initial relative humidity increased, the initiation temperature for crack healing decreased and the amount of healing at a given temperature (above the initiation temperature) increased.

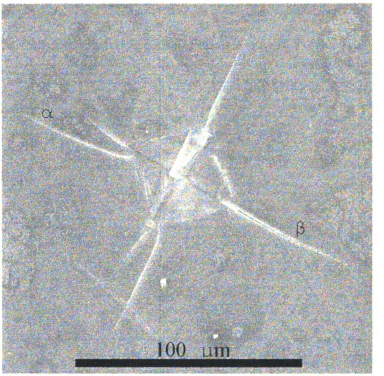

Figure 62 ESEM micrograph of the indention cracks in a soda-lime silica glass specimen at 21 °C and 14% initial relative humidity (Experiment D).

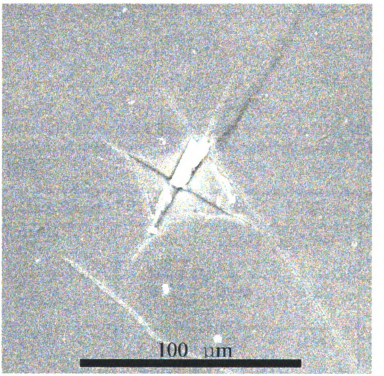

Figure 63 ESEM micrograph of the same indention crack shown in Figure 62 after 110 minutes at 430 °C (Experiment D).

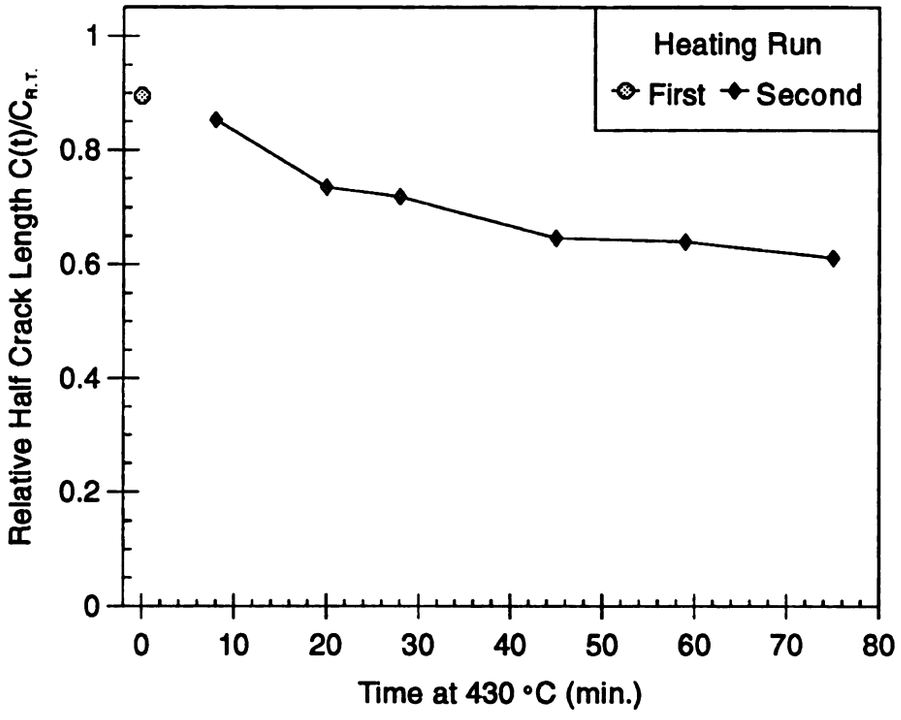

Figure 64 Relative change in length (C(T)/C(R.T.)) of crack β as a function of time at 430 °C for a glass specimen initially at 14 % r.h. observed in-situ in an ESEM (Experiment D).

Table 30 Relative half indent crack lengths after heating to 370, 400 and 430 °C for soda-lime silica glass samples with initial relative humidities of 8, 16, 32, and 64% (Experiments E-H).

Relative Crack Length	8 %r.h.	16 %r.h.	32 % r.h.	64 %r.h.
$\frac{C(370\ °C)}{C(R.T.)}$	1.000	1.000	0.994	0.750
$\frac{C(400\ °C)}{C(R.T.)}$	1.000	0.935	0.923	0.698
$\frac{C(430\ °C)}{C(R.T.)}$	0.725	0.696	0.857	*0.630*

* Cracks had indications of pinch-off along regions of the length of crack.

4.4.1.1.4.2 Effect of Humidity on Healing with Isothermal Holds at 430 °C

Case and co-workers [68-73] investigated of thermal fatigue of ceramics and ceramic composites and applied a semi-empirical relationship to describe the initially large change and eventual saturation of properties (e.g. elastic modulus and fracture strength) in time

$$P_N = P_o + D\left(1 - \exp(-\delta N)\right) \tag{10}$$

where P_N is the property value after N thermal shock cycles at a fixed temperature difference, P_o is the property value before thermal shock testing, D is the saturation constant (P_o - P_{sat}), P_{sat} is the steady-state property value after many cycles, and δ is the rate constant (rate at which saturation is reached). Case and Wilson [74] applied a general form of the same empirical relationship to describe the similar behavior found in mechanical fatigue of ceramics. Case et al. [75] derived a form of the empirical expression which described the saturation in crack length during thermal fatigue

$$a(N) = a_{sat} - (a_{sat} - a_o)\, e^{-BN} \tag{11}$$

Equation 11 can be rewritten to provide a candidate equation to describe the relative change in crack length as a function of time at 430 °C

$$\frac{c(t)}{c_o} = \left[\frac{c_{sat}}{c_o}\right] - \left[\frac{(c_{sat} - c_o)}{c_o}\, e^{-Bt}\right] \tag{12}$$

or

$$\frac{C(t)}{C(400\,^{\circ}C)} = V_1 - V_2\left[e^{-tV_3}\right] \qquad (13)$$

where C(t) is the crack length after time, t; at 430 °C, C(400°C) is the crack length at 400 °C, and where V_1, V_2, and V_3 are constants. The constant V_1 is related to the relative crack length at saturation ($C(t\rightarrow\infty)/C(400°C)$) (Figure 66). The decrease from the initial relative crack length to the saturated value of relative crack length is related to the constant V_2 and the initial rate of decrease in relative crack length is related to the constant V_3 (Figure 66).

Each of the data points in Figures 67 - 70 indicate a crack length measurement from an ESEM micrograph and the solid lines indicate a regression fit of the crack length data to Equation 13 using fitting parameters V_1, V_2, and V_3. When the specimen tested with an initial humidity level of 8% (Experiment E) reached 430 °C, the crack length decreased to less than 80% of the length at 400 °C (Figure 67). For times of 70 minutes or more at the 430 °C isothermal hold, the relative half crack length of the 8% relative humidity specimen (Experiment E) saturated reaching a steady state value of less than 40% of the crack length at 400 °C (Figure 67). For Experiments E - H, the relative half crack length and time were related effectively by Equation 13 (Table 31 and Figures 67 - 70), with the possible exception of the sample tested with a 64% initial humidity (Experiment H, Figure 70). The sample initially held at 64% relative humidity (Experiment H) had pinch-off along the crack length which indicated that Equation 13 only describes crack healing by crack tip regression and not healing in cases where pinch-off occurs.

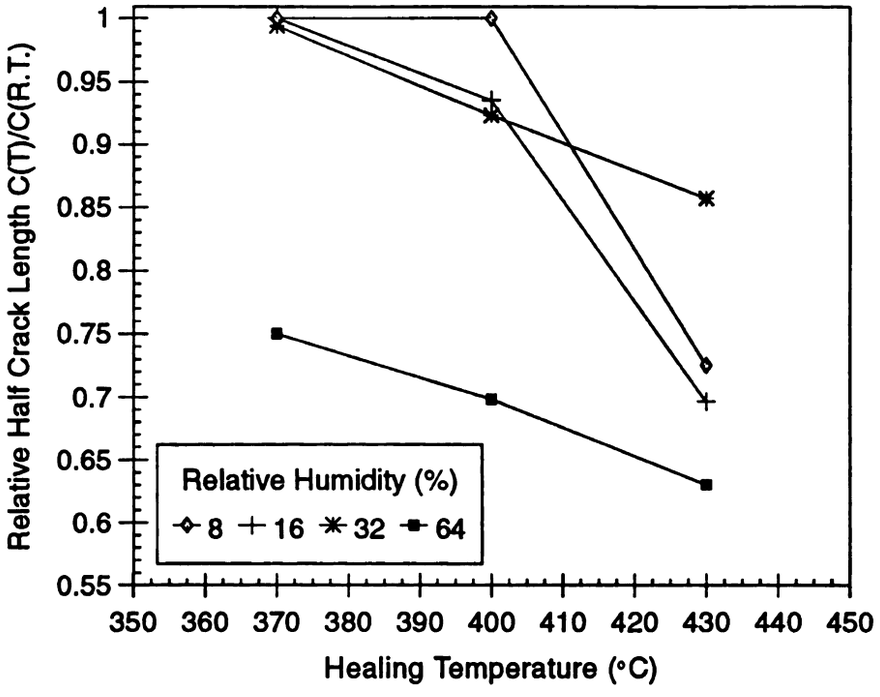

Figure 65 Relative change in crack length (C(T)/C(R.T.)) as a function of temperature for soda-lime silica glass specimens with different initial humidity levels observed in-situ in an ESEM (Experiments E-H).

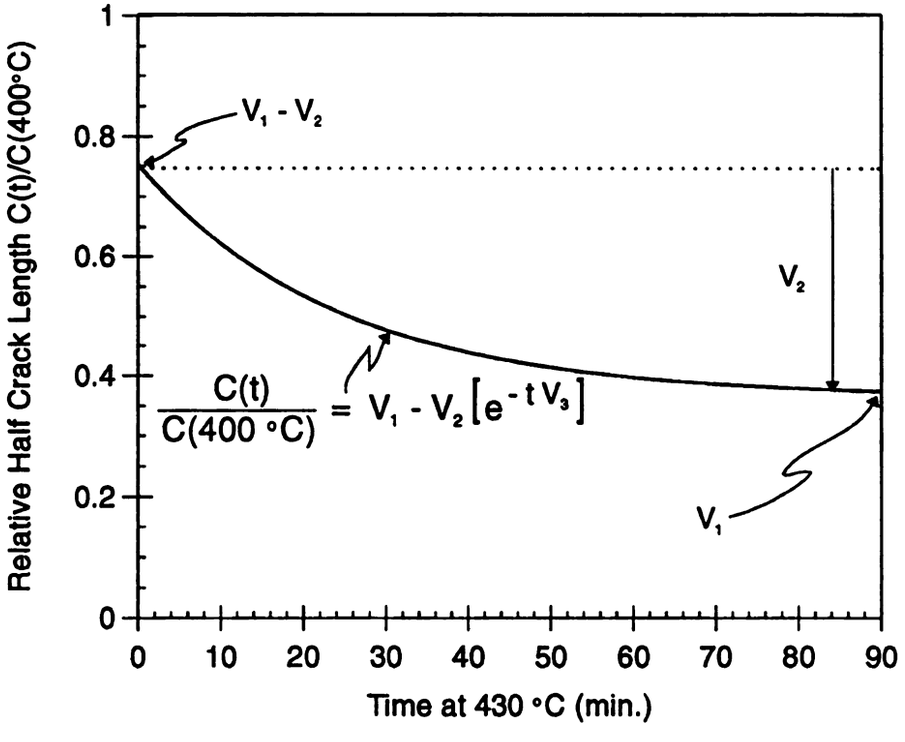

Figure 66 Plot of the general form of Equation 13 with the constants V_1 and V_2 shown and constant V_3 representing the initial rate of change of the relative crack length.

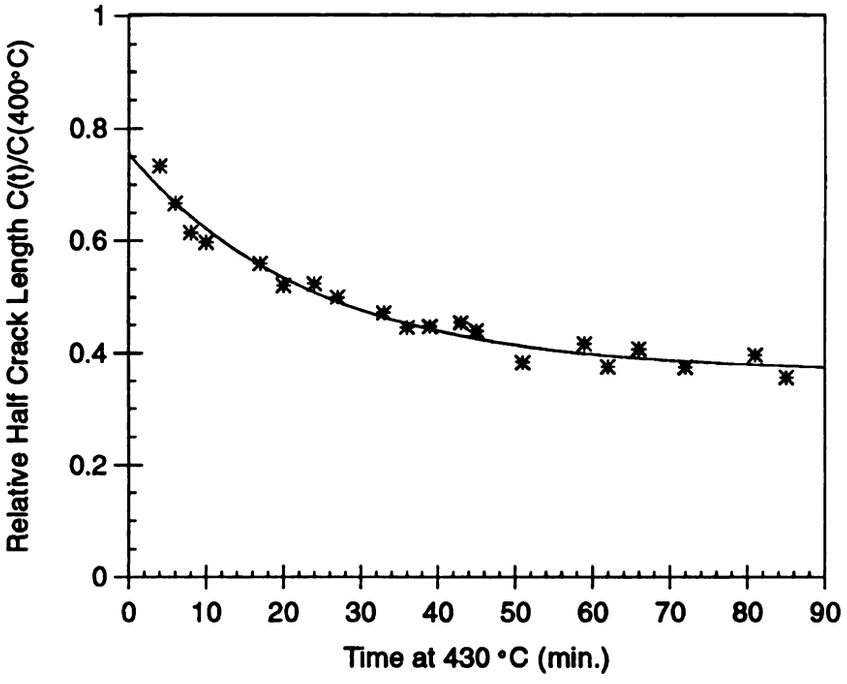

Figure 67 Relative change in crack length (C(T)/C(400°C)) for all 4 indent half cracks as a function of time at 430 °C for a glass specimen initially held at 8% r.h. (Experiment E). Data points indicate ESEM measurements. Curve is a least squares best fit to Equation 13.

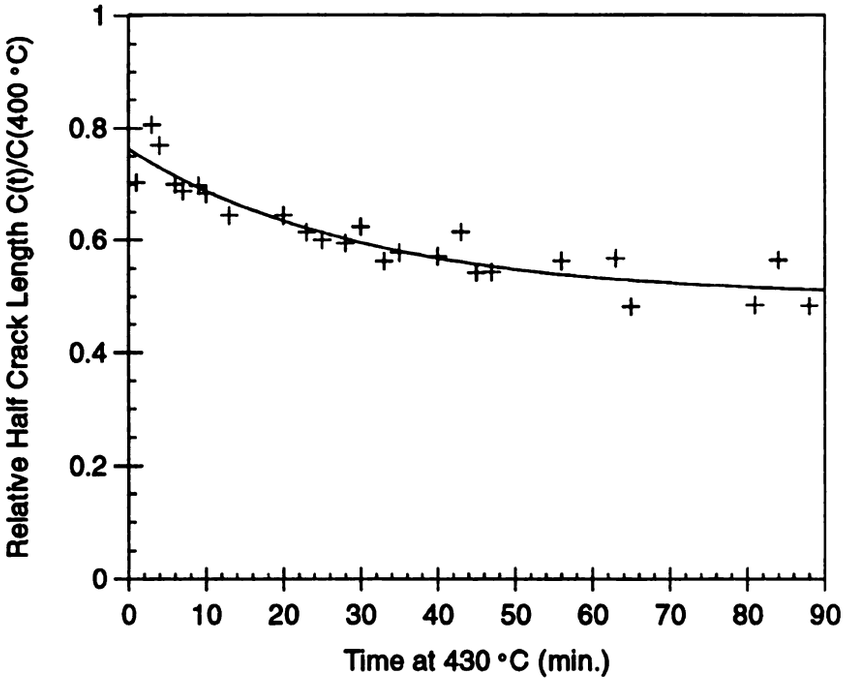

Figure 68 Relative change in crack length (C(T)/C(400°C)) for all 4 indent half cracks as a function of time at 430 °C for a glass specimen initially held at 16% r.h. (Experiment F). Data points indicate ESEM measurements. Curve is a least squares best fit to Equation 13.

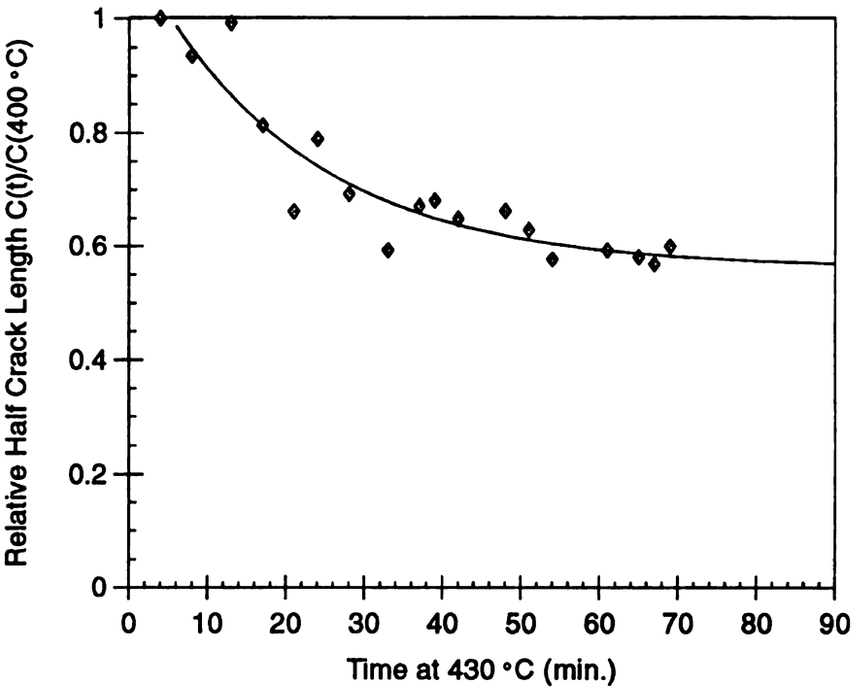

Figure 69 Relative change in crack length (C(T)/C(400°C)) for all 4 indent half cracks as a function of time at 430 °C for a glass specimen initially held at 32% r.h. (Experiment G). Data points indicate ESEM measurements. Curve is a least squares best fit to Equation 13.

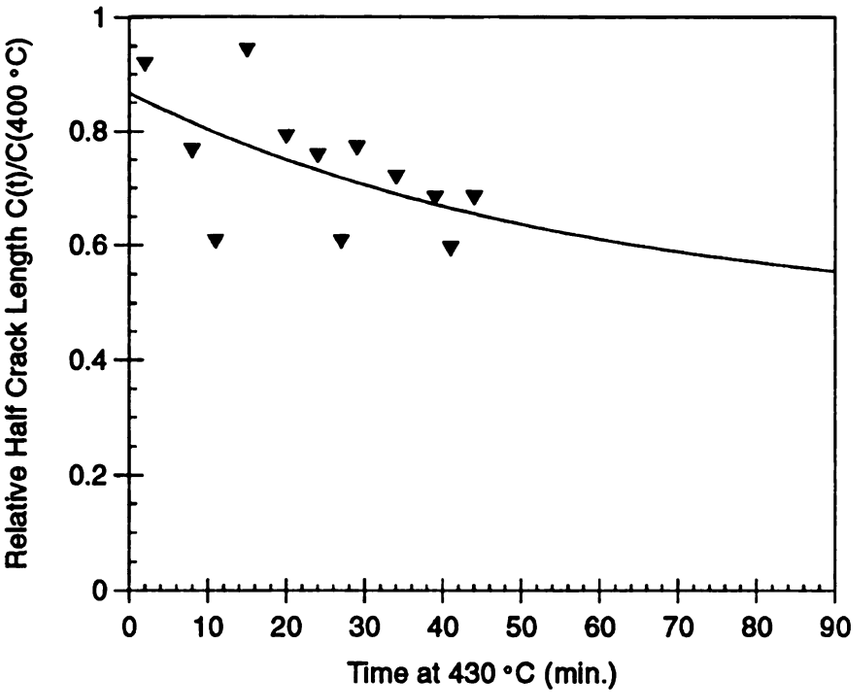

Figure 70 Relative change in crack length (C(T)/C(400°C)) for all 4 indent half cracks as a function of time at 430 °C for a glass specimen initially held at 64% r.h. (Experiment H). Data points indicate ESEM measurements. Curve is a least squares best fit to Equation 13.

The exponential fitting parameter, V_3, appears approximately constant over the range of humidity levels, indicating that V_3 is independent of humidity level for the crack healing of the soda-lime silicate specimens tested (Figure 71). If the time at temperature goes to infinity then the exponential term in Equation 13 goes to zero and $C(t=\infty)/C(400°C)$ becomes equal to V_1. Thus, V_1 represents the steady state relative half crack length or the final degree of crack healing. The steady state relative half crack length was similar for the 16, 32 and 64% initial r.h. specimens (Experiments F -H). The steady state relative half crack length was the lowest for the 8% initial r.h. specimen (Experiment E) indicating that the greatest healing occurred for the 8% r.h. sample.

For zero time at 430 °C the exponential term in Equation 13 goes to one and $C(t=0)/C(400°C)$ becomes equal to $\{V_1 - V_2\}$. The difference between V_1 and V_2 represents the initial relative half crack length upon reaching 430 °C after heating from 400 °C. The quantity $\{V_1 - V_2\}$ was smallest for the 8% relative humidity sample (Experiment E) thus for the lowest initial humidity there was the smallest amount of healing by the time 430 °C was initially reached (Figure 71). The 32 % r.h. sample (Experiment G) exhibited the largest amount of healing by the time the specimen reached 430 °C as shown by the large $\{V_1 - V_2\}$ values. The large deviation at 32% r.h. (Experiment G) compared to the 16 and 64% r.h. samples (Experiments F and H) indicated the need for further testing in the range of 16 to 64% initial relative humidity to see if there are maxima for the initial healing in the range of 16 to 64%. Experiments I through M were conducted at 48% initial relative humidity and the results are detailed in the Section 4.4.1.1.5.

Table 31 Fitting parameters, V_1, V_2, and V_3 and correlation coefficients for the least squares best fit of relative crack length as a function of time to Equation 13 (Figures 66-69) for initial relative humidities of 8, 16, 32, and 64% (Experiments E-H).

Initial Relative Humidity (%)	Fitting Parameter V1	Fitting Parameter V2	Fitting Parameter V3	Correlation Coefficient r
8	0.366	-0.389	0.0414	0.983
16	0.499	-0.264	0.0334	0.928
32	0.532	-0.565	0.0478	0.934
64	0.520	-0.350	0.0212	0.562

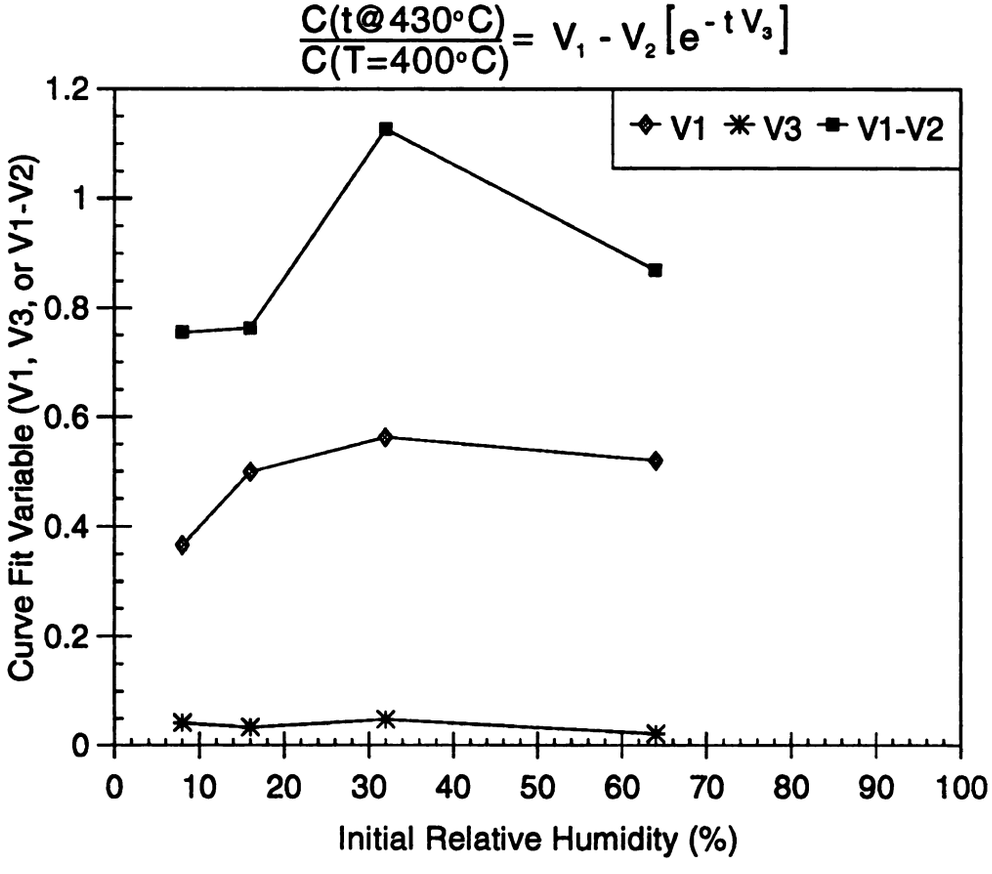

Figure 71 Plot of the fitting parameters, V_1, V_3, and V_1-V_2 as a function of the initial relative humidity for the least squares best fit of the relative crack length as a function of time to Equation 13 (Figures 67-70) (Experiments E-H).

4.4.1.1.5 Healing with New Hot Stage Heater (Experiments I-M)

Samples in Experiments I-M were held at an initial relative humidity of 48% before heating as described in Section 3.6.1.3.4. After another operator damaged the ESEM hot stage, a new heater complete with internal thermocouple was installed on the hot stage. For the samples of Experiments I-L heated to 430 °C, using a newly installed heater, no healing was observed for isothermal holds at 430 °C. The absence of healing in Experiments I-L was thought to be the result of a malfunction in the new hot stage heater. It was believed that the temperature which the sample underwent during testing was much lower than the temperature displayed by the hot stage. To investigate the actual sample temperature in relation to the temperature displayed by the hot stage, a sample was tested with an attached thermocouple (Figure 9, Experiment M).

In Experiment M, a sample with a thermocouple cemented to the surface was attached to a crucible as described in Section 3.6.1.3.5 (Figure 9). The crucible was placed in the hot stage and tested in an identical manner to Experiments E-H and I-L. The measured sample temperature was as much as 90 °C lower than the 430 °C temperature displayed by the hot stage. The large, 90 °C temperature difference between the sample temperature and the displayed ESEM temperature in Experiment M indicated a major problem with the new hot stage heater and the need for further investigation of the sample surface and hot stage temperature.

In Experiment G, a sample with initial humidity of 32% was found to begin healing at a temperature around 370 °C with less than a 1% change in crack length (Section 4.3.2.1.4.2). While in Experiment H, a sample with 64% initial relative

humidity had crack healing of 25% at 370 °C (Section 4.3.2.1.4.2). For the sample tested at 48% initial relative humidity in Experiment M, the only tangible positive result that can be reached from the combination of the isothermal holds at a hot stage displayed temperature of 430 °C, was that soda-lime silica glass held initially at 48% relative humidity does not heal at a temperature of approximately 340 °C for times of 90 minutes or less.

4.4.1.2 Further Temperature Measurement of New Hot Stage Heater

The sample surface temperature compared to the ESEM controller temperature reading was first investigated using a sample cemented in a crucible with a thermocouple bonded to the surface of the sample (as in Experiment M). When the ESEM temperature displayed was 400 °C, the thermocouple temperature was 343 °C (Table 32). When the ESEM display temperature was holding at 430 °C a voltmeter was placed in the sample chamber to read the thermocouple directly instead of using the vacuum pass-through ports on the ESEM door (as described in Section 3.6.1.3.5). The direct thermocouple reading inside the ESEM sample chamber was identical to the reading using the vacuum pass-through ports on the ESEM door which indicated that for past and future ESEM hot stage testing, a sample thermocouple temperature could be read using the vacuum pass through ports on the ESEM door.

With the old hot stage heater, the crucible had been a fixed part of the heater. To try to make the new hot stage similar to the old hot stage, the crucible was attached to the hot stage with silver paint. The specimen-mounted thermocouple temperature with the crucible affixed to the hot stage was 33 °C lower than the 400 °C

temperature displayed by the hot stage (Table 32). To help determine the temperature drop through the glass specimen, a thermocouple was silver painted directly (without a glass specimen) to a crucible which was affixed to the new hot stage. A temperature difference of 28 °C was measured between the thermocouple and the 400 °C temperature displayed by the hot stage (Table 32). The temperature drop through a glass specimen was only 5 °C, when the ESEM measured temperature was less than 550 °C (Table 32).

4.4.1.3 Heat Transfer Calculation of Temperature Differences of New Heater

To determine if the temperature differences measured in Section 4.4.1.2 were simply the result of heat lost due to heat transfer through the crucible and the glass specimen, heat transfer analysis was performed. Heat was transferred from the heater through the crucible and specimen via conduction, while the heat at the top surface was lost via free convection. The heat transfer problem was assumed to be a 1-D, steady state heat transfer with no energy generation and constant thermal conductivity within each different material. For these assumptions, the heat transfer rate is constant in the direction of the temperature gradient from the heater surface through the glass specimen surface [76] (Figure 72).

By treating the thermal resistance to conduction in an analogous manner to the electrical resistance through an electrical circuit, the heat transfer rate can be expressed as a function of the temperature drop across a given portion of the total resistance circuit and the resistance from that portion of the circuit [76]. The heat transfer rate, q_z, through the circuit from the heater to the air is equivalent to the heat transfer rate

through the circuit from the sample surface to the air (Figure 72), such that

$$q_z = \frac{T_{ESEM} - T_{air}}{R_{total}} = \frac{T_{Surface} - T_{air}}{R_{fcs}} \quad (14)$$

where T_{ESEM} is the temperature reading of the ESEM heater, T_{air} is the air temperature inside the ESEM sample chamber, $T_{surface}$ is the temperature at the sample surface, R_{total} is the thermal resistance of the total circuit from the heater to air, and R_{fcs} is the thermal resistance which results from free convection at the surface. The temperature at the sample surface can be found using Equation 14 can be rewritten as

$$T_{Surface} = T_{air} + \frac{T_{ESEM} - T_{air}}{R_{total} R_{fcs}} \quad (15)$$

where T_{air} and T_{ESEM} are known quantities and the thermal resistances R_{total} and R_{fcs} can be calculated.

Thermal resistance to heat transport via conduction is given by [76]

$$R_{conduction} = \frac{L}{kA} \quad (16)$$

where L is the thickness of the material in the direction of heat transfer, k is the thermal conductivity of the material, and A is the area of the material normal to the direction of heat transfer [76]. Thermal resistance to heat transport via convection is given by [76]

$$R_{convection} = \frac{1}{hA} \quad (17)$$

Table 32 Thermocouple temperature readings for three different testing conditions at different ESEM new hot stage heater temperatures.

Testing Conditions	T_{ESEM}= 400°C	T_{ESEM}= 430°C	T_{ESEM}= 500°C	T_{ESEM}= 550°C
Thermocouple Cemented to Glass Sample Crucible Set into Heater	340°C	366°C	421°C	459°C
Thermocouple Cemented to Glass Sample Crucible Silver Painted to Heater	367°C	392°C	452°C	492°C
Thermocouple Silver Painted to Crucible Crucible Silver Painted to Heater	372°C	397°C	457°C	500°C

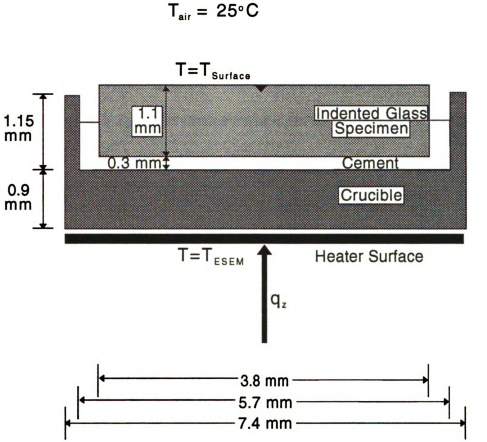

Figure 72 Schematic of the ESEM heating stage for heat transfer determination of the surface temperature.

where h is the free convection heat transfer coefficient of the gas [76]. The resistance of the total heat transfer circuit in Figure 72, R_{total}, is

$$R_{total} = \frac{L_{CB}}{k_{CB} A_{CB}} + \left[\left(\frac{L_{CBL}}{k_{CBL} A_{CBL}} \right)^{-1} + \left(\frac{L_{CS1}}{k_{CS1} A_{CS1}} \right)^{-1} \right]^{-1} + \left[\left(\frac{L_g}{k_g A_g} \right)^{-1} + \left(\frac{L_{CS2}}{k_{CS2} A_{CS2}} \right)^{-1} + \left(\frac{L_{CF}}{k_{CF} A_{CF}} \right)^{-1} \right]^{-1} + \frac{1}{h_{air} A_{air}} \quad (18)$$

where the subscript CB indicates the crucible bottom layer, CBL indicates the cement bonding layer, g indicates the glass layer, CS indicates the crucible sides and CF indicates the cement filler layer. The values for thickness, L, and area, A, for each of the layers indicated with subscripts in Equation 18 can be determined from Figure 72 and the values for k can be determined from handbook values [77] (Table 33). The surface transfer coefficient of air must be calculated for the free convection at the top surface. For the current case of no forced convection and lamellar air flow at a horizontal heated surface, the surface transfer coefficient can be determined [76]

$$h \approx 0.54 \frac{k_{air}}{L_P} \left[\frac{g \beta_{air} L_P^3 (T_s - T_{air})}{\nu_{air} \alpha_{air}} \right]^{\frac{1}{4}} \quad (19)$$

where L_P is the area of the surface divided by the perimeter of the surface, g is gravitational acceleration (m/s^2), β is the expansion coefficient, ν is the kinematic viscosity (m/s^2), α is the thermal diffusivity (m/s^2). For an ideal gas, the expansion coefficient, β, is equal to the inverse of the temperature of the gas (1/K). A temperature of 485.5 K was used to determine the material properties for free convection, as calculated from the average of the temperature at the surface and the

temperature of the gas. Using Table 34 and Equation 19, the calculated convective heat transfer coefficient, h_{air}, was 25.7 W/K.

Using the calculated value for h_{air}, the data from Table 33, and Equation 18, the total heat transfer circuit, R_{total} is 929.5 K/W. The temperature at the surface was 395 °C, using Equation 15. The heat transfer analysis of the temperature loss through the crucible and glass sample gave a derived temperature at the glass specimen surface of 395 °C while experimentally the temperature at the glass specimen surface was determined to be only 367 °C. To investigate the validity of the heat transfer model, the temperature drop through the glass specimen was determined using the model so that the calculated temperature drop could be compared to the experimentally determined temperature drop through the glass specimen of 5 °C (see end of Section 4.4.1.2).

To calculate the temperature drop through the glass specimen, the temperature must be determined at the location along the heat transfer path before the glass which resulted from the heat transferred from the heater. Recalling that the heat transfer rate, q_z, through each layer was assumed to be equal, the heat transfer can be expressed as (Figure 72)

$$q_z = \frac{T_{ESEM} - T_{air}}{R_{total}} = \frac{T_{ESEM} - T_{BG}}{R_{BG}} \qquad (20)$$

where the subscript BG indicates before glass, which refers to the location after the cement layer and before the glass layer along the heat transfer path depicted in Figure 72. The thermal resistance before the glass is (Figure 72)

Table 33 Property values for different layers of the sample and ESEM hot stage assembly for the total heat transfer resistance of Equation 18 (material properties from [77], dimensions from Figure 72).

Layer Subscript Designation	Material Layer Composed of or Closest Material	Thermal Conductivity, k (W/m K) at 400 °C	Thickness of layer, L (10^{-4} m)	Area of layer, A (10^{-5} m^2)
CB	Mullite	4.18	9	4.24
CBL	Mullite	4.18	3	2.55
g	Na-Ca-Si Glass	2.00	11	1.44
CS1	Mullite	4.18	3	1.69
CS2	Mullite	4.18	11.5	1.69
CF	Mullite	4.18	5.5	1.11

Table 34 Property values for free surface convection at the ESEM hot stage surface to determine the convective heat transfer coefficient, h_{air} (material properties from [76], dimensions from Figure 72).

A ($m^{2)}$	P (m)	L_P (m)	k_{air} (W/mK)	ν_{air} (m^2/s)	α_{air} (m^2/s)	β_{air} (1/K)
$4.24x10^{-5}$	$2.31x10^{-2}$	$1.84x10^{-3}$	$39.7x10^{-3}$	$36.9x10^{-6}$	$53.9x10^{-6}$	$2.06x10^{-6}$

$$R_{BG} = \frac{L_{CB}}{k_{CB} A_{CB}} + \left[\left(\frac{L_{CBL}}{k_{CBL} A_{CBL}} \right)^{-1} + \left(\frac{L_{CSI}}{k_{CSI} A_{CSI}} \right)^{-1} \right]^{-1} . \quad (21)$$

Using the data from Table 33 with Equations 20 and 21, the temperature directly before the glass was 397 °C. Thus, the temperature drop through the glass specimen was determined to be 3 °C from heat transfer analysis. The experimentally determined temperature drop through the glass specimen was 5 °C (see end of Section 4.4.1.2).

The similarity of the results demonstrates the soundness of the heat transfer analysis and consequently highlights that the difference in the displayed temperature and the sample temperature were the result of a large error in the ESEM hot stage temperature display rather than due to heat loss from heat transfer through the crucible and the glass specimen. A possible cause for the large error in the ESEM temperature could be that the thermocouple in the heater used by the hot stage controller was touching one of the heater wires. Regardless of the cause of the problem, the heater either needs to be replaced and/or each sample tested must have a thermocouple attached and measured independently from the ESEM hot stage controller.

4.4.2 Conventional Healing Experiments

Conventional crack healing experiments were performed on soda-lime silica glass, Coors alumina and microwave sintered alumina specimens. In conventional crack healing experiments, cracks were made in a specimen, aged, characterized, heated in a furnace. Changes in the cracks brought on by the healing cycle were noted.

4.4.2.1 Soda-Lime Silica Glass

Six different experiments with a total of 113 specimens and 654 cracks were used to investigate healing in soda-lime silica glass. Some specimens were heated after preparation and prior to indentation to relieve the residual stress in the specimen due to cutting and grinding.

4.4.2.1.1 Crack Healing and Strength Testing (Experiment 1)

Indented glass specimens were annealed in a large tube furnace to partially heal the cracks (Section 3.6.2.2.3). The crack lengths were measured optically from crack tip to crack tip before and after the thermal annealing cycle. The mean crack length after the 24 hour age in laboratory air for all 12 specimens was 201.3 ± 7.4 microns. The mean change in crack lengths, $\{2c_{heal} - 2c_{initial}\}$, was calculated for all 12 specimens (Table 35). The mean crack length changes for the thermally annealed samples (Specimens 1-10 in Table 35) were higher than the crack length changes for specimens only aged in air (Specimens 11-12 in Table 35) which indicates that significant crack healing occurred during the heat treatment at 600 °C. Out of the six indent cracks for each specimen, zero to six of the indent cracks displayed crack pinch-off when observed optically (Table 35). The change in crack length significantly decreased as the number of cracks which displayed pinch-off increased (Table 36).

For the thermally annealed specimens, the three-point bend Modulus of Rupture values ranged from 72.5 to 101.8 MPa (Table 37). For samples aged in air the Modulus of Rupture ranged from 46.3 to 47.9 MPa (Table 37). The higher Modulus of Rupture values for the thermally annealed specimens compared to the unannealed

Table 35 Change in crack lengths $\{2c_{initial} - 2c_{heal}\}$ for 6 cracks on each of ten soda-lime silica glass specimens annealed in the large tube furnace for 30 minutes at 600 °C and for 6 cracks on each of two glass specimens held at laboratory temperature.

Specimen Number	Temperature of Heat Treatment	$\{2c_{initial} - 2c_{heal}\}$ Mean and Standard Deviation (μm)	Number of indent cracks with pinch off
1	600 °C	34.6 ± 15.2	0
2	600 °C	24.5 ± 10.1	1
3	600 °C	1.4 ± 0.9	6
4	600 °C	16.2 ± 23.0	4
5	600 °C	1.2 ± 9.6	4
6	600 °C	14.7 ± 8.7	5
7	600 °C	32.4 ± 34.7	3
8	600 °C	45.7 ± 7.7	0
9	600 °C	2.2 ± 1.9	6
10	600 °C	12.8 ± 11.3	6
11	25 °C	2.3 ± 3.8	0
12	25 °C	1.8 ± 1.4	0

Table 36 Change in crack lengths $\{2c_{initial} - 2c_{heal}\}$ for groups of specimens from Table 35.

Specimens Included in Group	Temperature of Heat Treatment	$\{2c_{initial} - 2c_{heal}\}$ Mean and Standard Deviation (μm)	Number of indent cracks with pinch off per specimen
1 - 10	600 °C	18.5 ± 21.4	0 To 6
1 - 2, 8	600 °C	34.9 ± 14.8	0 To 1
3 - 6, 9 - 10	600 °C	7.9 ± 13.8	4 To 6
11 - 12	25 °C	2.0 ± 2.8	0

Table 37 Modulus of Rupture (stress at failure) for three-point bend testing of specimens of glass annealed in the large tube furnace for 30 minutes at 600 °C and of two glass specimens held at laboratory temperature.

Specimen Number	Temperature of Heat Treatment	Modulus of Rupture (MPa)
1	600 °C	101.8†
2	600 °C	76.0
3	600 °C	72.5
4	600 °C	92.2‡
5	600 °C	85.6
6	600 °C	95.1‡
7	600 °C	96.2‡
8	600 °C	88.8‡
9	600 °C	82.0‡
10	600 °C	93.6‡
11	25 °C	46.3
12	25 °C	47.9

† Indicates specimens which fractured outside of indent area
‡ Indicates specimens which fractured at the sample edge

specimens, indicates partial healing of the indent cracks occurred upon thermal annealing at 600 °C.

Optical micrographs were taken of the middle indents for: a) a specimen aged in air (Figures 73 and 74), b) a thermally annealed specimen which does not display pinch-off (Figures 75 and 77), and c) a thermally annealed specimen which displays pinch-off (Figures 78 and 80). The width of the cracks of the thermally annealed specimens were greater than 5 μm (Figures 76, 77, 79, and 80), while the width of the cracks of the unannealed specimens were around 1 μm or less (Figure 74). The indent cracks of specimens annealed at 600 °C had a larger crack width (Figures 73 - 80) and a shorter crack length (Table 36 and Figures 73 - 80) than the indent cracks of the specimen only aged at room temperature. The change in the appearance of the optical micrographs of indent cracks of the specimen without a thermal anneal (Figures 73 - 74) and of the specimens which were annealed (Figures 75 - 80), indicated that crack healing occurred upon thermal annealing. The healed cracks in cases where pinch-off did not occur (Figures 75 - 77) had a shorter distance from crack tip to crack tip than healed cracks in cases where pinch-off did occur (Figures 78 - 80, Table 36). For example, the change in crack length was 44.3 μm for the horizontal crack of indent B in Specimen 8 (Figures 75 - 77) and was 3.1 μm for the horizontal crack of indent B in Specimen 4 (Figures 78 - 80). However, if the crack length for the crack with pinch-off (Figures 78 - 80) was measured from the location of first pinch-off to the location of first pinch-off on the other side of the indent, then the change in crack length was 44.4 μm.

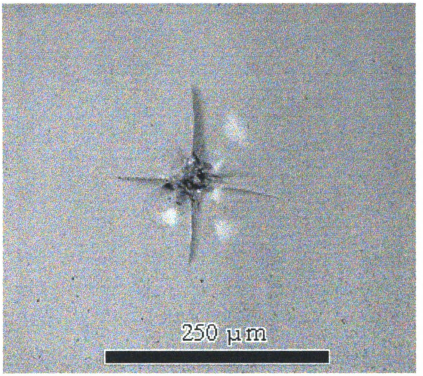

Figure 73 Optical micrograph of indent B of glass specimen eleven aged in room temperature air. Other specimens were annealed at 600 °C (Table 33). The horizontal crack in the unannealed specimen was approximately 190 µm in length.

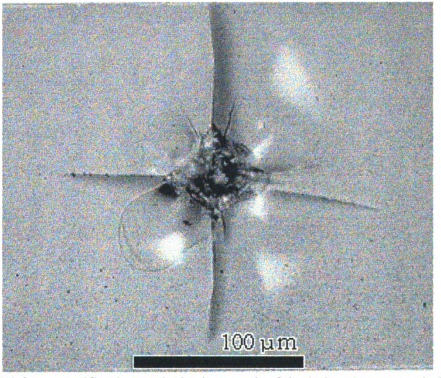

Figure 74 Higher magnification optical micrograph of the indent in unannealed glass shown in Figure 73. Unannealed crack widths were less than approximately 1.5 µm.

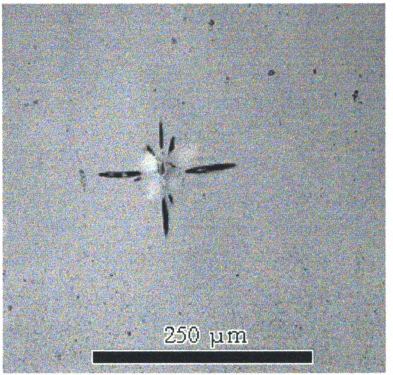

Figure 75 Optical micrograph of indent B of glass specimen eight annealed at 600 ℃ for 30 minutes in the large tube furnace. The horizontal crack in the annealed specimen was approximately 156 µm in length.

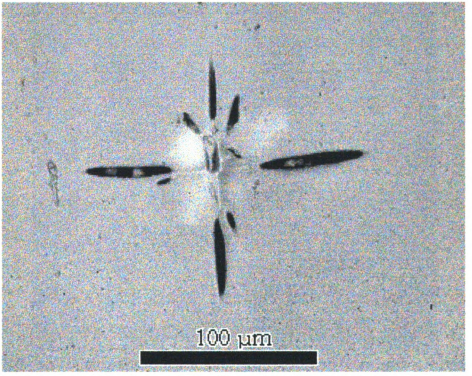

Figure 76 Higher magnification optical micrograph of the indent shown in Figure 75. The crack width increased during annealing to greater than approximately 6 µm.

Figure 77 Higher magnification optical micrograph of one of the indent cracks shown in Figure 76. The crack tip appears blunted after annealing.

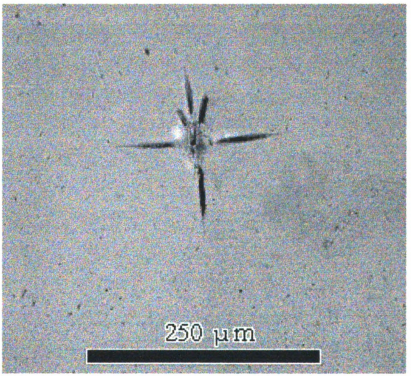

Figure 78 Optical micrograph of indent B of glass specimen four which was annealed at 600 °C for 30 minutes in the large tube furnace. The horizontal crack in the annealed specimen was approximately 184 µm in length.

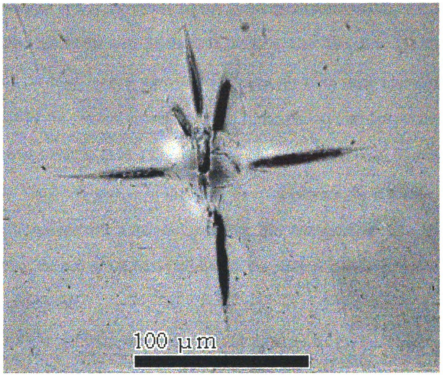

Figure 79 Higher magnification optical micrograph of indent shown in Figure 78. The crack width increased during annealing to greater than approximately 6 µm.

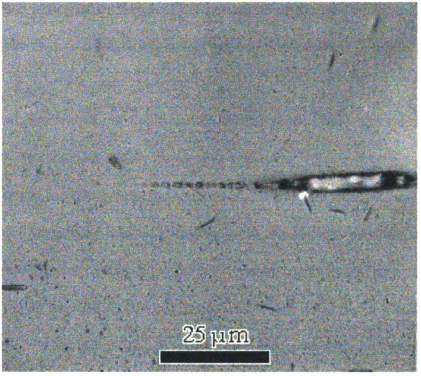

Figure 80 Higher magnification optical micrograph of one of the indent cracks shown in Figure 79. Extensive pinch-off at the end of the crack has occurred after annealing.

4.4.2.1.2 Surface and Sub-Surface Crack Healing (Experiment 2)

Indented glass specimens were annealed in the large tube furnace at 550 °C for 30 minutes and the crack lengths were measured optically from crack tip to crack tip before and after the thermal annealing cycle. In the optical microscope, the annealed cracks were observed to have a heavy portion and a very faint portion of the crack (Table 38). The heavy portion of the crack was characterized by a large crack opening displacement with a rounded crack tip. The faint portion of the crack extended from the end of the heavy portion of the crack and had negligible crack opening displacement.

Healing in the specimens was markedly different for the faint and heavy portions of the crack. The mean change in the crack length was about 17.7 μm for the faint portion of the crack and about 48.8 μm for the heavy portion of the crack (Table 38). Healing is indicated by the crack tip regression of the total crack by 17.7, as well as by the appearance of a negligible crack opening displacement in the faint portion of the crack.

Optical observations of the specimen surface alone cannot determine if the cracks below the specimen surface break into cylindrical voids and/or break into spheres as seen in internal cracks by Wang et al. [30], Gupta [31, 34], and Yen and Coble [32]. To investigate the crack healing below the surface, the thermally annealed specimens were fractured through the partially healed indent cracks using the Kirchner method [64]. The fracture surface of the specimens was observed in a conventional SEM as detailed in Section 3.6.2.2.3. A line of voids, quasi-circular in cross-section, was observed for a soda-lime silica glass specimen partially healed by a 30 minute

Table 38 Change in crack lengths $\{2c_{initial} - 2c_{heal}\}$ for heavy and faint portions of healed indent cracks for glass specimens annealed in the large tube furnace for 30 minutes at 550 °C. (Sample 1 fracture upon indentation with a 98 kg load).

Specimen Number	Indent Crack ($2c_1$ or $2c_2$)	Heavy Part of Healed Crack $\{2c_{initial} - 2c_{heal}\}$ (μm)	Faint Part of Healed Crack $\{2c_{initial} - 2c_{heal}\}$ (μm)
2	1	60.4	6.0
	2	54.3	6.8
3	1	18.8	2.4
	2	41.7	30.3
4	1	31.5	14.0
	2	29.6	20.7
5	1	54.8	41.8
	2	58.1	43.4
6	1	57.3	5.9
	2	71.5	5.2
Mean and Standard Deviation		48.8 ± 16.4	17.7 ± 14.9

heat-treatment at 550 °C (Specimen 6 Table 38, Figure 81 - 83). While this phenomenon needs to be investigated further, the voids seem similar to voids formed by crack healing and pinch-off discussed by previous researchers [30-32, 34].

4.4.2.1.3 Effects of Stress Relief Cycle (Experiment 3)

Crack healing in glass after 15 minutes of annealing at temperatures of 350 to 500 °C and below was investigated as described in Section 3.6.2.2.4 using the small tube furnace. Glass samples were prepared with a stress relief cycle of 550 °C for 30 minutes and aged in air for 24 hours after indentation. The mean crack length change ($\Delta c_{heal} = 2c_{initial} - 2c_{heal}$) ranged from −2.6 to 0.3 microns with standard deviations which ranged from 0.5 to 1.9 microns (Table 39). Δc_{heal} values of ±3 μm or less were within an individual investigator's standard error for crack length measurement in glass (Section 4.2.1). No significant crack healing occurred at temperatures below 500 °C for a 15 minute hold.

A survey of the effect of a stress relief cycle before aging on crack healing in glass was performed as described in Section 3.6.2.2.4 using the small tube furnace. Glass specimens prepared 1) with a stress relief cycle of 550 °C for 30 minutes (Cycle A from Section 6.6.2.2.2), 2) with a stress relief cycle of 600 °C for 60 minutes (Cycle B from Section 6.6.2.2.2), and 3) without a stress relief cycle were thermally annealed for times of 15, 30, 45, or 120 minutes and at temperatures of 525, 550, or 575 °C (Tables 40 - 42). When the glass specimen with stress relief cycle A was being thermally annealed at 575 °C for 15 minutes in the small tube furnace, the furnace controller thermocouple failed and the furnace reached an unknown maximum

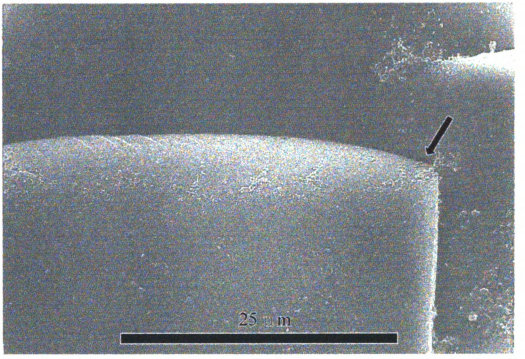

Figure 81 Conventional SEM micrograph of sub-surface portion of indent in glass specimen six, annealed at 550 ºC for 30 minutes in the large tube furnace. The specimen was fractured through the healed indent using Kirchner's method [64].

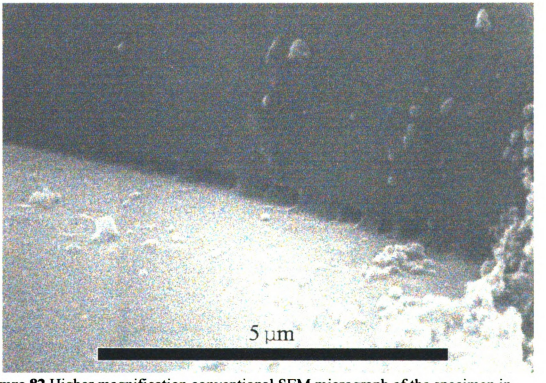

Figure 82 Higher magnification conventional SEM micrograph of the specimen in Figure 81 showing quasi-circular voids from region near the arrow of Figure 81.

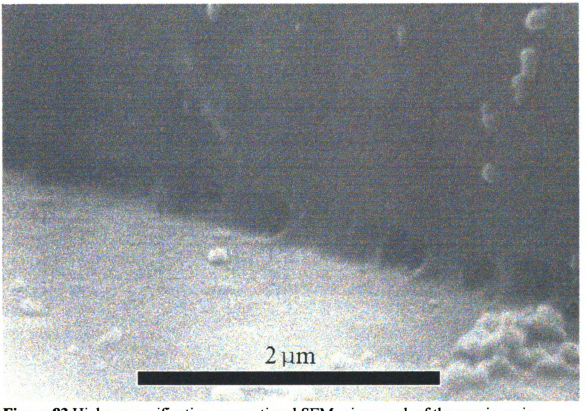

Figure 83 Higher magnification conventional SEM micrograph of the specimen in Figure 82 showing quasi-circular voids.

Table 39 Healed crack length change ($2c_{initial}$ - $2c_{heal}$) for glass specimens prepared with a stress relief cycle of 30 minutes at 550 °C, indented and aged in air for 24 hours, and annealed for 15 minutes in the small tube furnace (Experiment 3).

Temp. (°C)	350	375	400	425	450	475	500
Mean (μm) ($2c_{initial}$ - $2c_{heal}$)	0.0	-1.1	-0.1	-0.3	-2.6	0.3	0.1
Standard Deviation (μm)	0.9	1.9	1.3	0.9	0.5	1.0	1.8

Table 40 Healed crack length change ($2c_{initial}$ - $2c_{heal}$) for glass specimens prepared with a stress relief cycle of 30 minutes at 550 °C, indented and aged in air for 24 hours, and annealed in the small tube furnace (Experiment 3).

Temperature	525 °C		550 °C		575 °C	
Anneal Time	Mean (μm)	Standard Deviation (μm)	Mean (μm)	Standard Deviation (μm)	Mean (μm)	Standard Deviation (μm)
15 min.	6.7	3.8	5.2	2.7	61.3*	16.0*
30 min.	7.4	3.2	2.1	1.1	15.3	7.7
45 min.	1.7	1.2	10.6	7.6	28.0	3.7
120 min.	13.8	1.9	20.3	5.0	49.3	9.5

* Indicates sample for which thermocouple failure occurred.

Table 41 Healed crack length change ($2c_{initial}$ - $2c_{heal}$) for glass specimens prepared with a stress relief cycle of 60 minutes at 600 °C, indented and aged in air for 24 hours, and annealed in the small tube furnace (Experiment 3).

Temperature	525 °C		550 °C		575 °C	
Anneal Time	Mean (μm)	Standard Deviation (μm)	Mean (μm)	Standard Deviation (μm)	Mean (μm)	Standard Deviation (μm)
15 min.	*	*	7.9	1.7	7.2	3.8
30 min.	22.5	3.6	5.2	1.5	17.1	3.9
45 min.	3.8	2.2	3.8	4.4	31.7	1.5
120 min.	*	*	*	*	61.5	4.1

* Testing was not performed for this condition.

Table 42 Healed crack length change ($2c_{initial}$ - $2c_{heal}$) for glass specimens prepared without a stress relief cycle, indented and aged in air for 24 hours, and annealed in the small tube furnace (Experiment 3).

Temperature	525 °C		550 °C		575 °C	
Anneal Time	Mean (μm)	Standard Deviation (μm)	Mean (μm)	Standard Deviation (μm)	Mean (μm)	Standard Deviation (μm)
15 min.	*	*	-1.2	0.83	19.5	14.7
30 min.	6.1	2.3	2.5	1.3	1.9	1.1
45 min.	0.1	0.8	-4.0	4.3	-0.2	1.8
120 min.	*	*	*	*	0.6	0.9

* Testing was not performed for this condition.

temperature and so the Δc_{heal} value for the sample was not used in further analysis (Table 40).

For the specimens with stress relief cycle A (Table 40 and Figure 84) which were healed for 45 minutes or more, Δc_{heal} increased with time for each temperature and increased with temperature for each time (Figure 84). For times less than 45 minutes, no correlation of time and temperature with Δc_{heal} values was apparent (Figure 84).

The lack of correlation of Δc_{heal} with time and temperature for healing times less than 45 minutes indicated that either no crack healing was occurring for the shorter time periods or that crack length regression was not the dominant mechanism of crack healing. One other possible healing mechanism could have been a change of the crack tip shape. Hrma, Han, and Cooper [42] investigated indentation crack healing in glass at 600, 650, and 675 °C using optical microscopy (see Section 2.2.2 for description of Hrma et al.'s investigation). Hrma et al. [42] concluded that blunting of the crack tips via capillarity driven viscous flow of the glass occurred before regression of the crack lengths occurred. However, Hrma et al. [42] never directly observed blunting via optical microscopy. To determine if crack tip blunting occurred in the current study, the crack tips of the annealed samples were observed via electron microscopy. ESEM observation was unsuccessful in determining if crack tip blunting was occurring in the samples due to insufficient resolution. Observation of the samples with a field emission microscope (Camscan 44FE) was equally unsuccessful due to problems with sample charging even at accelerating voltages as low as 2 KeV.

For stress relief cycle B, testing for thermal annealing times of 45 minutes and above was performed at 575 °C (Table 41, Figure 85). The Δc_{heal} values for samples with stress relief cycles A and B which were healed at 575 °C, were within one standard deviation of each other (Tables 40 and 41, Figures 84 and 85). The samples tested without a stress relief cycle had little or no stress relief even for thermal annealing of 120 minutes at 575 °C as indicated by the indentation crack lengths (Table 42 and Figure 86). Since the specimens without a stress relief cycle exhibited a very different behavior from the specimens tested with a stress relief cycle, and since the specimens with a stress relief cycle displayed a very similar behavior to each other, further testing was performed using specimens which had a stress relief cycle at a temperature between 550 and 600 °C. The stress relief cycle temperature was determined from thermal mechanical analysis (TMA) and other high temperature experimentation by Chiu [57] for the same soda-lime silica glass used in this study. Chiu [57] reported a large increase in thermal expansion in the 550 - 600 °C range and chose a stress relief temperature of 580 °C for his work. Samples for Experiments 4 - 7 were prepared with a stress relief cycle at 587 °C (Section 3.6.2.2.2).

4.4.2.1.4 Effects of Aging Environment and Healing Temperature (Experiment 4)

Specimens prepared for testing as described in Section 3.6.2.2.1 were thermally annealed in sets of three for 60 minutes at 525, 538, 550, 563, and 575 °C (Table 43 and Figures 87 and 88). Each of the three samples in a set was aged in a different environment: 1) a desiccator with about 0 % r.h., 2) in laboratory air with about 45 % r.h. (Figure 89), and 3) a water chamber with about 100 % r.h..

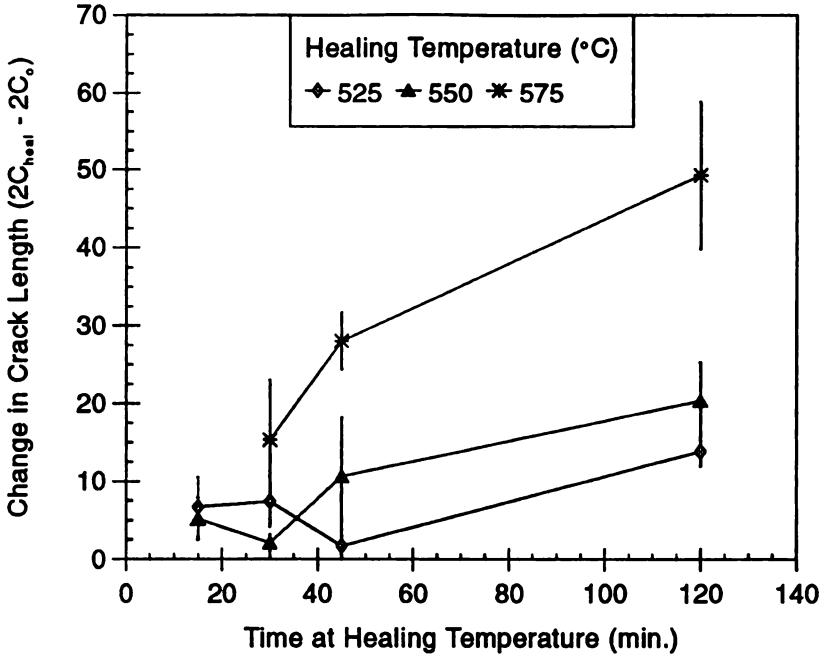

Figure 84 Mean crack length change ($2c_{initial}$ - $2c_{heal}$) versus healing time for glass specimens prepared with a stress relief cycle of 30 minutes at 550 °C, aged in air for 24 hours, and annealed in the small tube furnace (error bars indicate standard deviations of six cracks) (Experiment 3). $2c_{initial}$ values were approximately 221 μm.

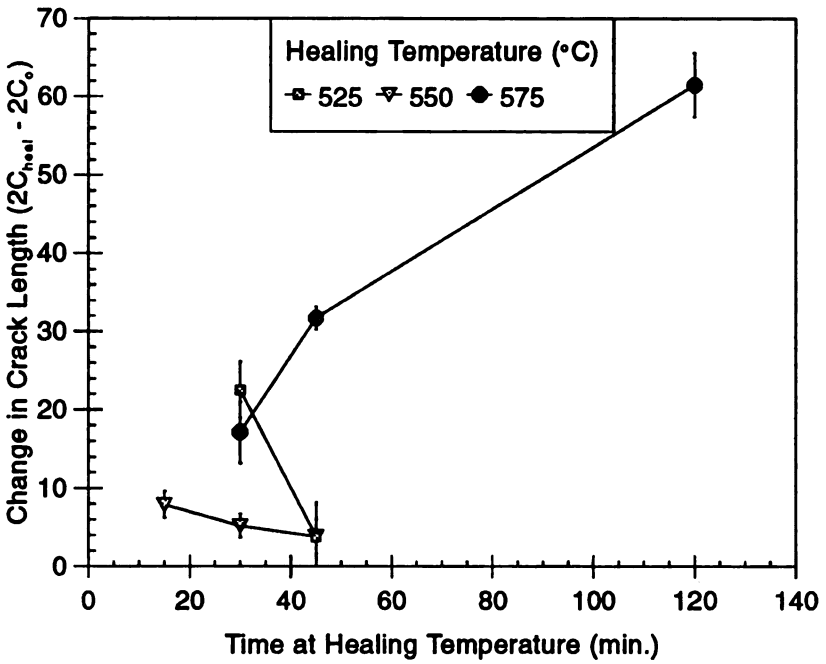

Figure 85 Mean crack length change ($2c_{initial}$ - $2c_{heal}$) versus healing time for glass specimens prepared with a stress relief cycle of 60 minutes at 600 °C, aged in air for 24 hours, and annealed in the small tube furnace (error bars indicate standard deviations of six cracks) (Experiment 3). $2c_{initial}$ values were approximately 219 μm.

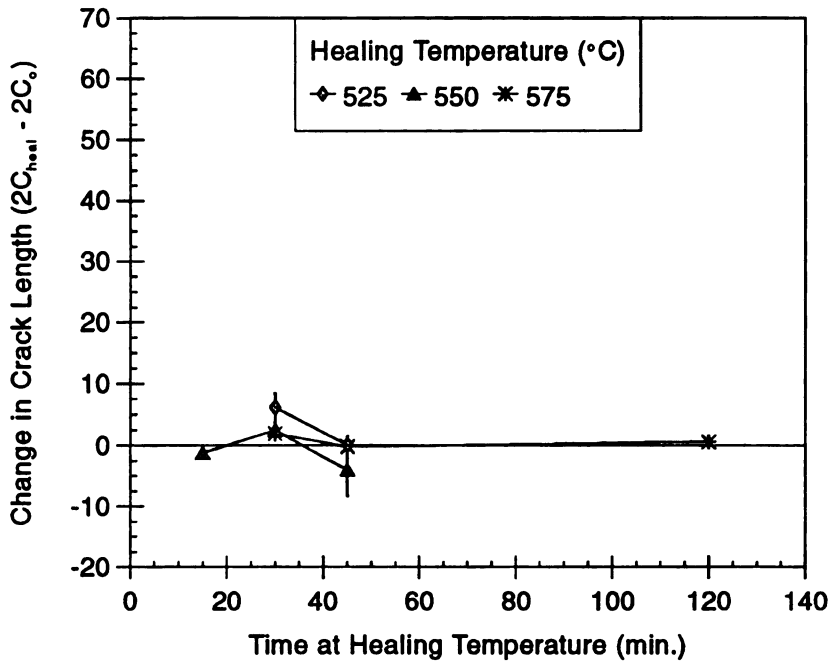

Figure 86 Mean crack length change ($2c_{initial}$ - $2c_{heal}$) versus healing time for glass specimens prepared without a prior stress relief cycle, aged in air for 24 hours, and annealed in the small tube furnace (error bars indicate standard deviations of six cracks) (Experiment 3). $2c_{initial}$ values were approximately 202 μm.

Table 43 Healed crack length change ($2c_{initial}$ - $2c_{heal}$) for glass specimens prepared with a stress relief cycle of 180 minutes at 587 °C (~8 °C/ minute ramp rate), aged for 24 hours, and annealed for 60 minutes in the small tube furnace (Experiment 4).

Aging Humidity	~0% r.h.		~45%		~100% r.h.	
Anneal Temperature	Mean (μm)	Standard Deviation (μm)	Mean (μm)	Standard Deviation (μm)	Mean (μm)	Standard Deviation (μm)
525 °C	27.1	5.0	32.3	2.0	39.7	5.4
538 °C	18.2	5.8	35.4	3.1	33.9	1.8
550 °C	23.6	3.7	35.0	2.0	31.4	7.9
563 °C	21.5	7.4	32.9	2.6	30.7	2.4
575 °C	15.6	1.8	25.3	3.6	21.0	8.8

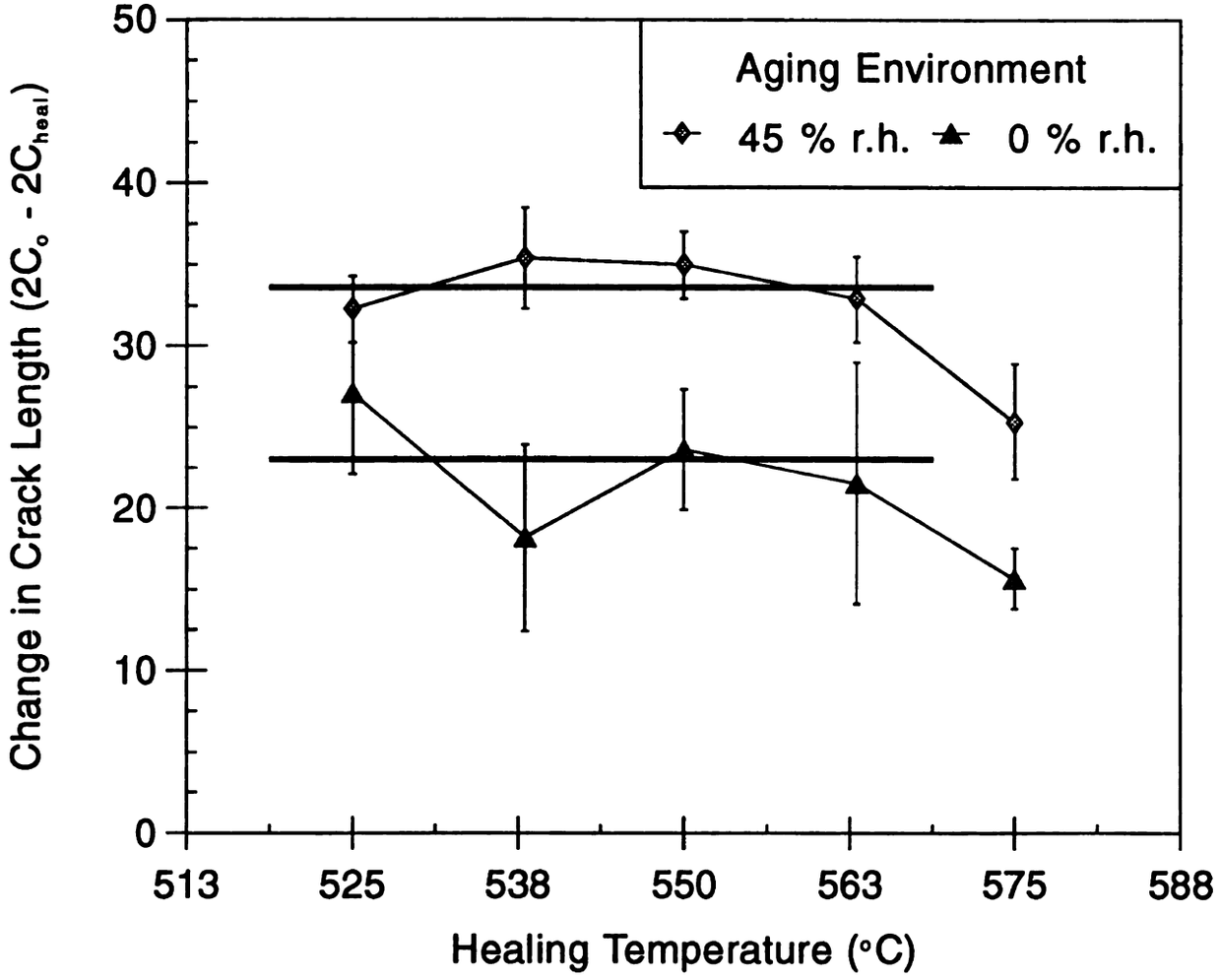

Figure 87 Mean crack length change ($2c_{initial}$ - $2c_{heal}$) versus healing temperature for glass specimens prepared with a stress relief cycle of 180 minutes at 587 °C (~8 °C/ minute ramp rate), aged for 24 hours in 0 or 45 % r.h., and annealed for 60 minutes in the small tube furnace (error bars indicate standard deviations of six cracks) (Experiment 4).

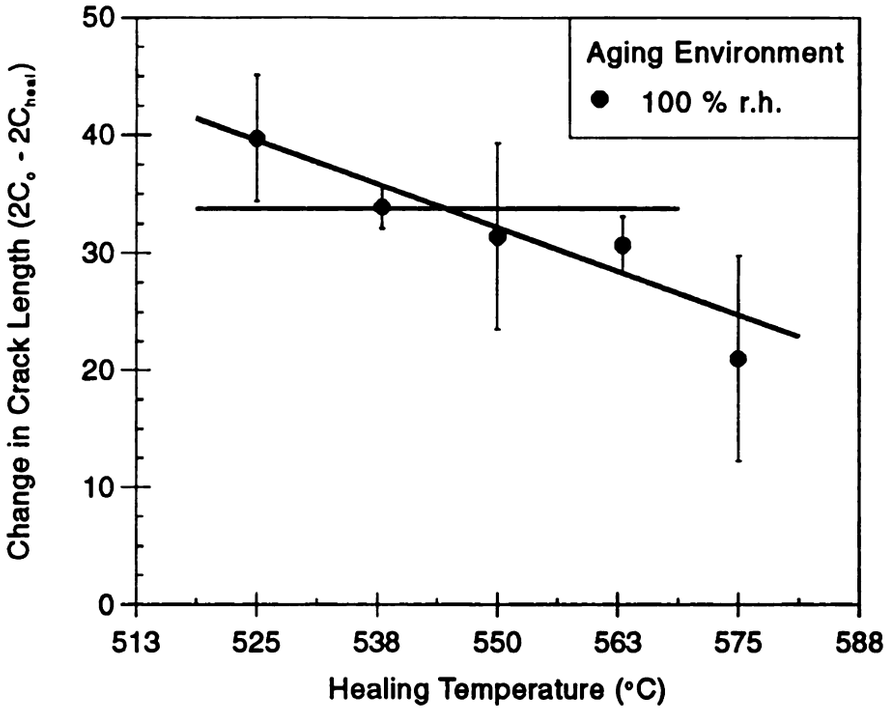

Figure 88 Mean crack length change ($2c_{initial}$ - $2c_{heal}$) versus healing temperature for glass specimens prepared with a 180 minute stress relief cycle at 587 °C (~8 °C/min. ramp rate), aged for 24 hours in 100 % r.h., and annealed for 60 minutes in the small tube furnace (error bars indicate standard deviations of six cracks) (Experiment 4).

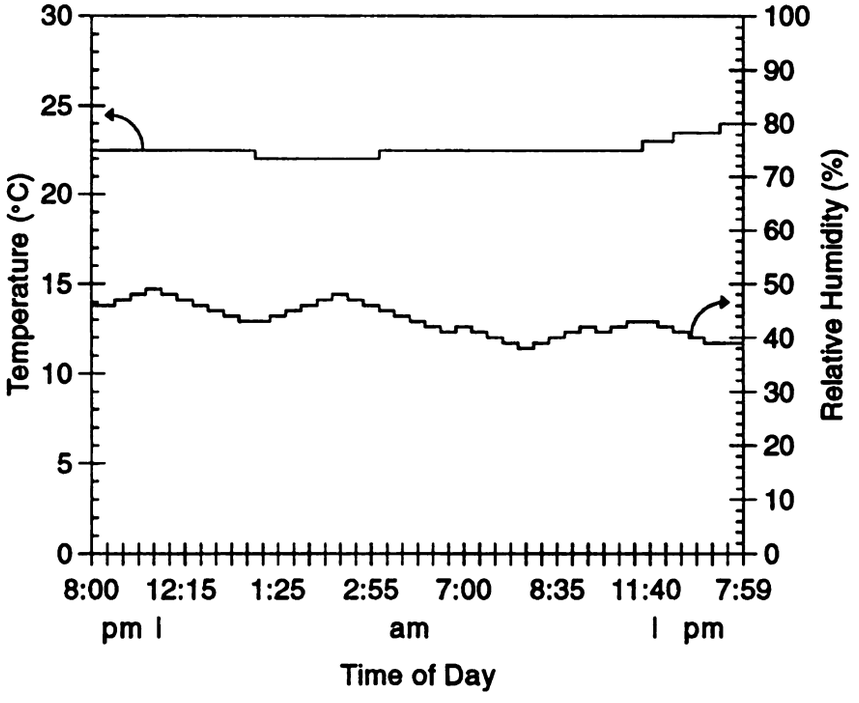

Figure 89 Circular chart recorder measurements of temperature and humidity during indent crack aging in air. Measurements were made during a day in the time period when healing experiments were performed.

4.4.2.1.4.1 Aging Environments of 0 and 45 % r.h.

For specimens aged in air in the temperature range of 525 to 563 °C, Δc_{heal} was 33.6 μm (upper horizontal line in Figure 87), while for specimens aged in a desiccator Δc_{heal} was 23 μm (lower horizontal line in Figure 87). The difference in healing of about 10 μm between specimens healed in air and in a desiccator is significant with respect to the error in crack healing measurement as discussed in Section 4.2.

With a difference in healing for samples aged in environments of 0 and 45 % r.h, water vapor appears to be a factor in the healing of glass. Section 4.4.2.1.4.2 discusses the physical effect of water on: a) the structure of glass, and b) properties such as the glass transition temperature and viscosity. The literature shows that water significantly reduces the viscosity of the glass and lowers the glass transition temperature (Section 4.4.2.1.4.2).

Aging samples in water vapor bearing environments results in water vapor adsorption by the freshly created indentation crack surfaces. The adsorbed water vapor can enter the glass structure via the crack surfaces before and/or during the annealing cycle as the temperature is increased. A glass surface layer containing incorporated water has a lower viscosity and glass transition temperature, T_g, than the bulk glass. Varying the aging conditions will alter the amount of water that enters the glass structure. Therefore, the magnitude of the decrement in viscosity and T_g may be a function of the ambient humidity. The higher Δc_{heal} for glass specimens aged in air compared to specimens aged in a desiccator is consistent with crack surface layers with higher amounts of incorporated water which results in a lower T_g and viscosity.

At 575 °C, Δc_{heal} decreased by 25% and 32% for specimens aged in air and in a

desiccator, respectively (Figure 87). The mean Δc_{heal} at 575 °C was about 10 μm greater for the specimen aged in air than for the specimen aged in a desiccator (Table 43) which was similar to the differences in Δc_{heal} observed for the two aging treatments for the temperatures between 525 and 563 °C (Figure 87).

The decrease in Δc_{heal} observed at 575 °C may be related to the specimen temperature being close to the transition temperature. As glass is heated vibrational amplitude of the ions increase with the increase in thermal energy [78]. As the glass approaches the glass transition temperature, structural rearrangements occur which absorb energy and change the specific volume of the glass [78]. The absorption of energy through molecular rearrangements could decrease the energy available for healing via atomic diffusion to the crack tip.

4.4.2.1.4.2 Review of Literature on the Presence of Water in Glass

The presence of water in glass and its effect on properties have been studied by many researchers [79-85]. Bartholomew [79] noted that many studies of water in glass investigated low water concentration introduced in the glass during the normal melting process. Water contents of more than a few tenths of a weight percent require a separate hydration processing step after the initial glass melt is made [79]. Processing using traditional melting techniques leads to water only in the form of hydroxyl groups only, while processing with a hydration step leaves hydroxyl groups and molecular water in the glass [79].

Scholze [80] described the presence of water as hydroxyl groups in the structure of glass. Scholze found that water is present in pure silica as free OH groups

which are bonded to only one Si atom (Figure 90) [80]. In alkali glasses, the OH groups hydrogen bond to the singly bonded nonbridging oxygen anions created by the alkali ion additions (Figure 90) [80]. The amount of bonded OH groups increases with increasing alkali content, since increasing the alkali content increases the number of nonbridging oxygens (NBOs) [80]. The addition of Al_2O_3 to alkali glasses with water present decreases the amount of bonded OH groups, since alumina causes the removal of NBOs [80]. The network change via the rupture of the Si-O-Si bridge from the formation of Si-OH group effects both the viscosity and glass transition temperature [80]. For example, in a 15:10:75 Na_2O-CaO-SiO_2 glass, the glass transition temperature decreased by 40 °C due to change in water content from 0.004 to 0.11 weight percent [80].

Jewell, Spess and Shelby [81] found that the water content of three different commercial soda-lime-silica glasses changed by remelting the glasses under flowing gas of different water vapor contents [81]. The water content of the as-received glasses ranged from about 0.015 to 0.045 weight percent and the water content of the reprocessed glasses ranged from 0.005 to 0.055 weight percent [81]. The glass transformation temperature decreased by approximately 20 °C with increasing water content for each of the three glasses [81]. The glass viscosity also decreased with increasing water content for each of the three glasses with the activation energy for viscous flow decreasing by 60 to 100 kJ/mol as the water content increased from about 0.008 to 0.048 wt. % [81]. Infrared spectra bands indicated that the water in the vitreous network was in the hydroxyl form which created NBOs [81]. The hydroxyl units interact with network via weaker hydrogen bond instead of the O^--R^+-O^- ionic

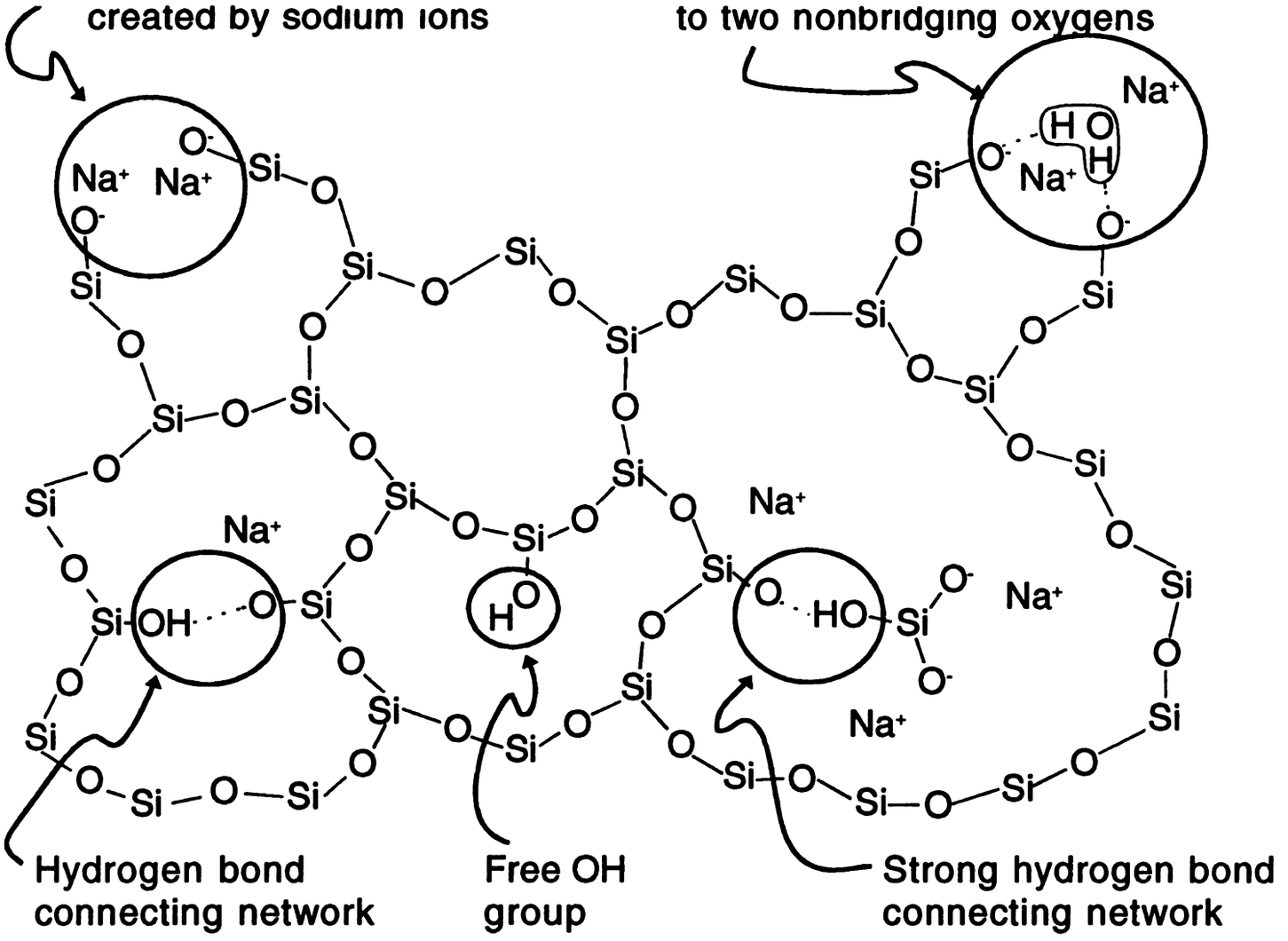

Figure 90 Two-dimensional schematic of the structure of glass with water present both as hydroxyl groups and as molecular water [after 78, 80].

link between NBOs formed by alkali or alkaline-earth ions, R^+ [81]. In the presence of the hydroxyl units, the network structure was nearly completely broken at the hydroxyl site and the effect on the flow behavior was increased compared to that from the presence of alkali or alkaline-earth ions [81].

Tomozawa et al. [82] studied the thermal properties of sodium silicate ($Na_2O{\cdot}3SiO_2$) glasses which underwent a high pressure, hydrothermal, hydration cycle to give water contents up to 8 weight percent [82]. Infrared spectroscopy found that water in the glass was in both the hydroxyl and molecular water form [82]. At water contents below 2 weight percent, infrared spectroscopy showed that the OH concentration increased rapidly with increasing water content and then reached a saturation concentration at about 6 weight percent water in the glass [82]. Infrared analysis also indicated that the molecular water concentration increased slowly at first as the water concentration increased up to about 6 weight percent, and then almost increased linearly [82]. The Si-OH content drastically lowered the glass transition temperature, T_g, since its presence was the result of broken Si-O-Si network bonds [82]. Thermogravimetric analysis (TGA) showed no water loss at temperatures below the glass transition temperature of 450 °C [82]. Tomozawa et al. comment that from the results of their work, the glass transition temperature is expected to drop linearly with low water content for most oxide glasses (where the water content is low and in the hydroxyl form) and that an 18 °C drop in T_g is expected for a 0.1 wt. % increase in the water content of the sodium silicate glass [82].

Schnatter et al. used resonant nuclear reaction to investigate hydrogen profiles of soda-lime silicate glass hydrated in D.I. water [83]. Plain soda-lime silica glass

(72.2 mol% SiO_2, 21.4% Na_2O, 6.4% CaO) had a hydration depth 0.2 μm after hydratation for 5 hours at 23 °C [83]. A nearly 50% decrease in the hydrogen concentration occurred in the plain soda-lime silica glass after a 12 hour age in vacuum at 25 °C, while there was only about a 20% decrease in hydrogen concentration after a one week age in air at 25 °C [83]. Commercial soda-lime silica glass (72 mol% SiO_2, 13% Na_2O, 5% CaO, 4% MgO, 3% Al_2O_3, 1% BaO, 1% B_2O_3, and 1% other oxides) had a hydration depth 0.06 μm after hydratation for 16 hours at 80 °C [83]. Approximately a 14% decrease in the hydrogen concentration occurred in the commercial soda-lime silica glass after a 12 hour age in vacuum at 25 °C, while there was no decrease in hydrogen concentration after a one week age in air at 25 °C [83].

Pantano et al. investigated the Auger Electron Spectroscopy (AES) compositional profiles of mobile ions in the ion-milled surface of soda-lime silica glass after exposure to air [84]. At the surface there was an increase in the concentration of Na atoms and a decrease in Si atoms which resulted in a layer below the surface where there was a depletion of the Na concentration and an enrichment of the Si concentration [84]. The Na and Si concentrations returned to the bulk concentrations of the glass at a depth of approximately 50 nm from the surface [84]. The surface reaction was a Na-H ion exchange between H from the adsorbed water and Na at the surface and from the subsurface [84]. Thus, Na enrichment at the surface from formation of a hydroxide and the resulting reaction causes a Na depletion region which tends to retard further reaction [84].

In his text on glass science Doremus [86] comments that the reaction of silicate

glasses with the atmosphere is almost always caused by a reaction with water in the atmosphere. The unsatisfied Si-O- and Si- bonds at the surface of the glass react rapidly with the atmospheric water to form SiOH groups [86]. The thermal history of the glass, the humidity, and the surface treatment after heating and cooling influence the thickness and structural arrangement of the glass's hydrated surface layer [86]. Rosington in a review of the surface chemistry of glass also comments that the previous thermal history of a glass surface can greatly affect the adsorption of hydroxyl groups to the surface [85]. At ambient temperatures, Doremus states that water vapor ions exchange predominantly with the alkali ions in the glass

$$H_2O + SiOR^+ = SiOH + ROH$$

where R is an alkaline-earth ion such as Na^+ [86]. Ionic diffusion through the hydrated layer formed on the glass surface is much higher than in the dry glass which Doremus suggests may possibly be due to a weakened network through which ions can more easily diffuse [86].

4.4.2.1.4.3 Aging Environment of 100 % r.h.

For specimens aged in a water chamber, the annealing temperature significantly affected healing with Δc_{heal} decreasing over the entire temperature range of 525 to 575 °C (Figure 88). In contrast for specimens aged in 0 or 45 % r.h., Δc_{heal} was approximately constant for healing temperatures of 525, 538, 550, and 563 °C (Figure 87). The continuous decrease in Δc_{heal} with increasing temperature for 100 % r.h. aging is consistent with crack surface layers having a greater amount of incorporated

water since this would reduce the T_g causing structural rearrangements to begin to occur which would absorb energy required for material transport to fill the crack and would result in reducing crack healing. A similar decrease in crack healing with increasing temperature was observed for specimens aged in 0 and 45 % r.h. and thermally annealed at 575 °C (Figure 87).

4.4.2.1.5 Effects of Aging Environment and Time at 525 °C (Experiment 5)

Specimens prepared for testing as described in Section 3.6.2.2.1 were thermally annealed in sets of three for 60, 90, 120, 150, and 180 minutes at 525 °C (Table 44 and Figure 91). Each of the three samples in a set was aged in a different environment: 1) a desiccator with about 0 % r.h., 2) in laboratory air with about 45 % r.h., and 3) a water chamber with about 100 % r.h.. The healing behavior for aged specimens thermally annealed at 525 °C for 60 minutes was markedly different in Experiment 5 (Table 44 and Figure 91) than Experiment 4 (Table 43 and Figures 87 and 88). Δc_{heal} for specimens healed 60 minutes at 525 °C in Experiment 4 were 27.1, 32.3, and 39.7 μm for 0, 45, and 100 % r.h. (Table 43), respectively, while in Experiment 5 the Δc_{heal} values were 1.0, 14.7, and -0.2 μm for 0, 45, and 100 % r.h., respectively (Table 44). Two possible factors could have led to the different behavior of the 525 °C/60 minute samples in Experiment 5 and the lack of a clear time dependence: 1) 525 °C is the temperature at which healing begins which could lead to a large scatter in results, and/or 2) the stress relief cycle heating and cooling rate of 10 °C/minute is too fast for complete stress relief. To determine if the low thermal annealing temperature was the problem in Experiment 5, Experiment 6 tested samples

Table 44 Healed crack length change ($2c_{initial}$ - $2c_{heal}$) for glass specimens prepared with a stress relief cycle of 180 minutes at 587 °C (10 °C/ minute ramp rate), aged for 24 hours, and annealed at 525 °C in the small tube furnace (Experiment 5).

Aging Humidity	~0% r.h.		~45%		~100% r.h.	
Anneal Time	Mean (μm)	Standard Deviation (μm)	Mean (μm)	Standard Deviation (μm)	Mean (μm)	Standard Deviation (μm)
60	1.0	1.3	14.7	5.7	-0.2	3.1
90	12.1	1.8	16.8	1.9	16.1	7.2
120	2.1	2.0	8.3	2.4	13.8	2.0
150	13.5	3.4	19.2	1.7	9.5	9.0
180	-4.2	0.9	9.3	1.9	6.0	3.8

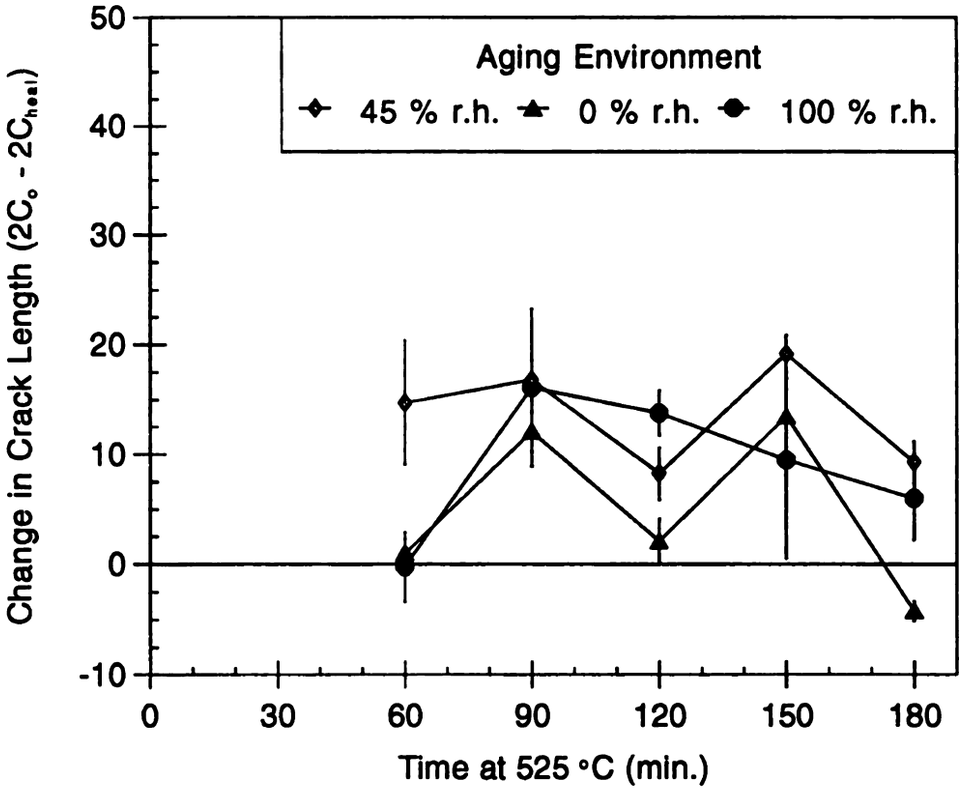

Figure 91 Mean crack length change ($2c_{initial}$ - $2c_{heal}$) versus healing time for glass specimens prepared with a stress relief cycle of 180 minutes at 587 °C (10 °C/ minute ramp rate), aged for 24 hours, and annealed at 525 °C in the small tube furnace (error bars indicate standard deviations of six cracks) (Experiment 5).

with the same stress relief cycle as in Experiment 5, but used a thermal annealing temperature of 575 °C.

4.4.2.1.6 Effects of Aging Environment and Time at 575 °C (Experiment 6)

Specimens prepared for testing as described in Section 3.6.2.2.1 were thermally annealed in sets of three for 60, 90, 120, and 150 minutes at 575 °C with each of the three samples in a set aged in a different environment: 1) a desiccator with about 0 % r.h., 2) in laboratory air with about 45 % r.h., and 3) a water chamber with about 100 % r.h. (Table 45 and Figure 92). While the Δc_{heal} value for the 100 % r.h. aged specimen healed for 60 minutes at 575 °C was essentially the same in Experiment 4 (39.7 µm, Table 43) and Experiment 6 (39.1 µm, Table 45), the Δc_{heal} values for the 0 and 45 % r.h. aged specimens were very different in Experiment 4 (27.1 and 32.3 µm, respectively, Table 43) and Experiment 5 (8.3 and 14.1 µm, respectively, Table 44). As in Experiment 5, no clear time dependent behavior for the 575 °C thermally annealed specimens was demonstrated in Experiment 6 (Figure 92).

4.4.2.1.7 Effects of Aging Environment and Time at 550 °C (Experiment 7)

Specimens prepared for testing with a 5 °C/minute stress relief cycle ramp rate as described in Section 3.6.2.2.1 were thermally annealed in sets of three for 60, 90, 120, 240, and 480 minutes at 550 °C with each of the three samples in a set aged in a different environment: 1) a desiccator with about 0 % r.h., 2) in laboratory air with about 45 % r.h., and 3) a water chamber with about 100 % r.h. (Table 44 and Figures 92 and 93). The healing in aged specimens thermally annealed at 550 °C for 60

Table 45 Healed crack length change ($2c_{initial}$ - $2c_{heal}$) for glass specimens prepared with a stress relief cycle of 180 minutes at 587 °C (10 °C/ minute ramp rate), aged for 24 hours, and annealed at 575 °C in the small tube furnace (Experiment 6).

Aging Humidity	~0% r.h.		~45%		~100% r.h.	
Anneal Time	Mean (μm)	Standard Deviation (μm)	Mean (μm)	Standard Deviation (μm)	Mean (μm)	Standard Deviation (μm)
60	8.3	2.0	14.1	2.0	39.1	9.5
90	8.3	1.2	11.9	1.9	6.5	6.4
120	2.7	2.1	4.0	1.7	6.1	2.6
150	2.8	1.0	18.7	2.4	25.7	6.0

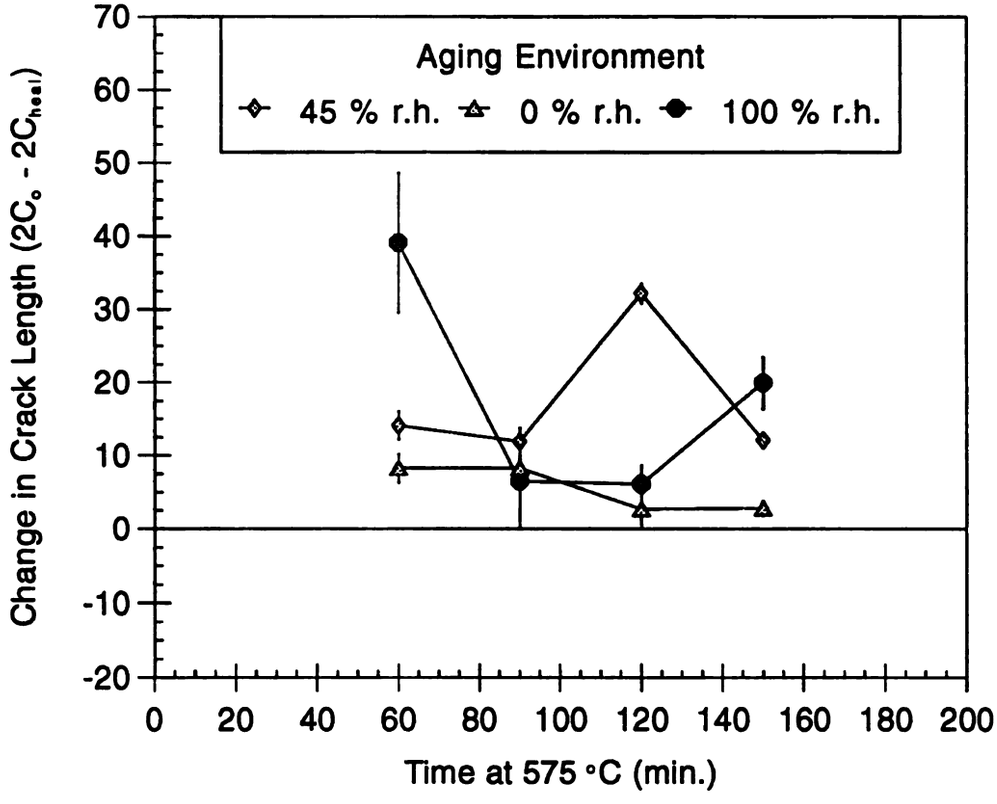

Figure 92 Mean crack length change ($2c_{initial}$ - $2c_{heal}$) versus healing time for glass specimens prepared with a stress relief cycle of 180 minutes at 587 °C (10 °C/ minute ramp rate), aged for 24 hours, and annealed at 575 °C in the small tube furnace (error bars indicate standard deviations of six cracks) (Experiment 6).

Table 46 Healed crack length change ($2c_{initial}$ - $2c_{heal}$) for glass specimens prepared with a stress relief cycle of 180 minutes at 587 °C (5 °C/ minute ramp rate), aged for 24 hours, and annealed at 550 °C in the large tube furnace (Experiment 7).

Aging Humidity		~0% r.h.		~45%		~100% r.h.	
Anneal		Mean (μm)	Standard Deviation (μm)	Mean (μm)	Standard Deviation (μm)	Mean (μm)	Standard Deviation (μm)
Time	Ramp Rate (°C / min.)						
60	5	35.3	3.8	46.7	2.5	56.2	9.3
60	5 & 2.5	33.0	1.1	43.2	2.9	37.8	4.6
90	5 & 2.5	36.8	1.5	49.1	5.7	55.2	3.7
120	5 & 2.5	34.9	1.9	40.7	3.2	44.6	5.6
240	5 & 2.5	50.3	3.3	69.9	4.3	66.7	6.6
480	5 & 2.5	41.5	2.3	63.5	5.4	52.6	4.0

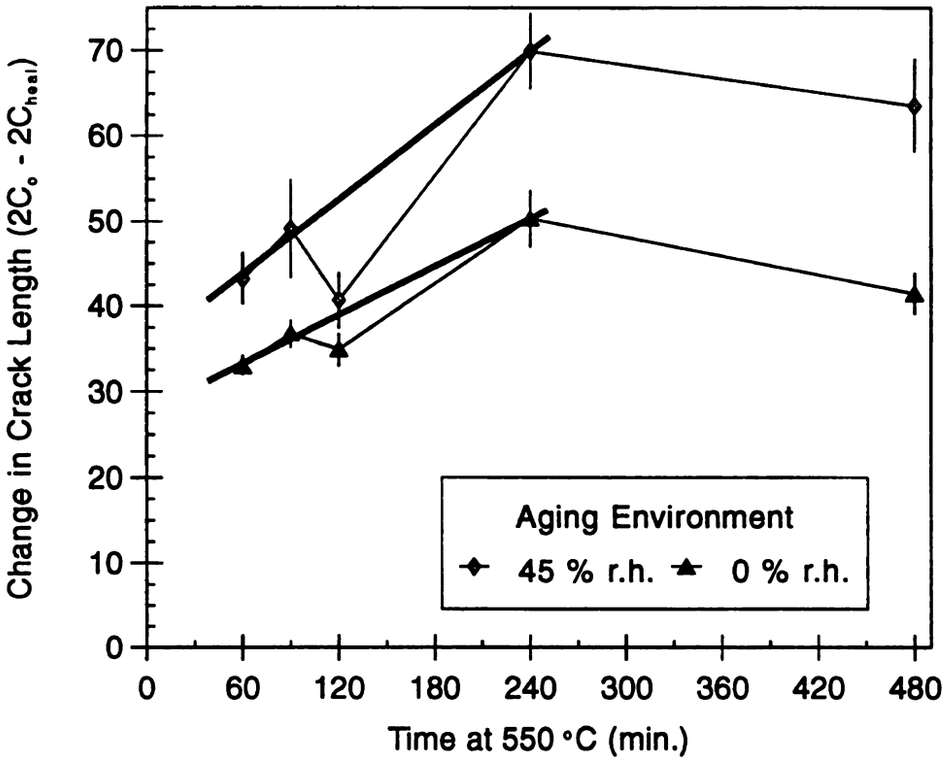

Figure 93 Mean crack length change ($2c_{initial}$ - $2c_{heal}$) versus healing time for glass specimens prepared with a stress relief cycle of 180 minutes at 587 °C (5 °C/ minute ramp rate), aged for 24 hours, and annealed at 550 °C in the large tube furnace (error bars indicate standard deviations of six cracks) (Experiment 7).

minutes was slightly higher in Experiment 7 (Table 46 and Figures 93 and 94) than Experiment 4 (Table 43 and Figures 87 and 88). The Δc_{heal} values in Experiment 4 were 23.6, 35.0, and 31.4 μm for specimens aged at 0, 45, and 100 % r.h. (Table 43), respectively, while in Experiment 7 the Δc_{heal} values were 33.0, 43.2, and 37.8 μm for specimens aged at 0, 45, and 100 % r.h., respectively (Table 46).

The higher values for Δc_{heal} in Experiment 7 compared to Experiment 4 were likely due to the use of different furnaces for thermal annealing in the two experiments. The large tube furnace of Experiment 7 has a larger temperature overshoot than the 1 or 2 °C overshoot of the small tube furnace of Experiment 4 which leads to a significantly larger maximum temperature (Table 47). To reduce the large 17 °C overshoot from the 5 °C/minute heating rate (Table 47) a second ramp rate of 2.5 °C/minute was used once the temperature reached 70% of the set temperature (in Kelvin). The lower heating rate reduced the temperature overshoot to only 6 °C (Table 47 and Figure 95).

For samples aged in air and thermally annealed for 60 minutes in Experiment 7, Δc_{heal} was about 10 μm greater than Δc_{heal} for specimens aged in a desiccator (Table 46 and Figure 93). Similar behavior was observed in Experiment 4 (Table 43, Figure 87). The difference in Δc_{heal} between samples aged in air and in a desiccator increased with thermal annealing time in Experiment 7 from about 10 microns at 60 minutes to about 22 microns after 480 minutes (Table 46 and Figure 93). For samples aged in air and samples aged in a desiccator, the Δc_{heal} increased with healing time for times of 60, 90 and 240 minutes and remained constant or decreased slightly at 480 minutes (Table 46 and Figure 93). The specimens healed for 120 minutes did not display an

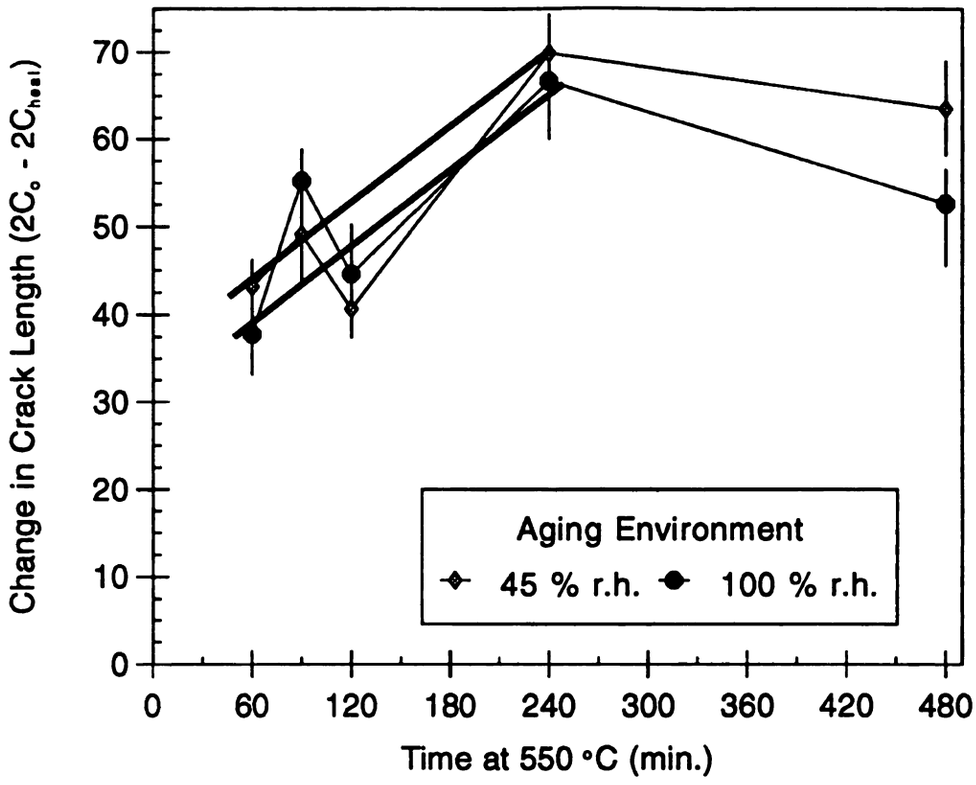

Figure 94 Mean crack length change ($2c_{initial}$ - $2c_{heal}$) versus healing time for glass specimens prepared with a stress relief cycle of 180 minutes at 587 °C (5 °C/ minute ramp rate), aged for 24 hours, and annealed at 550 °C in the large tube furnace (error bars indicate standard deviations of six cracks) (Experiment 7).

Table 47 Holding and maximum specimen temperature for glass specimens prepared with a stress relief cycle of 180 minutes at 587 °C (5 °C/ minute ramp rate), aged for 24 hours, and annealed at 550 °C in the large tube furnace (Experiment 7).

Time at T_{hold}	Ramp Rate (°C / min.)	Maximum Temperature, T_{max} (°C)	Holding Temperature, T_{hold} (°C)
60	5	570	553
60	5 & 2.5	559	553
90	5 & 2.5	555	549
120	5 & 2.5	555	547
240	5 & 2.5	557	547
480	5 & 2.5	557	549

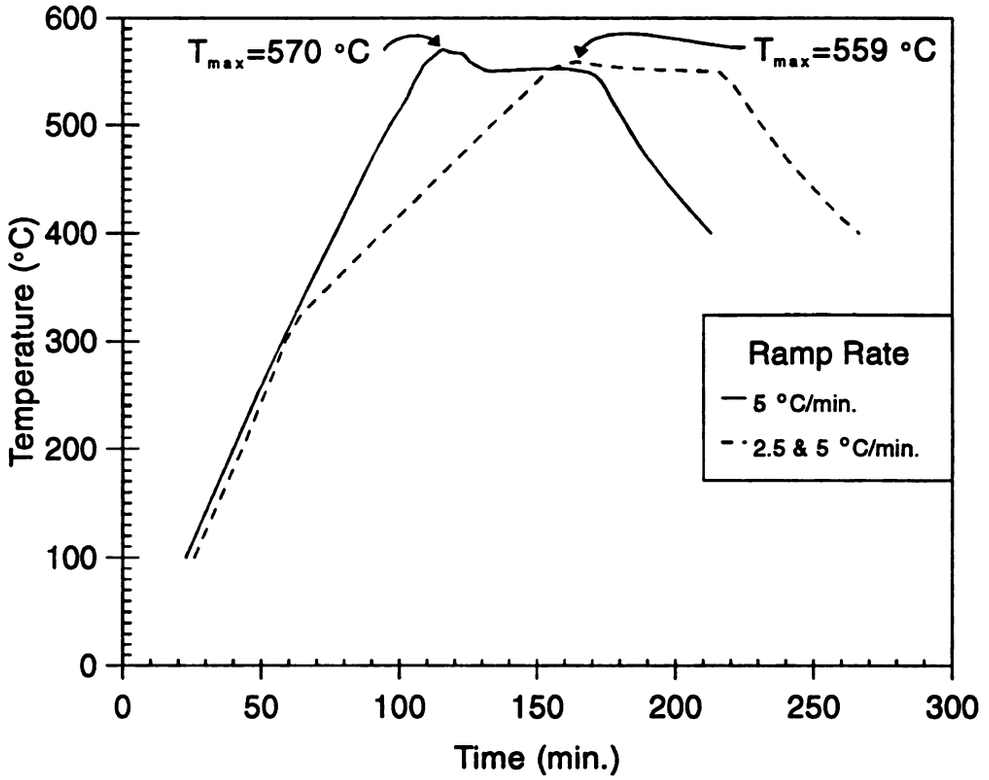

Figure 95 Temperature profile of two different thermal annealing ramp rates for glass specimens annealed for 60 minutes in the large tube furnace (Experiment 7).

increase Δc_{heal} compared to Δc_{heal} for the 90 minute specimen (Table 46 and Figure 93). Additional testing would be required to determine if a different behavior occurs for samples thermally annealed for times between 90 and 240 minutes or if the 120 minute sample run was an anomaly.

The specimens aged in a water chamber displayed thermal healing behavior similar to specimens aged in air with Δc_{heal} values which were within a standard deviation of each other for healing times between 60 and 480 minutes (Table 46 and Figure 94). In Experiment 4, the Δc_{heal} values for the specimens aged in air and in a water chamber and thermally annealed at 550 °C for 60 minutes were also within a standard deviation of each other (Table 43).

4.4.2.1.8 Residual Stress Relief Cycle Testing

Since the residual surface stresses created during machining can change the crack healing observed, the crack lengths of the indents made before and after different heating cycles were used to evaluate the residual surface stress in machined glass samples and the optimum heating conditions required to relieve the stress as described in Section 3.6.2.2.6. Eleven aged indents were measured before the samples underwent time-temperature heating cycles (Table 48). Within 23.5 to 24.5 hours after the specimens underwent a heating cycle, eleven new indents were made in the specimens, aged, and measured (Table 48).

Table 48 Pre-heat-treatment ($2C_R$) and post-heat-treatment ($2C_A$) mean and standard deviation of 22 indent crack lengths in glass specimens along with calculated residual stress relieved during small tube furnace heating cycles at different temperatures and times.

Pre-heat-treatment Mean and Standard Deviation $2C_R$ (μm)	Heat Treatment Cycle:		Post-heat-treatment Mean and Standard Deviation $2C_A$ (μm)	Stress Change $\Delta\sigma$ (MPa)
	Number	Time at Temperature (Minutes @ °C)		
202.5 ± 6.3	1	45 @ 550	214.9 ± 5.1	6.17
199.9 ± 6.6	2 ††	60 @ 600	214.3 ± 4.3	7.31
202.8 ± 6.9	3	~60* @ ~ 450* 60 @ 625	219.1 ± 3.4	8.10
200.6 ± 7.2	4 ††	60 @ 625	214.5 ± 4.6	7.02
205.5 ± 5.9	5 ††	60 @ 650	208.3 ± 4.3	1.35
203.8 ± 5.8	6 †	185 @ 587	216.1 ± 6.6	6.09
204.1 ± 7.1	7	60 @ 425 180 @ 587	212.3 ± 2.8	4.01
202.7 ± 6.8	ALL	ALL	214.3 ± 5.6	5.70

* Furnace was inadvertently unplugged on heating; after about an hour the furnace was turned back on and heating was continued to 625 °C.

† Two samples which had been stacked on top of each other before the heat treatment cycle were **not** bonded together after the heating cycle.

†† Two samples which had been stacked on top of each other before the heat treatment cycle were bonded together after the heating cycle.

4.4.2.1.8.1 Bulk Viscous Flow of Glass During Heating Cycle

For heat treatment cycles 2, 4, 5, and 6 (Table 48), two 75 mm X 75 mm X 1 mm (0.3 in. X 0.3 in. X 0.045 in.) glass squares were stacked upon each other and placed in the furnace next to the glass specimen being heat treated to relieve stress. Whether the two squares bonded together or not during the heat treatment cycle is indicated in Table 48. Bonding was not observed at 587 °C, but was observed at 600, 625, and 650 °C, indicating that viscous flow begins to occur at temperatures between 587 and 600 °C. Since viscous flow during heat treatment could lead to distorted surfaces, stress relief cycle temperatures of 587 °C and below were used to avoid surface irregularities.

The study of crack healing in glass by mechanisms other than viscous flow was one aim of Section 4.4.2.1. and thus annealing temperatures of 587 °C and below were used to investigate the healing behavior of glass. Since bonding was not observed below 587 °C (Table 48), bulk viscous flow should not have occurred during healing at temperatures of 575 °C or less (Sections 4.4.2.1). Although bulk viscous flow should not have occurred in the samples, viscous flow along the crack surfaces due to water absorption during aging may have occurred.

4.4.2.1.8.2 Residual Stress Relieved During Heating Cycle

The change in residual stress in each sample in Table 48 was calculated from the pre-heat-treatment mean crack lengths and the post-heat-treatment mean crack lengths (Table 48). Marshall and Lawn [87] describe a method for determining the residual stress relieved during heat treatment using indentation crack lengths made before and

after heat treatment. For two sets of indent cracks created at the same indentor load, the change in stress, $\Delta\sigma_R$, due to thermal heat treatment is described by [87]

$$\Delta\sigma_R = \frac{K_c}{\sqrt{4/\pi}}\left[C_R\right]^{-\frac{1}{2}}\left[\left(\frac{C_A}{C_R}\right)^{\frac{3}{2}} - 1\right] \qquad (22)$$

where K_c is the fracture toughness, C_R is the pre-heat-treatment half indent crack length, and C_A is the post-heat-treatment half indent crack length. For soda-lime-silica glass, the fracture toughness is about 0.75 $MN/m^{1.5}$ [88] and substituting this value into Equation 22 resulted in the following equation

$$\Delta\sigma_R = 0.665\,\frac{MN}{m^{1.5}}\left[C_R\right]^{-\frac{1}{2}}\left[\left(\frac{C_A}{C_R}\right)^{\frac{3}{2}} - 1\right]. \qquad (23)$$

Equation 23 was used to calculate the change in residual stress in each sample using the pre-heat-treatment mean crack lengths and the post-heat-treatment mean crack lengths (Table 48). According to the $\Delta\sigma_R$ values calculated from Equation 23, residual stress ranging from 1.35 to 8.10 MPa was relieved during heat treatment (Table 48).

To get a qualitative view of the effect of heat treatments on the residual stress relief, the pre- and post- heat-treatment mean crack lengths (Table 48) were plotted as a function of the heat treatment cycle number (Table 48) in Figure 96, where each data point represented the mean of 22 indent cracks and the vertical bars represent the standard deviations from the mean. Horizontal lines represent the mean pre- and post-heat-treated crack lengths for all seven heat treatment cycles (Figure 96). The pre-heat-treated crack lengths for each specimen was within one standard deviation of the

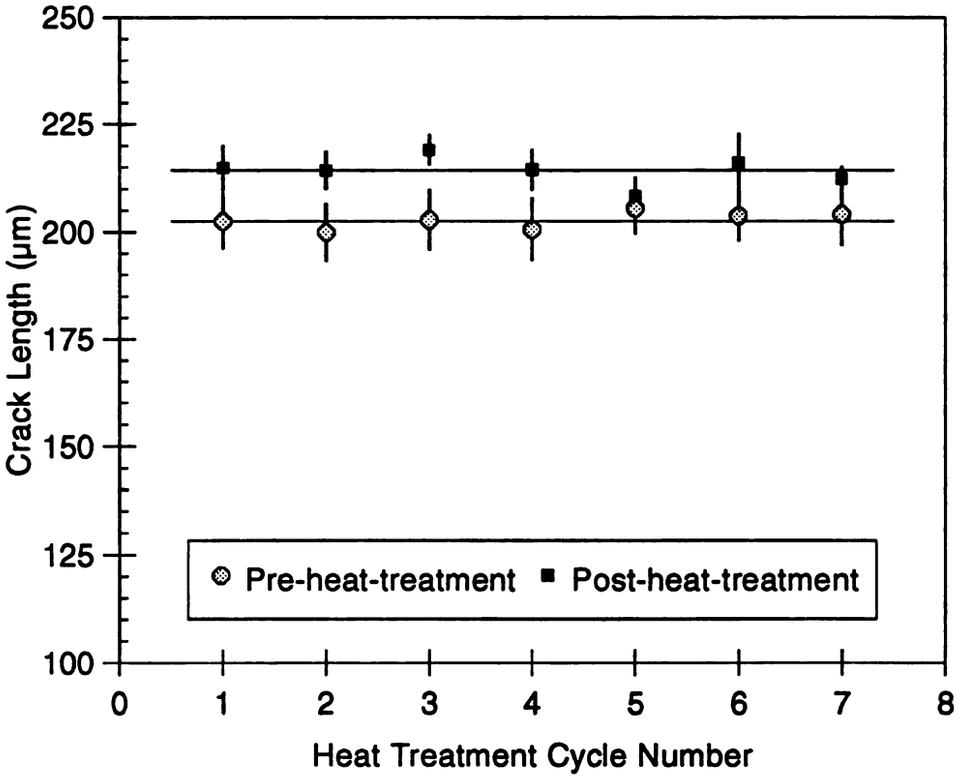

Figure 96 Pre- and post-heat-treatment mean of 22 indent crack lengths of glass specimens heat treated in different cycles as indicated in Table 48 (data points indicate means, vertical bars indicate standard deviations from mean, and horizontal lines indicates means for all seven cycles together).

group mean for all the samples tested. For the post-heat-treated crack lengths of the specimens, the specimens thermally heated in cycle 3 and 5 appear to be greater than one standard deviation from the group mean for all samples tested.

4.4.2.1.8.3 Statistical Analysis of Heat Treatment Cycles

The pre- and post- heat-treatment group means were compared statistically using a two-tailed *t*-test. To test if the two random and independent population means, μ_1 and μ_2, were equal (or if $\mu_2 - \mu_1 = 0$), the population was assumed to be normal or approximately normal and the population sizes, n_1 and n_2, were large ($n_1 = n_2 = 152$). The decision alternatives were

$$H_o: \mu_2 = \mu_1 \quad (or\ \mu_2 - \mu_1 = 0)$$
$$H_1: \mu_2 \neq \mu_1 \quad (or\ \mu_2 - \mu_1 \neq 0) \quad .$$

The test statistic, t^*, followed the *t* distribution with $n_1 + n_2 - 2$ degrees of freedom and was determined by the following equation [89]

$$t^* = \frac{\mu_2 - \mu_1}{s(\mu_2 - \mu_1)} \tag{24}$$

where

$$s(\mu_2 - \mu_1) = \sqrt{\frac{s_2^2}{n_2} + \frac{s_1^2}{n_1}} \tag{25}$$

and where s_2 and s_1 were the standard deviations of population 2 and 1, respectively.

The value for the *t* distribution was determined from a table [89] by the degrees of freedom, n, and the α risk. The α risk was the risk of incorrectly concluding that the hypothesis H_o was true. The α risk used was 0.01. The decision rules were:

$$\textit{If } |t^*| \leq t(1 - \alpha/2; n), \textit{ conclude } H_o: \mu_2 = \mu_1$$
$$\textit{If } |t^*| > t(1 - \alpha/2; n), \textit{ conclude } H_1: \mu_2 \neq \mu_1 \quad .$$

The test statistic for the pre- and post- heat-treatment group means was calculated using Equation 24 and the data in Table 49 to be $t^* = 16.24$. With n = 152 + 152 - 2 = 302, the value for t (1 - α/2; n) was 2.592. Since $t^* > t$ (1 - α/2; n), the conclusion reached was that the pre- and post- heat-treated group means were not equivalent. The statistically significant increase in mean crack length for specimens indented after heat treatment indicates significant residual stress was relieved during heat treatment.

Heat treatment cycles 3 and 5 had a post-heat-treatment specimen mean which were statistically different from the post-heat-treatment group mean (Table 49), while all of the pre-heat-treatment specimen means were statistically the same as the pre-heat-treatment group mean, indicating that these heat treatment cycles were no better or worse at removing residual stress than the other cycles. The post-heat-treatment mean for heat treatment cycle 5 was statistically lower than the other heat treatment cycles indicating that heat treatment at 650 °C would not be desirable to remove residual stress.

The significantly higher sample post-heat-treatment mean for heat treatment cycle 3 was unexpected because the furnace was inadvertently unplugged on heating

Table 49 Calculated t^* values for glass specimens using Equation 24 with data from Table 48. Hypothesis decisions for comparison of individual glass heat treatment cycle specimen means with the overall pre- and post- heat-treatment group means using $\alpha = 0.01$, n = 172, and $t\ (1-\alpha/2;\ n) = 2.609$.

Pre-heat-treatment		Heat Treatment Cycle Number:	Post-heat-treatment	
Test Statistic t^*	Same mean as group mean for α risk = 0.05		Test Statistic t^*	Same mean as group mean for α risk = 0.05
-0.138	Yes	1	0.509	Yes
-1.853	Yes	2	0.000	Yes
0.064	Yes	3	5.611	No
-1.287	Yes	4	1.110	Yes
2.039	Yes	5	-5.864	No
0.812	Yes	6	1.217	Yes
0.869	Yes	7	-2.586	Yes

and after about an hour the furnace was turned back on to continue heating to 625 °C. Two additional heat treatment cycles were investigated to determine whether the increased post-heat-treatment crack lengths resulted from the hold at 425 °C or from heat treatment at 625 °C. For heat treatment cycle 4 (625 °C for 60 minutes), a significant increase in specimen mean was not observed. To determine if holding at a temperature around 425 or 450 °C resulted in the increased specimen mean, the temperature for heat treatment cycle 7 was temporarily held at 425 °C for 60 minutes before the temperature was increased and held at 625 °C, as in heat treatment cycle 6. Heat treatment cycle 7 did not have a statistically higher specimen mean (Table 49) indicating that the 425 °C hold was not responsible for the statistically higher mean in heat treatment cycle 3.

The heat treatment cycles which were most effective in relieving residual stress in glass specimens (as represented by the largest mean crack length) had maximum heat treatment temperatures below 650 °C and were heated continuously up to the maximum heat treatment temperature (Table 49). Consequently, glass specimens which were heat treated for other experiments as a part of the current investigation were heat treated at a maximum holding temperature of less than 600 °C and were continuously heated to the maximum hold temperature.

4.4.2.1.8.4 Analysis of a 4 Month Age after Heat Treatment Cycle

For specimens aged in laboratory air for 4 months **before** post-heat-treatment indentation testing was performed (Table 50), the post-heat-treatment mean crack lengths were significantly larger than the group post-heat-treatment mean crack lengths

of Table 48 indicating that a significantly larger amount of residual stress was relieved compared to the heat-treatment cycles in Table 48 (Table 51). To check if the four month age was responsible for the increased stress relief or if it was the heat treatment at 525 °C, another specimen with identical heat treatment was tested after a 24 hour age. The specimen aged for 24 hours after heat treatment at 525 °C for 60 minutes had post-heat-treatment mean crack lengths which were significantly larger than the group post-heat-treatment mean crack length of Table 48 (Table 51). The data from Tables 50 and 51 indicate that for future glass sample preparation, the best heat treatment for residual stress relief would be at 525 °C for 60 minutes or at 425 °C for 180 minutes.

4.4.2.1.8.5 Analysis of Stress Relief Cycles A-E of Experiments 3-7

The post-Stress-Relief-Cycle mean and standard deviation crack lengths were calculated for the Stress Relief Cycles A-E used in Experiments 3-7 (Table 52). The residual stress relieved in Cycles A and B is much larger than the residual stress relieved in Cycles C, D, and E (Table 52). However, comparison of the mean crack lengths for Stress Relief Cycles C, D, and E to the specimens which did not have a stress relief cycle demonstrates that Cycles C, D, and E did relieve some residual stress.

4.4.2.2 Polycrystalline Alumina

Two different experiments with a total of 72 specimens and 540 cracks were used to investigate healing in polycrystalline alumina. Healing in two different types of

Table 50 Mean and standard deviation for pre-heat-treatment ($2C_R$) and post-heat-treatment ($2C_A$) crack lengths in glass specimens. The specimens were heat treated and then aged for either 4 months or 24 hours before post-heat-treatment indentation.

Pre-heat-treatment Mean and Standard Deviation $2C_R$ (μm)	Heat Treatment Cycle:		Time After Heat Treatment Cycle and Before Indenting for Post-heat-treatment Testing	Post-heat-treatment Mean and Standard Deviation $2C_A$ (μm)
	Number	Time at Temperature (Minutes @ °C)		
197.1 ± 6.9	8	180 @ 425	4 Months	222.0 ± 2.2
197.6 ± 9.0	9	60 @ 525	4 Months	221.1 ± 6.7
206.8 ± 8.1	10	60 @ 525	24 Hours	223.1 ± 8.2

Table 51 Calculated t^* values for glass specimens aged for either 24 hours or 4 months using Equation 24 and Table 50 data. Hypothesis decisions for comparison of individual heat treatment cycle means with the overall pre-heat-treatment and post-heat-treatment group means from Table 48 using $\alpha = 0.01$, n = 172, and $t\ (1\text{-}\alpha/2;\ n) = 2.609$.

Pre-heat-treatment		Heat Treatment Cycle Number:	Post-heat-treatment	
Test Statistic t^*	Same mean as Table 48 group mean for α risk = 0.05		Test Statistic t^*	Same mean as Table 48 group mean for α risk = 0.05
-3.564	No	8	11.79	No
-2.554	No	9	4.54	No
2.262	No	10	4.87	No

Table 52 Mean and standard deviation for post-Stress-Relief-Cycle ($2C_A$) crack lengths in glass specimens with Stress Relief Cycles A-E which were tested in Experiments 3-7.

Stress Relief Cycle (Described in Section 3.6.2.2.2)	Number of Cracks Measured	Post-Stress-Relief-Cycle Mean and Standard Deviation $2C_A$ (μm)		
		45 % r.h. age	0 % r.h. age	100 % r.h. age
A	72	221.3 ± 5.5	*	*
B	54	219.2 ± 5.2	*	*
C	30	208.1 ± 5.2	186.8 ± 5.8	230.3 ± 9.0
D	54	210.2 ± 5.5	187.1 ± 6.0	232.1 ± 8.4
E	36	210.0 ± 7.1	185.9 ± 5.3	228.6 ± 12.1
None	54	201.8 ± 7.4	*	*

* Specimens not tested in this aging environment.

alumina was investigated as a function of time, temperature, and crack aging environment.

4.4.2.2.1 Effects of Aging Humidity and Temperature in Two Aluminas (Experiment 1)

Coors and microwave sintered alumina specimens were prepared as described in Section 3.6.2.3.2 with three indents aged for an initial 24 hour cycle in 45 % r.h. followed by a second 24 hour cycle in 0, 45, or 100 % r.h., and three other indents on the same specimen were aged for only a single 24 hour cycle in 0, 45, or 100 % r.h.. The crack lengths were measured optically from crack tip to crack tip before and after the thermal annealing cycle. Samples were annealed for 60 minutes at 1005, 1237, or 1469 °C with a single heating rate (Figure 97) or with two heating rates (Figure 98). Healing temperatures were measured via an R-Type thermocouple placed next to the specimens in the furnace. The mean and standard deviation of the change in crack lengths, Δc_{heal}, (where $\Delta c_{heal} = 2c_{heal} - 2c_{initial}$) was calculated for all specimens (Table 53 and 54).

The first three sets of alumina samples tested were thermally annealed with a single heating rate of 10 °C/minute (Table 53 and 54) and had a large temperature overshoot of up to 46 °C (Figure 97). Consequently, the remaining six sets of samples (Table 53 and 54) were annealed with an initial ramp rate of 10 °C/minute followed by a reduced ramp rate of 2.5 °C/minute after the sample had increased to 84% of the set temperature (in units of K). The dual ramp rate significantly reduced the temperature overshoot by 20 to 30 °C (Figure 98, Tables 53 and 54).

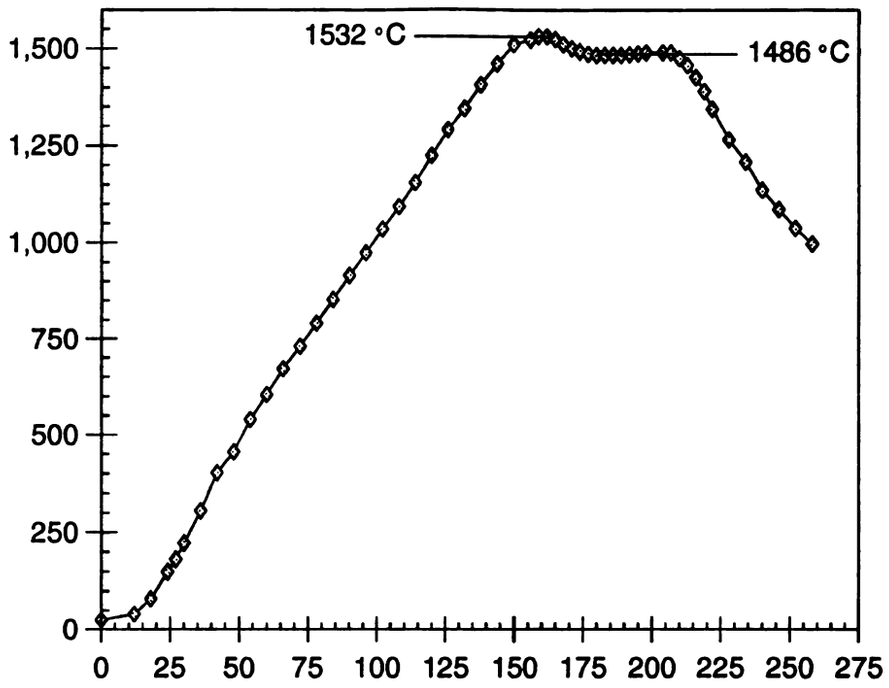

Figure 97 Plot of the Coors and microwave alumina samples' temperature as a function of time for a ramp rate of 10 °C per minute up to the hold temperature of 1469 °C (Experiment 1).

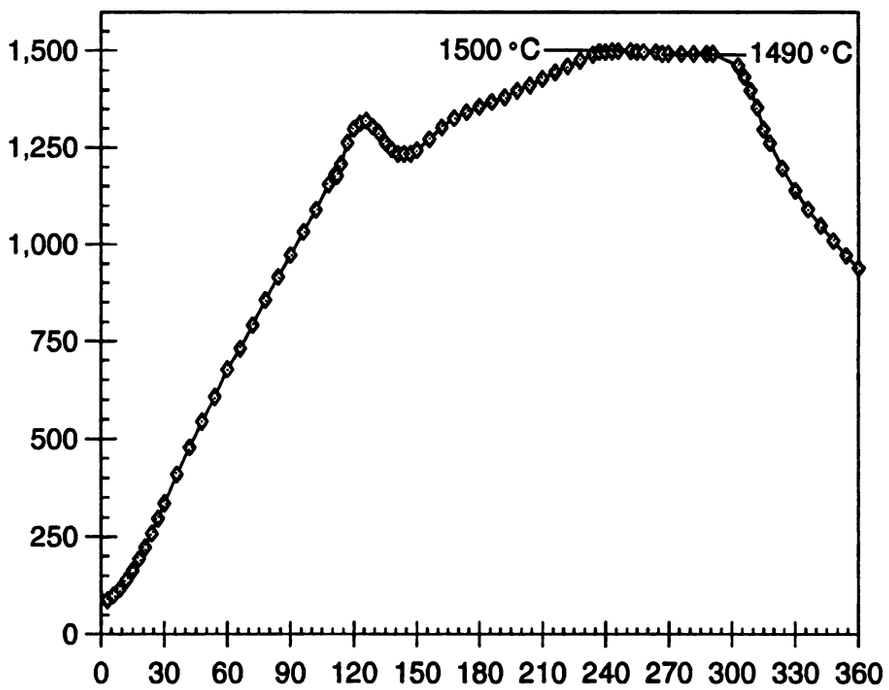

Figure 98 Plot of the Coors and microwave alumina samples' temperature as a function of time for a ramp rate of 10 °C per minute up to 1175 °C followed by a ramp rate of 2.5 °C per minute up to the hold temperature of 1469 °C (Experiment 1).

Table 53 Mean and standard deviation of the healed crack length change ($2c_{initial}$ - $2c_{heal}$) after 60 minutes at healing temperature for Coors alumina specimens with indents aged for a single 24 hour period in an environment of 0, 45, or 100 % r.h. and indents aged for 24 hours in 45 % r.h. before a second 24 hour age in an environment of 0, 45, or 100 % r.h.. Temperature was measured via an R-Type thermocouple placed in the furnace next to the specimens.

Environment of Single Age and of Second Cycle in Double Age	Experimental Measurements	Nominal Healing Temperature (°C)		
		1005	1237	1469
0 % r.h.	Holding Temperature (°C)	1007**	1245**	1469**
	Maximum Temperature (°C)	1015**	1252**	1483**
	Healing of Cracks with a Single Age (μm)	23.0±4.8	63.9±29.4	126.5±16.5
	Healing of Cracks with a Double Age (μm)	16.8±8.1	49.5±21.8	127.0±27.4
45 % r.h.	Holding Temperature (°C)	1005*	1205*	1486*
	Maximum Temperature (°C)	1034*	1236*	1532*
	Healing of Cracks with a Single Age (μm)	19.5±13.0	50.6±8.0	169.7±23.7
	Healing of Cracks with a Double Age (μm)	23.3±6.9	71.2±12.2	130.2±22.1
100 % r.h.	Holding Temperature (°C)	1000**	1130**	1490**
	Maximum Temperature (°C)	1011**	1159**	1500**
	Healing of Cracks with a Single Age (μm)	20.0±9.7	24.1±16.1	114.4±10.6
	Healing of Cracks with a Double Age (μm)	21.3±19.9	31.7±13.3	113.3±16.0

* Heating rate was 10 °C/minute to set temperature.

** Heating rate initially 10 °C/minute up to 84% of set temperature (in units of K) and then 2.5 °C/minute to set temperature.

Table 54 Mean and standard deviation of the healed crack length change ($2c_{initial}$ - $2c_{heal}$) after 60 minutes at healing temperature for microwave sintered alumina with indents aged for a single 24 hour period in an environment of 0, 45, or 100 % r.h. and indents aged for 24 hours in 45 % r.h. before a second 24 hour age in an environment of 0, 45, or 100 % r.h.. Temperature was measured via an R-Type thermocouple placed in the furnace next to the specimens.

Environment of Single Age and of Second Cycle in Double Age	Experimental Measurements	Nominal Healing Temperature (°C)		
		1005	1237	1469
0 % r.h.	Holding Temperature (°C)	1007**	1245**	1469**
	Maximum Temperature (°C)	1015**	1252**	1483**
	Healing of Cracks with a Single Age (μm)	15.4±6.9	36.6±33.6	35.7±11.5
	Healing of Cracks with a Double Age (μm)	37.5±17.7	54.4±19.1	35.5±24.0
45 % r.h.	Holding Temperature (°C)	1005*	1205*	1469*
	Maximum Temperature (°C)	1034*	1236*	1483*
	Healing of Cracks with a Single Age (μm)	27.1±28.5	30.8±27.6	78.0±26.2
	Healing of Cracks with a Double Age (μm)	5.4±7.7	32.4±19.4	5.8±28.0
100 % r.h.	Holding Temperature (°C)	1000**	1130**	1490**
	Maximum Temperature (°C)	1011**	1159**	1500**
	Healing of Cracks with a Single Age (μm)	38.1±25.3	44.4±39.5	60.0±13.9
	Healing of Cracks with a Double Age (μm)	25.3±24.8	28.1±27.3	104.1±35.6

* Heating rate was 10 °C/minute to set temperature.

** Heating rate initially 10 °C/minute up to 84% of set temperature (in units of K) and then 2.5 °C/minute to set temperature.

4.4.2.2.1.1 Healing in Coors Alumina (Experiment 1)

For Coors alumina, the crack length change after annealing (Δc_{heal}) increased linearly with increasing healing temperature (Figure 99), and was characterized by a single best fit line with positive slope regardless of the indent crack aging conditions (Figure 99). For Coors alumina, Δc_{heal} was about 17 μm at 1000 °C and about 130 μm at 1500 °C (Figure 99).

Aging for a single cycle at 0% r.h. or for two cycles (with the first cycle at 45% r.h. and the second at 0% r.h.) did not appear to change the healing behavior (Figure 100) indicates that the humidity during aging does not affect crack healing, or that the effect of humidity during aging is small enough to be within the experimental error of crack length measurement. The specimens which underwent a single aging cycle in either 0, 45, or 100 % r.h. behaved identically at the lowest annealing temperature of 1005 °C (Figure 101). At 1469 °C the specimen healed at 45 % r.h. had a significantly larger Δc_{heal} (Figure 101) than the specimens aged at 0 or 100 % r.h. which had similar Δc_{heal} values. Thus at 1005 °C, aging does not affect healing, while Δc_{heal} is affected for anneals at 1469 °C (Figure 101). The differing results for the environmental consequences on Δc_{heal} may be related to the experimental protocol of measuring the crack length after 30 minutes of aging, which may expose the newly formed cracks to air for the (approximately) 20 minutes needed to measure the cracks. The exposure could lead to adsorption of water vapor from the air which is not desorbed during the subsequent 23.5 hours of aging in 0% r.h.. To aid in determining the effect of the aging environment, the experimental procedure in Experiment 2 was adjusted as follows: 1) the specimens were immediately placed in their respective

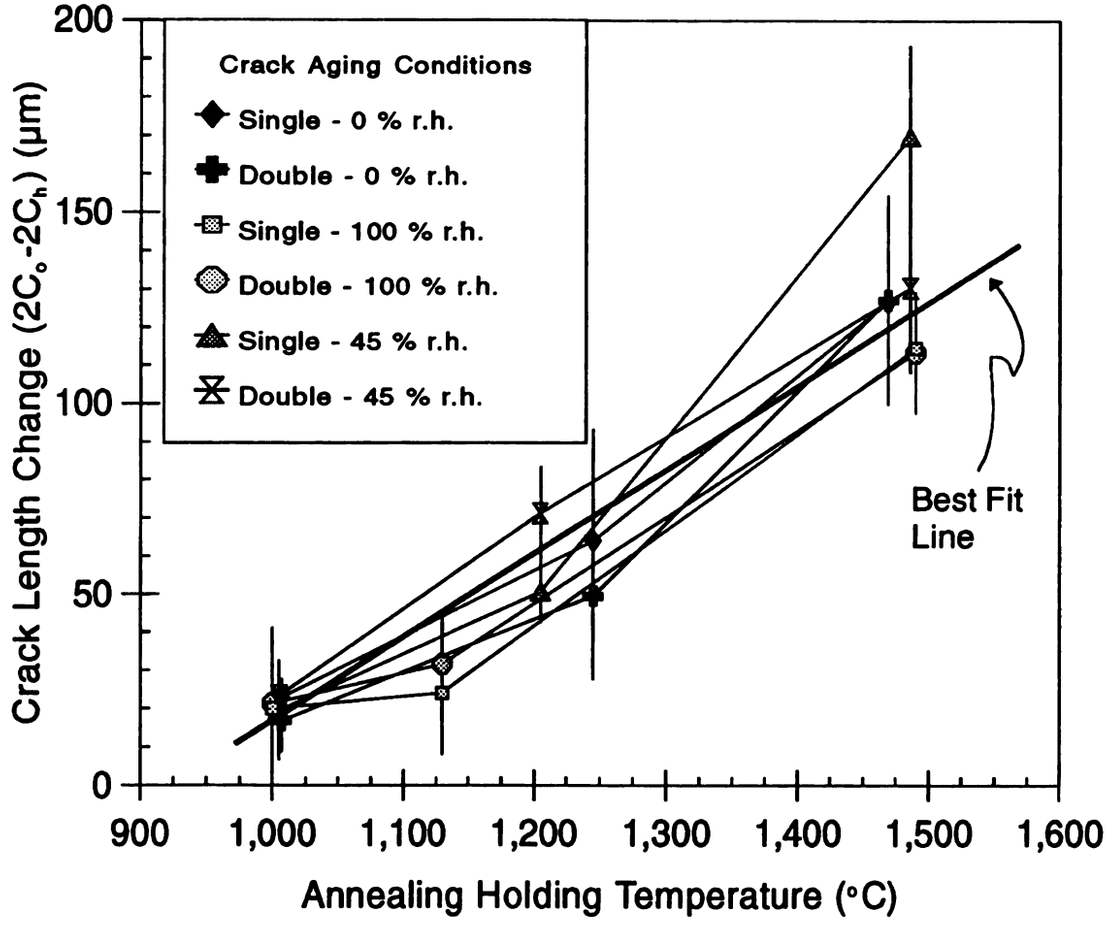

Figure 99 Mean crack length change ($2c_{initial}$ - $2c_{heal}$) versus healing temperature for Coors alumina specimens annealed for 60 minutes in the large tube furnace (error bars indicate standard deviations of six cracks). Before annealing, indent cracks underwent a single age of 24 hours in 0, 45, or 100 % r.h. or a double age with an initial 24 hour age in 45 % r.h. followed by a 24 hour age in 0, 45, or 100 % r.h. (Experiment 1).

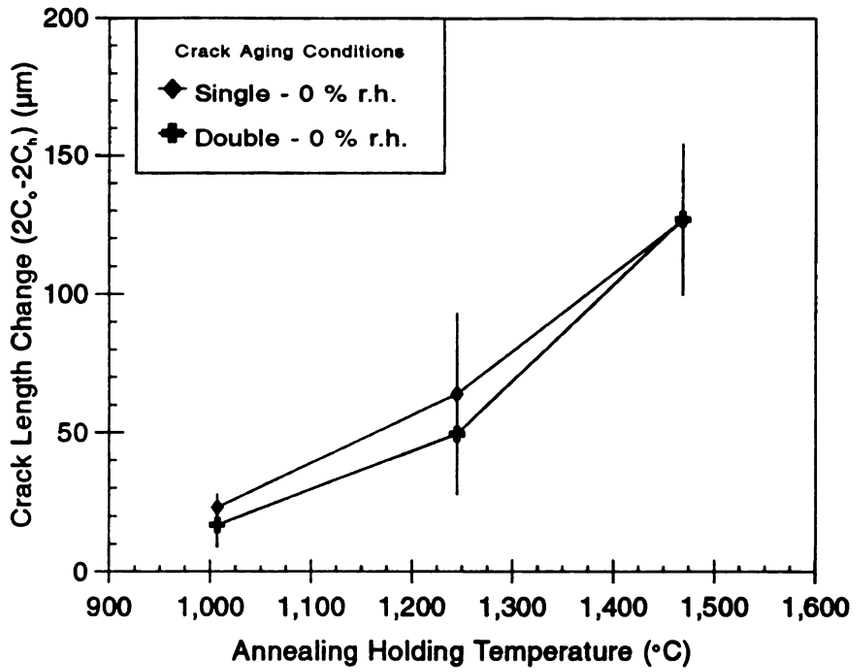

Figure 100 Mean crack length change ($2c_{initial}$ - $2c_{heal}$) versus healing temperature for Coors alumina specimens annealed for 60 minutes in the large tube furnace (error bars indicate standard deviations of six cracks). Before annealing, indent cracks underwent a single age of 24 hours in 0 % r.h. or a double age with an initial 24 hour age in air followed by a 24 hour age in 0 % r.h. (Experiment 1).

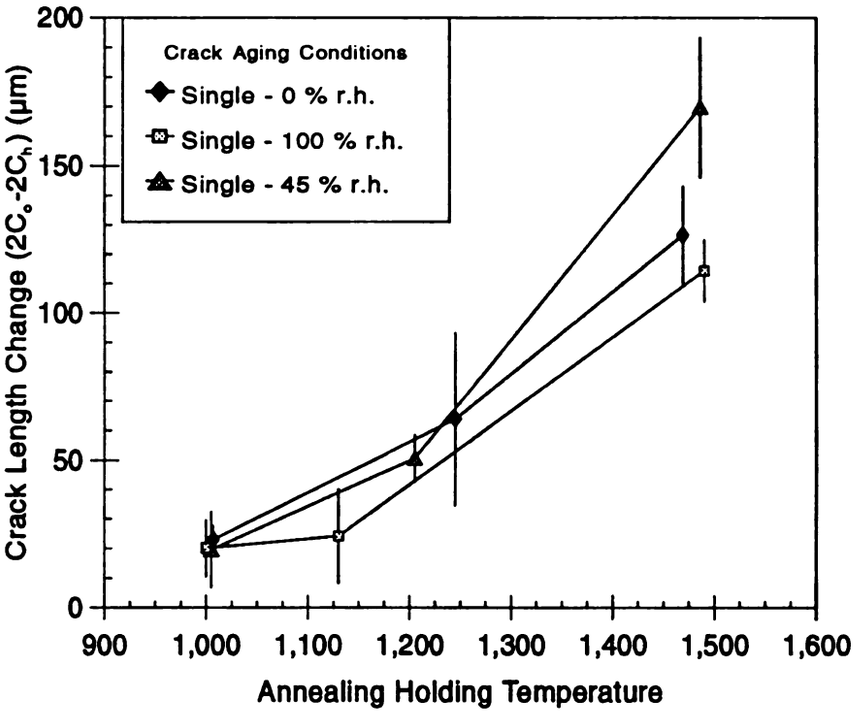

Figure 101 Mean crack length change ($2c_{initial}$ - $2c_{heal}$) versus healing temperature for Coors alumina specimens with a single age of 24 hours in 0, 45, or 100 % r.h. before annealing for 60 minutes in the large tube furnace (error bars indicate standard deviations of six cracks) (Experiment 1).

aging environments after the indent cracks were made, 2) no crack length measurements were made until after 24 hours of aging and directly before the specimens were to be thermally annealed, and 3) only 3 indents were made (instead of 6) in each specimen to help reduce the time required to measure the crack lengths.

4.4.2.2.1.2 Healing in Microwave Sintered Alumina (Experiment 1)

For microwave sintered alumina, Δc_{heal} only increased slightly with increasing healing temperature (Figure 102) as compared to the healing observed in Coors alumina (Figure 99). For the microwave sintered alumina, Δc_{heal} was about 23 μm at 1000 °C and 55 μm at 1500 °C (Figure 102). Δc_{heal} at 1000 °C in the microwave sintered alumina was similar to the Δc_{heal} in Coors alumina (23 μm from Figure 102 compared to 17 μm from Figure 99), while at 1500 °C Δc_{heal} for Coors was much greater than in the microwave sintered alumina (126 μm from Figure 99 compared to 55 μm from Figure 102).

For Δc_{heal}, the overall standard deviation was about 23 μm for all microwave sintered alumina specimens (Table 54) and about 15.5 μm for all the Coors alumina specimens (Table 53). The difference in overall standard deviations of about 7.5 μm cannot be simply a function of the grain size, since microwave sintered alumina grain size was 21 μm compared to the Coors alumina grain size of 2.1 μm (Section 4.1.2). The larger standard deviations for crack healing in microwave sintered alumina was likely due to the chipping associated with indentation cracks in microwave sintered alumina compared to the indentation cracks in the Coors alumina (Figure 103). A single major crack extends from the corners of each of the four indent impressions for

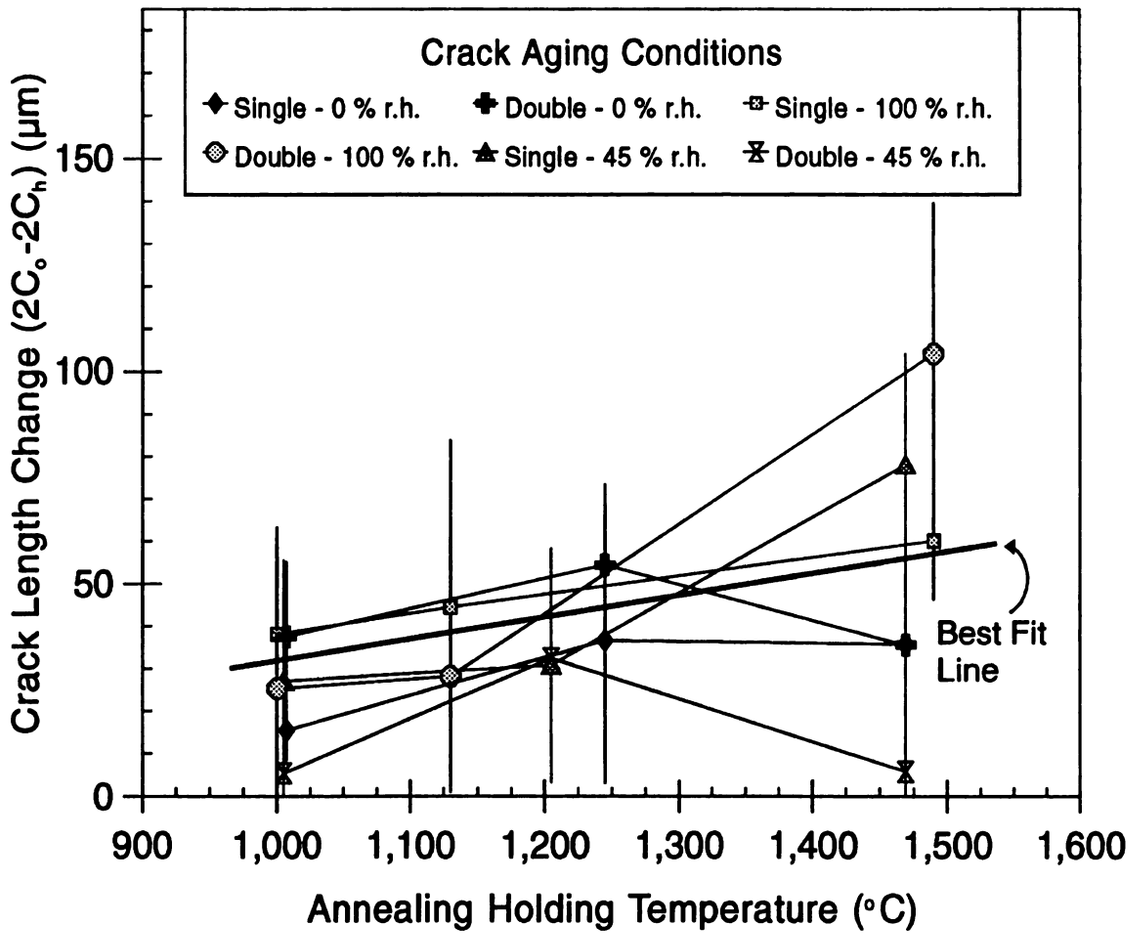

Figure 102 Mean crack length change ($2c_{initial}$ - $2c_{heal}$) versus temperature for microwave sintered alumina specimens annealed for 60 minutes in the large tube furnace (error bars indicate standard deviations of six cracks). Before annealing, indent cracks underwent a single 24 hours age in 0, 45, or 100 % r.h. or a double age with an initial 24 hour age in air followed by a 24 hour age in 0, 45, or 100 % r.h. (Experiment 1).

Coors alumina specimens, while for the microwave sintered alumina specimens, multiple cracks of significant length extend from each indent impression corner (Figure 103). To avoid the larger standard deviations of Δc_{heal} and the lack of uniformity of the indents, Coors alumina was tested exclusively in the remaining experiments on the healing in polycrystalline alumina.

4.4.2.2.2 Effects of Aging Humidity, Time, and Temperature in Coors Alumina (Experiment 2)

Fifty four specimens with a total of 324 cracks were tested as described in Section 3.6.2.3.3 and aged for 24 hours in 0, 45, or 100 % r.h.. Three specimens were aged for 235 hours in 0, 45, or 100 % r.h.. The initial crack lengths were essentially identical regardless of the aging environment with mean and standard deviation lengths of 279.8 ± 12.2, 279.3 ± 12.0, and 280.6 ± 13.0 μm for 108 cracks aged for 24 hours in 0, 45, or 100 % r.h., respectively. After aging, the specimens were thermally annealed in sets of three for 60, 90, 120, 180, or 1410 minutes at 1005, 1121, 1237, 1353, or 1469 °C (Table 55).

4.4.2.2.2.1 Post-Annealing Crack Length Measurements (Experiment 2)

After annealing, the crack length was NOT measured from crack tip to crack tip as in previous experiments. Locating the crack tip during optical measurement was difficult in cases where the crack opening displacement decreased slowly and continuously along the crack length. Also, crack tip to crack tip measurements were not sufficient to characterize the crack healing behavior where pinch-off or other discontinuous

Table 55 Mean and standard deviation of the healed crack length change ($2c_{initial}$ - $2c_{heal}$) for Coors alumina specimens aged for 24 hours in air, a desiccator, or a water chamber before annealing in the large tube furnace (Experiment 2). Temperature was measured via an R-Type thermocouple placed next to the samples in the furnace.

Annealing			Healed Crack Length Change (μm)		
Holding Temperature (°C)	Maximum Temperature (°C)	Time (min.)	Aging in ~ 0% r.h.	Aging in ~ 45% r.h.	Aging in ~ 100% r.h.
1007	1015	60	54.4±9.2	49.0±10.6	69.4±16.9
1007	1019	90	104.7±19.3	91.9±16.2	847.9±7.1
1000	1011	120	87.2±9.7	79.0±7.4	105.2±12.2
1037	1075	1410	109.5±13.4	107.8±10.9	114.5±14.2
1137	1143	60	77.7±8.7	69.2±17.6	71.7±11.3
1129	1133	90	99.4±12.7	104.9±21.4	110.9±6.8
1126	1129	120	104.7±11.5	111.3±12.2	90.0±21.9
1234	1243	60	83.4±8.0	70.1±16.8	104.4±11.6
1234	1247	90	128.6±8.6	141.2±30.2	125.4±4.5
1234	1242	120	118.9±22.8	123.2±22.1	113.5±16.7
1237 *	1237 *	180	84.4±13.7	88.5±12.7	103.0±18.9
1237 * †	1237 * †	180 †	84.5±12.6†	99.3±19.0†	120.1±8.3†
1351	1359	60	101.5±25.1	126.4±21.0	100.3±15.2
1362	1369	90	150.5±18.1	146.0±11.0	159.7±27.9
1355	1364	120	142.2±16.1	143.3±15.9	120.7±43.0
1479	1486	60	153.9±20.9	144.4±17.2	146.7±19.9
1469 *	1469 *	90	140.5±22.0	175.8±17.4	178.5±22.8
1472	1478	120	175.6±14.7	171.6±15.0	169.8±19.6

* Holding and maximum temperature not recorded.

† Specimens aged in environment for 235 hours instead of 24 hours.

decreases in the crack opening displacement occurred along the crack length. To overcome the problems associated with crack tip to crack tip measurements, the minimum continuous crack length, $2C_{MC}$, was used to characterize the crack healing behavior (Figure 104). $2C_{MC}$ was measured from the location closest to the indent impression where the crack appeared to be pinched-off to the location closest to the indent impression where the crack appeared to be pinched-off (Figure 104). Examples of the region of first pinch-off are given on labeled micrographs in Section 4.4.2.2.3, which discusses the crack healing morphology changes in Coors alumina.

4.4.2.2.2.2 Healing Time and Aging Environment (Experiment 2)

Δc_{heal} increased for 1005 °C samples annealed for 90 minutes compared to samples annealed for 60 minutes (Figure 105). The increase in Δc_{heal} for 90 minutes of annealing at 1005 °C occurred for each aging environments (0, 45, 100 % r.h., Figure 106). For specimens annealed for 120 minutes at 1005 °C, the increase in Δc_{heal} was very small or non-existent compared to specimens annealed for 90 minutes (Figure 106). Trends for Δc_{heal} for 60, 90, and 120 minutes at 1121 and 1469 °C (Figure 107 and 108) were similar to those for annealing for the same times at 1005 °C (Figure 105).

Δc_{heal} increases linearly with temperature when time and aging humidity are held constant (Figure 109). The correlation coefficients for the linear best fit lines for the 60 and 120 minute healing times in Figure 109 were 0.971 and 0.942, respectively. The slopes of the linear best fit of Δc_{heal} and temperature for healing times of 60 and 120 minutes in Figure 109 were 0.185 and 0.192 μm/K, respectively (Figure 109).

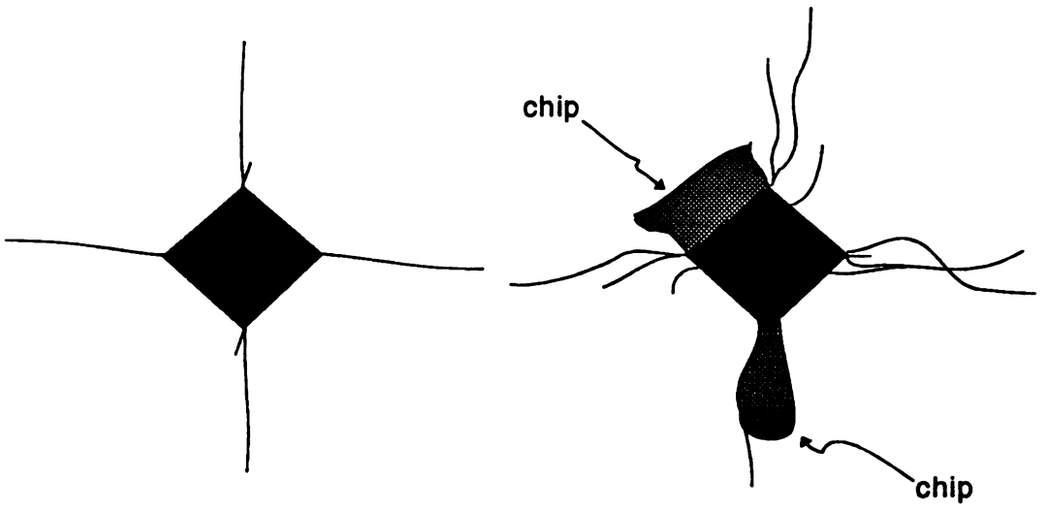

Figure 103 Schematic of Vickers indents made in Coors alumina and microwave sintered alumina. In the Coors alumina specimens, one major crack extends from each of the four indent impression corners. In microwave sintered alumina, chipping occurs and multiple cracks extend from the indent impression corners.

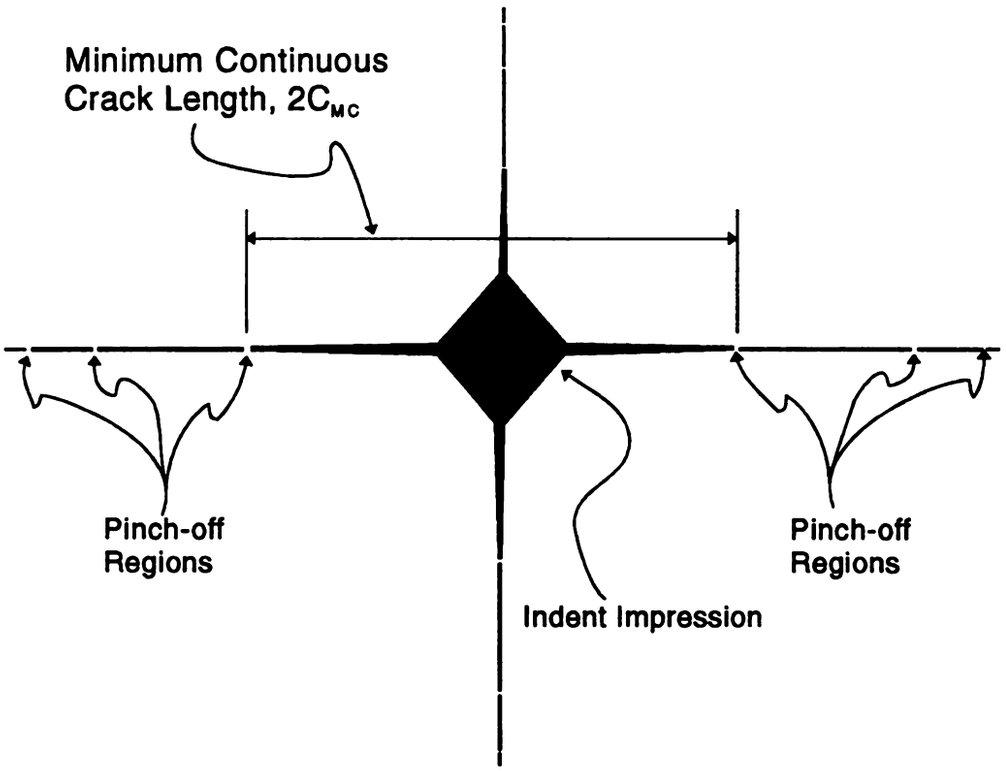

Figure 104 Schematic of the minimum continuous crack length, $2C_{MC}$, as measured for conventionally healed Coors alumina specimens in Experiment 2.

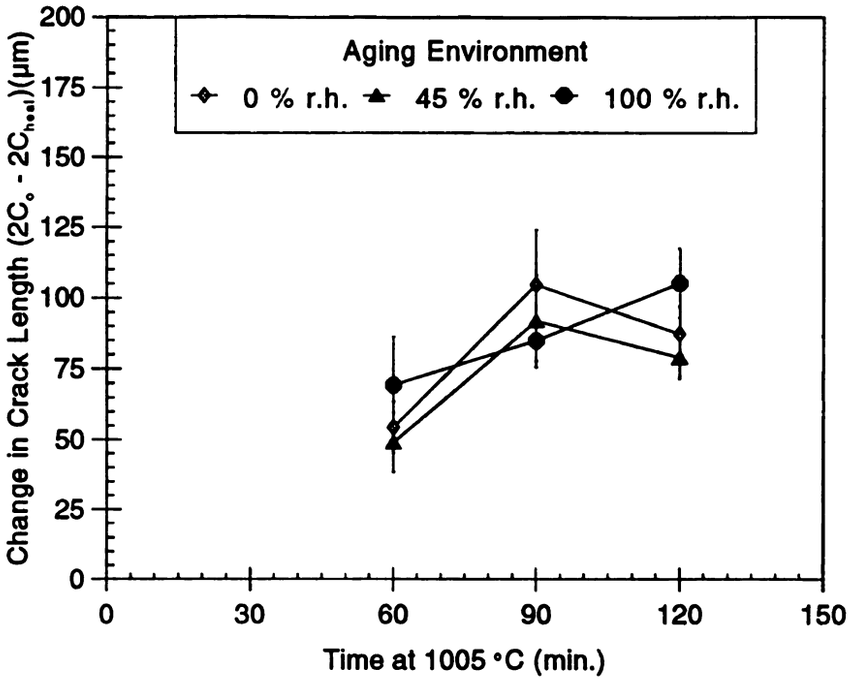

Figure 105 Mean crack length change ($2c_{initial}$ - $2c_{heal}$) versus healing time for Coors alumina specimens aged for 24 hours in air, a desiccator, or a water chamber before annealing for up to 120 minutes at 1005 °C in the large tube furnace (error bars indicate standard deviations of six cracks) (Experiment 2).

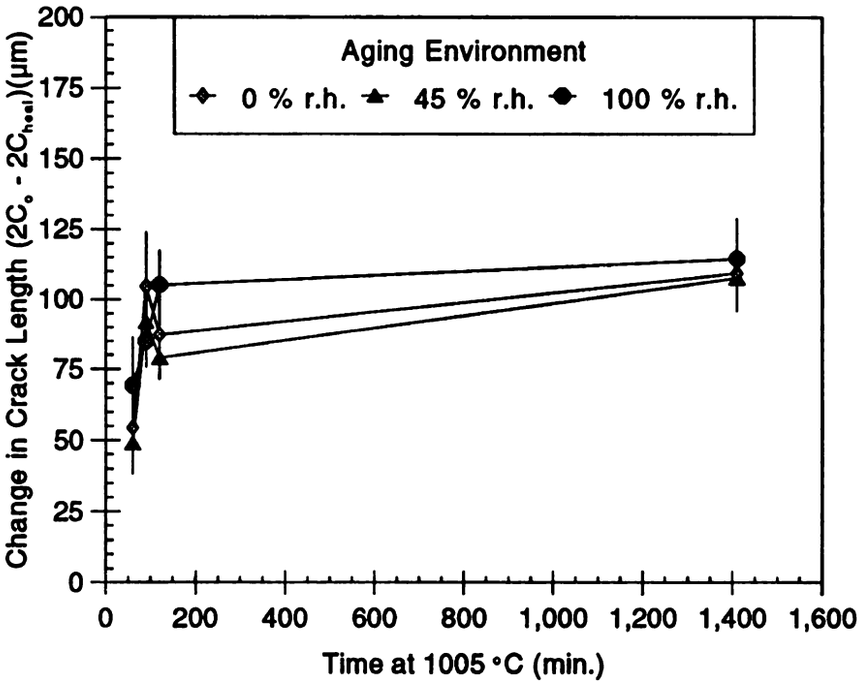

Figure 106 Mean crack length change ($2c_{initial}$ - $2c_{heal}$) versus healing time for Coors alumina specimens aged for 24 hours in air, a desiccator, or a water chamber before annealing for up to 1410 minutes at 1005 °C in the large tube furnace (error bars indicate standard deviations of six cracks) (Experiment 2).

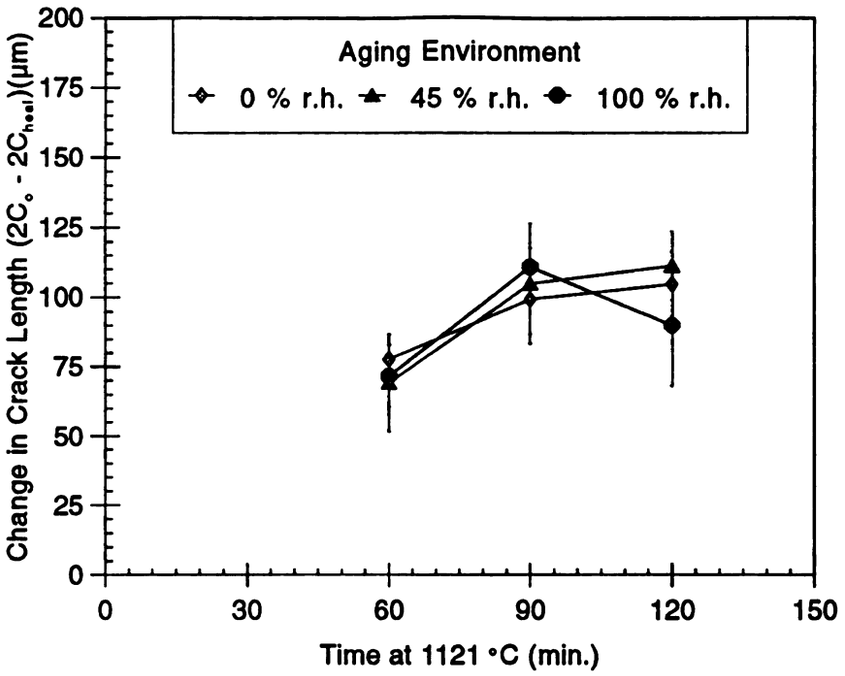

Figure 107 Mean crack length change ($2c_{initial}$ - $2c_{heal}$) versus healing time for Coors alumina specimens aged for 24 hours in air, a desiccator, or a water chamber before annealing for up to 120 minutes at 1121 °C in the large tube furnace (error bars indicate standard deviations of six cracks) (Experiment 2).

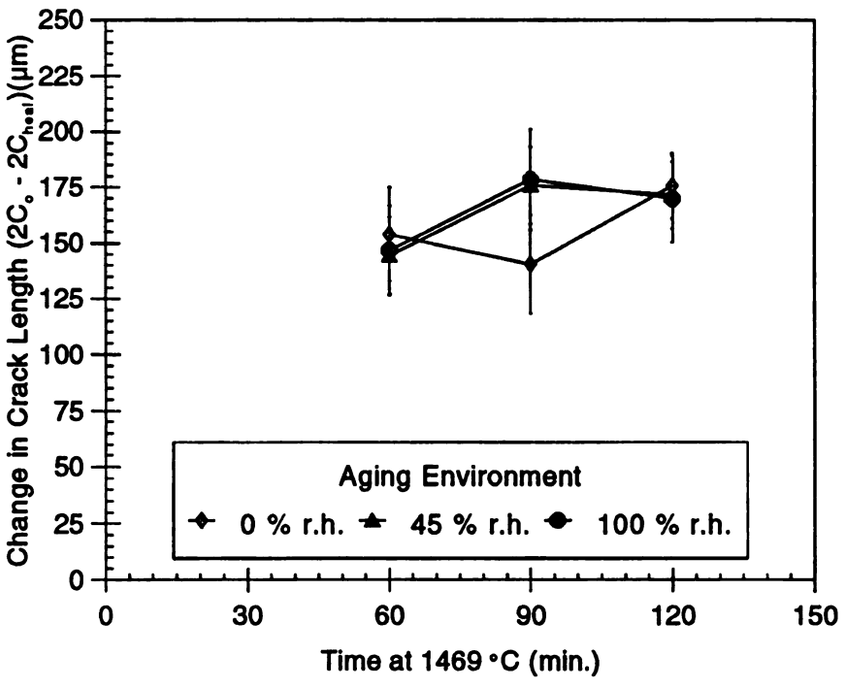

Figure 108 Mean crack length change ($2c_{initial}$ - $2c_{heal}$) versus healing time for Coors alumina specimens aged for 24 hours in air, a desiccator, or a water chamber before annealing for up to 120 minutes at 1469 °C in the large tube furnace (error bars indicate standard deviations of six cracks) (Experiment 2).

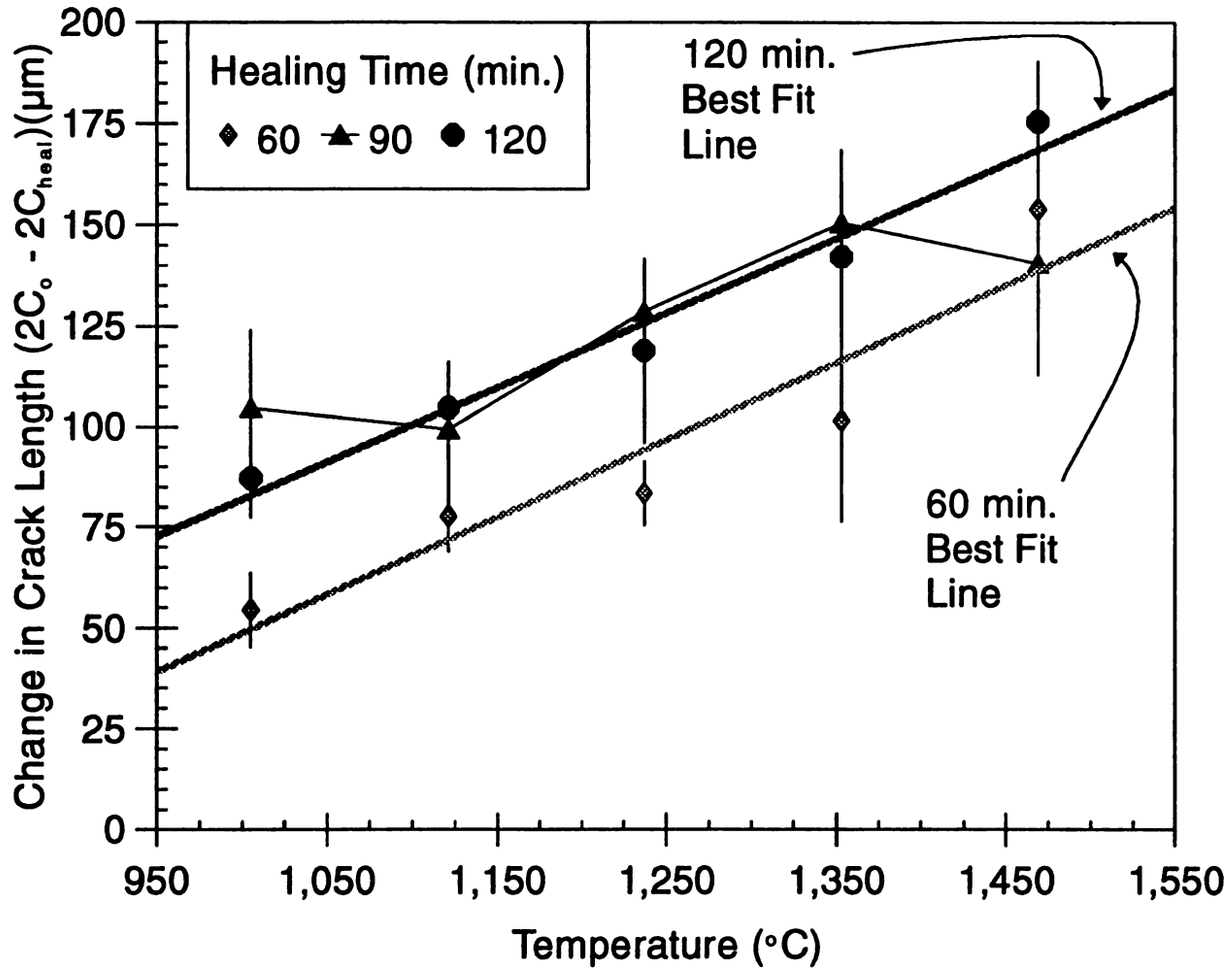

Figure 109 Mean crack length change ($2c_{initial}$ - $2c_{heal}$) versus healing temperature for Coors alumina specimens aged for 24 hours in a desiccator before annealing for 60, 90, or 120 minutes in the large tube furnace (error bars indicate standard deviations of six cracks) (Experiment 2).

With nearly identical slopes for healing at 60 and 120 minutes in Figure 109, only the intercepts change with the healing times.

4.4.2.2.2.3 Aging Environment Effect on Healing (Experiment 2)

The Δc_{heal} values for specimens: 1) aged in 0, 45, or 100 % r.h., 2) annealed for identical times, and 3) identical temperatures were within a standard deviation of each other for annealing at 1005, 1121 1469 °C (Figures 105 - 108). Healing at 1005, 1121, and 1469 °C was either not significantly affected by the aging. The samples aged for 235 hours in 0, 45, and 100 % r.h. environments and annealed at 1237 °C for 180 minutes also did not show a significant effect of aging humidity (Table 55).

With no measurable effect of aging environment, all samples annealed for the same time and temperature (regardless of aging conditions) could be grouped together in data analysis to determine the effect of annealing time and temperature on Δc_{heal}. The linear best of Δc_{heal} and temperature for all fifteen samples and 90 cracks annealed for 60 minutes was 0.188 μm/K with a correlation coefficient of 0.932 (Figure 110).

If there is an effect of aging environment, aging for a longer time could increase the effect, but no significant change in Δc_{heal} occurred after 235 hours of aging (Table 55), which is further evidence that aging environment had no effect on healing in Coors alumina. The current data cannot show conclusively that aging environment has NO effect on healing (since indenting and aging in the identical environment would be needed). However, one of the goals of this study was to see if aging in a different environment before thermal annealing could be used in an industrial setting to help increase crack healing; to that end, the Table 55 and Figures

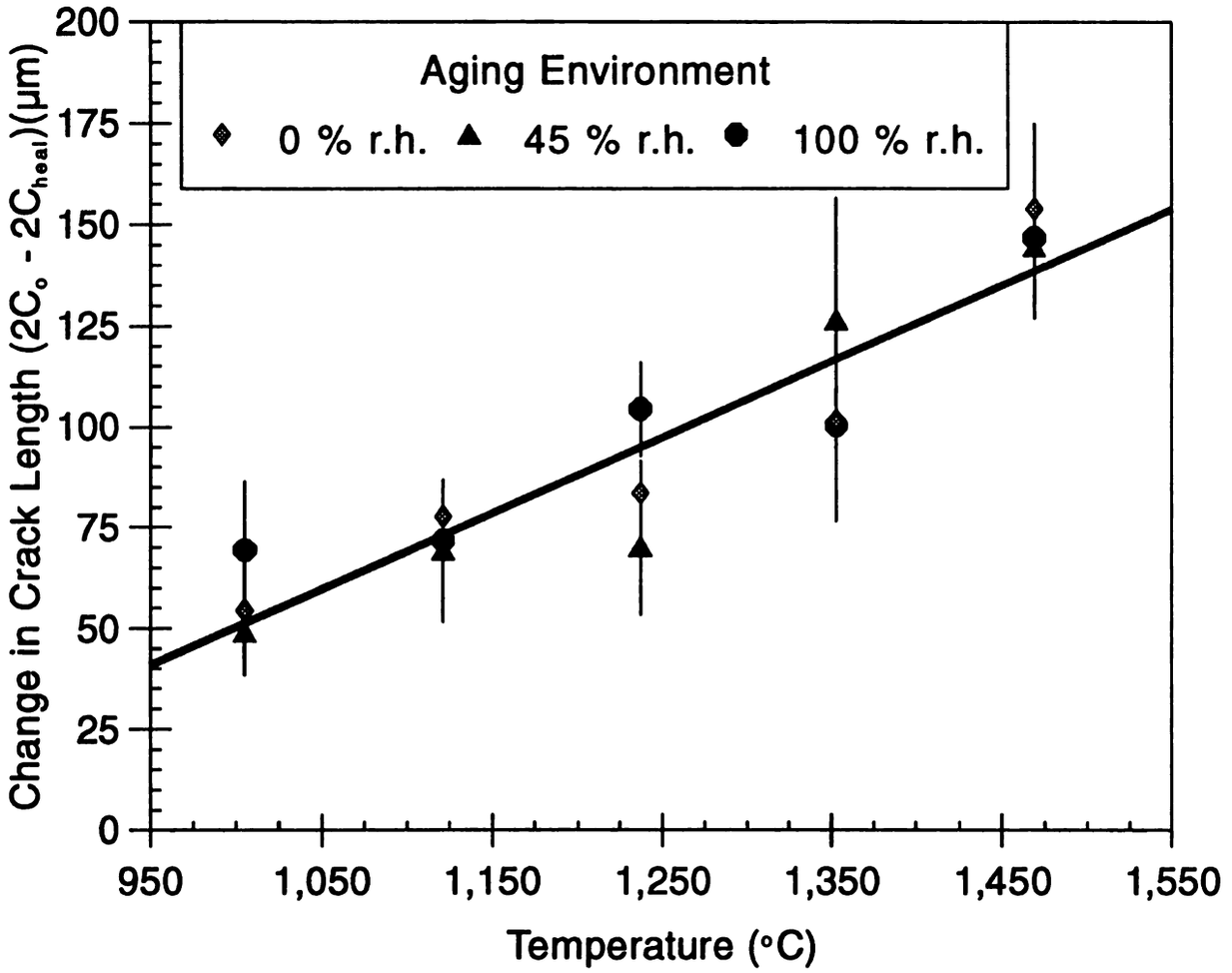

Figure 110 Mean crack length change ($2c_{initial}$ - $2c_{heal}$) versus healing temperature for Coors alumina specimens aged for 24 hours in air, a desiccator, or a water chamber before annealing for 60 minutes in the large tube furnace (error bars indicate standard deviations of six cracks) (Experiment 2).

105 - 110 show that aging in different environments does NOT alter thermal healing to a large enough extent to warrant consideration for use in an industrial setting.

Aging indented samples in environments with water vapor present results in water vapor adsorption by the freshly created indentation crack surfaces. In glass specimens, the adsorbed water vapor can enter the glass structure via the crack surfaces before and/or during the annealing cycle and can reduce the viscosity and consequently affect the healing behavior (Section 4.4.2.1.4.1). However, in Coors alumina effects of aging environment on healing are assumed to be dominated by the interaction (or lack thereof) of water vapor with the Al_2O_3 structure. The lack of an aging environment effect on healing in the Coors alumina indicates that the interaction between water vapor and the Al_2O_3 crystal structure is small to non-existent.

Many alumina ceramics are processed with sintering aids which result in an decrease the volume fraction of porosity and the introduction of a glassy phase at the grain boundaries [8]. For indented alumina specimens with a glassy phase, the adsorbed water vapor might enter the glassy grain boundary phase and effect healing via a decrease in the viscosity of the grain boundary phase. The Coors alumina used in the present study is reported to be 99.9% Al_2O_3 (chemically) and so should have relatively little glassy phase at the grain boundaries. To investigate if the water vapor would interact with a glassy grain boundary phase in alumina and result in an increase in healing, future conventional healing experiments with alumina could use Coors AD-90 since Coors AD-90 is 10% glass.

4.4.2.2.2.4 Time and Temperature Effect on Healing (Experiment 2)

The measurements for all three samples and all 18 cracks for each time/temperature annealing condition were taken as a single set to obtain one mean and standard deviation for each time/temperature annealing condition (Figure 111), since the best fit line described the data in Figure 110 well and since there was no noticeable difference or trend with the aging environment. Δc_{heal} increased for all annealing temperatures as the annealing time increased from 60 minutes to 90 minutes (Figure 111). The differences in Δc_{heal} for annealing times of 90 and 120 minutes are within the standard deviations for the Δc_{heal} values (Figure 111). For long annealing times such as 1410 minutes, the Δc_{heal} at 1005 °C increases slightly with time (Figure 112). More annealing times between 120 and 1410 minutes and above 1410 minutes would be required to determine conclusively the degree of increase in Δc_{heal} with healing time at 1005 °C and other temperatures.

Δc_{heal} increases for annealing times of 60 and 120 minutes as the annealing temperature increases from 1005 to 1469 °C (Figure 113). For annealing at 120 minutes, Δc_{heal} was approximately 25 to 30 microns larger than the Δc_{heal} at 60 minutes over the temperature range of 1005 to 1469 °C (Figure 113). A large increase in Δc_{heal} at 1469 °C compared to the increases between the other temperatures, may indicate that Δc_{heal} does not increase linearly with temperature (Figure 113). Δc_{heal} for 90 minutes of annealing was nearly identical in value and behavior to the 120 minute healing and consequently was not shown in Figure 113 to avoid obscuring data points.

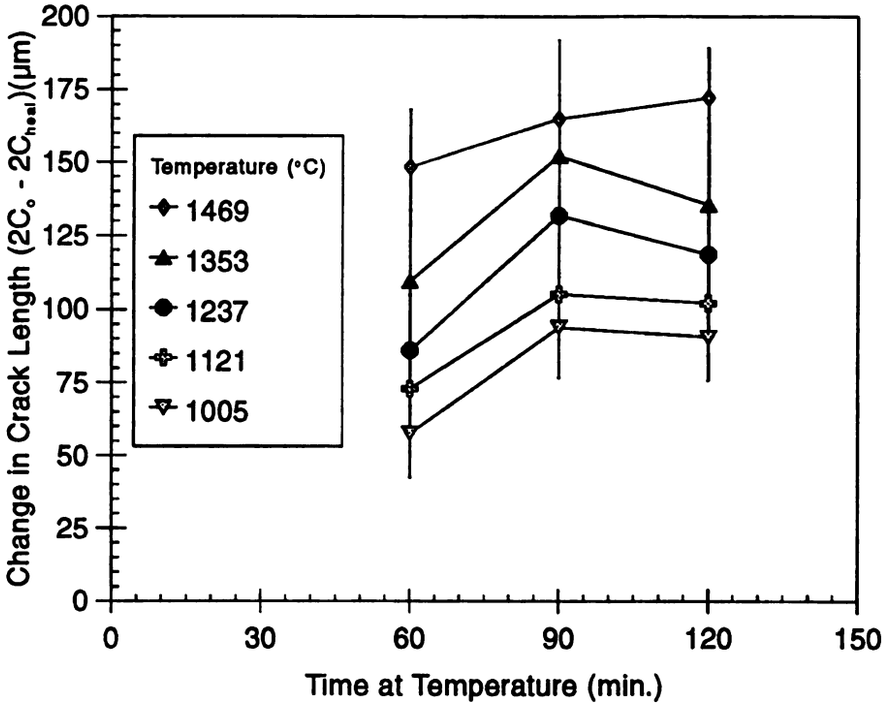

Figure 111 Mean crack length change ($2c_{initial}$ - $2c_{heal}$) versus healing time for Coors alumina specimens annealed for up to 120 minutes in the large tube furnace (error bars indicate standard deviations of 3 specimens and 18 cracks) (Experiment 2).

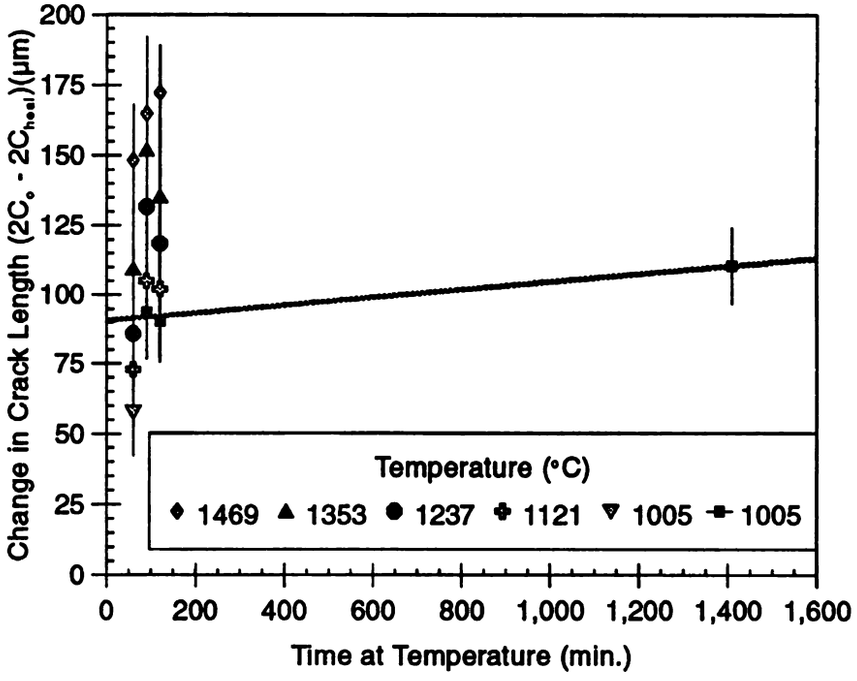

Figure 112 Mean crack length change ($2c_{initial}$ - $2c_{heal}$) versus healing time for Coors alumina specimens annealed for up to 1410 minutes in the large tube furnace (error bars indicate standard deviations of 3 specimens and 18 cracks) (Experiment 2). The best fit line is for annealing at 1005 °C for times of 90 to 1410 minutes.

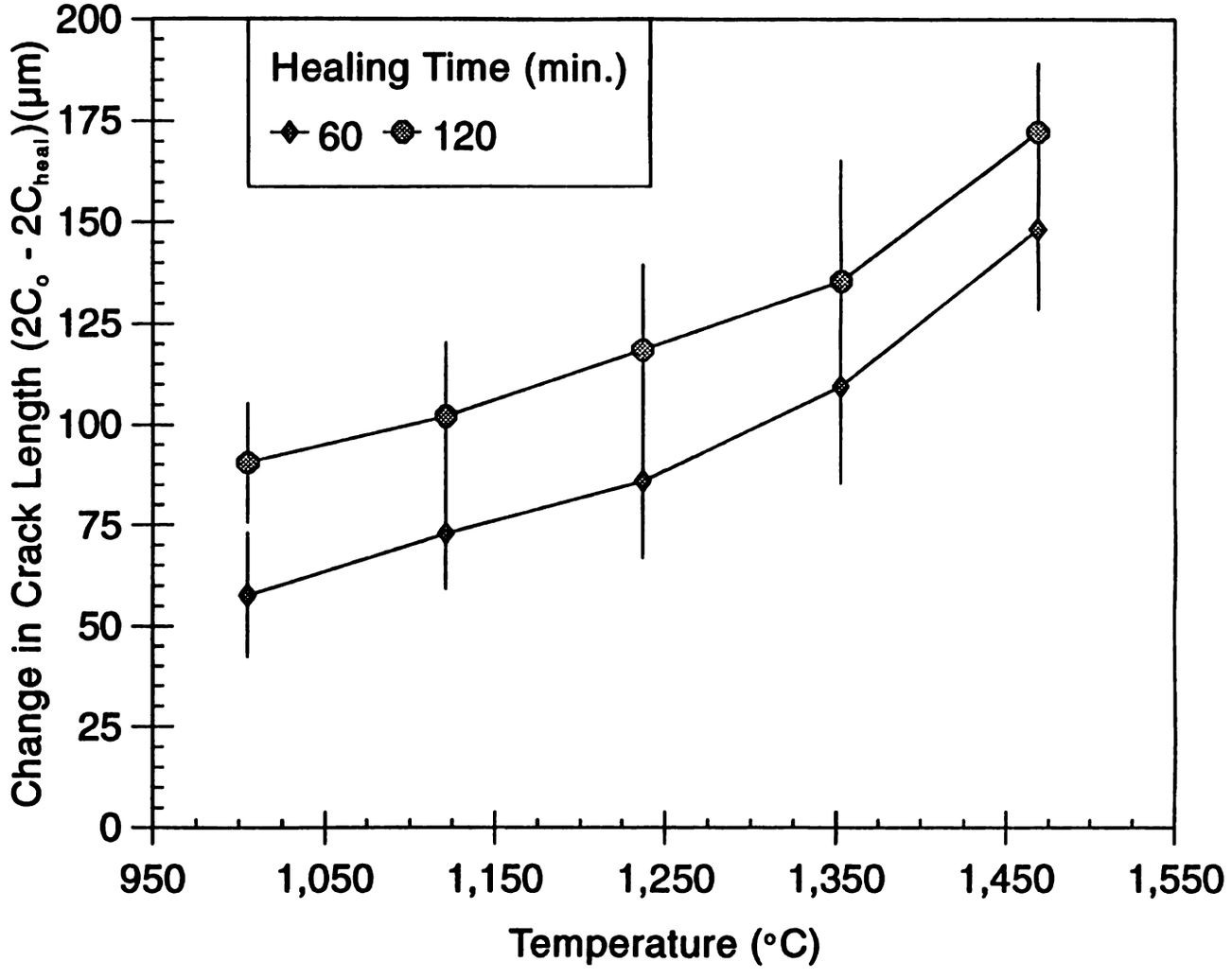

Figure 113 Mean crack length change ($2c_{initial}$ - $2c_{heal}$) versus healing temperature for Coors alumina specimens annealed for 60 or 120 minutes in the large tube furnace (error bars indicate standard deviations of 3 specimens and 18 cracks) (Experiment 2).

4.4.2.2.2 Crack Morphology Changes in Coors Alumina

The crack morphology of healed indent cracks in two Coors alumina specimens annealed in Experiment 2 for 120 minutes was investigated (Figures 114 - 117 and 117 - 123) using a field emission SEM (Camscan 44FE). The specimens were observed **without** a conductive coating. The accelerating voltage used to image the specimens was 4 KeV. Micrographs were taken along the path of the original as-indented crack. In the micrographs specific pores and grains were identified and labeled to act as reference points indicating the relative location from one micrograph to the next.

For the uncoated specimen aged in 0 % r.h. and annealed at 1353 °C for 120 minutes, the first pinch-off region of healing between the indent and the crack tip is indicated (Figure 114). The region (where pinch-off first occurs) appears to be a grain partially bridging the crack before annealing and after annealing is completely healed across the open crack (Figure 114). For the region of the indent crack from the indent impression to the crack tip (indicated in Figure 114), the crack opening displacement (COD) is non-zero except for the first pinch-off region. At a greater distance from the indent impression than the indicated crack tip (Figure 115), a trace similar in appearance to thermally etched grain boundaries occurs along parts of what was likely the pre-annealed path of the crack (Figure 115). Open voids are present along the crack trace (Figure 116). At further distances away from the crack tip (approximately 40 -45 μm), the trace of the crack becomes less pronounced and open voids are not evident (Figure 117).

The trace of the crack is visible in optical microscopy. However, it is very

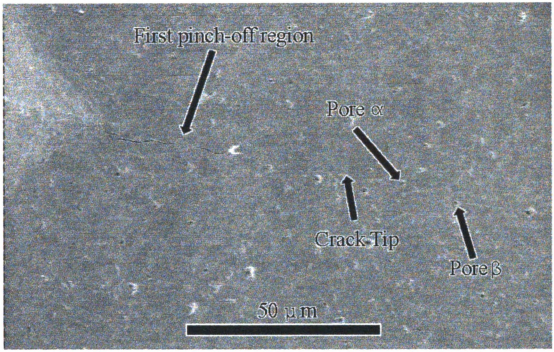

Figure 114 Conventional Field Emission SEM micrograph of an indent crack in the Coors alumina specimen annealed at 1353 ℃ for 120 minutes in a large tube furnace. The first healed region, the crack tip and the location of pores α and β (reference points for Figures 115, 116, and 117).

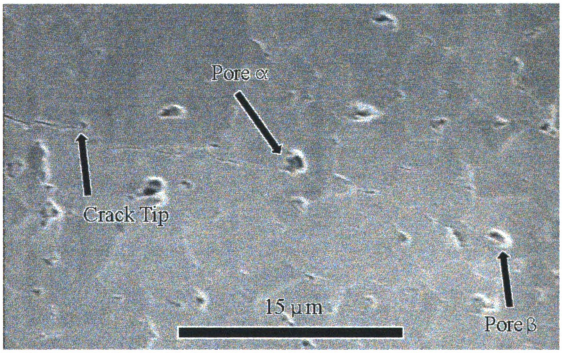

Figure 115 Conventional Field Emission SEM micrograph of the crack in Figure 114 (Coors alumina annealed at 1353 ℃ for 120 minutes in the large tube furnace). The healed region located at a greater distance from the indent impression than the crack tip and pores α and β (for reference).

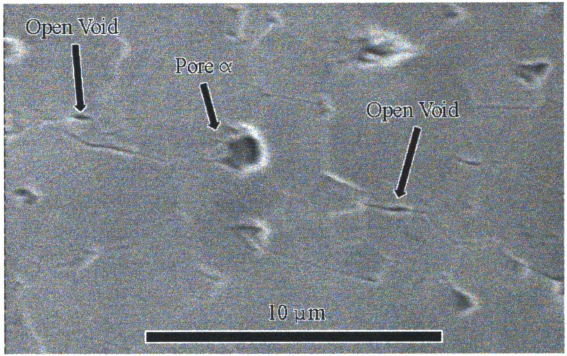

Figure 116 Conventional Field Emission SEM micrograph of the healed portion of the crack in Figure 115 (Coors alumina annealed at 1353 ℃ for 120 minutes in the large tube furnace). Open voids of less than 2 μm in length and pore α (for reference).

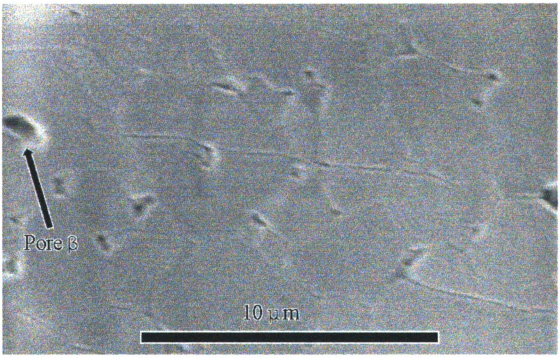

Figure 117 Conventional Field Emission SEM micrograph of the healed crack (Figure 114) (Coors alumina annealed at 1353 ℃ for 120 minutes in the large tube furnace). The surface trace of the healed crack resembles the thermally etched grain boundaries of the Coors alumina. Pore β is included for reference.

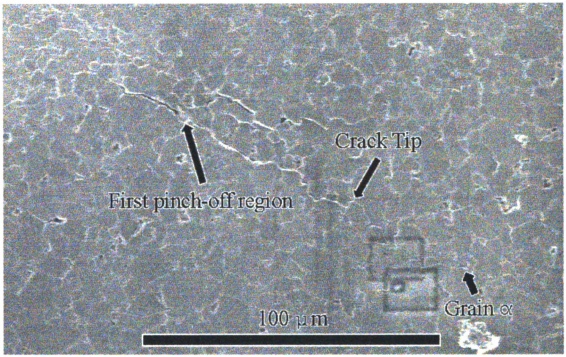

Figure 118 Conventional Field Emission SEM micrograph of an indent crack in the Coors alumina specimen annealed at 1469 °C for 120 minutes in the large tube furnace. The first healed region, the crack tip. Grain α serves as a reference point for Figures 119, 120, and 121.

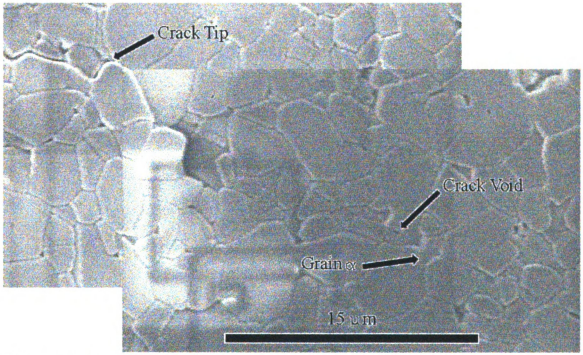

Figure 119 Conventional Field Emission SEM micrograph of the crack in Figure 118 (Coors alumina annealed at 1469 °C for 120 minutes in the large tube furnace). The healed region after the crack tip, a crack void. Grain α for reference.

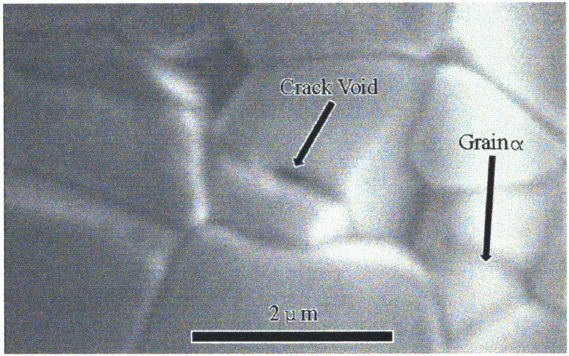

Figure 120 Conventional Field Emission SEM micrograph of the healed portion of the crack (Figure 119) (Coors alumina annealed at 1469 ℃ for 120 minutes in the large tube furnace). The circular crack void of less than 0.3 μm in diameter. Grain α is included for reference.

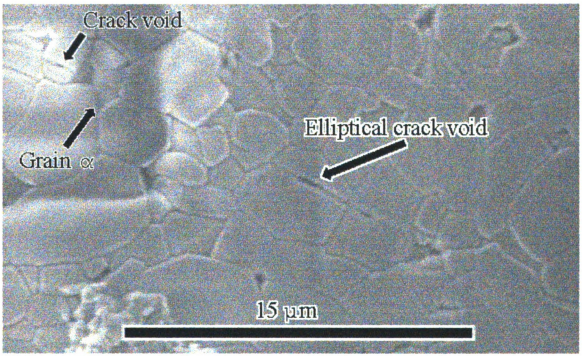

Figure 121 Conventional Field Emission SEM micrograph of the healed crack (Figure 118) (Coors alumina annealed at 1469 ℃ for 120 minutes in the large tube furnace). The circular crack void, an elliptical crack void.

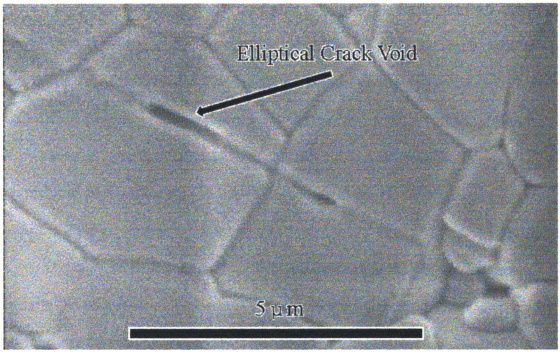

Figure 122 Conventional Field Emission SEM micrograph of the healed portion of the crack (Figure 121) (Coors alumina annealed at 1469 ºC for 120 minutes in the large tube furnace). The elliptical crack void has pinched off into an elliptical crack void approximately 1.3 µm in length and a nearly circular crack void of 0.3 µm in length.

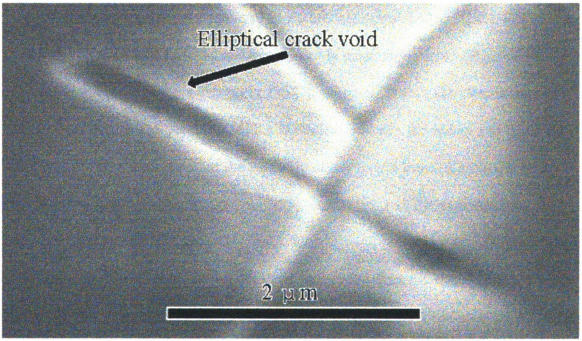

Figure 123 Conventional Field Emission SEM micrograph of the healed crack (Figure 121) (Coors alumina annealed at 1469 ºC for 120 minutes in the large tube furnace). The elliptical crack void with a maximum crack opening displacement (COD) of approximately 0.2 µm.

difficult in optical crack length measurements to discern the location of the end of the open crack. The difficulty in distinguishing the crack tip from the crack trace results from the slow and continuous decrease in crack opening displacement and the lower resolution of the optical microscope compared to a field emission SEM. Also, due to the presence of regions of crack healing at smaller distances from the indent impression than the crack tip (Figure 117), measurements of the distance to the crack tip do not describe healing behavior well.

The distance from the midpoint of the indent impression to the first healed region in the micrograph (Figure 114) was 63 μm and the same distance measured optically was 66 μm. Consequently, to overcome the problems associated with crack tip measurements, the minimum continuous crack length, $2C_{MC}$, was measured optically for the annealed cracks in Coors alumina for Experiment 2 (Section 4.4.4.2).

For the uncoated specimen aged in air and annealed at 1469 °C for 120 minutes, the thermal etching at grain boundaries is more pronounced (Figure 118 - 123) than for the specimen annealed at 1353 °C (Figures 114 - 117). For the crack annealed at 1469, a first pinch-off region is evident between the indent and crack tip (Figure 118). The distance from the midpoint of the indent impression to the first healed region in the micrograph (Figure 118) was 54 μm and the same distance measured optically was 52 μm.

At a greater distance from the indent impression than the indicated crack tip (Figure 119), a faint trace of the crack can be observed which follows an intergranular and transgranular path (Figure 119). Open voids along the length of the crack trace are almost exclusively found in grains as opposed to along grain boundaries (Figure

119). The voids were approximately circular (Figure 120) or elliptical in cross section (Figure 121). The elliptical void which was approximately 1.3 μm long and 0.3 μm across (Figure 122) and the circular void which was approximately 0.2 μm in diameter (Figure 123) may have pinched-off from a longer elliptical crack (Figure 122).

4.4.3 Microwave Healing in Polycrystalline Alumina

A total of 15 specimens and 180 cracks were used to investigate microwave healing of 49 and 98 N Vickers indent cracks in Coors alumina. Annealing was performed with microwave heating with ramp rates of 10 or 75 °C/minute and (for comparison) with conventional heating with a ramp rate of 10 °C/minute (Section 3.6.3.2).

Specimens were prepared as described in Section 3.6.3.1 and aged for 24 hours in 45 % r.h. to allow the indent crack growth to saturate. After aging, the mean and standard deviation crack lengths were 287.6 ± 14.8 and 454.1 ± 24.6 μm for the ninety 49 and the ninety 98 N indent cracks, respectively. After annealing crack lengths were measured from crack tip to crack tip (Table 56 and 57).

4.4.3.1 Healing in Conventional and Microwave Annealing

Δc_{heal} at 1237 °C was greater than 45 μm for all specimens regardless of heating type or heating rate (Table 56 - 57 and Figures 124 and 125). A small increase in Δc_{heal} for all specimens occurred upon increasing the annealing temperature to 1295 °C (Figure 124 - 125). At temperatures above 1353 °C, healing increased dramatically for all specimens.

Δc_{heal} at 1469 °C for the 98 N indent cracks was from 50 to 100 μm larger than

the Δc_{heal} for the 49 N indent cracks (Table 57 and Figures 124-125). The larger Δc_{heal} for 98 N indent cracks is not necessarily unexpected since the initial crack lengths were 50% longer for the 98 N indents than for the 49 N indents. The relative crack healing values ($\Delta c_{heal}/2c_{initial}$), were almost identical for the 49 and 98 N indent cracks in samples heated via microwaves and those heated conventionally, regardless of the heating rate (Figure 126). The only significantly different $\Delta c_{heal}/2c_{initial}$ values for the 49 and 98 N indent cracks were at 1353 °C for microwave heating with a slow ramp rate of 10 °C/minute (Figure 126), the cause of which is not apparent.

4.4.3.2 Differences in Microwave and Conventional Healing

At temperatures of 1295 °C and above, Δc_{heal} microwave heating was greater than from conventional heating for both 49 and 98 N indent cracks (Figure 124 and 125). The difference in Δc_{heal} for conventional and microwave heating increased dramatically at temperatures of 1353 °C and above for all heating types and rates (Figure 126). The difference in Δc_{heal} between microwave and conventional heating at 1411 °C was greater than 70 and 100 μm for the 49 and 98 N indent cracks, respectively (Figures 124 and 125). The difference in relative crack healing between conventional and microwave heating at 1411 °C was greater than 20% (Figure 126).

The large increase in healing at temperatures above 1295 °C for microwave heated cracks compared to conventionally heated cracks could be the result of: 1) enhanced diffusion via microwave heating (compared to diffusion in conventional heating at the same temperatures), 2) a different healing mechanism in microwave healing than for conventional healing, or 3) the temperatures for microwave heating

Table 56 Mean and standard deviation of the healed crack length change ($2c_{initial}$ - $2c_{heal}$) for Coors alumina specimens aged for 24 hours in 45 % r.h. before a 60 minute anneal by microwave heating. (Maximum temperature was within ±2 °C of set temperature).

Heating Ramp Rate (°C/min.)	Set and Holding Temperature (°C)	Healed Crack Length Change (μm)	
		49 N Indent	98 N Indent
10	1237	46.9 ± 17.7	72.1 ± 23.4
	1295	84.1 ± 14.4	114.3 ± 9.0
	1353	151.5 ± 17.7	175.6 ± 21.8
	1411	199.1 ± 10.1	338.0 ± 9.2
	1469	199.1 ± 9.2	337.9 ± 8.8
75	1237	84.8 ± 13.5	99.7 ± 21.3
	1295	68.3 ± 18.3	96.4 ± 33.5
	1353	91.0 ± 17.7	155.3 ± 20.1
	1411	136.9 ± 27.8	216.0 ± 16.4
	1469	157.1 ± 53.2	273.0 ± 30.6

Table 57 Mean and standard deviation of the healed crack length change ($2c_{initial}$ - $2c_{heal}$) for Coors alumina specimens aged for 24 hours in 45 % r.h. before annealing for 60 minutes by conventional heating. Temperature overshoot above the set temperature from a 10 °C/minute ramp rate resulted in higher holding and maximum temperatures.

Set Temperature (°C)	Holding Temperature (°C)	Maximum Temperature (°C)	Healed Crack Length Change (μm)	
			49 N Indent	98 N Indent
1237	1245	1291	50.0 ± 19.7	76.0 ± 21.0
1295	1309	1344	59.9 ± 16.1	77.0 ± 18.1
1353	1354	1394	53.3 ± 9.5	60.1 ± 18.3
1411	1426	1464	66.0 ± 17.5	113.5 ± 21.8
1469	1469	1515	99.0 ± 17.9	146.8 ± 31.7

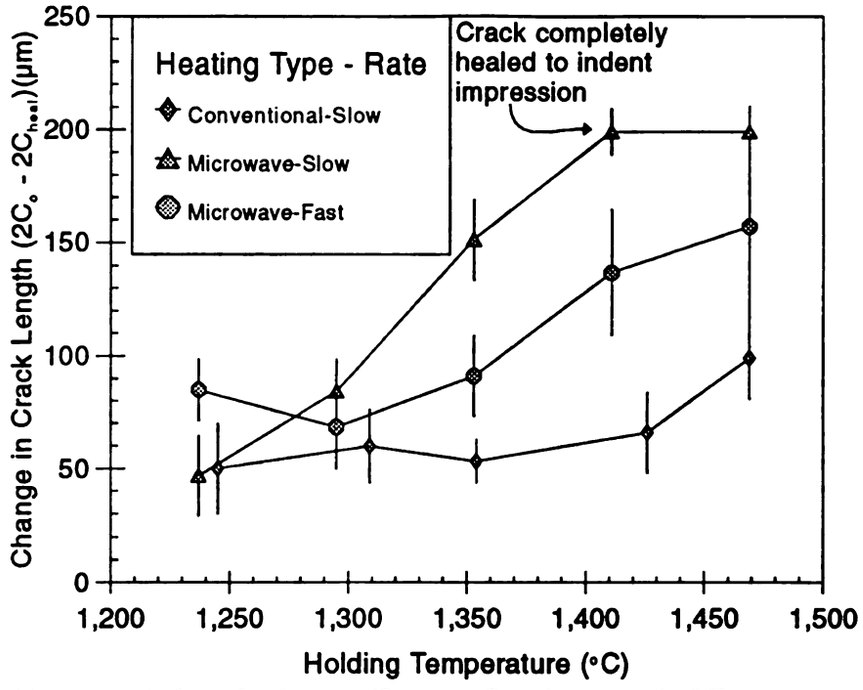

Figure 124 Mean crack length change ($2c_{initial}$ - $2c_{heal}$) versus holding temperature for 49 N Vickers indent cracks in Coors alumina which were aged for 24 hours in 45 % r.h. before annealing for 60 minutes with conventional or microwave heating at slow or fast rates (10 or 75 °C/min.) (error bars indicate standard deviations of six cracks).

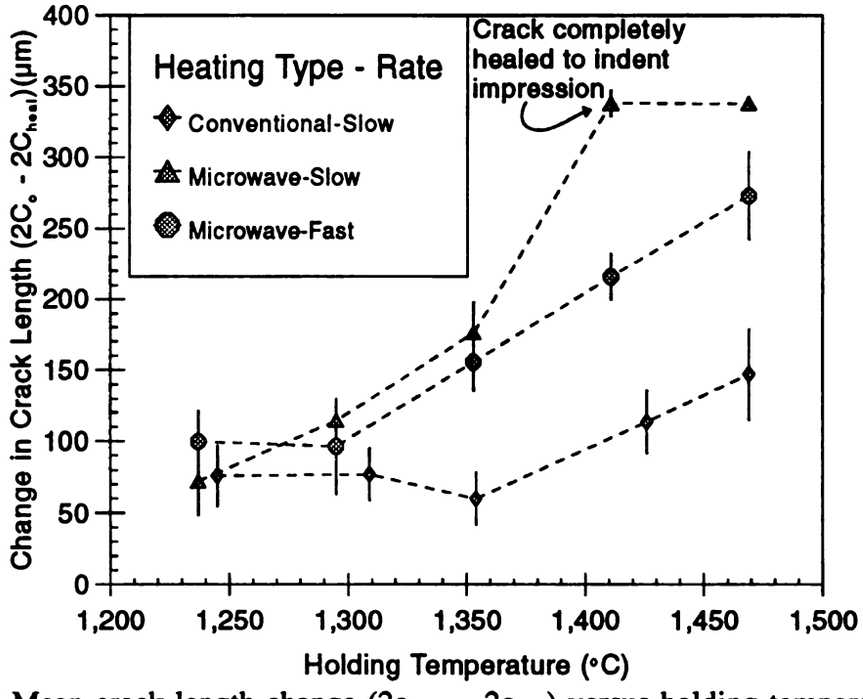

Figure 125 Mean crack length change ($2c_{initial}$ - $2c_{heal}$) versus holding temperature for 98 N Vickers indent cracks in Coors alumina which were aged for 24 hours in 45 % r.h. before annealing for 60 minutes with conventional or microwave heating at slow or fast rates (10 or 75 °C/min.) (error bars indicate standard deviations of six cracks).

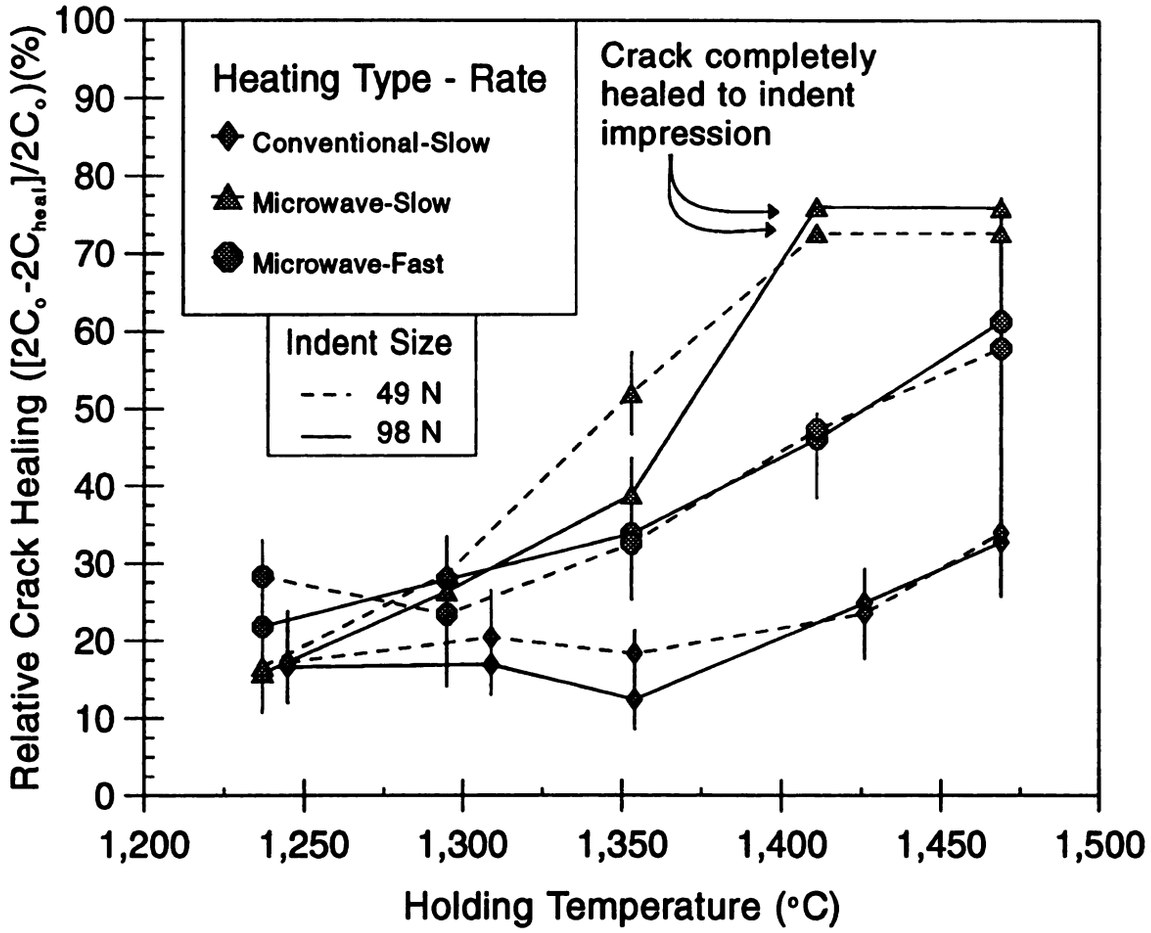

Figure 126 Relative change in crack length ($\{2c_{initial} - 2c_{heal}\}/2c_{initial}$) versus holding temperature for 49 and 98 N Vickers indent cracks in Coors alumina which were aged for 24 hours in 45 % r.h. before annealing for 60 minutes with conventional or microwave heating at slow or fast rates (10 or 75 °C/minute) (error bars indicate standard deviations of six cracks).

actually being larger than measured. The microwave heating literature has many examples of enhanced behavior observed in microwave heating compared to conventional heating (Section 4.4.3.4). While some authors suggest that the apparent increase from microwave heating results from underestimates of the actual specimen temperature by 100 - 400 °C, other authors have shown that the temperature measurement in microwave heating is within ±20 °C (Section 4.4.3.4). In the current crack healing study, the microwave heating curves would have to be shifted in the positive x-direction by 125 °C to account for the difference in microwave and conventional healing (Figure 127). However, microwave heated specimens, with a slow ramp rate and shifted 125 °C in the positive x-direction (Figure 127) to simulate an adjustment for temperature measurement errors, would still have larger Δc_{heal} values compared to conventional healing (Figure 127). Section 4.4.4 discusses work to determine the healing diffusion activation energies for the conventional and microwave heating in the current crack healing study.

4.4.3.3 Healing Differences Between Slow and Fast Microwave Heating

At temperatures of 1295 °C and below, $\Delta c_{heal}/2c_{initial}$ for slow and fast microwave healing are not significantly different, while at temperatures of 1353 °C and higher $\Delta c_{heal}/2c_{initial}$ for slow microwave heating becomes much larger than for fast microwave heating (Figure 126). A specimen with a slower heating rate would be at temperatures high enough for healing to take place for longer times than a specimen with a faster heating rate and consequently heal more. Conventional healing of Coors alumina in Section 4.4.2.2 revealed healing after 60 minute annealing cycles for temperatures as

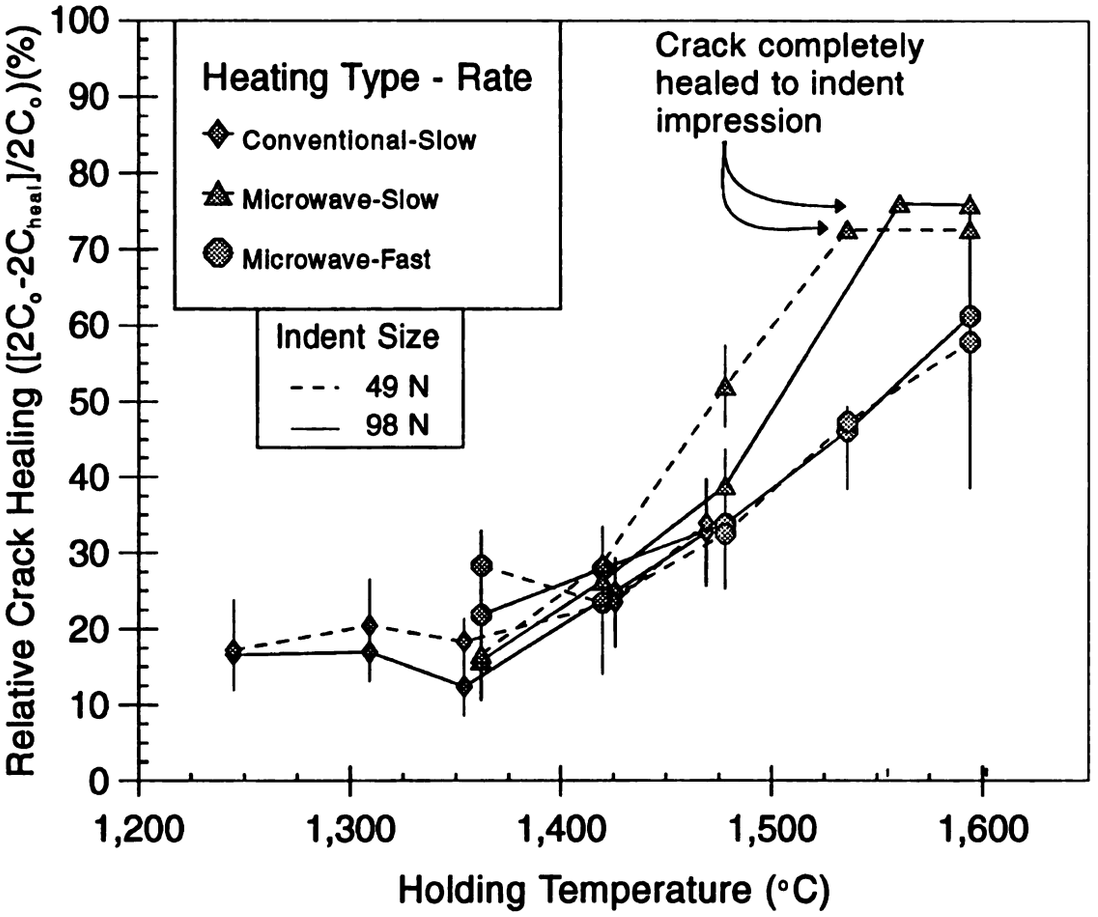

Figure 127 Relative change in crack length ($\{2c_{initial} - 2c_{heal}\}/2c_{initial}$) versus holding healing temperature for 49 and 98 N Vickers indent cracks in Coors alumina which were aged for 24 hours in 45 % r.h. before annealing for 60 minutes with conventional or microwave heating at slow or fast rates (10 or 75 °C/minute) (error bars indicate standard deviations of six cracks). Microwave heating temperatures were increased 125 °C to simulate an adjustment for possible errors in measurement.

low as 1005 °C. A sample heated with a slow ramp rate (10 °C/minute) to 1295 °C, would be at temperatures above 1005 °C for about 50 minutes more than a sample heated with a fast ramp rate (75 °C/minute) which would spend only a total of 8 minutes above 1005 °C. However, healing was essentially the same for slow and fast microwave heating at 1295 °C (Table 56 and Figure 127) indicating that the amount of time a specimen spent between 1005 and 1295 °C did not significantly effect microwave healing behavior.

At 1411 °C, the relative crack healing for slow microwave heating is approximately 28% higher than for fast microwave heating (Figure 127) and the Δc_{heal} values for 49 and 98 N indent cracks were 62 and 122 μm higher, respectively (Table 56). A specimen heated with a slow ramp rate to 1411 °C, would spend 20 more minutes at temperatures above 1295 °C than a specimen heated with a fast ramp rate which would spend a total of only 3 minutes at temperatures above 1295 °C. Thus, while time above 1005 °C did not effect microwave healing, time above 1295 °C DOES effect microwave healing. The small difference between the slow and fast microwave heating rates until temperatures above 1295 °C is similar to the microwave heating behavior observed in sintering of alumina. Significant sintering rates in alumina were not observed by Janney and Kimrey until temperatures of about 1250 °C and above [90]. The similarity of conventional and microwave healing at temperatures of 1295 °C and below, along with the increase in healing for slow microwave heating at temperatures above 1295 °C indicates that the microwave enhancement occurs at temperatures above 1300 °C and is increased by the time at temperatures above 1300 °C and not just the time at the maximum holding temperature.

4.4.3.4 Literature Review of Diffusion during Microwave Heating

Janney and Kimrey studied diffusion in alumina during microwave heating [90-92]. Janney and Kimrey investigated oxygen diffusion in single crystal alumina under microwave and conventional heating with ^{18}O tracer diffusion experiments [91]. For temperatures of 1500 - 1800 °C, the diffusion of the oxygen was greatly increased by microwave heating as compared to conventional heating [91]. The activation energy of ^{18}O diffusion was 390 and 650 kJ/mol (4.04 and 6.74 eV) under microwave and conventional heating, respectively [91].

Janney and Kimrey also studied sintering of alumina and found the apparent activation energy for conventional and microwave sintering of a high purity alumina (Sumitomo AKP-50) to be 575 and 160 kJ/mol (5.96 and 1.66 eV), respectively [92]. While pores in alumina are eliminated in the early stages of conventional sintering, in microwave sintering pores in alumina were eliminated in the later sintering stages which resulted in a reduction in the grain size of microwave sintered alumina specimens compared to the grain size of samples sintered conventionally to similar final densities [92]. Janney and Kimrey hypothesize that the reduction of grain size from microwave sintering indicates that there is an increase of bulk or grain boundary diffusion under microwave heating more than an increase of surface diffusion [92]. The authors comment that structural and kinetic differences occur during microwave and conventional sintering which make comparison of the calculated activations energies actually a comparison of two different processes [92].

Smith, Janney and Mayotte investigated grain growth in dense, hot pressed alumina after microwave and conventional annealing cycles [92]. The grain growth in

microwave heating was accelerated compared to grain growth in conventional heating [92]. The activation energies for grain growth were 480 and 590 kJ/mol (4.98 and 6.12 eV) for microwave and conventional heating, respectively [92]. Janney et al. comment that the difference in grain boundary growth activation energy was smaller than the difference in sintering activation energy because grain boundary growth was the same process structurally in both microwave and conventional heating while the sintering activation energy represents both diffusional and structural differences in microwave and conventional heating [92].

Nightingale et al. studied the sintering and grain growth of 3 mol% yttria zirconia under microwave and conventional heating [93]. The densities of samples sintered with microwave heating were higher at lower temperatures compared to samples heated conventionally [93]. For samples less than 96 % theoretically dense, the grain size of microwave heated specimens was smaller than that for specimens of similar density which were heated conventionally [93]. The grain size/density effect in microwave heating was attributed to a greater increase in lattice diffusion during microwave heating than surface or grain-boundary diffusion [93]. For 3 mol% yttria zirconia samples which were greater than 96 % theoretically dense, grain growth was found to be accelerated in microwave heating and resulted in exaggerated grain growth [93].

Cheng et al. [94] studied the densification of alumina during microwave and conventional sintering by measurement of density, shrinkage and grain size [94]. The sintering rates for microwave heating were found to be much higher than for conventional heating [94]. The sintering shrinkage and the grain size data were fit to

densification rate and grain growth rate models [94]. Data fit to the model indicated that the grain growth during microwave heating was lattice diffusion controlled [94]. The model for densification rate show that the diffusion coefficient for microwave sintering at 1200 °C was 3 times that for conventional sintering [94].

Wroe and Rowley [95] studied the sintering of 3 mol% yttria zirconia using a hybrid furnace which allowed the simultaneous application of microwave and radiant heat [95]. Radiant heating elements in the hybrid furnace could increase the sample temperature while microwave power could be applied continuously, switched on or off, or pulsed [95]. Compared to sintering by conventional heating only, microwave-assisted sintering was found to be enhanced with final densities higher for all samples sintered in a microwave field [95]. To achieve the same value of linear shrinkage the microwave-assisted sintering temperature was about 80 - 100 °C lower than conventional sintering [95].

In Wroe and Rowley's hybrid furnace investigation [95], when the electric field was switched off during densification, the shrinkage nearly stopped before resuming along the shrinkage versus temperature curve for conventional heating [95]. Conversely, when the electric field was switched on during conventional heating the shrinkage increased rapidly and eventually followed the shrinkage versus temperature curve for microwave heating [95]. The shrinkage behavior after switching the microwave field on or off indicates that the microwave enhancement is non-thermal in nature and is consistent with being dependent on the microwave generated electric field, E [95]. Enhancement of either volume or grain boundary diffusion by the microwave field is implied since there was evidence of microwave enhancement only

in the densification stage of sintering and not during the initial sintering stage [95].

Temperature measurement problems have been cited as a possible explanation for the diffusion increase in sintering via microwave heating. If the temperature during microwave sintering was actually higher than measured then that could account for the reported microwave enhancement of diffusion. However, temperature would have to be underestimated by 100 to 400 °C if there was no microwave enhancement [90, 92, 95]. Janney et al. [91] have simultaneously measured the temperature in the microwave furnace with a thermocouple, 2-color IR pyrometer, and a fiber optic light pipe [91]. Temperature agreement of ±20 °C was found among the different methods for samples of silicon carbide, silicon/silicon nitride, alumina and zirconia at temperatures of 500 - 1500 °C [91]. Janney et al. [91] further verified microwave heating temperature measurements, when, below the 1410 °C melting point, they found no melting of a silicon sample while at temperatures above the melting temperature large pools of silicon were observed [91].

Some have suggested that there is an error in temperature measurement for microwave heated samples which resulted from the grain boundaries being at a higher temperature than the grains [96]. The higher temperature is suggested to be the result of grain boundaries which couple more with the microwaves than the bulk, absorbing more microwave energy [96]. The enhanced sintering of ceramics would then be the result of accelerated grain boundary diffusion caused by grain boundaries which are at a significantly higher temperature than the bulk temperature (which is the measured and reported temperature) [96]. Johnson [96] investigated this possibility using heat flow calculations for a model system of alumina grains with diameters of 10 μm and

of grain boundaries which readily absorb microwave energy [96]. The heat flow calculations indicated that for the small dimensions of grain boundary thicknesses and grain sizes involved, the temperature difference between the grain boundaries and grains will be a small fraction of a degree [96].

Wroe and Rowley discuss the possibility that an error in microwave heating temperature measurement results from specimen surface temperatures being lower than the bulk [95]. Samples heated in a conventional furnace absorb heat at the sample surface into the bulk, while samples heated in a microwave furnace generate heat throughout the entire specimen volume and loose heat at the surface [95]. If the sample temperature was lower than the surface temperature then a difference in properties would be expected at the surface compared to the bulk. However, a detailed study of grain size in microwave sintered samples showed a uniform microstructure indicating a uniform temperature existed during microwave heating [95].

4.4.4 Diffusional Healing Model

In this dissertation, Stevens and Dutton's model for high-temperature static-fatigue crack growth [56] is applied to the description of the temperature dependence of crack healing for indentation cracks in Coors alumina specimens subjected to both conventional and microwave heating. As a background for this study, crack healing studies by Raj et al. [55] and by Wang et al. [30] are re-analyzed.

4.4.4.1 Review of Healing in LiF by Raj et al. [55]

Partial (100) cleavage cracks were made in lithium fluoride single crystals of dimensions with 5 mm X 5 mm X 10 mm (Figure 127) [55]. The initial crack front was observed optically in the [100] direction by focusing into the crystal [55].

The specimens were thermal annealed in air at temperatures of 636 to 760 °C. A mean crack length was calculated from optical measurements at six positions along crack front (Figure 128) [55]. After a 40 hour-long transient phase, the crack healing rate reached a steady state [55]. During the transient phase the crack morphology may be undergoing a change to an equilibrium crack shape which then remains relatively constant with an equilibrium value of crack tip radius during the steady state healing phase. The portion of Raj's data which is re-analyzed in this dissertation, is the steady-state healing data.

The crack tip profile was similar at all temperatures, with the crack healing process leading to crack tip blunting [55]. Raj et al. fit their crack healing data to an Arrenhius function (Figure 129) [55], which yielded an activation energy of 0.868 eV (83.7 kJ/mol) for temperatures below 700 °C (Figure 129). The same Arrenhius plot shows an activation energy of 2.00 eV (192.9 kJ/mol) for temperatures above 700 °C (Figure 129). Raj et al. conclude that for $T > 700$ °C healing in LiF was dominated by volummetric diffusion since the experimentally-determined activation energy of 2.0 eV is similar to value of 2.20 eV (212.3 kJ/mol) found for the volummetric activation energy for fluorine diffusion [reference 8 in [55]]. For $T < 700$ °C, Raj et al. assumed crack healing to be dominated by surface diffusion, and the argument presented by Raj et al. was the "surface diffusion activation energy is expected to be about half that for

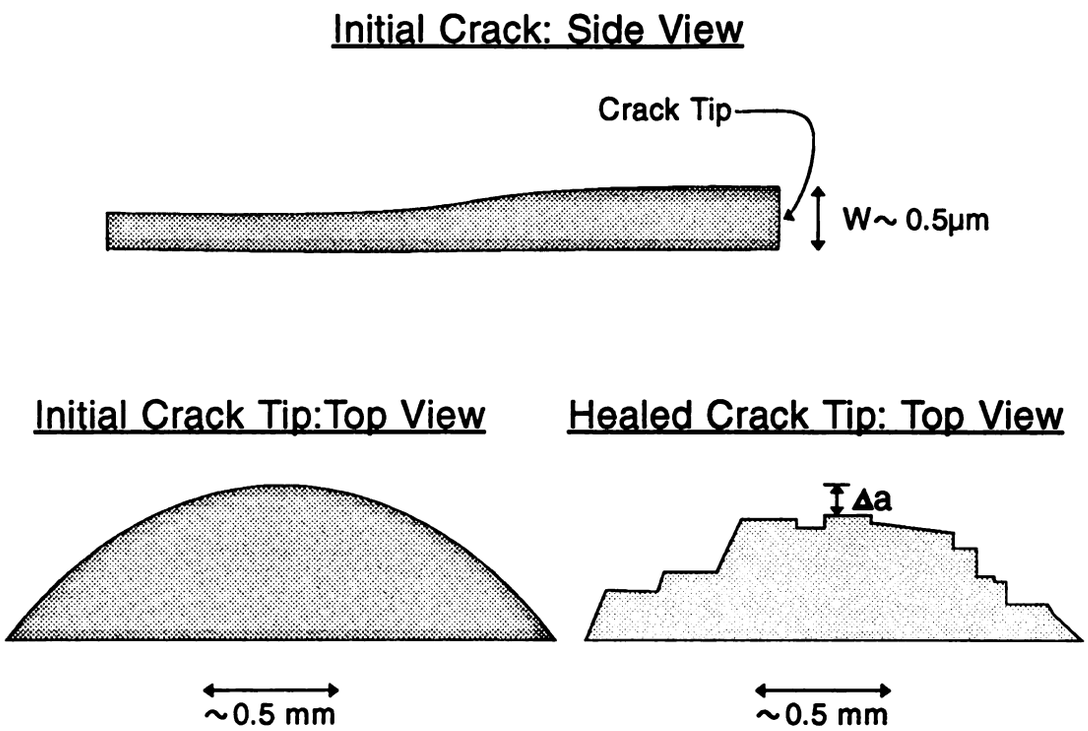

Figure 128 Schematic of cracks used by Raj et al. [55] to study crack healing in LiF single crystal samples.

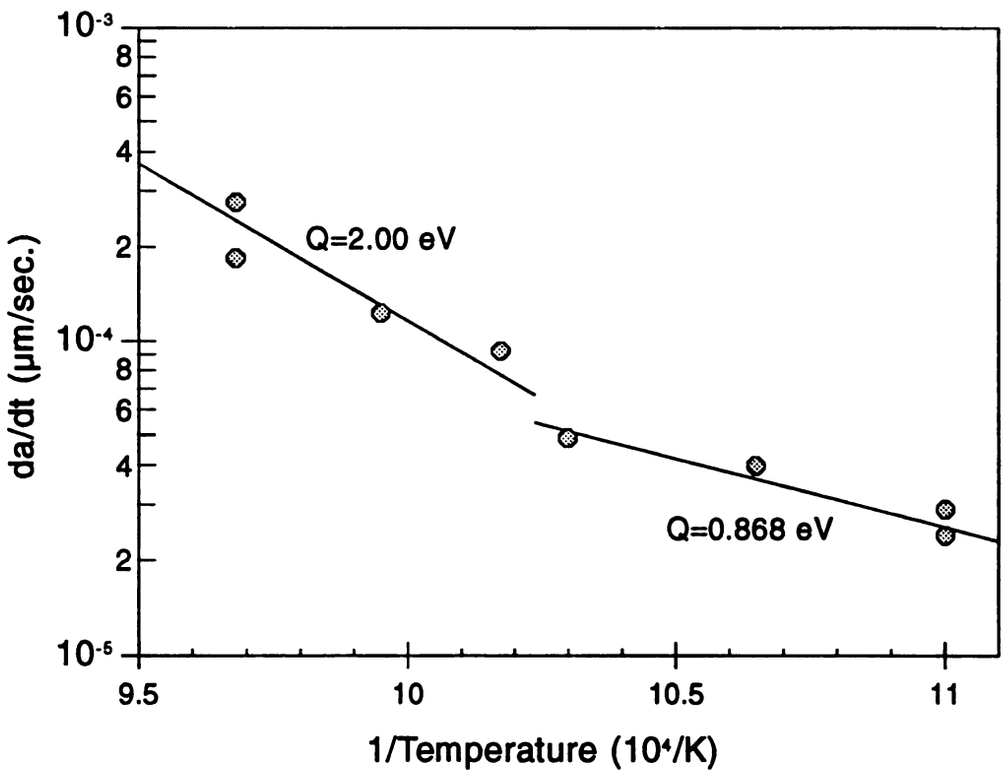

Figure 129 Plot used by Raj et al. to determine the activation energy for healing in single crystal LiF [55].

volume diffusion" or approximately 1.10 eV (106.2 kJ/mol) [55].

4.4.4.2 Review of Healing in LiF by Wang et al. [30]

Wang and Harmer [30] used in-situ optical microscopy to observe healing of internal cracks in 10 mm X 5 mm X 3 mm single crystals of LiF. A laser pulse created three mutually orthogonal penny-shaped internal cracks approximately 1 mm long on the {100} planes in the specimens [30].

During isothermal annealing in the temperature range of 620 °C to 820 °C, the cracks healed in stages marked by distinct morphological changes: 1) pinching-off of plane cracks into cylindrical pores aligned in the radial direction away from the crack center, 2) ovulation of cylindrical <110> pores into square-shaped pores, 3) regression of cylindrical <100> pores, 4) development and regression of large plate-shaped pores or subcracks, and 5) shrinkage of isolated pores [30].

At a particular annealing temperature, Wang cooled the LiF specimens to room temperature (at a rate of 20 °C/minute) and then removed the specimen from the furnace for optical microscopy of the pore morphology and subcrack dimensions [30]. The subcrack shrinkage rate was strongly effected by the subcrack's maximum COD, but not by the initial subcrack length or by annealing time [30]. Consequently, the shrinkage rates were measured at a given subcrack thickness of approximately 0.2 μm by choosing similar parent-cracks and subcracks [30]. The mean and standard deviations of the crack shrinkage rates were determined by measurements on three to ten subcracks [30].

The activation energy associated with subcrack healing was inferred [30] from

the Stevens and Dutton model [56]. Stevens and Dutton initially derived their model for static fatigue crack growth, but Wang et al [30] demonstrate that the model can successfully describe crack healing. For the case of no externally applied stress the Stevens and Dutton model [56] becomes

$$\frac{\partial a}{\partial t} = \frac{\pi D}{R \ln\left(\frac{L_o}{R}\right)} \left[1 - \exp\left(\frac{\gamma \Omega}{R k T}\right)\right] \tag{26}$$

where a is the crack length, t is time, D is the diffusivity, R is the radius of curvature of the crack edge, L_o is the distance from the crack edge to the external bulk surface, γ is the surface free energy, Ω is the atomic volume, k is the Boltzmann's constant, and T is the temperature [30]. Wang et al. [30] re-write Equation 26 as

$$\frac{\partial a}{\partial t} = \frac{C}{T} \exp\left(-\frac{Q}{kT}\right) \tag{27}$$

where Q is the activation energy for diffusion that dominates the crack healing process.

$$C = \frac{\pi D_o \gamma \Omega}{k R^2 \ln\left(\frac{L_o}{R}\right)} \tag{28}$$

D_o is the preexponential diffusion factor. Wang et al. [30] find an activation energy for subcrack healing of 2.0 eV (192.7 kJ/mol) (Figure 130).

4.4.4.3 Re-Examination Raj et al. [55] and Wang et al. [30]

Wang et al. [30] state that the activation energy calculated using the Stevens and Dutton model and their data for the healing of internal cracks in LiF agree with Raj's activation energy for volume diffusion mechanism that Raj et al. [55] infer from their data for healing surface cracks in LiF. Wang et al. [30] add that although Raj et al. report surface-diffusion dominated healing at low temperatures, surface diffusion should not be significant in their (Wang's [30]) study since no direct surface path existed from the internal cracks to external surface for the laser-induced cracks. However, unlike the Wang study, Raj et al. [55] used only an Arrenhius form to analyze their data [Figure 6 in reference [30]]. Raj et al. reference the Stevens and Dutton paper [56], but they failed to apply the Stevens and Dutton model to their data.

When the Dutton and Stevens model [56] was used to plot Raj's [55] crack healing data, the re-plotted Raj [55] data gives a single activation energy for diffusion of 1.48 eV (142.8 kJ/mol). No evidence for two activation energies is seen in the re-plotted data (Figure 131). A single activation energy implies a single diffusion process, but Raj's Arrenhius plot (apparently with two differing slopes) had been interpreted by both Raj [55] and subsequently by Wang [30] as indicative of two distinct diffusion processes which dominate at differing temperature regimes.

A value of C = 1.4×10^9 μm*K/s was obtained from the intercept of the authors' re-plot of Wang's healing data, least-squares fit to the Stevens and Dutton model, Equation 27 (Figure 130). The authors extrapolated intercept value for C was similar to the 2.2×10^9 μm*K/s value reported by Wang et al. [30], also extrapolated from the intercept of their data. In addition to determining C via the intercept, Wang et al. [30]

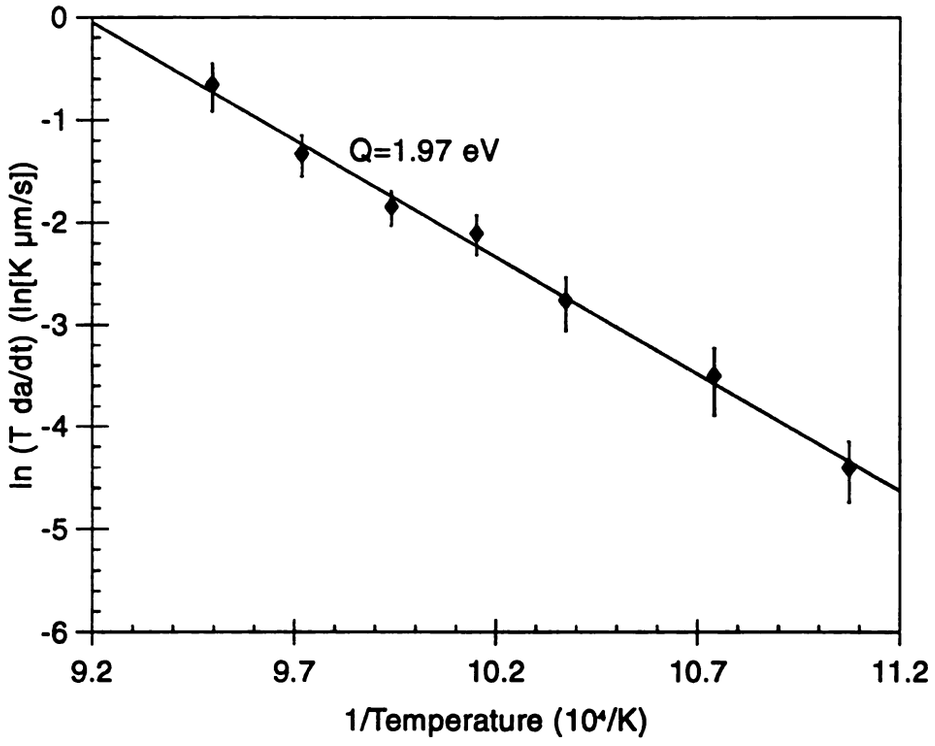

Figure 130 Plot to determine the activation energy for healing using model of Stevens and Dutton [56] for data of laser induced cracks in LiF by Wang et al. [30].

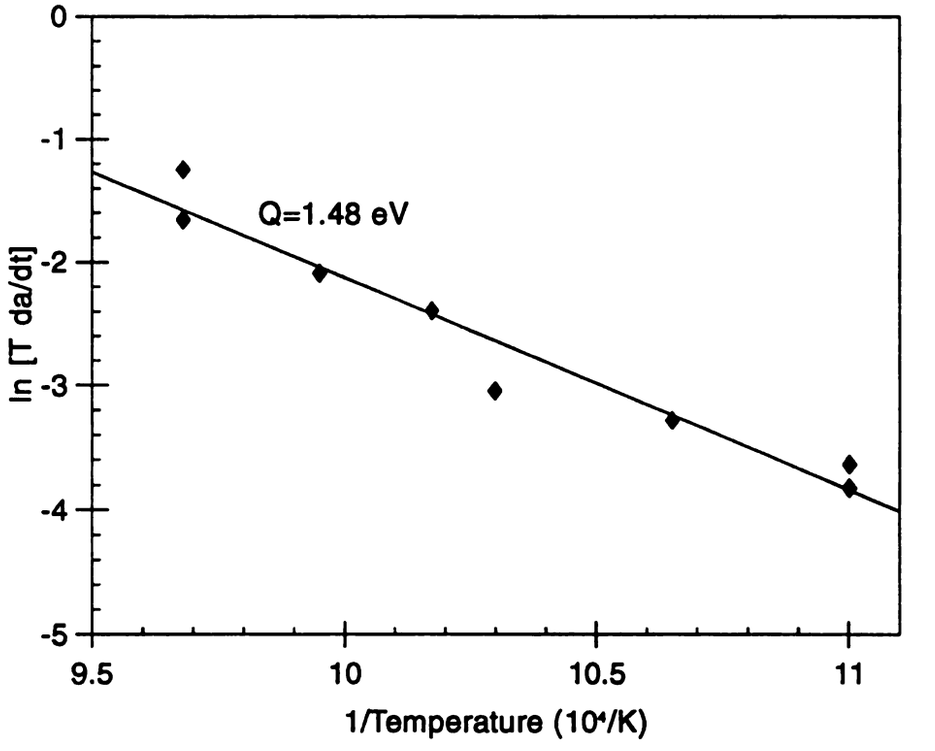

Figure 131 Determination of the activation energy using model by Stevens and Dutton [56] for healing of data of Raj et al. [55] for racks in LiF.

found C = $8.7x10^9$ μm*K/s using Equation 28 and the data: D_o = to 6.3 cm^2/s (for single vacancy migration in fluorine, reference 29 cited by Wang [30]), γ = 0.34 J/m^2, Ω = $1.6x10^{-23}$ cm^3, k = $1.38x^{-23}$ J/atom/K, R = 0.1 μm, and L_o = 1 mm (where each parameter is defined in Equations 27 and 28). However, when the present authors recalculated C based on Equation 28 and the data listed here, a C value of $8.7x10^{11}$ μm*K/s, which (to two significant figures) is precisely two orders of magnitude larger than the C value reported by Wang et al. [30].

The two-orders-of-magnitude shift in the value of C significantly affects Wang's D_o value, which is $1.64x10^{-2}$ cm^2/s as calculated from Equation 28 using their value for C which is two orders of magnitude smaller than the literature value Wang et al. [30] quote for diffusion (from reference 29 as cited by Wang et al. [30], D_o = 6.3 cm^2/s). No value for D_o was determined by Raj et al. [55] for the healing in LiF, but D_o can be calculated from the Stevens and Dutton model [56]. From Figure 131, the intercept of the best fit line was 15.03 which results in a C value of $3.37x10^6$ μm*K/s (Equation 27). The average crack tip width in the Raj et al. study [55] was 0.32 μm, implying a crack tip radius, R, of 0.16 μm. Lo, the distance from the crack tip to the specimen surface was 0.37 cm. D_o was $7x10^{-5}$ cm^2/s using Equation 28 with γ = 0.34 J/m^2, Ω = $1.6x10^{-23}$ cm^3 [30], R = 0.16 μm, and L_o = 0.37 cm. D_o found from Wang's healing data [30] was three orders of magnitude higher than D_o calculated value from Raj's data using Equation 28 [55].

The difference of the single activation energy for diffusion of 1.5 eV for the crack healing study by Raj et al. [55] with the Q of 2.0 eV for healing of internal cracks Wang et al. coupled with the several orders of magnitude difference in

magnitude of D_o between the two healing studies, indicates that different diffusional healing processes were occurring in the two studies. The difference in Q and D_o values could also be the result of the dramatic difference in crack systems together with the inability of the model by Stevens and Dutton [56] to account for these differences with the geometric terms R and L_o. The possibility of the differences in crack systems leading to different Q and D_o values demonstrates the importance of having identical crack systems in order to compare diffusive crack healing.

4.4.4.2 Conventional Healing in Coors and Microwave Sintered Alumina

The Coors alumina healing data from Section 4.4.2.2.1 shows a linear relationship when plotted to Equation 27, with a correlation coefficient of 0.981 (Figure 132). A large scatter in crack lengths for microwave sintered alumina results in a large data scatter when plotted to Equation 27 (Figure 132). The slopes for the Coors alumina and microwave sintered alumina were -10245 and -4414 (K), respectively (Figure 132), corresponding to activation energies of 0.883 and 0.380 eV for Coors alumina and microwave sintered alumina, respectively. The activation energy for Coors alumina is more than twice that of microwave sintered alumina, however, the large uncertainty in the microwave sintered alumina activation energy makes any final conclusions about the similarities or differences between the two aluminas difficult.

Gupta [97] gathered surface diffusion activation energies in polycrystalline and single crystal alumina from the literature. The activation energies for surface diffusion in healing-like processes such as thermal grooving, scratch smoothing, and void breakup ranged from 3.26 to 5.77 eV while the activation energies for surface

diffusion in the initial stage of sintering ranged from 2.43 to 2.77 eV. Kingery et al. [24] show self-diffusion coefficients for oxygen in alumina with many of the data sets for diffusion at temperatures above 1500 °C. One typical data set shows an activation energy for oxygen ion diffusion in polycrystalline alumina of 4.72 eV and a preexponential diffusion factor of 1.48 cm^2/s [24]. However, the only data points for temperatures between 1200 and 1422 °C have a different activation energy for oxygen self diffusion in alumina of 1.76 eV and a preexponential diffusion factor of $2.5x10^{-9}$ cm^2/s [24]. In grain boundary grooving experiments, Tsoga et al. [98] values for surface diffusion activation energies and preexponential factors at temperatures below 1450 °C were lower than other experimenters found for temperatures above 1450 °C. In regard to the creep of polycrystalline alumina, Richerson [8] comments that for grain sizes of 5 to 60 μm, lattice diffusion of Al^{3+} ions controls the creep process, while for finer grain-sized alumina and for temperatures below 1400 °C, creep is controlled by Al^{3+} diffusion along the grain boundaries. For the present study, at 1005 - 1469 °C the activation energies in Coors and microwave sintered alumina of 0.883 and 0.380 eV were much lower than the values of 2.43 to 2.77 eV reported in the literature for surface diffusion at temperatures above 1500 °C. However, surface diffusion activation energies at temperatures less than 1500 °C for diffusion studies [24], grain boundary grooving experiments [97], and creep [8] are in the range of 1.76 to 2.66 eV, which are comparable to the values found for the healing of Coors and microwave sintered alumina.

4.4.4.3 Conventional and Microwave Healing in Coors Alumina

Section 4.4.3 discussed healing in Coors alumina from conventional and microwave healing. Applying the data recorded in Section 4.4.3 to the model by Stevens and Dutton [56] allows a direct comparison of the activation energies for healing in conventional and microwave heating (Figure 133). The slope is directly proportional to the activation energy (Equation 27), thus the activation energy for conventional healing was smaller than that of either microwave heating rates while the slow microwave heating had a larger activation energy than the fast microwave heated sample (Figure 133 - 135).

Isolation of only one type of heating on a single plot, reveals that the activation energies appeared to be equivalent for the 49 and 98 N indent cracks with the same type and rate of heating (Figure 136 - 137). The 49 and 98 N indent cracks on a given sample, had identical thermal histories. The identical activation energies imply that an similar diffusion process likely occurred for the 49 and 98 N indent crack for the same thermal history. The reason for differing intercept values for 49 and 98 N indent cracks (Figure 136 - 137) will be analyzed later in this section. The intercept is related to the preexponential diffusion factor, D_o, the crack tip radius, r, and the length from the crack tip to the bulk surface, L (Equation 28).

The 49 and 98 N indent cracks were used together for determining the best fit line and thus the activation energy for a given heating type and rate. To accomplish this, the mean difference, Δy, between the ln (T dc/dt) values for the 49 and 98 N indent cracks at each of the 5 temperatures was determined for each heating type and rate. The mean difference, Δy, was 0.34, 0.41, 0.39 for conventional heating at a slow

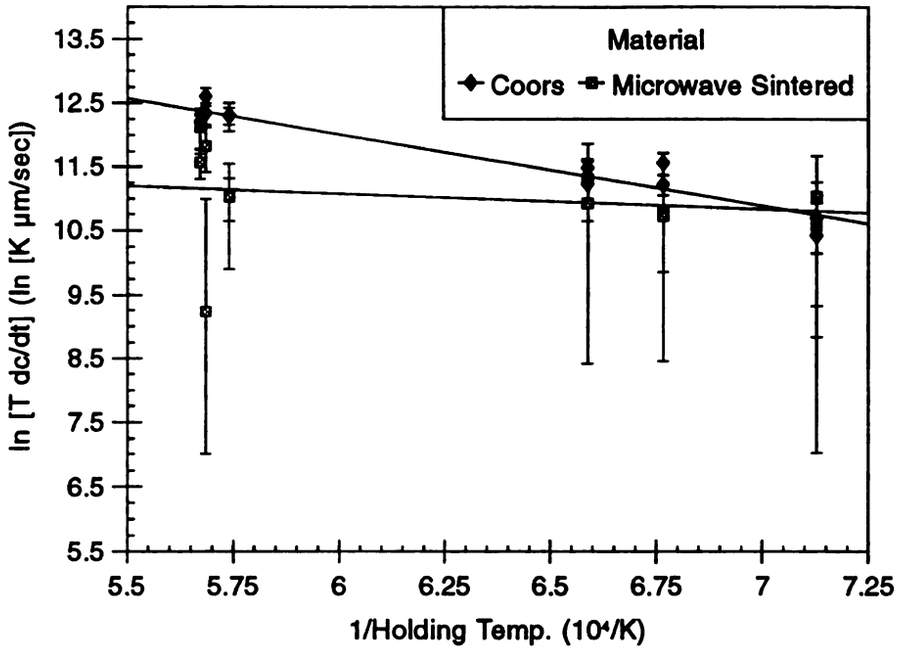

Figure 132 Healing for cracks in alumina heated conventionally at a slow rate of 10 °C/ minute (data from Conventional Healing in Alumina Experiment 1, Section 4.4.2.2.1). The lines represent a least-squares fit of the data to the model by Stevens and Dutton [56]. (Error bars indicate standard deviations of six cracks).

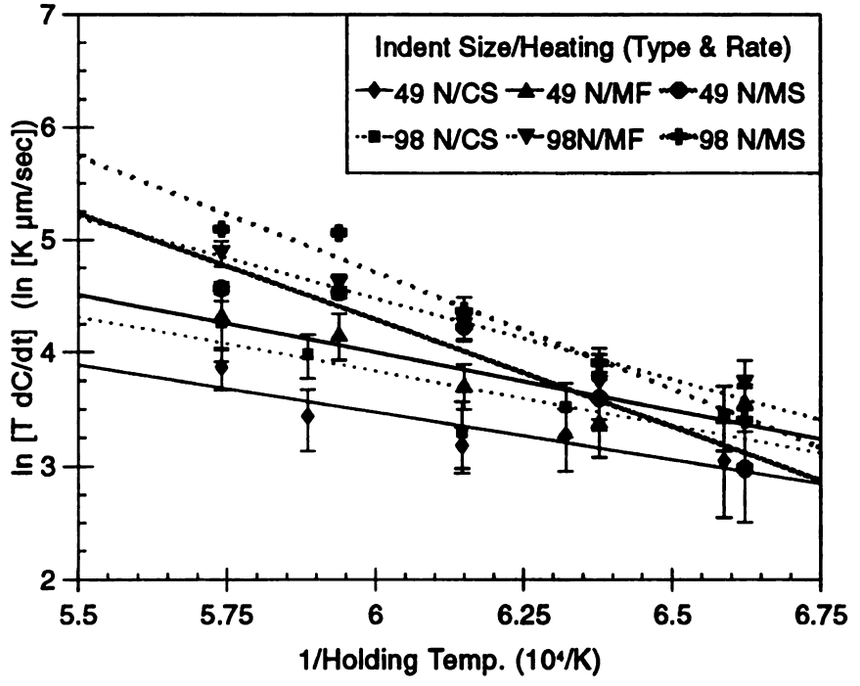

Figure 133 Healing for cracks heated conventionally at a slow rate of 10 °C/min. (CS) or heated via microwaves at a slow (MS) or fast (MF) rate of 75 °C/min. (data from Section 4.4.3). The lines represent a least-squares fit of the data to the model by Stevens and Dutton [56]. (Error bars indicate standard deviations of six cracks).

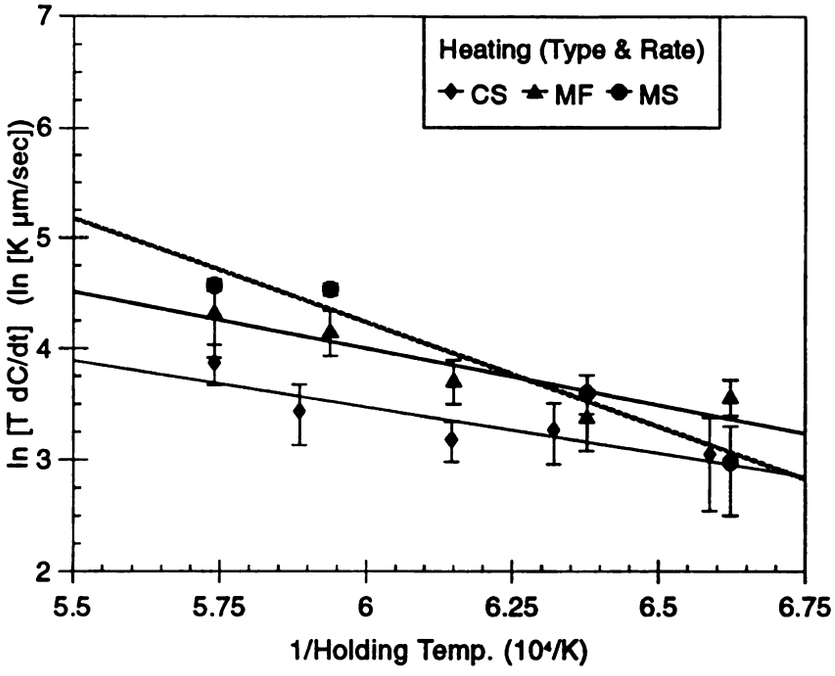

Figure 134 Healing of 49 N cracks heated conventionally at a slow rate of 10 °C/min. (CS) or heated via microwaves at a slow (MS) or fast (MF) rate of 75 °C/min. (data from Section 4.4.3). The lines represent a least-squares fit of the data to the model by Stevens and Dutton [56]. (Error bars indicate standard deviations of six cracks).

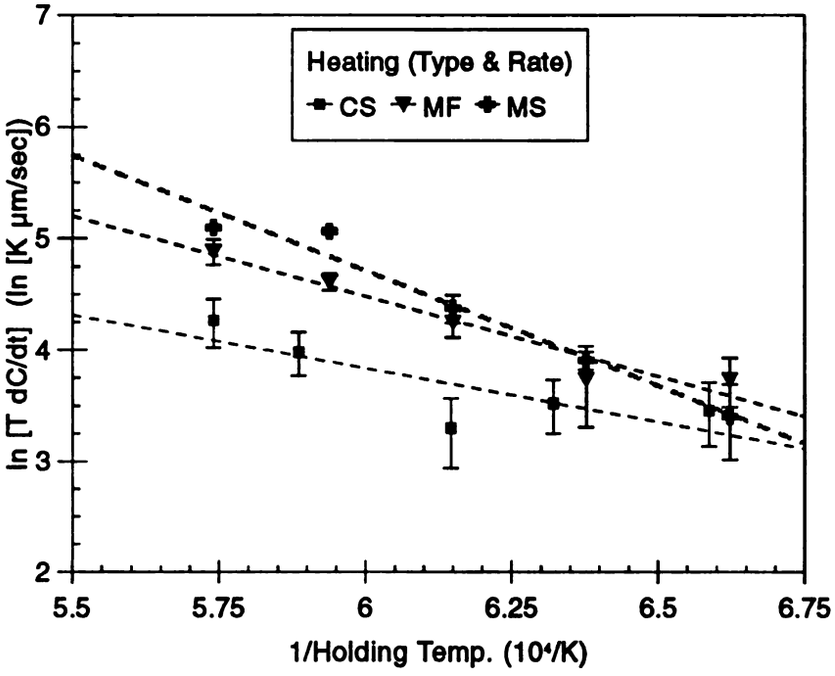

Figure 135 Healing of 98 N indent cracks heated conventionally at a slow rate of 10 °C/min. (CS) or via microwaves at a slow (MS) or fast (MF) rate of 75 °C/min. (data from Section 4.4.3). The lines represent a least-squares fit of the data to the model by Stevens and Dutton [56]. (Error bars indicate standard deviations of six cracks).

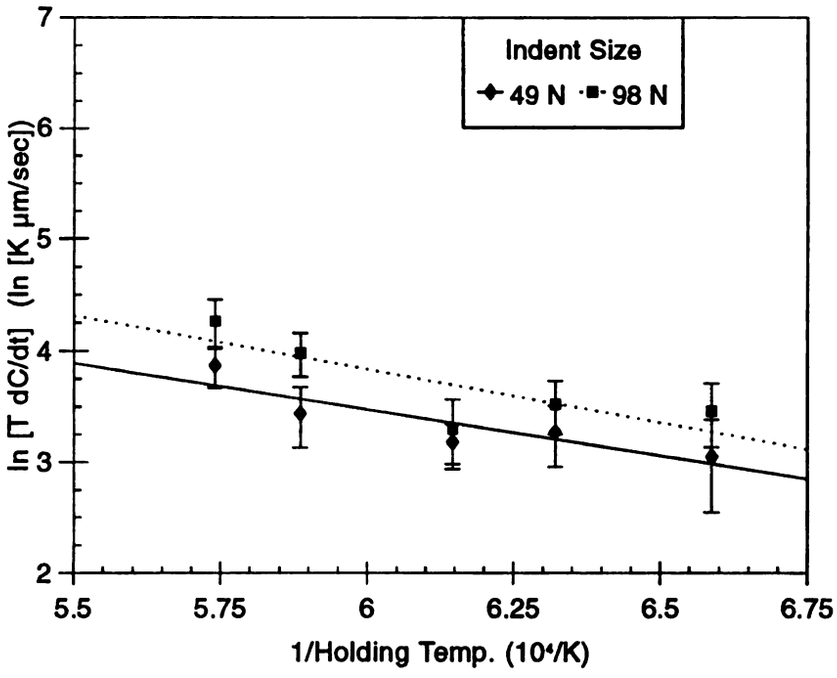

Figure 136 Healing for 49 and 98 N indent cracks heated conventionally at a slow rate of 10 °C/min. (CS) (data from Section 4.4.3). The lines represent a least-squares fit of the data to the model by Stevens and Dutton [56]. (Error bars indicate standard deviations of six cracks).

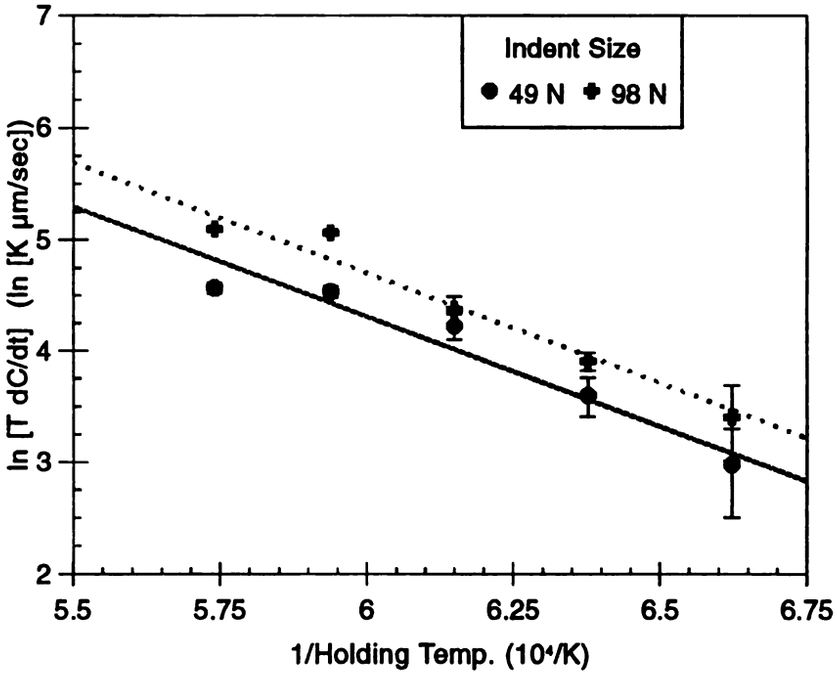

Figure 137 Healing for 49 and 98 N indent cracks heated via microwaves at a slow (MS) rate of 10 °C/min. (data from Section 4.4.3). The lines represent a least-squares fit of the data to the model by Stevens and Dutton [56]. (Error bars indicate standard deviations of six cracks).

ramp rate, microwave heating at a fast ramp rate, and microwave heating at a slow ramp rate, respectively. The ln(T dc/dt) data of the 49 N indents and the {ln (T dc/dt) - Δy} data of the 98 N indents were combined and a best fit line of the combined data was determined (Figure 138).

The activation energies determined from the combined data were 0.77, 1.06, and 1.70 eV for slow conventional, fast microwave, and slow microwave heating, respectively. The activation energy for diffusional healing in Coors alumina was higher for microwave heating than in conventional healing and the highest activation energy for diffusional healing for the microwave heating was at the slower rate.

As discussed in Section 4.4.3.4, some investigators attribute reported differences between microwave and conventional diffusion to an under-measurement of the actual specimen temperature during microwave heating. To test whether temperature measurement errors could account for the difference observed in activation energies for healing in microwave and conventional healing in the present study, the temperatures for the microwave specimens were adjusted to force the activation energies to be identical to the activation energy for healing of Coors alumina with conventional heating (Figure 139). The result is that the temperatures for fast and slow microwave heating would have to be DECREASED by 255 and 555 °C, respectively, to obtain the same activation energy found for conventional heating. Since it is highly unlikely that the temperatures were over-estimated by 255 or 555 °C during microwave heating, the experimental data in conjunction with the Stevens and Dutton model demonstrate that the diffusion differences in microwave and conventional heating cannot be entirely the result of temperature measurement errors.

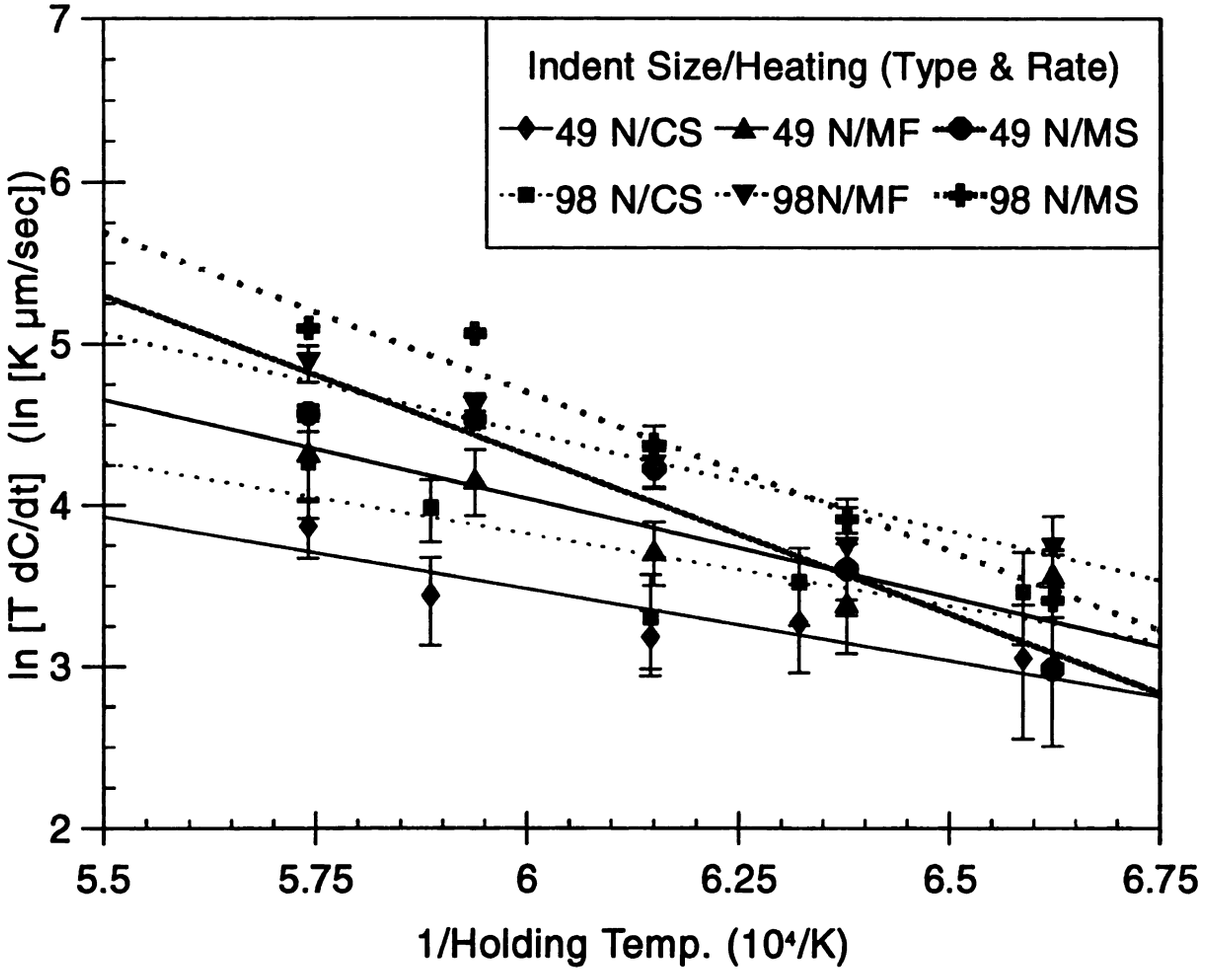

Figure 138 Healing for 49 and 98 N indent cracks heated conventionally at a slow rate of 10 °C/min. (CS) or heated via microwaves at a slow (MS) or fast (MF) rate of 75 °C/min. (data from Section 4.4.3). The lines represent a least-squares fit of the data to the model by Stevens and Dutton [56]. Equal slopes were forced for data with identical thermal histories. (Error bars indicate standard deviations of six cracks).

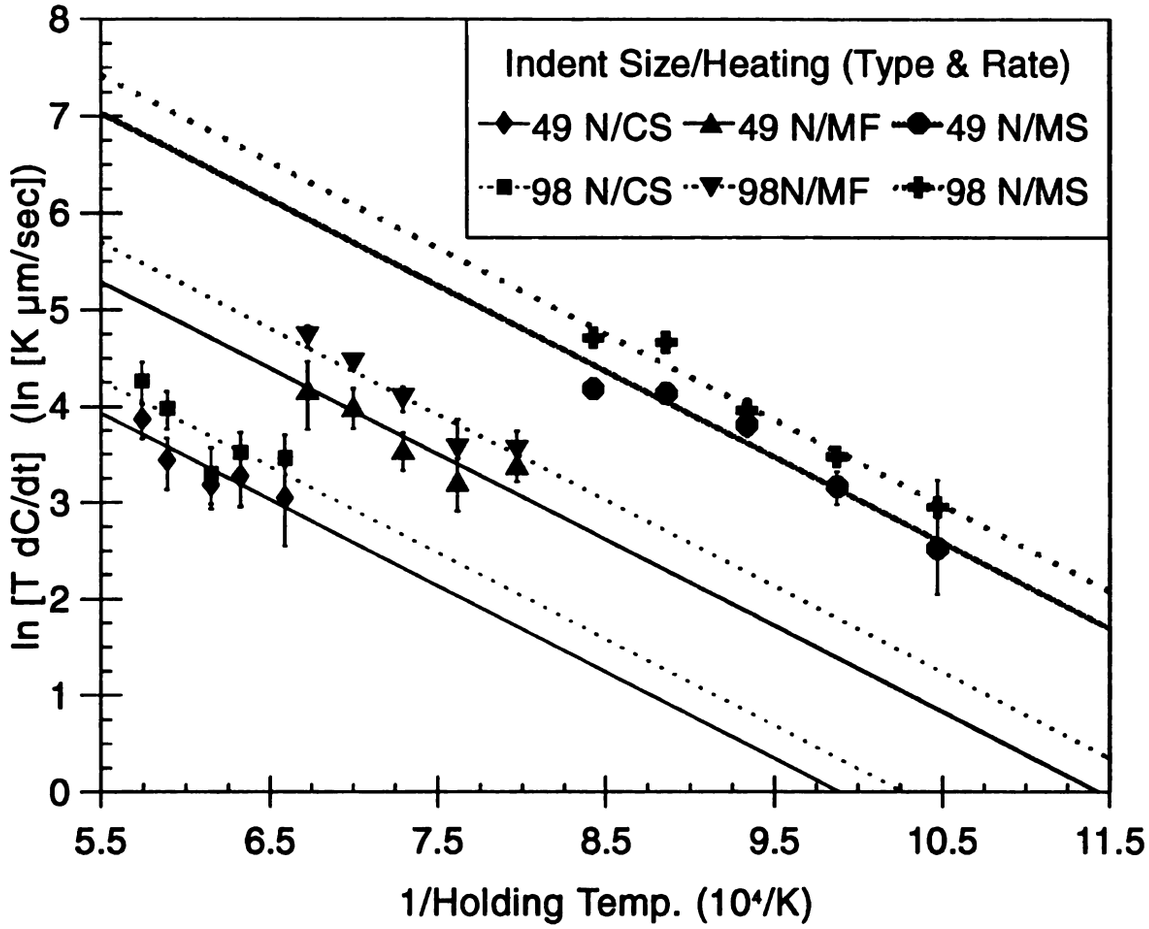

Figure 139 Healing for 49 and 98 N indent cracks heated conventionally at a slow rate of 10 °C/ minute (CS) or heated via microwaves at a slow (MS) or fast (MF) rate of 75 °C/ minute (data from Section 4.4.3). The lines represent a least-squares fit of the data to the model by Stevens and Dutton [56]. Equal slopes were forced for data with identical thermal histories. The fast and slow microwave data has been forced to be equal by subtracting 255 and 555 °C, respectively, from the measured microwave healing temperatures (Error bars indicate standard deviations of six cracks).

The preexponential diffusion factor, D_o, can be determined from the intercept of the plots to Stevens and Dutton's model [56] (Figure 132 - 138) and the material property data for alumina, γ equals $1x10^3$ ergs/cm^2 [56], Ω equals $1.4x10^{-23}$ cm^3 [56], k equals $1.38x10^{-16}$ ergs/atom*K, L equals the grain size of Coors alumina which was 2.1 μm, and r equals the crack tip radius which can be taken as the atomic radius of $6x10^{-4}$ μm [56] since cracks in ceramics have traditional been treated as being atomically sharp. The preexponential factors for the 49 N indents in Figure 136 were $1.29x10^{-10}$, $1.67x10^{-9}$, and $1.93x10^{-7}$ cm^2/s for slow conventional, fast microwave, and slow microwave heating, respectively. If the geometric factors, L and r, are identical for the 49 and 98 N indent cracks then the values for the preexponential factor are different. Using the same L and r values for the 98 N indents, results in preexponential factors from Figure 136 of $1.81x10^{-10}$, $2.52x10^{-9}$, and $2.58x10^{-7}$ cm^2/s for slow conventional, fast microwave, and slow microwave heating, respectively.

Since the 49 and 98 N indents were on the same sample, one might expect D_o(49N) to be equal to D_o(98N). If the D_o values for both indent sizes were nominally identical, then values for L and r cannot both be the same for 49 and 98 N indents. If it is assumed that L is still equal to the grain size (as was described by Dutton and Stevens [56] in their model), then L would be the same for both indent sizes. The crack tip radius, r, would need to be different for the different indents if the D_o values are to be approximately identical. As a first approximation for r, the crack tip radius for a crack of length, 2c, could be considered to differ for the 49 and 98 N as $\{6x10^{-4}\mu m*\sqrt{(1000/c)}\}$, then the preexponential factors for the 49 N indents from Figure 136 become $8.05x10^{-10}$, $1.04x10^{-8}$, and $1.20x10^{-6}$ cm^2/s for slow conventional, fast

microwave, and slow microwave heating, respectively, and for the 98 N indents become 7.25×10^{-10}, 1.01×10^{-8}, and 1.14×10^{-6} cm^2/s for slow conventional, fast microwave, and slow microwave heating, respectively.

5. SUMMARY AND CONCLUSIONS

5.1 Static Fatigue Crack Growth

Specimen preparation techniques need to be improved to eliminate the torsional stresses that develop as a result of non-parallelness of the bonded tabs (Section 4.3.1.3, and 4.3.2). For the indented polycrystalline alumina specimens, no crack growth was observed at 10% r.h. level (at least for the load levels and times used for the polycrystalline alumina specimens studied) (Section 4.3.2). The static fatigue process for the alumina specimens observed to date takes place with a mean crack velocity such that the crack growth can be observed, at least for increments on the scale of the grain dimension (Section 4.3.2). The in-situ observation of the environmental-assisted growth of the indent cracks revealed that during static fatigue of alumina, grain bridging occurs (Section 4.3.2).

The crack paths followed during static fatigue in Coors alumina were semi-tortuous with bridging grains behind the crack tip and crack tip deflection on the order of the diameter of a single grain (Figures 29-31, 35-38 in Sections 4.3.2.3, 4.3.2.5, and 4.3.2.6). During static fatigue of Coors alumina, significant growth of both cracks upon the first static fatigue cycle, followed by limited small crack growth for the subsequent static fatigue cycle (Section 4.3.2). The static fatigue in several alumina specimens with different applied stress-time paths appeared to show very similar static

fatigue behavior for a plot of relative change in crack length as a function of constant applied tensile stress (Section 4.3.2.7).

5.2 Crack Healing

5.2.1 In-Situ ESEM Observation of Soda-Lime Silica Glass

In-situ electron microscopy was used to observe healing of semi-macro indent cracks in soda-lime silica glass in a humid environment using an Environmental Scanning Electron Microscope (ESEM). Crack healing occurred at initial humidities as low as 8% and at temperatures as low as about 400 °C (Section 4.3.2.1.2). In the absence of debris wedged within the crack, healing began at the crack tip and moved toward the indent impression (Figure 58 in Section 4.3.2.1.1).

Multiple crack pinch-off was observed as a mechanism of crack healing at temperatures above 500 °C (Figures 50 - 53 in Section 4.3.2.1.1). Changing crack morphology rather than a simple crack closing indicated that the healing mechanism was not adhesion due to intermolecular forces [33, 35] (Figures 48 - 53 in Section 4.3.2.1.1). Crack pinch-off behavior observed in the soda-lime silica glass (Figure 50 in Section 4.3.2.1.1) was similar to that seen in other ceramic materials by other investigators [30-31, 34].

Debris in a crack hindered complete crack healing (Figures 54 - 58 in Section 4.3.2.1.1). The interaction between crack surface debris and the crack healing process implies that mechanically fatigued ceramic materials could have healing impeded by the debris formed during cycling.

As the initial humidity for glass samples was increased, the temperature at

which crack healing initiated decreased (Section 4.3.2.1.4.1). Healing for an initial humidity of 8 % r.h. did not begin until a heating to a temperatures above 400 °C, while for initial humidity of 64 % changes large in crack length occurred by 370 °C (Section 4.3.2.1.4.1). The crack length change for an isothermal hold at 430 °C was found to be described by an empirical equation (Equation 4 in Section 4.3.2.1.4.2) and the constants of the empirical equation appeared to be functions of the initial relative humidity (Section 4.3.2.1.4.2).

5.2.2 Conventional Healing

5.2.2.1 Soda-Lime Silica Glass

Healing in soda-lime silica glass was investigated in six different experiments on 113 specimens and 654 cracks by measuring Vickers indent crack lengths before and after thermal annealing in a conventional furnace (Section 4.4.2.1). Annealing of Vickers indented glass specimens for 30 minutes at 600 °C, resulted in a measurable decrease in crack length and an two-fold increase in the three-point bend strength (Section 4.4.2.1.1). Conventional microscopy of the partially healed indent cracks healed at temperatures 600 °C, show crack tip blunting (Figure 77) and pinch-off (Figure 80). SEM microscopy of a fracture surface of a glass specimen healed at 550 °C, revealed subsurface crack morphology changes (Figure 83) similar in appearance to crack morphology changes reported in the literature [30-32, 34].

Glass specimens without a stress relief cycle before indentation exhibited a very different behavior from specimens with a stress relief cycle consisting of heating to 550 - 500 °C with very slow cooling (Section 4.4.2.1.3). Change in crack length

from healing, Δc_{heal}, was constant with temperature from 525 to 563 °C for specimens aged in 0 and 45 % r.h. (Section 4.4.2.1.4.1) while Δc_{heal} for specimens aged in 100 % r.h. decreased constantly with temperature (Section 4.4.2.1.4.3). Specimens aged for 24 hours in 45 % r.h. had about 10 μm greater Δc_{heal} heal than specimens aged in 0 % r.h. (Section 4.4.2.1.4.1). The difference in healing for specimens aged in different levels of relative humidity was attributed to water vapor entering into the glass structure during aging and/or during annealing, which subsequently resulted in a local decrease in the glass transition temperature and viscosity along the crack surfaces (Section 4.4.2.1.4.1).

Bulk viscous flow was not found in the soda-lime silica specimens at temperatures of 587 °C or less, but was observed to occur at temperatures of 600 °C and above (Section 4.4.2.1.8.1). The difference between the mean of 22 measured indent crack lengths for 11 Vickers indents made in "as-machined" specimens and in the same specimens after undergoing a heating cycle was used to analyze the stress relieved during the heating cycle (Section 4.4.2.1.8.2). Heating cycles at temperatures of 550 °C and higher in the small tube furnace and large tube furnace all resulted in specimens with similar mean crack lengths after annealing of 210-215 μm (Tables 35 and 38 in Section 4.4.2.1.8.2), while the specimens heated in the Lindburg box furnace and specimens heated in the small tube furnace to temperatures of 525 °C and below had the largest mean crack lengths after heating of 220 μm (Tables 37 and 39 in Section 4.4.2.1.8.2).

5.3.2.2 Conventional Healing in Polycrystalline Alumina

Healing in polycrystalline alumina was investigated for two different alumina materials in two different experiments on 72 specimens and 540 cracks by measuring Vickers indent crack lengths before and after thermal annealing in a conventional furnace (Section 4.4.2.2). No effect of humidity of the aging environment was found in healing of Coors alumina or microwave sintered alumina (Section 4.4.2.2.1). Δc_{heal} increased dramatically between 1237 and 1469 °C in Coors alumina, but was relatively insensitive to temperature change in microwave sintered alumina (Section 4.4.2.2.1). The increase in Δc_{heal} from annealing times of 60 to 90 minutes was on the order of 30 μm for temperatures from 1005 to 1469 °C, while the change in Δc_{heal} from 90 to 120 minutes was within the experimental error of the crack length measurements (Section 4.4.2.2.2). Δc_{heal} was 25 to 50 μm greater for 98 N indent cracks compared to indent cracks made with a 49 N load (Section 4.4.3). However, the relative crack healing ($\Delta c_{heal}/2c_{initial}$) was found to nearly identical for the 49 and 98 N indent cracks (Section 4.4.3).

5.3.3 Microwave Healing

Healing in polycrystalline Coors alumina was investigated for 15 specimens and 180 cracks by measuring Vickers indent crack lengths before and after thermal annealing in a microwave or conventional furnace (Section 4.4.2.2). Δc_{heal} due to microwave healing was approximately the same as conventional healing for temperatures of 1237 and 1295 °C (Section 4.4.3). At temperatures of 1353 °C and higher, the percent relative change in crack length ($\Delta c_{heal}/2c_{initial}$) was 15 to 50 % higher from microwave

healing than conventional healing (Section 4.4.3). Microwave heating at a slow ramp rate of 10 °C/minute resulted in a greater amount of healing than microwave heating at a fast ramp rate of 75 °C/minute (Section 4.4.3).

5.3.4 Crack Healing Model

A re-analysis of work by Wang et al. [30] and Raj et al. [55] were made (Section 4.4.4.1.3). The diffusive crack healing in single crystal LiF by Raj et al. [55] was controlled by only a single activation energy (using the model Stevens and Dutton [56]) and not two different activation energies reported by Raj et al. [55] (Section 4.4.4.1.3). Re-analysis of the diffusive healing of internal cracks in LiF by Wang et al. [30] showed that the preexponential diffusion factor (D_o = 1.64x10^{-2} cm^2/s) was two orders of magnitude lower than reported by Wang et al. [30] (Section 4.4.4.1.3). Also, a preexponential diffusion factor (D_o = 7x10^{-5} cm^2/s) was determined for the healing work of Raj et al. [55] since one was not determined by the authors (Section 4.4.4.1.3). The preexponential factors for healing in LiF experiments by Wang et al. [30] and Raj et al. [55] were orders of magnitude lower than diffusion literature values for self-diffusion in LiF (D_o = 6.3 cm^2/s [30]).

The Stevens and Dutton model [56] was used to analyze the activation energy for the diffusive healing in alumina of the present work (Section 4.4.4.2). For Coors alumina and microwave sintered alumina conventionally heated to temperatures between 1005 and 1469 °C, the activation energies were 0.883 and 0.380 eV, respectively (Section 4.4.4.2). The activation energy for Coors alumina is more than twice that of microwave sintered alumina, however, the large uncertainty in the

microwave sintered alumina activation energy due to the large variation in crack lengths makes any final conclusions about the activation energies for the two aluminas difficult (Section 4.4.4.2). The diffusion activation energies and preexponential factors are lower than reported in the literature [24, 97], but some evidence exists in the literature for lower values at temperatures below 1500 °C [8, 24, 98] (Section 4.4.4.2).

The activation energies determined for slow conventional, fast microwave, and slow microwave heating were 0.77, 1.06, and 1.70 eV, respectively (Section 4.4.4.3). The activation energy for diffusional healing in Coors alumina was higher for microwave heating than in conventional healing and the highest activation energy for diffusional healing under microwave heating was at the slower rate (Section 4.4.4.3). The fast and slow microwave heating temperatures would have to be DECREASED by 255 and 555 °C, respectively, to obtain the same activation energy with the Stevens and Dutton model [56] found for conventional heating, indicating that the effect of microwave heating cannot be entirely due to temperature under-measurement.

6. REFERENCES

1. R.C. Buchanan, Class notes for Ceramic Engineering 201: University of Illinois (Fall 1986).

2. E.D. Case, Class notes for MSM 250: Michigan State University (Spring 1994).

3. D.W. Richerson, Modern Ceramic Engineering: Properties, Processing, and Use in Design, Marcel Dekker, New York (1982).

4. W.D. Kingery, H.K. Bowen, D.R. Uhlmann, Introduction to Ceramics, 2nd Edition, John Wiley and Sons, New York (1976).

5. W.D. Callister, Jr., Materials Science and Engineering: An Introduction, John Wiley and Sons, New York (1985).

6. N.E. Dowling, Mechanical Behavior of Materials: Engineering Methods for Deformation, Fracture, and Fatigue, Prentice Hall, Englewood Cliffs, New Jersey (1993).

7. R.W. Hertzberg: Deformation and Fracture Mechanics of Engineering Materials, 2nd Edition, John Wiley and Sons, New York (1976).

8. Modern Ceramic Engineering - Properties, Processing, and Use in Design, D.W. Richerson, Marcek Dekker, New York (1982).

9. Alumina - Processing, Properties, and Applications, E. Dörre, H. Hübner, Springer-Verlag. New York (1984).

10. T.A. Michalske, B.C. Bunker, S.W. Freiman, "Stress corrosion of ionic and mixed ionic/covalent solids," J. Am. Ceram. Soc., 69 [10], 721-24 (1986).

11. S.W. Freiman, G.S. White, E.R. Fuller Jr., "Environmentally enhanced crack growth in soda-lime glass," J. Am. Ceram. Soc., 68 [3], 108-112 (1985).

12. T.A. Michalske, S.W. Frieman, "A molecular Mechanism for stress corrosion in vitreous silica," J. Am. Ceram. Soc., 66 [4], 284-288 (1983).

13. G. Himsolt, H. Knoch, H. Huebner, F.W. Kleinlein, "Mechanical properties of hot-pressed silicon nitride with different grain structures," J. Am. Ceram. Soc., 62 [1-2], 29-32 (1979).

14. S. Baskaran, S.B. Bhuduri, D.P.H. Hasselman, "Effect of crystallites on subcritical crack growth and strain-rate sensitivity of cordierite glass-ceramics," J. Am. Ceram. Soc., 68 [3], 112-119 (1985).

15. P.F. Becher, "Slow crack growth behavior in transformation-toughened Al_2O_3-$ZrO_2(Y_2O_3)$ Ceramics," J. Am. Ceram. Soc., 66 [7], 485-488 (1983).

16. B.J. Pletka, S.M. Wiederhorn, "A comparison of failure predictions by strength and fracture mechanics techniques," J. Mat. Sci., 17, 1247-68 (1982).

17. S.M. Wiederhorn, S.W. Freiman, E.R. Fuller Jr., C.J. Simmons, "Effects of water and other dielectrics on crack growth," J. Mat. Sci., 17, 3460-3478 (1982).

18. A.G. Evans, "A method for determining the time-dependent failure characteristics of brittle materials - and its application to polycrystalline alumina," J. Mat. Sci., 7, 1137-1146 (1972).

19. S.M. Wiederhorn, L.H. Bolz, "Stress corrosion and static fatigue of glass," J. Am. Ceram. Soc., 53 [10] 543-548 (1970).

20. S.M. Wiederhorn, "Influence of water vapor on crack propagation in soda-lime glass," J. Am. Ceram. Soc., 50 [8] 407-414 (1967).

21. T. Fett and D. Munz, "Lifetime prediction for ceramic materials under constant and cyclic loads;" pp. 161-74 in Lifetime Prediction Methodologies and Data for Ceramic Materials: ASTM STP 1201, American Society for Testing and Materials, Philadelphia (1994).

22. G. Choi, S. Horibe, "Static fatigue in ceramic materials: influences of an inertgranular glassy phase and fracture toughness," J. Mat. Sci., 28, 5931-5936 (1993).

23. S.M. Wiederhorn, H. Johnson, A.M. Diness, A.H. Heuer, "Fracture of glass in vacuum," J. Am. Ceram. Soc., 57 [8] 336-41 (1974).

24. W.D. Kingery, H.K. Bowen, D.R. Uhlmann, Introduction to Ceramics, Second Edition, Wiley-Interscience, New York (1976).

25. D. S. Jacobs and I. W. Chen, "Mechanical and environmental factors in the cyclic and static fatigue of silicon nitride," J. Am. Ceram. Soc., 77[5], 1153-61, (1994).

26. T. A. Michalske and S. W. Freiman, "A molecular mechanism for stress corrosion in vitreous silica," J. Am. Ceram. Soc., **66[4]**, 284-88, (1983).

27. T. A. Michalske and B. C. Bunker, "Slow fracture model based on strained silicate structure," J. Appl. Phys., **56[10]**, 2686-93, (1984).

28. W. Wong-Ng, G. S. White, and S. W. Freiman, "Application of molecular orbital calculations to fracture mechanics: effect of strain on charge distribution in silica," J. Am. Ceram. Soc, **75[11]**, 3097-102 (1992).

29. T. A. Michalske, "The stress corrosion limit: its measurement and implications;" pp. 277 - 289 in Fracture Mechanics of Ceramics, Volume 5, edited by R. C. Bradt, A. G. Evans, D. P. H. Hasselman, and F. F. Lange, Plenum Press, New York (1983).

30. Z. Wang, Y.Z. Li, M.P. Harmer, Y.T. Chou, "Thermal healing of laser-induced internal cracks in lithium fluoride crystals," J. Am. Ceram. Soc., 75 [6], 1596-1602 (1992).

31. T.K. Gupta, "Crack healing and strengthening of thermally shocked alumina," J. Am. Ceram. Soc., 59 [5-6], 259-62 (1976).

32. C.F. Yen, R.L. Coble "Spheroidization of tubular voids in alumina crystals at high temperatures," J. Am. Ceram. Soc., 55 [10], 507-09 (1972).

33. E.D. Case, J.R. Smyth, O. Hunter Jr., "Microcrack healing during the temperature cycling of single phase ceramics;" pp. 507-530 in Fracture Mechanics of Ceramics, Vol. 5, Plenum Press, N.Y. (1983).

34. T.K. Gupta, "Crack healing in thermally shocked MgO," J. Am. Ceram. Soc., 58 [3-4], 143 (1975).

35. M.K.C. Holden, V.D. Frechette, "Healing of glass in humid environments," J. Am. Ceram. Soc., 72 [11], 2189-93 (1989).

36. R.L. Lehman, R.E. Hill Jr., G.H. Sigel Jr., "Low-temperature crack closure in fluoride glass," J. Am. Ceram. Soc., 72 [3], 474-77 (1989).

37. A.M. Thompson, H.M. Chan, M.P. Harmer, R.F. Cook, "Crack healing and stress relaxation in Al_2O_3-SiC 'nanocomposites'," J. Am. Ceram. Soc., 78 [3], 567-71 (1995).

38. B. Stavrinidis, D.G. Holloway, "Crack healing in glass," Phys. Chem. Glass, 24 [1] 19-25 (1983).

39. T.A. Michalske, E.R. Fuller Jr., "Closure and repropogation of healed cracks in silicate glass," J. Am. Cer. Soc., 68 [11], 586-90 (1985).

40. F.A. Nichols, "On the spheroidization of rod-shaped particles of finite length" J. Mat. Sci., 11, 1077-82 (1976).

41. F.A. Nichols, W.W. Mullins, "Surface- (interface-) and volume-diffusion contributions to morphological changes driven by capillarity" Trans. Met. Soc. AIME, 233 [10], 1840-48 (1965).

42. P. Hrma, W.T. Han, A.R. Cooper, "Thermal healing of cracks in glass," J. Non-Cryst. Solids, 102, 88-94 (1988).

43. D.C. Cassidy, N.A. Gjostein, "Capillarity-induced smoothing of glass surfaces by viscous flow," J. Am. Cer. Soc., 53 [3], 161-68 (1970).

44. A. Kishi, K. Fueki, K. Kitzawa, "Surface viscous flattening kinetics of soda-lime silicate glass by sinusoidal profile decay method," J. Non-Cyst. Sol., 33, 95-102 (1979).

45. F.F. Lange, T.K. Gupta, "Crack healing by heat treatment," J. Am. Ceram. Soc., 53 [1], 54-55 (1970).

46. F.F. Lange, K.C. Radford, "Healing of surface cracks in polycrystalline Al_2O_3," J. Am. Ceram. Soc., 53 [7], 420-21 (1970).

47. J.T.A. Roberts, B.J. Wrona, "Crack healing in UO_2," J. Am. Ceram. Soc., 56 [6], 297-99 (1973).

48. G. Bandyopadhyay, J.T.A. Roberts, "Crack healing and strength recovery in UO_2," J. Am. Ceram. Soc., 59 [9-10], 415-19 (1976).

49. G. Bandyopadhyay, C.R. Kennedy, "Isothermal crack healing and strength recovery in UO_2 subjected to varying degrees of thermal shock," J. Am. Ceram. Soc., 60 [1-2], 48-50 (1977).

50. M. Tomozawa, K. Hirao, P.E. Bean, "Origin of strength increase of abraded or indented glass upon annealing," J. Am. Ceram. Soc., 69 [8] C186-88 (1986).

51. K. Hirao, M. Tomozawa, "Kinetics of crack tip blunting of glasses," J. Am. Ceram. Soc., 70 [1], 43-48 (1987).

52. T.K. Gupta, "Kinetics of Strengthening of Thermally Shocked MgO and Al_2O_3," J. Am. Ceram. Soc., 59 [9-10], 448-49 (1976).

53. S.F. Flegler, J.W. Heckman Jr., K.L. Klomparens, Scanning and Transmission Electron Microscopy: An Introduction, W.H. Freeman and Company, N.Y. (1993).

54. G.D. Danilatos, "Introduction to the ESEM Instrument," Microscopy Research and Technique 25, 354-361 (1993).

55. R. Raj, W. Pavinich, C.N. Ahlquist, "On the sintering rate of cleavage cracks," Acta Metall., 23, 399-403 (1975).

56. R.N. Stevens, R. Dutton, "The propagation of Griffith cracks at high temperatures by mass transport processes," Mater. Sci. Eng., 8, 220-34 (1971).

57. C.C. Chiu, "Thermal quench of brittle materials," PhD Dissertation at Michigan State University (1991).

58. K.Y. Lee, L.C.G. Cropsey, B.R. Tyszka, E.D. Case, "Grain size, density, and mechanical properties of alumina batch-processed in a single-mode microwave cavity," Materials Research Bulletin, 32 [3], 287-295 (1997).

59. K.Y. Lee, E.D. Case, J. Asmussen, Jr., and M. Siegel; pp. 473 in Ceramic Transactions Volume 59, American Ceramic Society, Columbus, OH (1995).

60. K.Y. Lee, E.D. Case, J. Asmussen, Jr., and M. Siegel; pp. 491 in Proceedings of the 11th ESD Advanced Composites Conference, Ann Arbor, MI (1993).

61. CRC Handbook of Chemistry and Physics: 1st Student Edition, Ed. by R.C. Weast, CRC Press Inc., Boca Ralton, Florida (1988).

62. B.R. Lawn, Fracture of Brittle Solids - Second Edition, Cambridge University Press, New York, NY (1993).

63. G. R. Anstis, P. Chantikul, B.R. Lawn, D.B. Marshall, "A critical evaluation of indentation techniques for measuring fracture toughness: I, direct crack measurements," J. Am. Ceram. Soc., 64 [9], 533-38 (1981).

64. H.P. Kirchner, "Damage penetration at elongated machining grooved in hot-pressed Si_3N_4," J. Am. Ceram. Soc., 67 [2] 127-32 (1984).

65. Lt. Luke Cropsey, "Statistical analysis of hardness and fracture values from single-mode microwave sintered alumina," Independent study project report for Dr. E.D. Case at Michigan State University, July 2, 1996.

66. R. Morrell, Handbook of Properties of Technical and Engineering Ceramics: Part2 Data Reviews - Section I High-Alumina Ceramics, HMSO Books, London (1987).

67. L. Ewart, S. Suresh "Crack propagation in ceramics under cyclic loads" J. Mat. Sci., 22, 1173-92 (1987).

68. W.J. Lee, E.D. Case, "Cyclic Thermal Shock in SiC-Whisker-Reinforced Alumina Composite, " Mat. Sci. Eng., A119, 113-26 (1989).

69. W.J. Lee, E.D. Case, "Thermal Fatigue in Polycrystalline Alumina, " J. Mat. Sci., 25, 5043-54 (1990).

70. Y. Kim, W.J. Lee, E.D. Case, "Thermal Fatigue Behavior of Ceramic Matrix Composites: A Comparison Among Fiber Reinforced Whisker Reinforced, Particulate Reinforced, and Monolithic Ceramics, "; pp. 871-81 in Proceedings for Composites, 5th Technical Conference, Technomic Publishing, Lancaster, PA (1990).

71. Y. Kim, W.J. Lee, E.D. Case, "Thermal Fatigue in SiC Fiber Reinforced Aluminosilicate Glass Ceramic Composite;" pp. 479 in Metal and Ceramic Matrix Composites: Processing, Modeling and Mechanical Behavior, Eds. R.B. Bhagat, A.H. Clever, P. Kuman, A.M. Ritter, The Minerals, Metals, and Materials Society, Warrendale, PA (1990).

72. W.J. Lee, E.D. Case, "Comparison of Saturation Behavior of Thermal Shock Damage in a Variety of Brittle Materials, " Mater. Sci. Eng., A154, 1-9 (1992).

73. E.D. Case, Y. Kim, W.J. Lee, "Thermal Fatigue of Ceramics and Ceramic Composites;" pp. T1123-T1136 in 24th International SAMPE Technical Conference, Volume 2 Advanced Materials: Meeting the Econcomic Challenge, Eds. T.S. Reinhart, M. Rosenov, R.A. Cox, E. Strickholt, Society for the Advancement of Material and Processing Engineering, Covina, CA (1992).

74. B.A. Wilson, E.D. Case, "Comparison of Mechanical Fatigue with Thermal Fatigue in Ceramics," Scripta Met. Mat., 28, 1571-76 (1993).

75. E.D. Case, Y. Kim, W.J. Lee, "Cyclic thermal shock in SiC whisker reinforced alumina and in other ceramic systems;" pp. 393-406 in Thermal Shock and Thermal Fatigue Behavior of Advanced Ceramics, Ed. by G.A. Schneider, G. Petzow, Kluwer Academic Publishers, Netherlands (1993).

76. F.P. Incropera, D.P. DeWitt, Fundamentals of Heat and Mass Transfer, 3rd Edition, John Wiley and Sons, New York, NY (1990).

77. Thermophysical Properties of High Temperature Solid Materials, Ed. by Y.S. Touloukian, Macmillan Company, New York, NY (1967).

78. D.G. Holloway, The Physical Properties of Glass, Wykeham Publications Ltd., London (1973).

79. R.F. Bartholomew, "High-water containing glasses," J. Non-Cryst. Solids, 56 [1-3], 331-42 (1983).

80. H. Scholze, "Gases and Water in Glass: Part Two," Glass Industry, 47 [11], 622-28 (1966).

81. J.M Jewell, M.S. Spess, J.E. Shelby, "Effect of water concentration on the properties of commercial soda-lime-silica glass," J. Am. Ceram. Soc., 73 [1], 132-35 (1990).

82. M. Tomozawa, M. Takata, J. Acocella, E.B. Watson, T. Takamori, "Thermal properties of sodium silicate ($Na_2O{\cdot}3SiO_2$) glasses with high water content," J. Non-Cryst. Solids, 56[1-3], 343-48 (1983).

83. K.H. Schnatter, R.H. Doremus, W.A. Lanford, "Hydrogen analysis of soda-lime silicate glass," J. Non-Cryst. Solids, 102, 11-18 (1988).

84. C.G. Pantano Jr., D.B. Dove, G.Y. Onoda Jr., "AES compositional profiles of mobile ions in the surface of glass," J. Vac. Sci. Technol, 13 [1], 414-18 (1976).

85. D.R. Rosington, "Surface chemistry of glass;" pp. 513-43 in Introduction to Glass Science, Eds. L.D. Pye, H.J. Stevens, W.C. LaCourse, Plenum Press, N.Y. (1972).

86. R.H. Doremus, Glass Science, John Wiley and Sons, N.Y. (1973).

87. D.B. Marshall, B.R. Lawn, "Strength degradation of thermally tempered glass plates," J. Am. Ceram. Soc., 61 [1-2], 21-27 (1978).

88. I.J. McColm, Ceramic Hardness, Plenum Press, New York, NY (1990).

89. J. Neter, W. Wasserman, G.A. Whitmore, Applied Statistics, 4th Edition, Allyn and Bacon, Boston, MA (1993).

90. M.A. Janney, H.D. Kimrey, "Microstructure evolution in microwave sintered alumina;" pp. 382-90 in Ceramic Transactions Vol. 7: Advances in Sintering, American Ceramic Society, Westerville, OH (1990).

91. M.A. Janney, H.D. Kimrey, W.R. Allen, J.O. Kiggans, "Enhanced diffusion in sapphire during microwave heating," J. Mater. Sci., 32 [5], 1347-55 (1997).

92. M.A. Janney, H.D. Kimrey, "Diffusion-controlled processes in microwave-fired oxide ceramics," MRS Symp. Proc., 289, 215-27 (1989).

93. S.A. Nightengale, D.P. Dunne, H.K. Worner, "Sintering and grain growth of 3 mol% yttria zirconia in a microwave field," J. Mater. Sci., 31, 5039-43 (1996).

94. J. Cheng, J. Qiu, J. Zhou, N. Ye, "Densification kinetics of alumina during microwave sintering," MRS Symp. Soc., 269, 323-28 (1992).

95. R. Wroe, A.T. Rowley, "Evidence of a non-thermal microwave effect in the sintering of partially stabilized zirconia," J. Mater. Sci., 31, 2019-26 (1996).

96. D.L. Johnson, "Microwave heating of grain boundaries in ceramics," J. Am. Ceram. Soc., 74 [4], 849-50 (1991).

97. T.K. Gupta, "Instability of Cylindrical Voids in Alumina," J. Am. Ceram. Soc., 61 [5-6], 191-95 (1978).

98. A. Tsoga, P. Nikolopoulos, "Groove angles and surface mass transport in polycrystalline alumina," J. Am. Ceram. Soc., 77[4], 954-60 (1994).

APPENDICES

APPENDIX A

APPENDIX A: SATURATION BEHAVIOR IN CYCLIC AND STATIC FATIGUE IN CERAMICS

A.1 Literature Review

A.1.1 Fatigue in Ceramics

To begin to understand fatigue in ceramics it is necessary to understand that in ceramics "fatigue" is a word that is not just used to describe the behavior of a material under varying load (as in metals), but is used for many different phenomena observed in ceramics [A.1]. Examples include the phenomenon of: "static fatigue" where strength reductions under a constant applied load result from environmental effects (corrosion at the crack tip), and "thermal fatigue" where the strength decreases from repeated thermal shock. For ceramics, the term "cyclic mechanical fatigue" is used to describe behavior of ceramics under varying mechanical load. This, then, is the equivalent of the term "fatigue" used in metals literature.

A.1.2 Cyclic Fatigue

Historically, cyclic mechanical fatigue in literature has not been investigated in detail until the last decade (beginning in the mid-1980's). The reason for this was that since most common ceramics do **not** have dislocation motion and so would not have crack tip plasticity and consequently would not be subject to cyclic fatigue [A.2]. Early experimental investigators compared cyclic mechanical fatigue with static fatigue and

attributed strength decreases merely to stress corrosion at the crack tip [A.3]. A standard text ceramic materials states that while failure from mechanical fatigue occurs in metals it is rare in ceramics, adding that static fatigue from stress corrosion is common in ceramics [A.4].

Gui [A.5] tested alumina samples in both static and cyclic fatigue [A.5]. The specimens were tested in tension/compression to determine the number of cycles or the time to failure for different stress levels. The cyclic fatigue life was significantly shorter than the static fatigue lifetime for the same maximum applied stress level. However, Gui's [A.5] results were questioned as possibly being the result of batch variability of the samples [A.6] and subsequent static and cyclic fatigue testing by other investigators (for a different material) found no appreciable difference in failure lifetimes with the authors adding that stress corrosion of cracks was the likely mechanism causing failure [A.7]. Later several groups of authors used compact tension specimens in both static and cyclic fatigue to measure the crack length as a function of time for an applied stress intensity (or stress intensity range in the case of cyclic fatigue) [A.8, A.9]. Dauskardt et al. [A.8] and Reece et al. [A.9] showed that for two different materials the crack length did not increase with time in static loading, while the crack length increased significantly in cyclic loading, giving some of the first conclusive and accepted evidence that cyclic fatigue occurred in ceramics.

The bulk of the research which has followed has used three different types of experimental testing. The most common experimental techniques include fatigue crack growth of long cracks in compact tension specimens [A.10 - A.13] or flexure specimens [A.14 - A.16], crack growth of notched cyclic compression specimens

[A.17 - A.22], and fatigue life for different levels of applied **stress** in flexure or standard tensile specimens [A.23 - A.27]. Newer, less common, experimental techniques include measuring the strain as a function of stress at each cycle for standard tension specimens cyclically loaded with different levels of maximum applied stress and reporting the plastic strain as a function of stress for each cycle [A.28, A.29] or reporting the calculated elastic modulus as a function of cycles [A.30, A.31].

The experimental technique of fatigue crack growth measurements in ceramics is the same as in metals. The crack length is measured at preselected numbers of cycles and the stress intensity and crack growth rates are calculated in the same way as in metal specimens (for details on calculations see standard fatigue texts [A.32, A.33]). The data are graphed as crack growth rate ($\frac{da}{dN}$) versus stress intensity range (ΔK). The data, when plotted in log-log, follow Paris Law as do metals

$$\frac{da}{dN} = C(\Delta K)^m \tag{A.1}$$

where C is a constant and m is the slope of the linear region [A.32]. For metals the exponent, m, in Equation A.1 has a value of 2 to 4. For ceramics the exponent is much higher ranging from 21-42 for different materials [A.9, A.10, A.12].

Fatigue life experimental testing of ceramics in cyclic fatigue is also very similar to that in metals except that in ceramics **stress**-life curves are used and not **strain**-life as with metals. Stress-life instead of strain-life is used for most ceramics due to the lack of appreciable plastic strain and absence of dislocation movement in ceramics.

In an investigation which used a newer experimental technique for investigation of cyclic fatigue in ceramics, Liu and Chen [A.28] tested the fatigue behavior of 3-

mol%-yttria-stabilized tetragonal zirconia polycrystals (3Y-TZP) using uniaxial tension-compression. Liu and Chen's investigation revealed a hysteresis effect in the stress versus plastic strain curve (Figure A.1). The total strain was measured in the experiment and the plastic strain was found by using the elastic modulus to obtain the elastic strain contribution. The plastic strain was found by subtracting out the elastic strain contribution to the total strain. The plastic strain in ceramics is the strain resulting from the aggregate crack opening displacements by all the microcracks which open in cyclic loading. The plastic strain is used instead of the total strain because the strain is dominated by the elastic strain contribution in ceramics. The plastic contribution to strain from microcracking is extremely small compared to plastic strain from dislocations in metals (Figure A.1).

Upon initial loading, the beginning of the stress-plastic strain loop has an infinite slope since initially there is only elastic strain and no plastic strain. As the loading continues, the slope changes to a finite positive slope which the authors attribute to a decrease in the elastic modulus caused by microcracking. Upon unloading, the curve has a constant slope until low loading levels are reached and then the slope becomes infinite again or nearly infinite. Slope changes indicate a smaller decrease in plastic strain which the authors attribute to closure of microcracks.

Upon reloading of the specimen for another loading cycle, the initial curve of the reloading cycle does not follow the unloading curve of the previous curve, but rather is vertical which the authors attribute to the elastic modulus being undegraded from the beginning of the previous cycle. The undegraded elastic modulus is attributed to friction resulting from the contact sliding of microcrack surfaces which

oppose the reversal of plastic deformation.

Another characteristic of the stress-plastic strain curves is that when the test specimens are unloaded to zero stress after several cycles, the hysteresis loops are still at a finite residual strain. This residual strain is an accumulation of damage. The amount of damage accumulated increases with each cycle, but decreases with successive cycles. Liu and Chen [A.28] note that damage levels are affected more by increases in mean stress than for increases in stress amplitude, which is shown by plots of cumulative plastic strain versus cycles for varying maximum stress and mean stress (Figure A.2). The stress-plastic strain curves (Figure A.1) showed a decrease in the initial slope of unloading as the number of cycles was increased which was attributed to a decrease in elastic modulus as damage was accumulated. Failure in the majority of specimens was traced to internal flaws (usually near the surface) which were formed during or before sintering. Fatigue lifetime was controlled by crack propagation, most likely [A.28].

A.1.3 Thermal Fatigue

Case et al. [A.35 - A.39] noted that thermal fatigue damage in ceramics first accumulates rapidly then saturates at a sufficiently high number of loading cycles. At least for low cycle fatigue damage, Case et al. [A.35 - A.39] found that the damage saturation behavior may be described by the equation

$$P(N) = P_o + D(1 - \exp(-\delta N)). \qquad \text{(A.2)}$$

The parameter P is a measurable material property (e.g. elastic modulus) that changes as a function of the fatigue-induced damage. P(N) is the value of P following N

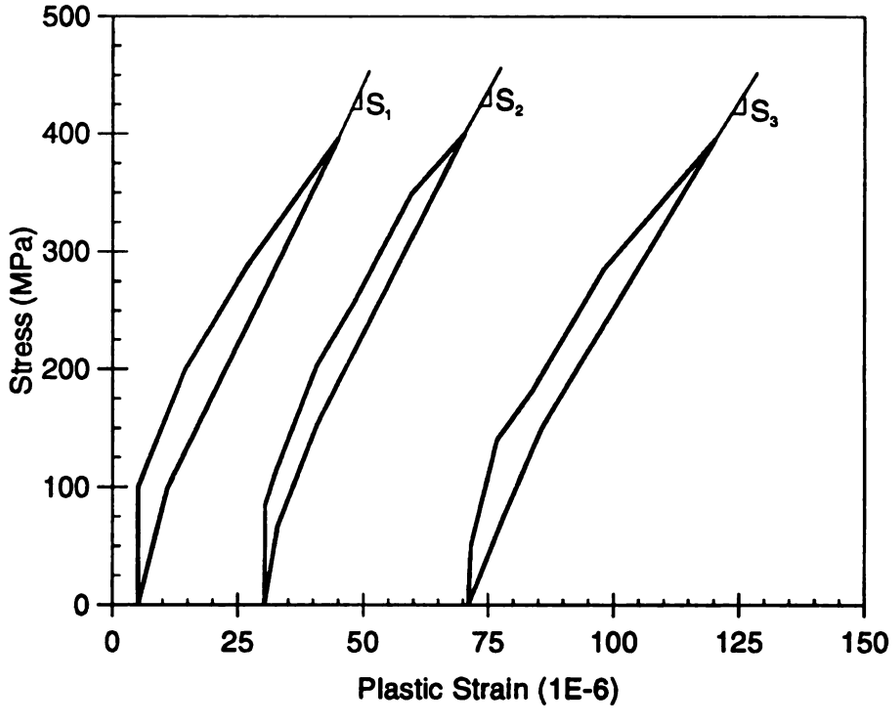

Figure A.1 Hysteresis loops of 3Y-TZP. Note the change (S_1>S_2>S_3) and the shifts of loops due to strain accumulation (from [A.28]).

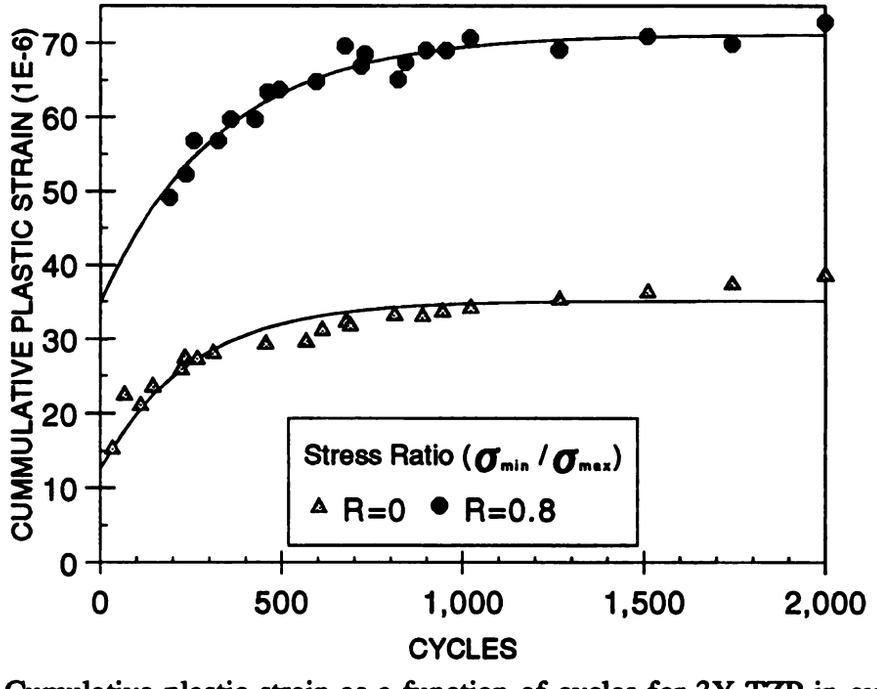

Figure A.2 Cumulative plastic strain as a function of cycles for 3Y-TZP in cyclic mechanical fatigue (from [A.28]). Solid curves are a regression analysis using Equation A.2.

fatigue cycles at a fixed stress level. P_o is the microcrack-free value of the property P and D is the saturation constant. (For large N, P(N) approaches P_o + D.) For thermal fatigue, Case et al. [A.35 - A.39] noted that the parameters P employed to monitor damage evolution have included elastic modulus, internal friction, strength, and hardness.

A.2 Results and Discussion

Figure A.3 shows the fit of the mechanical fatigue data from Liu and Chen [A.29] to Equation A.2. The data points in Figure A.3 indicate the data originally collected by Liu and Chen [A.28] . The lines through the data points indicate the linear best-fit regression analysis of Liu and Chen's [A.28] data, performed by Wilson and Case using Equation A.2 [A.34]. The accumulation of plastic strain with cyclic fatigue is described quite well by Equation A.2 with regression correlation coefficients, r, ranging from 0.944 to 0.999 (Figure A.3).

Wilson and Case [A.41] performed similar analysis on data collected by Ewart and Suresh [A.18]. Ewart and Suresh measured crack growth as a function of the number of fatigue cycles for compact tension specimens of alumina (Al_2O_3). The authors [A.18] were trying to better understand the mechanisms causing fatigue damage in ceramics. For one single edge notched cyclic compression test, the sample was removed and ultrasonically cleaned every 5,000 cycles and in the other test the sample was not ultrasonically cleaned. Figure A.4 shows the data collected by Ewart and Ewart and Suresh deduce that this reduction is caused by the accumulation of debris along the Suresh with the curve in the figure being generated by Wilson and

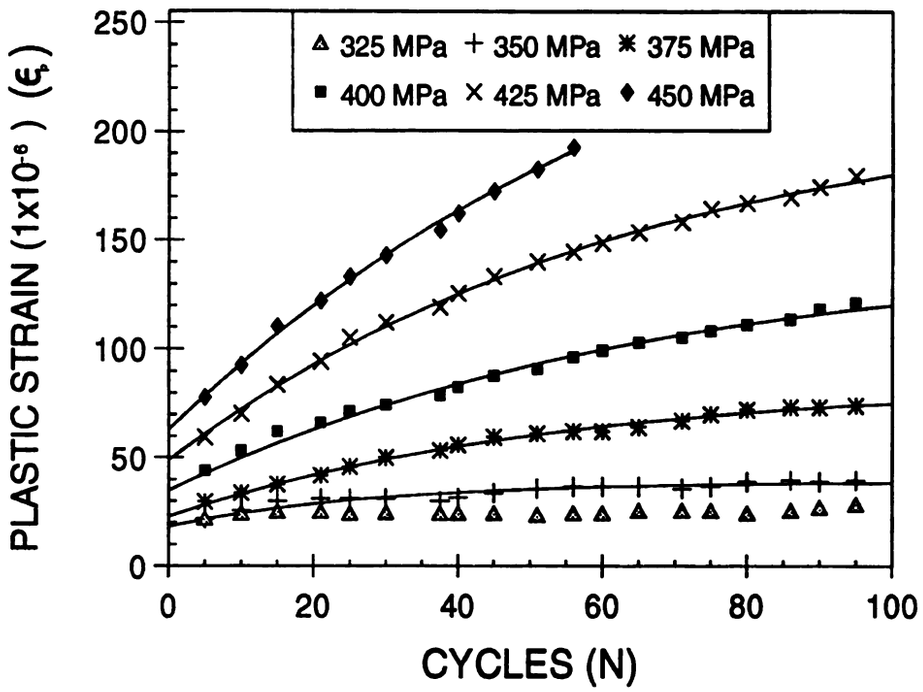

Figure A.3 Regression analysis using Equation A.2 (solid curves) for the low cycle mechanical fatigue of Mg-PSZ [A.34, A.28].

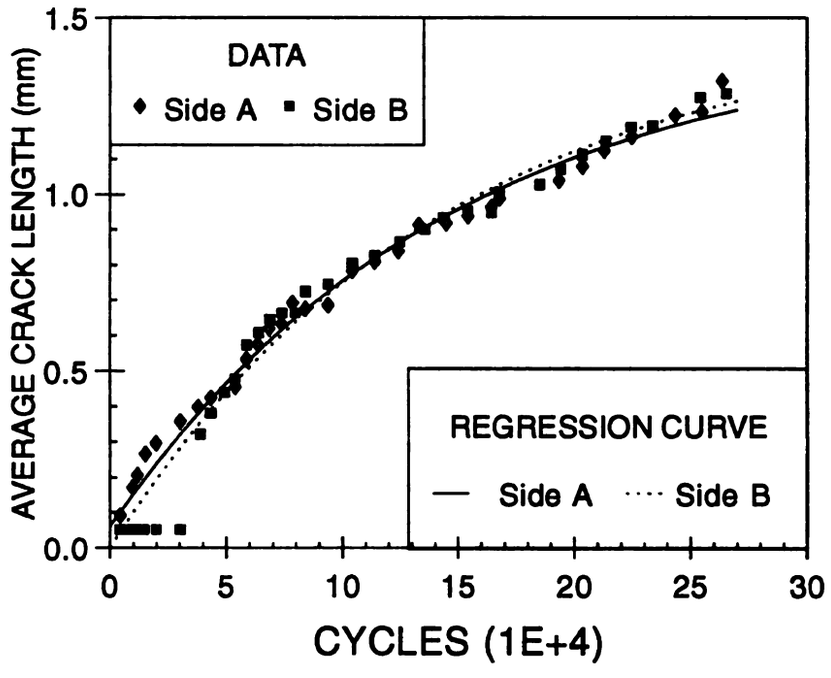

Figure A.4 Regression analysis using Equation A.2 for the mechanical fatigue of polycrystalline alumina at R=10 at maximum stress of -268 MPa for a specimen ultrasonically cleaned after every 5,000 cycles [A.42, A.18].

Case with a linear least squares regression of the ultrasonically cleaned data to Equation A.2. Equation A.2 describes the accumulation of fatigue damage in ceramics quite well with a correlation coefficient of 0.984 [A.41] (Figure A.4). As can be seen in Figure A.4, for the specimen that was not ultrasonically cleaned the crack growth was reduced. crack faces (from damaged grains and grain boundaries) which reduces the effective driving force for future crack advance [A.18].

Wilson and Case [A.34] also applied the equation describing damage accumulation in fatigue of ceramics (Equation A.2) to mechanical fatigue data of Steffen, Dauskardt and Ritchie [A.10]. Steffen et al. [A.10] collected data to produce crack growth as a function stress intensity data (Figure A.5). Wilson and Case [A.34] used the actual crack length data originally collected by Steffen et al. [A.10] to perform a linear regression to Equation A.2 to analyze the damage accumulation in the material. The resulting best-fit curve to the data (Figure A.6) has a correlation coefficient of 0.984 [A.34].

A.3 Conclusions

In summary, ceramics **do** have cyclic mechanical fatigue, not just an environmental effect of stress corrosion at the crack tip. Common cyclic mechanical fatigue testing of ceramics uses methods similar or identical to fatigue experimentation in metals. Specifically, crack growth measurements with subsequent fitting to Paris' Law and **stress**-life testing are commonly investigated. More recent experimental work has found a hysteresis effect in the stress versus plastic strain curves. Wilson and Case [A.34, A.41, A.42] use an equation describing the damage saturation behavior of

ceramics in thermal fatigue developed by Case et al. [A.35 - A.40] to describe cyclic mechanical fatigue data of many investigators.

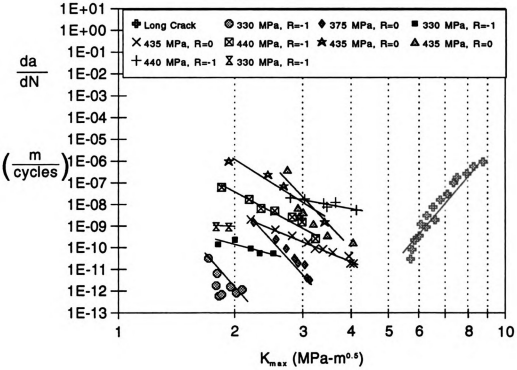

Figure A.5 Crack growth rate as a function of stress intensity, K_{max} (from [A.10]).

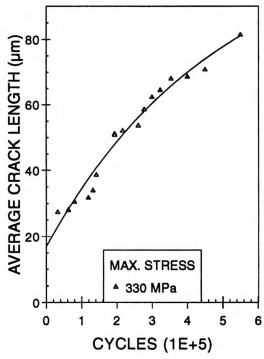

Figure A.6 Regression analysis (solid curve) using Equation A.2 for the mechanical fatigue of Mg-PSZ [A.34, A.10].

A.4 References for Appendix A

A.1 L.S. Williams, "Fatigue and Ceramics;" pp. 245-302 in Mechanical Properties of Engineering Ceramics, W.W. Kriegel, H. Palmour III Eds., Interscience Publishers, N.Y. (1960).

A.2 S.M. Wiederhorn, B.J. Hockey, D.W. Roberts, Philisophical Magazine, 28, 783 (1973).

A.3 D.A. Krohn, D.P.H. Hasselman, "Static and Cyclic Fatigue Behavior of a Polycrystalline Alumina," Journal of the American Ceramic Society, 55 [4], 208-11 (1972).

A.4 W.D. Kingery, H.K. Bowen, D.R. Uhlmann, Introduction to Ceramics 2nd Edition, John Wiley and Sons, N.Y. (1976).

A.5 F. Guiu, "Cyclic Fatigue of Polycrystalline Alumina in Direct Push-Pull," J. Mater. Sci., 13 [6] 1357-61 (1978).

A.6 A.G. Evans, "Fatigue in Ceramics," International J. of Fracture, 16 [6] 485-98 (1980).

A.7 T. Kawakubo, K. Komeya, "Static and Cyclic Fatigue Behavior of a Sintered Silicon Nitride at Room Temperature," J. Am. Ceram. Soc., 70 [6] 400-05 (1987).

A.8 R.H. Dauskardt, W. Yu, R.O. Ritchie, "Fatigue Crack Propogation in Transformation-Toughened Zirconia Ceramic," J. Am. Ceram. Soc., 70 [10] C248-C252 (1987).

A.9 M.J. Reece, F. Guiu, M.F.R. Sammur, "Cyclic Fatigue Crack Propogation in Alumina under Direct Tension-Compression Loading," J. Am. Ceram. Soc., 72 [2] 348-52 (1989).

A.10 A.A. Steffen, R.H. Dauskardt, R.O. Ritchie, "Cyclic Fatigue-Crack Propogation in Ceramics: Long and Small Crack Behavior;" pp. 745-52 in Fatigue '90, Proceedings of the 4th International Conference on Fatigue and Fatigue Thresholds, Vol. 2, H. Kitagawa, T. Tanaka Eds., Materials Component Engineering Publications Ltd., Edgbaston, U.K. (1990).

A.11 R.H. Dauskardt, M.R. James, J.R. Porter, R.O. Ritchie, "Cyclic Fatigue-Crack Growth in a SiC-Whisker-Reinforced Alumina Ceramic Composite: Long- and Small-Crack Behavior," J. Am. Cer. Soc., 75 [4] 759-71 (1992).

A.12 H. Kishimoto, A. Ueno, H. Kawamoto, "Crack Propogation of Sintered Silicon Nitride under Cyclic Loads (Influence of Difference in Material) JSME Int J Ser 1 34 [3] 361-6 (1991).

A.13 A. Ueno, H. Kishimoto, H. Kawamoto, M. Asakura, "Crack Propogation Behavior of Sintered Silicon Nitride Under Cyclic Load of High Stress Ratio and High Frequency," pp. 733-38 in Fatigue 90: Proceedings of the 4th International Conference on Fatigue and Fatigue Thresholds, Materials and Component Engineering Publications, Burmingham, UK (1990).

A.14 Y. Mutoh, M. Takahashi, T. Oikawa, H. Okamoto, "Fatigue Crack Growth of Long and Short Cracks in Silicon Nitride," pp. 211-25 in Fatigue of Advanced Materials, R.O. Ritchie, R.H. Dauskardt, B.N. Cox Eds., Mat. Comp. Eng. Publ., Edgbaston, U.K. (1991).

A.15 D.C. Cardonia, C.J. Beevers, Formation and Growth of Short Fatigue Cracks in a Zirconia-Ceria Alloy," Scripta Met 23 [6] 945-50 (1989).

A.16 D.C. Cardona, C.J. Beevers, "Fatigue Behavior of Zirconia-Ceria Alloys," pp. 1023-29 in Fatigue 90: Proceedings of the 4th International Conference on Fatigue and Fatigue Thresholds, Materials and Component Engineering Publications, Burmingham, UK (1990).

A.17 L. Ewalt, S. Suresh, "Dynamic Fatigue Crack Growth in Polycrystaline Alumina under Cyclic Compression," J. Mater. Sci. Lett., 5, 774-8 (1986).

A.18 L. Ewalt, S.Suresh, "Crack Propogation in Ceramics under Cyclic Loads," J. Mater. Sci., 22, 1173-92 (1987).

A.19 A.A. Morrone, S.R. Nutt, S. Suresh, "Fracture Toughness and Fatigue Crack Growth Behavior of an Al_2O_3-SiC Composite, " J. Mater. Sci., 23, 3206-13 (1988).

A.20 S. Suresh, L.A. Sylva, "Room Temperature Fatigue Crack Growth in Cemented Carbides, " Mat. Sci. Eng., 83, L7-10 (1986).

A.21 S. Suresh, L.X. Han, "Fracture of Silicon Nitride-Silicon Carbide Whisker Composites under Cyclic Loads," J. Am. Ceram. Soc., 71 [3], C158-C161 (1988).

A.22 L.A. Sylva, S. Suresh, "Crack Growth in Transforming Ceramics under Cyclic Tensile Loads," J. Mater. Sci., 24, 1729-38 (1989).

A.23 H. Kamiya, M. Takatsu, K. Ohya, M. Ando, A. Hattori, "Effect of Microstructure on Cyclic Fatigue Properties of Al_2O_3 Composites," J. Ceram. Soc. Jpn., Int. Ed., 98 [5], 469-476 (1990).

A.24 M. Masuda, T. Soma, M. Matsui, I. Oda, "Fatigue of Ceramics (Part 1)- Fatigue Behavior of Sintered Si_3N_4 under Tension-Compression Cyclic Stress," J. Ceram. Jpn. Inter. Ed., 96, 275-80 (1988).

A.25 M. Masuda, N. Yamada, T. Soma, M. Matsui, I. Oda, "Fatigue of Ceramics (Part 2)- Cyclic Fatigue Properties of Sintered Si_3N_4 at Room Temperature," J. Ceram. Jpn. Inter. Ed., 97, 509-14 (1989).

A.26 M. Masuda, T. Soma, M. Matsui, I. Oda, "Fatigue of Ceramics (Part 3)- Cyclic Fatigue Behavior of Sintered Si_3N_4 at High Temperature," J. Ceram. Jpn. Inter. Ed., 97, 601-07 (1989).

A.27 M. Masuda, M. Matsui, "Fatigue in Ceramics (Part 1)- Static Fatigue Behavior of Sintered Si_3N_4 under Tensile Stress," J. Ceram. Jpn. Inter. Ed., 98, 86-95 (1990).

A.28 S-Y Liu, I-W Chen, "Fatigue of Yittria-Stabilized Zirconia: I, Fatigue Damage, Fracture Origins, and Lifetime Predictions," J. Am. Ceram. Soc., 74 [6], 1197-1205 (1991).

A.29 S-Y Liu, I-W Chen, "Fatigue Deformation Mechanisms of Zirconia Ceramics," J. Am. Ceram. Soc., 75 [5], 1191-204 (1992).

A.30 L.M. Butkus, L.P Zawada, G.A. Hartman, "Fatigue Test Methodology and Results for Ceramic Matrix Composites at Room and Elevated Temperatures," pp. 52-68 in Cyclic Deformation, Fracture, and Nondestructive Evaluation of Advanced Materials, Eds. M.R. Mitchell, O. Buck, American Society for Testing and Materials, Philadelphia (1992).

A.31 S. Mall, G.D. Tracy, "Fatigue Behavior of a Quasi-Isotropic Ceramic Composite under Tensile Fatigue Loading," pp. 628-37 in Proceedings for Composites, 6th Technical Conference, Technomic Publishing, Lancaster, PA (1991).

A.32 N.E. Dowling, Mechanical Behavior of Materials: Engineering Methods for Deformation, Fracture, and Fatigue, Prentice Hall, Englewood Cliffs, New Jersey (1993).

A.33 S.T. Rolfe, J.M. Barsom, Fracture and Fatigue Control in Structures: Applications of Fracture Mechanics, Prentice Hall, Englewood Cliffs, New Jersey (1987).

A.34 B.A. Wilson, E.D. Case, "Comparison of Mechanical Fatigue with Thermal Fatigue in Ceramics," Script Met. Matal., 28, 1571-76 (1993).

A.35 W.J. Lee, E.D. Case, "Cyclic Thermal Shock in SiC-Whisker-Reinforced Alumina Composite," Mat. Sci. Eng., A119, 113-26 (1989).

A.36 W.J. Lee, E.D. Case, "Thermal Fatigue in Polycrystalline Alumina," J. Mat. Sci., 25, 5043-54 (1990).

A.37 Y. Kim, W.J. Lee, E.D. Case, "Thermal Fatigue in SiC Fiber Reinforced Aluminosilicate Glass Ceramic Composite;" p. 479 in Metal and Ceramic Matrix Composites: Processing, Modeling and Mechanical Behavior, Eds. R.B. Bhagat, A.H. Clever, P. Kuman, A.M. Ritter, The Minerals, Metals, and Materials Society, Warrendale, PA (1990).

A.38 Y. Kim, W.J. Lee, E.D. Case, "Thermal Fatigue Behavior of Ceramic Matrix Composites: A Comparison Among Fiber Reinforced Whisker Reinforced, Particulate Reinforced, and Monolithic Ceramics;" pp. 871-81 in Proceedings of the American Society for Composites, 5th Technical Conference, Technomic Publishing, Lancaster, PA (1990).

A.39 W.J. Lee, E.D. Case, "Comparison of Saturation Behavior of Thermal Shock Damage in a Variety of Brittle Materials," Mat. Sci. Eng., A154, 1-9 (1990).

A.40 E.D. Case, Y. Kim, W.J. Lee, "Thermal Fatigue of Ceramics and Ceramic Composites;" pp.T1123 in 24th International SAMPE Technical Conference, Volume 2 Advanced Materials: Meeting the Economic Challenge, Eds. T.S. Reinhart, M. Rosenov, R.A. Cov, E. Strickholt, Society for the Advancement of Material and Process Engineering, Covina, CA (1992).

A.41 B.A. Wilson, E.D. Case, "Low Cycle Mechanical and Thermal Fatigue of Ceramics and Ceramic Composites, with Consideration of Debris Accumulation Effects," pp. 931-40 in Proceedings of the American Society for Composites, Technomic Publishing Co., Lancaster, PA (1993).

A.42 B.A. Wilson, E.D. Case, "Further Study of an Equation Describing Damage Saturation Behavior in Fatigue of Ceramics and Ceramic Composites," pp. 518-31 in Advanced Composites Technologies, ESD (The Engineering Society), Ann Arbor, MI (1993).

APPENDIX B: CRACK LENGTH DATA FROM CONVENTIONAL HEALING EXPERIMENTS, MICROWAVE HEALING EXPERIMENTS, AND STRESS RELIEF CYCLE TESTING

The crack length measurement raw data is recorded for the conventional healing of glass experiments (Tables B.1 - B.7), the stress relief cycle testing in glass (Table B.8), the conventional healing of alumina experiments (Tables B.9 - B.10), and the microwave healing of alumina experiments (Table B.11).

Table B.1 Crack lengths (μm) from conventional healing of soda-lime silica glass (Conventional Healing of Glass Experiment 1, Section 4.4.2.1.1).

Specimen Number	Temperature (°C)	2C At 24 hr.	2C After Anneal
1	600	209.8	155.9
		197.9	140.9
		202.3	176.8
		196.2	171.8
		206.3	189.2
		180.1	150.5
2	600	202.1	169
		197.4	183.7
		212.7	188.6
		210.3	170
		202.7	191.5
		202	177.6
3	600	214.9	213.1
		204.6	203.2
		205.4	204
		186.3	186.8
		211.3	209.1
		203.3	201.5
4	600	194.5	197.3
		183.6	198.5
		186.9	183.8
		199.4	177.3
		203.8	160.4
		201.2	155

Table B.1 (cont'd).

Specimen Number	Temperature (°C)	2C At 24 hr.	2C After Anneal
5	600	207.7	197.6
		197.5	206.2
		198.9	208.3
		198.6	203.1
		206	189.9
		199.4	196
6	600	206	196.4
		203.4	205.1
		208	190.2
		200.5	183.5
		200.1	174
		199.6	180.5
7	600	209.6	193.2
		201.9	199.4
		207.6	132.3
		196.9	110.3
		197.9	192.2
		185.4	177.4
8	600	204.6	165
		197.2	143.8
		209.2	164.9
		195.9	145.4
		208.2	154.4
		203.8	171.2

Table B.1 (cont'd).

Specimen Number	Temperature (°C)	2C At 24 hr.	2C After Anneal
9	600	208.2	208.2
		202.5	201.8
		195.7	195.5
		207.8	204.6
		210.5	206.3
		206.4	201.8
10	600	204.4	167.5
		207.2	192.8
		206.7	197.4
		198.9	194.2
		211.1	206.6
		200.9	193.8
11	25	202.5	195.3
		193.5	193.9
		196.8	190.7
		206	209.3
		202.7	202.7
		194.4	190.5
12	25	206.6	202.9
		201.2	199.5
		208.1	207
		191	191.3
		203.1	199.7
		180.3	178.9

Table B.2 Crack lengths (μm) from conventional healing of soda-lime silica glass (Conventional Healing of Glass Experiment 2, Section 4.4.2.1.2).

Specimen Number	Temperature (°C)	2C At 24 hr.	2C After Anneal
1	550	N.M.	N.M.
		N.M.	N.M.
2	550	197.5	191.5
		185.9	179.1
3	550	205.3	202.9
		200.8	170.5
4	550	200.7	186.7
		191.5	170.8
5	550	197.7	155.9
		191.3	147.9
6	550	206.8	200.9
		194.6	189.4

Table B.3 Crack lengths (μm) from conventional healing of soda-lime silica glass (Conventional Healing of Glass Experiment 3, Section 4.4.2.1.3).

Temperature (°C)	Time (min)	Stress Relief Cycle	30 min.	24 hr.	After Anneal
350	15	A	203.3	220.9	221.7
			206.1	224.3	225.1
			207.3	227.3	226.4
			202.7	221.1	219.5
			204.1	222.4	222.6
			204.7	223.2	223.7
375	15	A	197.8	215.2	217.1
			190.3	206.4	205
			197.6	215.7	217.1
			200.7	219.6	223.3
			197.4	215.1	217.5
			186.4	209.7	208.5
400	15	A	176.3	208	207.6
			190.2	218.6	221.2
			191.1	220.7	221.2
			191.5	221.8	221.4
			194.2	225	225.2
			194.8	225.1	223.4
425	15	A	199.5	219.3	220
			199.8	219.4	220.4
			198	218.8	218.6
			200.9	221.7	220.2
			200.5	219.8	220.9
			200.7	219.3	220.2

Table B.3 (cont'd).

Temperature (°C)	Time (min)	Stress Relief Cycle	30 min.	24 hr.	After Anneal
450	15	A	201.5	212	213.8
			198.4	210	213
			201.2	212	215.3
			205.5	219.2	221.2
			203.9	216.4	219.1
			195.7	209.7	212.7
475	15	A	208.8	227.8	227.2
			194.5	212.1	212.1
			208	224.3	224.4
			203.6	219.3	220.7
			198	217.1	215.7
			203.8	222.4	221.1
500	15	A	202.8	220.6	220.7
			197.4	220.8	217.1
			202.7	221.4	222.9
			197.8	213.7	215.5
			198.2	217.9	217.4
			201.1	218.7	219.1
525	15	A	199.1	220.8	218.1
			198.5	221.4	217.3
			200.8	222.2	215.6
			203.1	223.8	210.2
			203.7	223.2	213.9
			201.1	222.5	218.6

Table B.3 (cont'd).

Temperature (°C)	Time (min)	Stress Relief Cycle	30 min.	24 hr.	After Anneal
550	15	A	198	214.8	210.8
			180	200.8	190
			199.6	216.3	212.9
			199.1	218.6	215.6
			197	216.6	210.7
			202.5	218	213.7
550	15	B	186.1	203.8	193.4
			189.5	205.9	198.9
			195.2	211.3	203.8
			197.3	213.3	208.2
			197	212.8	203.8
			196.3	212.6	204.3
550	15	None	183	190.2	191.9
			190	196.1	198.9
			189.3	195.2	196.2
			189.7	198.7	199
			189.7	198.9	199.8
			185.2	193.7	194.3
575	15	A	205.7	223.3	154
			206	231.1	139.8
			208	229	180.5
			205.2	227.9	176.8
			204.1	224.6	180.8
			206.5	225.1	161.6

Table B.3 (cont'd).

Temperature (°C)	Time (min)	Stress Relief Cycle	30 min.	24 hr.	After Anneal
575	15	B	204	222.7	207.2
			207.5	224.2	219.6
			197.9	213.8	208.5
			203.3	218.7	212.1
			202.9	220.6	216
			202.3	218	211.5
575	15	None	179.3	194.9	180
			186.1	201	195.7
			189	205.1	188.9
			193.2	207.7	191.3
			180.3	195.5	144.2
			181.8	195.2	182.3
525	30	A	205.9	227.5	219.6
			204.2	226.5	213.5
			196.5	224.1	220
			209.1	230.3	221.4
			202.6	220.6	213.6
			201.6	220.4	217.1
525	30	B	202	219.1	201.2
			207.1	225.1	204.3
			204.6	222.6	203.6
			208.5	226.7	199.3
			205.7	223.8	200.7
			207.9	226.8	200

Table B.3 (cont'd).

Temperature (°C)	Time (min)	Stress Relief Cycle	30 min.	24 hr.	After Anneal
525	30	None	189.4	200.8	197.2
			178.9	195	192.2
			195	210.1	203
			197.1	209.9	202.9
			197.1	210.8	201.4
			199.4	210.9	204
550	30	A	204.7	225.1	221.9
			204.2	224.8	221.2
			202.9	221.8	221.4
			206.9	223.9	222.7
			200.1	218	216
			207.2	225.4	223.5
550	30	B	197	220.9	217.7
			205.8	227.1	225.1
			202.2	220.7	214.2
			204	225.7	218.7
			202.4	222.3	218.8
			202.3	222.2	217.8
550	30	None	184.5	212.5	209.1
			207.2	227.5	221.2
			201.4	217.9	215.2
			175	220.4	217.6
			196.6	212.7	211.4
			198.8	211.2	209.1

Table B.3 (cont'd).

Temperature (°C)	Time (min)	Stress Relief Cycle	30 min.	24 hr.	After Anneal
575	30	A	209.9	229.7	223.4
			209	228.3	202.1
			202.2	221.5	215.5
			205.2	223.9	211.9
			204.7	225.6	206.3
			207	226.2	204.3
575	30	B	207.9	226.9	207.2
			206	227.2	206.7
			206.4	223	210.1
			204.4	219.7	199.6
			207.1	223.5	212.9
			205.5	222.7	204
575	30	None	161.7	178.8	176.7
			189.5	200.7	198.8
			190.3	203	199.6
			191	203.1	203.3
			191.8	204.5	202.5
			196.4	207.9	205.5
525	45	A	205.8	224	221.5
			207.4	224.1	223.8
			202.2	216.8	214.9
			204.7	220	216.5
			191.4	210.5	210.4
			194.8	210.9	208.8

Table B.3 (cont'd).

Temperature (°C)	Time (min)	Stress Relief Cycle	30 min.	24 hr.	After Anneal
525	45	B	203.6	220.1	216.1
			204.7	220.6	214.7
			200.1	220.1	215.9
			184.9	212.7	206.1
			204.6	220.9	219.3
			203	220.2	219.8
525	45	None	193.7	208.2	208.4
			183.3	195.1	196.5
			183.3	195.6	195.4
			192.3	203	202.7
			179.9	198	197
			191.5	208	207.3
550	45	A	202.1	218.9	200.1
			207.2	225.9	225
			204.4	223.5	220.3
			205	223.6	217
			200.4	220.2	199.2
			202.8	222.3	209
550	45	B	201.7	218.6	215.4
			191.7	210	206.1
			204.9	219.8	224.8
			201.6	218.3	213.9
			207.2	224	216.5
			206.3	221	212.3

Table B.3 (cont'd).

Temperature (°C)	Time (min)	Stress Relief Cycle	30 min.	24 hr.	After Anneal
550	45	None	174.4	195.5	199.4
			179	191.1	192.4
			195.9	206.6	206.8
			200.5	211.2	215.4
			171.1	183.9	196.9
			186.3	198.8	200.3
575	45	A	204.9	220.2	189.3
			196.8	216	185.4
			206.3	223.4	190.6
			196.4	208.3	184.3
			199.7	213.8	190.8
			210.5	225.1	198.3
575	45	B	200.7	214.2	183.3
			202.6	215.3	183.7
			205.5	219.4	185.5
			205.1	220.5	191.3
			206.1	218.9	186.9
			209.6	224.2	191.6
575	45	None	193.8	206.9	203.5
			197.4	210.7	212.3
			195.4	207	208.5
			187.8	194.1	195.2
			191.3	201.3	202.5
			186.6	200.9	200.2

Table B.3 (cont'd).

Temperature (°C)	Time (min)	Stress Relief Cycle	30 min.	24 hr.	After Anneal
525	120	A	207.8	224.8	210.2
			202.1	211.8	201.5
			193.9	211.5	197.5
			203.5	213.6	199.7
			203.5	218.8	205.7
			205	225.1	208.5
550	120	A	201.1	223.5	200.2
			201.3	225.5	205.2
			202.3	225.2	206.3
			195.7	219.9	191.3
			207.9	228.2	216
			202.6	225.7	207.5
575	120	A	206	220.6	166.8
			205.7	220.1	158.2
			205.1	218.4	165.2
			205.4	219.7	166
			207.7	213.7	176
			202.6	219.8	184.5

Table B.3 (cont'd).

Temperature (°C)	Time (min)	Stress Relief Cycle	30 min.	24 hr.	After Anneal
575	120	B	204.5	219.6	155.9
			199.9	215.5	160.5
			201.8	214.9	150.3
			203.1	216.4	159.6
			206.6	221.9	155.7
			205	219.3	156.9
575	120	None	194.1	205.8	205
			193.9	203.2	203.9
			191.6	203	203.6
			195	206.1	204.3
			190.4	203.3	202.1
			186.4	195.9	195

Table B.4 Crack lengths (μm) from conventional healing in soda-lime silica glass (Conventional Healing of Glass Experiment 4, Section 4.4.2.1.4).

Annealing Cycle		Aged in 0 %r.h.		Aged in 45 %r.h.		Aged in 100 %r.h.	
Temperature (°C)	Time (min.)	2C Before	2C After	2C Before	2C After	2C Before	2C After
525	60	193.1	166.5	203	171.1	246.7	206.7
		192.7	160.5	209	178.4	248.1	205
		186.6	158.5	198.7	168.6	231	201.3
		185.2	156.2	208.2	174.3	245.5	203.6
		190.6	174	205.7	174.5	242.2	205.2
		192.8	162.9	205.5	169.6	241	194.3
538	60	184.9	162.1	204.6	170.8	226	192.9
		183.9	160.5	213.5	175.3	224.5	189.1
		181.6	157.4	207.8	167.3	231.5	198.8
		175	165.2	210.2	176.6	213.4	182
		174.9	163.3	209	173.8	230.8	196.7
		180.5	163.4	210.2	179.1	235.9	199
550	60	188.9	161.6	215.5	179.3	231.4	192.7
		187.5	168.3	214.2	178.1	213.3	172.1
		185.5	163.4	210.5	175.8	238.3	210.1
		190	160.5	203.6	165.6	233.8	203.8
		189.4	168.9	213.5	181.4	232.8	199.4
		187.5	164.5	206.7	173.9	225.8	208.8

Table B.4 (cont'd).

Annealing Cycle		Aged in 0 %r.h.		Aged in 45 %r.h.		Aged in 100 %r.h.	
Temperature (°C)	Time (min.)	2C Before	2C After	2C Before	2C After	2C Before	2C After
563	60	191.6	164	216.2	185.2	228.8	196
		188.6	153.9	209.1	174.7	223.2	195.1
		183.8	167	194.1	158.5	231.5	199.1
		174.2	161.8	200.1	163.8	226.1	192.2
		181.9	164.1	211.6	182.1	216.7	187.8
		179.6	159.8	215.7	185.2	216.5	188.3
575	60	190.3	176	202.2	180.6	235.8	208.5
		193.2	178	212.7	187.9	235.4	221
		195.2	175.7	208.1	182.2	225.7	215
		192.9	176.9	203.3	182.9	225.1	211.2
		188.7	174.6	209.5	179.6	230.8	195.1
		193.7	179	211.2	181.8	222.1	197.9

Table B.5 Crack lengths (μm) from conventional healing in soda-lime silica glass (Conventional Healing of Glass Experiment 5, Section 4.4.2.1.5).

Annealing Cycle		Aged in 0 %r.h.		Aged in 45 %r.h.		Aged in 100 %r.h.	
Temperature (°C)	Time (min.)	2C Before	2C After	2C Before	2C After	2C Before	2C After
525	60	187.8	186.7	216.5	198.9	238.6	238
		186.1	185	217.4	204.8	235.8	236.6
		183.5	181.3	209.5	197.6	221.4	215.6
		184.5	185	213.4	187.9	230.8	231.1
		181.7	178.8	207.5	200.2	228.9	233.2
		174.2	175.1	210.2	196.7	231.6	234
525	90	194.3	179.4	197.9	180.5	241.9	230.3
		191.4	182.7	207.6	189.4	236.9	233.8
		191.1	178.8	214.4	198.3	243.6	219.5
		195.4	183.3	213.9	200.2	241.4	218.5
		192.3	180.5	201.2	185.5	234.9	219
		191.5	178.7	206.4	186.9	227.7	208.7
525	120	184.2	181.5	212.5	208	239.5	225.5
		182.2	180.8	214.5	207.5	239	225.7
		191	186.4	204.4	195.9	239.7	227.7
		190	185.6	215.6	207.8	241.7	225
		185.7	185.9	217.1	207.5	240.8	225.1
		183.9	184.4	212.4	200.2	240.6	229.6

Table B.5 (cont'd).

Annealing Cycle		Aged in 0 %r.h.		Aged in 45 %r.h.		Aged in 100 %r.h.	
Temperature (°C)	Time (min.)	2C Before	2C After	2C Before	2C After	2C Before	2C After
525	150	198.6	184.9	213	194.9	244	242.5
		187	172.1	209.3	187.6	244.4	243.1
		197.8	179.2	196.9	175.4	228.7	223.9
		183.9	169	208.2	190.2	244.4	238.5
		192.1	181.2	215.3	197.9	213.6	188.8
		193	185.2	219.1	200.5	228.2	209.5
525	180	185.7	189.6	204.5	195.2	219.6	219.5
		185	189.5	197.3	190.8	230.5	222.8
		184.2	187.7	213.5	202.1	227.8	219
		184.4	187.8	196.9	185.7	227.8	224.3
		181.8	185.7	210.9	203.9	225.6	221.3
		183	189.1	212.3	202.1	231.5	220

Table B.6 Crack lengths (μm) from conventional healing in soda-lime silica glass (Conventional Healing of Glass Experiment 6, Section 4.4.2.1.6).

Annealing Cycle		Aged in 0 %r.h.		Aged in 45 %r.h.		Aged in 100 %r.h.	
Temperature (°C)	Time (min.)	2C Before	2C After	2C Before	2C After	2C Before	2C After
575	60	188.7	179.7	213.4	198.6	235.4	185.8
		195.9	185.6	213.8	202	240.4	211.2
		187.2	177.7	215.8	200.5	236.9	211.2
		193.7	188.8	212.3	200.8	236.1	201.1
		193.8	187.5	208.2	194	243.1	196.1
		193.2	183.6	213.9	196.7	245.3	197.3
575	90	190.2	182.6	217	207.2	221.8	214.4
		181.4	172.6	216.9	206.1	220.7	210.4
		180.9	174	216.7	201.5	217.8	200.5
		190.6	183	211.7	198.5	220.8	214.9
		198.8	188.3	208.4	196.3	217.2	218.6
		197.6	189.2	208.6	198.4	231.7	232.2
575	120	186.9	183.2	201	165.4	218.7	212.8
		188.5	184.1	205.4	171.8	224.5	221.8
		182.7	181.9	206.5	174.7	220.6	216.2
		177.3	177.1	207	173.1	221.7	213.7
		185.2	179.3	204.8	174.2	230.6	220
		180	179.1	205.4	174.7	230.2	225.4
575	150	189.3	185.7	214.3	197.6	232.2	212.4
		188.8	184.5	213	195.7	232.8	209
		182.7	180.7	212.5	196.6	230.8	194
		170.1	168.7	212.1	193	224.4	198.5
		184.3	180.9	211.5	188.9	238.4	219.3
		179.3	177.2	211.3	190.6	237.7	209.3

Table B.7 Crack lengths (μm) from conventional healing in soda-lime silica glass (Conventional Healing of Glass Experiment 7, Section 4.4.2.1.7).

Annealing Cycle		Aged in 0 %r.h.		Aged in 45 %r.h.		Aged in 100 %r.h.	
Time (min)	Ramp Rate (°C/min)	2C Before	2C After	2C Before	2C After	2C Before	2C After
60	5	178	140.7	199.3	152	229.2	162.7
		190.2	151.7	203.2	155.6	237.1	184.8
		179.8	147.5	217.5	170.5	229.7	160.2
		178	149.3	212.8	164.1	239	181.7
		186.6	146.7	212.4	164.1	238.8	192.3
		188.9	153.6	214.5	173.3	231.5	186.6
60	5 and 2.5	187.8	154.5	213.5	171.5	234.6	187.5
		186.5	151.9	221.1	181.9	234.3	194.8
		185.4	154	212.1	170.7	203.9	170.6
		189.3	155.4	215.1	169.8	219.8	184.2
		186.3	153.6	212.4	169.3	230.3	193
		193.5	161.3	216.9	168.5	228.3	194.3
90	5 and 2.5	189.1	154	211.2	172.7	239.1	186.3
		190.6	154.6	198.8	141.7	228.2	175.3
		186.4	148.2	215.4	168.1	243.4	191.7
		185.2	149.9	213.9	165.9	243.7	190.3
		189.9	153.2	216	163.6	240.8	178.9
		193.9	154.6	219.3	168.1	236.3	178.1

Table B.7 (cont'd).

Annealing Cycle		Aged in 0 %r.h.		Aged in 45 %r.h.		Aged in 100 %r.h.	
Time (min)	Ramp Rate (°C/min)	2C Before	2C After	2C Before	2C After	2C Before	2C After
120	5 and 2.5	187.3	152.8	217.6	179.4	229.9	188.9
		175.9	143	208.4	171.4	231.8	190.9
		189.2	151.6	214.5	176.2	215.1	172.6
		185.1	148	213.2	167.2	228.8	187
		189	155	216	174.5	233.7	177
		188.6	155.6	200.2	157.1	219.5	174.7
240	5 and 2.5	172.1	128.9	188.2	117.2	224.4	165.7
		185.6	133.4	199.4	136.1	232.7	169
		176.4	123.3	204.1	138.9	243.7	167
		180.1	129.7	207.6	135.6	242.8	167.9
		186.5	134.1	204.8	132.8	228.6	165.1
		186.7	136.1	203.8	127.8	228.7	165.8
480	5 and 2.5	184.8	144.2	215.9	147.3	202.3	157.5
		186.2	140.4	213.1	142.6	196.6	144.4
		189.3	149.4	209.8	149.4	206.1	152.3
		184.5	143	201.9	144.9	209.2	157.7
		182.6	139.8	210.4	152.7	235	178.7
		186.4	147.8	205.6	138.6	231.7	175

Table B.8 Crack lengths (μm) from residual stress relief testing in soda-lime silica glass (Residual Stress Relief Cycle Testing, Section 4.4.2.1.8).

Heating Cycle Number	Before Cycle	After Cycle	Heating Cycle Number	Before Cycle	After Cycle
1	182.4	219.6	2	189.8	220.5
	203.6	220.4		193.1	222.5
	198.8	214.1		199.3	212.3
	203.7	204.6		204.8	210.9
	206.8	204.1		197.1	214
	207.1	220.5		205.6	219.2
	191.8	216		200.4	213.6
	207	222.1		201.7	210.9
	206.5	219.4		205.5	208.2
	210.3	210.9		205.9	215.7
	209.1	216.4		196.5	212.5
	203.8	213.4		191.8	213.8
	187	205.9		194.8	214.8
	191.3	215.4		198.3	214.9
	201.6	218.2		208.9	215.9
	206.7	216.2		206.6	220
	201.6	218.3		208.6	217.8
	206.6	217.7		205.5	214.7
	204.5	209.8		197.6	204.5
	195.2	219.5		205.8	217.9
	203.9	215		197.4	209.9
	206.9	211		182.5	209.5

Table B.8 (cont'd).

Heating Cycle Number	Before Cycle	After Cycle	Heating Cycle Number	Before Cycle	After Cycle
3	208.3	221.5	4	196.7	219.8
	200.5	216.4		191.5	224.4
	193.6	217.3		207	209.4
	204.7	220.4		205.2	217.5
	193.6	223.9		204.3	208.9
	187.6	219.3		200	205.1
	186.3	212.3		185	211.3
	212.8	221.7		195	221.6
	206.1	216		203.2	209.6
	206.9	216.7		204.6	210.9
	203.4	223.8		211.9	214.6
	206.3	224		209.1	212.7
	209.7	217.6		189.4	216.7
	211.1	215.6		204	212.1
	203.4	213.3		202.7	214.6
	203.7	221.9		191.4	215.9
	210.3	222.7		202.3	215.7
	200.6	220.7		189.1	216.8
	205.8	219.8		205.7	215.6
	205.2	222.4		207.1	217.1
	198.8	215.2		205.2	209.7
	202.5	216.7		203.6	219.9

Table B.8 (cont'd).

Heating Cycle Number	Before Cycle	After Cycle	Heating Cycle Number	Before Cycle	After Cycle
5	208.8	208.5	6	206.3	219.8
	211.3	213.1		211.7	219.5
	204.6	200.7		207.6	205.9
	203.9	208.3		206.6	220.5
	209.4	202.2		208.4	218.6
	208	208.1		201.4	220.3
	203.2	205.9		204.4	215.9
	195	202.7		209.1	216.3
	209.1	210.8		197.7	213.9
	212.5	215.2		201.3	211.3
	198.2	209.7		193	218.1
	203.5	208.5		196.3	224.3
	188	207.9		209.6	221.6
	208.7	209.3		210.9	221.2
	207.1	210.5		199.4	217.7
	213.9	215.2		192	215.6
	199.5	209.6		197.7	223
	205.7	211.5		204	221.3
	208.9	212.1		210.5	194.1
	206.7	207.5		209.9	215.3
	209.1	208.8		202.3	213.6
	206.5	197.3		202.6	207.4

Table B.8 (cont'd).

Heating Cycle Number	Before Cycle	After Cycle	Heating Cycle Number	Before Cycle	After Cycle
7	185.8	213.9	8	199.4	224
	193	213.1		198.8	224.1
	207.9	207.7		205.1	221.9
	207.5	215		200.8	224.4
	208.8	211.9		203.9	220.6
	201.4	214.6		203	224
	209.2	206.4		190.1	222.3
	207.5	213.1		200.9	223
	208.1	209.8		197.4	220
	209.5	208		198.1	216.7
	207.4	0		200.3	221.1
	209.1	0		205.2	222
	203.9	211.7		191.5	226.2
	207.9	208.7		196.9	222.6
	203.5	213.6		188.3	224.7
	205.4	216.2		198.3	220.7
	207.3	212.5		198.7	220.4
	206.1	216.3		177.3	221
	185.6	211.6		189.2	219.3
	196.7	215.7		192.2	223.4
	210.2	212.2		200.3	222.8
	208.4	214.2		204.2	218

Table B.8 (cont'd).

Heating Cycle Number	Before Cycle	After Cycle	Heating Cycle Number	Before Cycle	After Cycle
9	203.6	207.1	10	215.3	217.1
	203.3	209.5		208.2	223.8
	199	222.5		207.3	194.9
	209	225.7		191.8	223.6
	205.5	222.6		213.7	225.5
	198.3	222.7		213.9	223.2
	199.2	230.5		211.6	230.7
	196.4	231.4		214.1	230.1
	197.6	227.2		209.8	206.9
	204.9	228.9		208.6	227.3
	201.8	222.7		202.9	227.1
	194.8	213.2		192.4	226.5
	196.1	214.9		196.9	225.6
	207.4	222.4		206	232.1
	196.2	216.5		201.4	222.1
	197.7	208.8		190.5	231.9
	180	226.6		216.3	225.9
	196.9	222.2		212.5	222.1
	203.6	223.7		216.8	222.4
	207.7	218.3		211.4	217.9
	170.2	221		205.2	222.4
	190	225		212.3	228.2

Table B.9 Crack lengths (μm) from conventional healing of alumina at a nominal temperature of 1005 °C (Conventional Healing of Alumina Experiment 1, Section 4.4.2.2.1). (N.A. indicates Not Applicable and N.M. indicates Not Measured)

Second 24 hr. Aging (% r.h.)	Coors Alumina				Microwave Sintered Alumina			
	30 min.	24 hr.	48 hr.	After Anneal	30 min.	24 hr.	48 hr.	After Anneal
0	279.4	276.6	267.8	253.6	363.1	389.3	391.4	362.6
	264.1	277.6	265.6	255	387	399.6	398.2	361.8
	277.3	292.1	293.5	270.2	373.7	376.7	378.3	369.9
	270.8	270.6	267.3	236.6	398.2	402.6	403.3	358.4
	268.7	286	276.3	260.8	408.2	443.7	442.1	403.3
	270.8	287.4	272	265.8	433	432.8	430.7	363.2
	275.6	272.1	N.A.	255.7	362.2	356.2	N.A.	343.8
	267.5	274.2	N.A.	246.2	364.3	375.1	N.A.	355.1
	264.5	275.5	N.A.	247.7	390	409.5	N.A.	387.2
	246.3	243.1	N.A.	218.9	352.7	353.9	N.A.	352.4
	277.7	267.5	N.A.	250.9	383.8	395.1	N.A.	376.7
	283.5	285.5	N.A.	260.5	384.3	379.6	N.A.	361.8

Table B.9 (cont'd)

Second 24 hr. Aging (% r.h.)	Coors Alumina				Microwave Sintered Alumina			
	30 min.	24 hr.	48 hr.	After Anneal	30 min.	24 hr.	48 hr.	After Anneal
45	292.2	289.5	286.6	268.2	348.3	358.2	351.3	353
	298.4	274.8	277.5	263	402.4	403	399.9	399.1
	293.6	294.1	282.2	250.3	408.3	412.5	412.1	403.3
	276.4	281.9	276	243.2	379.8	411	409.9	403.4
	314.3	307.6	291.8	269	283.1	310.4	302.9	305.1
	289.2	286.4	286.3	267.2	350.2	343.2	341.2	321.3
	281.7	280.5	N.A.	269.9	345.9	349.2	N.A.	352.9
	262.5	281.8	N.A.	268	422.6	416.6	N.A.	372.4
	277.3	292.6	N.A.	248.3	430.3	453.3	N.A.	417.6
	280.1	287.1	N.A.	258.3	397.8	407.7	N.A.	425.8
	297.7	307.4	N.A.	296.5	440	440.5	N.A.	399.2
	276.5	279.1	N.A.	270.7	397.9	402.2	N.A.	339
100	291.8	292.9	296.6	263.4	309.5	319.5	331.2	335.3
	288.9	297.2	309.6	247.6	252.1	250.8	257.9	253.1
	265.5	270.3	274.4	239.8	389.9	394.7	399.4	353.8
	293.6	302	288	279.4	397.9	390.8	398.6	330.2
	275.9	298.9	292.7	253.4	380.8	386.6	394.5	371
	289.9	296.7	298.9	256.1	406.2	412.5	412.1	398.5
	302.2	295.5	N.A.	212	379.6	403.2	N.A.	346
	274.8	303.4	N.A.	274.6	404.7	400.7	N.A.	371
	285.5	298.7	N.A.	221	383.7	382.3	N.A.	369
	281.3	286.7	N.A.	266.2	362.6	393.7	N.A.	379
	288.8	292.6	N.A.	240.3	389.3	403.9	N.A.	374.7
	265.6	285.6	N.A.	239.9	336.7	376.9	N.A.	292.3

Table B.10 Crack lengths (μm) from conventional healing of alumina at a nominal temperature of 1237 °C (Conventional Healing of Alumina Experiment 1, Section 4.4.2.2.1). (N.A. indicates Not Applicable and N.M. indicates Not Measured)

Second 24 hr. Aging (% r.h.)	Coors Alumina				Microwave Sintered Alumina			
	30 min.	24 hr.	48 hr.	After Anneal	30 min.	24 hr.	48 hr.	After Anneal
0	280.4	307.3	309.5	207.4	428.3	438.2	430.9	270.5
	283.6	286.1	286.3	186.8	380.3	290.6	389.5	277.1
	291.7	298.6	303.9	190.3	361	361.3	361.3	296.8
	278	285.5	284.5	186.3	366.5	384	384	275.6
	288.9	294.8	287.6	168.4	401.5	400.9	400.9	269.5
	284	284.9	286.9	172.4	407.5	406.3	406.3	248.7
	273.7	286	N.A.	201.8	413.5	420.9	N.A.	268.7
	281.9	284.9	N.A.	231.2	401.1	417.7	N.A.	347.6
	280	287.9	N.A.	194.2	442.5	361.4	N.A.	256.5
	260.3	299.7	N.A.	155	391.3	387	N.A.	319.7
	289.9	303.8	N.A.	186	380	398.8	N.A.	300.6
	276.7	293.3	N.A.	227.9	428.7	447.9	N.A.	325.7

Table B.10 (cont'd)

Second 24 hr. Aging (% r.h.)	Coors Alumina				Microwave Sintered Alumina			
	30 min.	24 hr.	48 hr.	After Anneal	30 min.	24 hr.	48 hr.	After Anneal
45	250.5	0	309.7	239.6	N.M	223.6	262.1	230.5
	248.8	0	296.4	209.8	N.M	220	224.4	192.6
	260.7	277.8	293.9	237.1	N.M	252.5	249.8	247.3
	246.6	290.5	291.4	216.8	N.M	245.5	242	220.7
	N.M.	N.M.	N.M.	N.M.	N.M	274.8	287	220.3
	N.M.	N.M.	N.M.	N.M.	N.M	223.7	225.5	185.3
	N.M	290.3	N.A.	250.4	N.M	254.2	N.A.	194.4
	N.M	266.3	N.A.	217.4	N.M	275.5	N.A.	219.8
	N.M	294.6	N.A.	243.4	N.M	249.9	N.A.	238
	N.M	294	N.A.	231.7	N.M	202.9	N.A.	207.2
	N.M.	N.M.	N.M.	N.M.	N.M.	N.M.	N.M.	N.M.
	N.M.	N.M.	N.M.	N.M.	N.M.	N.M.	N.M.	N.M.
100	305.5	307.3	299.2	266.3	411.9	414.1	415.4	387.3
	284.6	294.9	280.9	242	430.2	430.9	425.4	373
	300.8	315.3	295.5	251.7	359.7	356.5	354.3	357.6
	293.3	305.6	296.9	256.2	367.3	375.6	366.2	362.3
	293.5	300.4	288.4	284.6	393.9	412	415.2	401.1
	301.3	301.6	293.6	263.8	424.2	448.6	450.4	376.5
	295.3	278.6	N.A.	263.5	399.7	403.2	N.A.	347.3
	311.2	299.2	N.A.	259.3	413.4	421.7	N.A.	424.5
	290.7	283.5	N.A.	283.8	453	454.6	N.A.	426.6
	290.9	287.7	N.A.	265.1	403.9	427	N.A.	413.9
	281.7	289.2	N.A.	270.7	380	391	N.A.	271.1
	318.4	307.2	N.A.	258.6	387.5	375.9	N.A.	323.6

Table B.11 Crack lengths (μm) from conventional healing of alumina at a nominal temperature of 1469 °C (Conventional Healing of Alumina Experiment 1, Section 4.4.2.2.1). (N.A. indicates Not Applicable and N.M. indicates Not Measured)

Second 24 hr. Aging (% r.h.)	Coors Alumina				Microwave Sintered Alumina			
	30 min.	24 hr.	48 hr.	After Anneal	30 min.	24 hr.	48 hr.	After Anneal
0	293.4	293.4	305.2	164	377.9	378.6	377.2	365.1
	284.2	291.5	293.3	166	365.5	365	365.3	365
	297.9	298.2	301.1	157.1	424.9	424.4	420.9	384.5
	301.6	301.4	300.2	173.9	420.6	420	418.7	348.8
	288.5	282.3	283.2	213.7	355	378.1	346	309.7
	307.7	302.8	305.7	151.9	349.3	366.3	373.5	315.8
	278.1	278.4	N.A.	183.1	374.5	378	N.A.	346.6
	280.9	296.7	N.A.	168.6	395.7	417.9	N.A.	392.5
	289	289.9	N.A.	165.2	394	400.4	N.A.	352.2
	289.4	304	N.A.	179.2	380	384.4	N.A.	351.8
	288.7	313.8	N.A.	163.2	374.2	380.4	N.A.	357.8
	296	305	N.A.	169.8	330.6	342.3	N.A.	288.5

Table B.11 (cont'd)

Second 24 hr. Aging (% r.h.)	Coors Alumina				Microwave Sintered Alumina			
	30 min.	24 hr.	48 hr.	After Anneal	30 min.	24 hr.	48 hr.	After Anneal
45	N.M	N.M	298.8	190.7	N.M	N.M	249.4	214.4
	N.M	N.M	296.3	126.7	N.M	N.M	236.3	229.5
	N.M	N.M	270.6	155.6	N.M	N.M	261.4	313
	N.M	N.M	285.2	135	N.M	N.M	262.8	258.1
	N.M	N.M	281.6	163.4	N.M	N.M	249.6	220.5
	N.M	N.M	287.6	167.7	N.M	N.M	212.3	201.5
	N.M	302.3	N.A.	91.2	N.M	409.8	N.A.	309.5
	N.M	279.3	N.A.	99.4	N.M	377.8	N.A.	303.1
	N.M	307.4	N.A.	128.5	N.M	394.9	N.A.	309.2
	N.M	293.7	N.A.	137.6	N.M	284.3	N.A.	215.1
	N.M	291.1	N.A.	154.2	N.M	376.3	N.A.	266.7
	N.M	270	N.A.	114.8	N.M	347.5	N.A.	319.3
100	N.M.	299.9	288.4	178	N.M.	395.8	405.2	262
	N.M.	289.4	293.3	170.6	N.M.	405.6	405.2	268.9
	N.M.	306.8	310	187.8	N.M.	382	395.8	337.9
	N.M.	311.6	304.7	182.5	N.M.	431	442.2	305.3
	N.M.	272.4	285.2	206.2	N.M.	362.5	388.2	305.3
	N.M.	297.9	300.7	177.5	N.M.	392.1	388	320.9
	294	311.5	N.A.	188.2	392.4	417.7	N.A.	358.7
	270	275.4	N.A.	174.7	382.3	399.8	N.A.	336.8
	292.8	302	N.A.	177.1	409	437.4	N.A.	404.3
	287.8	290.8	N.A.	174.6	429.4	445.3	N.A.	375.7
	293	301.2	N.A.	202.2	377.7	399.2	N.A.	321.2
	268.9	287.8	N.A.	165.7	425.2	408.6	N.A.	351.3

Table B.12 Crack lengths (μm) from conventional healing in Coors alumina (Conventional Healing of Alumina Experiment 2, Section 4.4.2.2.2).

Annealing Cycle		Aged in 0 %r.h.		Aged in 45 %r.h.		Aged in 100 %r.h.	
Temperature (°C)	Time (min.)	2C Before	2C After	2C Before	2C After	2C Before	2C After
1005	60	258.4	208.8	253.3	216.1	282	187.7
		279.1	215	284.2	245.4	269.9	183
		285.4	226.6	258.6	191.1	259.6	193.1
		288	229.4	296.7	239.3	270.4	221.4
		256.1	219.9	263.7	217.7	254.4	185.6
		283.8	224.6	278.4	231.4	269.2	218.6
1005	90	262.3	178.5	278.4	170.1	283.3	204
		272	179.6	272.7	189.1	273.5	197.7
		269.1	169.2	294.6	178.6	289.5	191.6
		306.2	167.6	291.9	197.5	282.5	194.3
		267.4	176.1	278.8	208.7	292.2	209.4
		298.2	176.1	299.4	220.4	290.2	204.7
1005	120	283.3	190.2	281.1	187.9	289.1	179.7
		264.9	185	264.8	186.5	307.2	178
		270.2	177.8	273.7	199.7	268.9	179
		279.5	190.9	273.5	203.5	289	190.2
		270.1	200.2	263.3	187	270	166.1
		264.9	165.4	262.5	180.1	291.1	191
1037	1410	268.8	171.7	286.6	187.3	272.9	163.6
		258.2	132.1	268.9	176.7	276.4	176.8
		262.1	168.7	273.5	166.9	272.6	177.6
		272.1	168.1	287.1	160.5	247.2	113.9
		265.1	136.9	296.1	181.5	279.4	156.8
		264.7	156.7	270.6	163.2	282.5	155.4

Table B.12 (cont'd).

Annealing Cycle		Aged in 0 %r.h.		Aged in 45 %r.h.		Aged in 100 %r.h.	
Temperature (°C)	Time (min.)	2C Before	2C After	2C Before	2C After	2C Before	2C After
1121	60	275.9	207.7	279.1	221.3	283.7	207.3
		274.3	201.3	298.6	203	282.4	214.2
		295.1	199.2	307.5	233.6	272.8	199.2
		277.7	199.6	291.8	208.8	286.9	197.2
		284.5	207.7	268.3	204.4	258.9	188.4
		290.8	216.8	255.2	214.3	265.8	214
1121	90	271.8	159.5	282.9	190.4	291.6	177.6
		287.4	166.7	264.8	194.1	283	175.4
		276.5	186.4	300	175.7	272.8	161.2
		274.8	188.8	294.4	158.3	291.2	182.2
		260.3	169.2	287.9	179.5	290	167.2
		275.3	179.1	273.1	175.9	271.4	171
1121	120	276.3	175.9	298.5	182.2	259.4	202.7
		297	171.4	290.8	164.1	259.3	153
		284.9	179.3	282.1	188.6	295.4	185.4
		290.2	190.5	282.9	183.5	298.7	228.7
		292.8	205.2	271.9	164.3	283.6	168.1
		301	191.8	291.5	167.4	279.1	195.6
1237	60	289.3	199.9	274.2	211.8	287.5	180.5
		287.1	208.3	255.7	194.7	303.7	217.3
		271.2	198.8	272	201.3	296	199.6
		290.4	195.2	289.9	191.8	279	178.9
		301.4	213.5	255.4	209.9	297.1	181.1
		275	198.5	274.8	192.2	297.7	177.1

Table B.12 (cont'd).

Annealing Cycle		Aged in 0 %r.h.		Aged in 45 %r.h.		Aged in 100 %r.h.	
Temperature (°C)	Time (min.)	2C Before	2C After	2C Before	2C After	2C Before	2C After
1237	90	279.4	154.1	293.4	169.8	302.5	167.3
		290.5	168.8	274.3	181.3	279	155.7
		299.8	169.6	290.5	124.9	297.4	172.9
		296.8	165.9	292.7	164.3	296	172.8
		276.9	158.5	306.9	121	297.2	172.6
		291.5	146.4	312	161.1	296.1	174.8
1237	120	289.7	169.5	293	154.2	273.8	160.6
		264.9	181.8	268.6	170.2	296	164.2
		261.9	156.6	283.3	155.4	273.8	148.3
		289.8	136.9	259.5	157	289.2	164.7
		292	151.8	285.9	124.5	259.3	155.7
		272.8	160.9	279.9	169.8	266.7	184.4
1237	180 a	250.6	195.4	264.3	189.7	270.4	164.3
		263.2	174.7	276.4	193.3	268.6	160.3
		264.4	180.6	275.6	174.3	279.7	195
		250.6	162.8	258	170.3	255.8	178.1
		268.7	172.1	267.2	191.7	267.9	163.4
		265.1	170.8	285.1	176.3	270.8	134.1
1237	180 b	275	209.3	281	166.2	271.4	151.2
		270	196.9	279	166.3	295.7	163.4
		267	184.9	274.3	182.9	299.3	184.9
		281.7	181.2	280.3	157.4	274.8	168.9
		251.4	164.8	278.8	193.2	272.4	147.4
		263.6	164.8	264.5	195.9	288.8	166.3

Table B.12 (cont'd).

Annealing Cycle		Aged in 0 %r.h.		Aged in 45 %r.h.		Aged in 100 %r.h.	
Temperature (°C)	Time (min.)	2C Before	2C After	2C Before	2C After	2C Before	2C After
1353	60	261.8	189	294.3	162.9	289.4	189.7
		259	194.4	292.6	172.3	269.1	181.4
		286.1	149	279.2	188.6	279.8	195.7
		278.6	162.2	278.8	163.6	271.8	180.2
		277.2	168.5	293.3	145.5	286.8	158.3
		272.1	163	297.8	144.8	277.5	167.6
1353	90	286.7	135.8	295.2	136.3	299.3	177.5
		271.4	116.2	283.7	146.4	296.4	115
		291.7	158.8	289.3	155.4	269.2	125.1
		280.5	116.9	281.2	125.4	295.4	135.4
		275.9	152.7	282.2	148.1	292.2	148.8
		300.9	123.5	292	136.3	320.5	113.2
1353	120	269.3	118.7	269.6	132.7	264.5	134.7
		279.1	117.3	288	163.8	273.1	138.8
		283.4	148.9	280.7	143.9	175	149.3
		291.5	133.2	290.6	142	293.5	141.9
		263.6	147.4	276.4	138.3	287.5	144.6
		287.4	155.7	276.4	101.3	281.2	141.2
1469	60	281.4	161.2	286.1	133.3	265.7	97.8
		274.7	106	282.7	150.1	263.4	144.7
		268	133	272.7	121.7	261.7	132.5
		270.9	120.9	275.5	130.1	270.9	116.4
		286	106.7	264.5	149.9	259.6	122.7
		265.7	95.8	274.1	104.4	280.1	107.2

Table B.12 (cont'd).

Annealing Cycle		Aged in 0 %r.h.		Aged in 45 %r.h.		Aged in 100 %r.h.	
Temperature (°C)	Time (min.)	2C Before	2C After	2C Before	2C After	2C Before	2C After
1469	90	270.9	139.4	269	85.6	304.5	119.6
		293	139.4	288.7	108.6	268.3	129.4
		277.4	162.9	276.1	99	281.8	89.2
		255.7	139.2	266.8	98.1	280.8	76.3
		266.4	116.4	282.6	138.9	273.8	116.4
		278.1	101.3	300.6	99.1	286.2	93.8
1469	120	280.4	95.5	278.2	86.4	268.7	106.7
		253.3	86.7	271.6	111.9	275.6	106.2
		287	124.5	271.7	87.1	282.9	134
		268.5	96.6	262.3	91.6	288.9	90.3
		288.2	124.3	278.8	103	280.2	132.4
		281.9	78	256.3	109.6	283.1	91.3

Table B.13 Crack lengths (μm) from conventional and microwave healing in Coors alumina (Microwave Healing of Alumina, Section 4.4.3).

Annealing Cycle			49 N Indent		98 N Indent	
Temperature (°C)	Heating Type	Heating Rate (°C/min.)	2C Before	2C After	2C Before	2C After
1237	Conventional	10	278.4	253.5	469.8	415.2
			291.3	231.6	431.4	372.2
			286.7	266.3	447.8	352.7
			299	236.9	456	262.7
			287.3	224.5	465.4	414.9
			294.4	224.1	466	365.5
	Microwave	10	292	259.3	440.6	400
			258.8	232.2	461.3	386.4
			287.4	249.5	431.9	374.3
			283.3	231.7	463.3	347.3
			275.8	223.7	469.8	389.2
			291.1	210.5	447.1	384.4
	Microwave	75	319.2	239.6	437.5	358.8
			300.9	203.8	484.1	348.8
			295.1	197.6	480.4	387.1
			296.8	198.1	449.2	366.8
			282.6	214.7	451.8	329.7
			305.2	237.1	435.9	349.5

Table B.13 (cont'd).

Annealing Cycle			49 N Indent		98 N Indent	
Temperature (°C)	Heating Type	Heating Rate (°C/min.)	2C Before	2C After	2C Before	2C After
1295	Conventional	10	306.9	273.8	454.6	359.4
			306.66	245.7	457	381.4
			305.9	253.3	441.5	397.6
			289.8	204.7	464	365.5
			297.6	241.3	466.6	397.4
			269.8	198.5	450.7	371.2
	Microwave	10	291.3	189.8	394.1	270
			308.5	231.7	430.8	315.7
			296.7	224.4	418.8	307.9
			284.5	207.9	448.5	334
			282.3	211.4	458.8	361.6
			299.4	192.7	466.4	342.7
	Microwave	75	301.1	204.1	476	370.2
			297.5	213.9	450.4	354.7
			290.8	219.3	488.2	414.2
			273.1	209.8	469.4	312
			296.6	245.8	447.2	348.9
			291.1	247.4	409.4	362

Table B.13 (cont'd).

Annealing Cycle			49 N Indent		98 N Indent	
Temperature (°C)	Heating Type	Heating Rate (°C/min.)	2C Before	2C After	2C Before	2C After
1353	Conventional	10	306.8	243.8	493.6	452.8
			293.8	240.7	498.2	414.6
			291.2	235.3	490.7	441
			276.4	238.4	479.8	442.1
			284	219.1	489.4	420.7
			287.3	242.7	465.5	385.2
	Microwave	10	274.3	152.2	448.8	318.2
			306.3	138.2	457.7	278.8
			279.6	128.6	450.3	260.7
			285.7	113.4	467.8	279.2
			294.5	158.3	442.9	247.1
			305.6	146.1	448.7	278.6
	Microwave	75	268.7	177	486	330.2
			278.7	170.3	463.6	296.5
			299.8	231.7	454.9	326
			273.8	172.9	458.5	271.3
			292.3	225.7	457.7	325.4
			276.5	166.3	437.8	277.1

Table B.13 (cont'd).

Annealing Cycle			49 N Indent		98 N Indent	
Temperature (°C)	Heating Type	Heating Rate (°C/min.)	2C Before	2C After	2C Before	2C After
1411	Conventional	10	284.4	190.2	420.1	322.2
			279	224	484.5	350.5
			256	208.7	453.3	354.2
			291.6	216	442.7	326.9
			283.4	236.3	434.5	348.5
			282.4	205.7	483.2	334.9
	Microwave	10	285.1	75	446.6	107
			265.2	75	431.1	107
			285.6	75	448.5	107
			264	75	445.9	107
			281.4	75	437.5	107
			263.1	75	460.6	107
	Microwave	75	281.8	191.4	464.5	239.6
			284.4	157.6	462	263
			272.6	130.4	482.9	250.9
			304.5	135.5	468.1	263
			296.5	173.8	469.7	233.8
			293.8	123.5	461.2	249.1

Table B.13 (cont'd).

Annealing Cycle			49 N Indent		98 N Indent	
Temperature (°C)	Heating Type	Heating Rate (°C/min.)	2C Before	2C After	2C Before	2C After
1469	Conventional	10	274.4	176.9	462.9	347.2
			315.8	180.5	455.9	255.8
			291.3	210.1	443.5	301.5
			289.7	199.8	439.3	286.5
			276.2	190.5	442.4	338.1
			294.7	190.5	445.4	279.7
	Microwave	10	285.1	76.7	446.6	110.9
			265.2	71.9	431.1	102.2
			285.6	79.5	448.5	108.3
			264	77.1	445.9	107.7
			281.4	71.8	437.5	108.5
			263.1	73.1	460.6	105.5
	Microwave	75	265.2	127	469.8	180.6
			264.6	66.2	445.8	128
			282.8	87.4	443	211.3
			268.1	81.7	428.1	189.7
			265	218.2	448.5	155.1
			279.8	102.6	437.6	169.9